ABSTRACT

Title of Dissertation:	NONLINEAR SEISMIC PERFORMANCE OF SELF-CENTERING ECCENTRICALLY BRACED FRAME STRUCTURES WITH REPLACEABLE HYSTERIC DAMPER
	Arshia Keivan Esfahani, Doctor of Philosophy, 2018
Dissertation directed by:	Professor, Yunfeng Zhang, Department of Civil and Environmental Engineering

The focus of this dissertation is on numerical simulation study of self-centering eccentrically braced frame (SCEBF) buildings subjected to seismic ground motion. Self-centering EBF with replaceable fuse devices can be designed to provide the strength and stiffness comparable to conventional steel EBFs while maintaining plumbness and sustaining repairable structural damage concentrated to seismic fuse devices under design basis earthquakes.

This study aims to investigate the seismic system behavior of three common configuration types of self-centering EBFs including the K-type, D-type, and Y-type

SCEBFs. Analytical formulas are derived for the key strength and stiffness values of these three types of SCEBF module frames. Two different types of finite element models, one with refined meshes in ANSYS and another with primarily frame members in SAP2000, are developed and calibrated with experiment data. Comparison with analytical results further verifies the finite element models. In addition to nonlinear static analysis results, the nonlinear time history analysis results show that residual drifts of the SCEBFs are negligibly small and damages in the structure are concentrated to hysteric damper under design basis earthquakes. Additionally, a parametric study of the three types of SCEBFs with three different levels of PT cables' initial stress has been done to validate the approach to tuning the self-centering EBF's seismic behavior. The parametric study results suggest that key structural parameters such as the equivalent yield strength and the post-gap opening stiffness of SCEBFs can be adjusted through properly selecting post-tensioning cable' length and initial stress levels.

A new metallic hysteric damper called TPAD was developed to be utilized in proposed SCEBF structures. TPAD is a trapezoidal plate connected to a round rod, and its design is inspired by the design of TADAS devices [1]. It is optimized based on fracture investigation [2] through parametric studies. In parametric studies, cyclic loading has been applied to TPADs with different properties to investigate the overall behavior of TPADs. It is found that TPAD's height (h), slope ratio (α) and thickness (t) significantly affect the ductility of TPAD.

NONLINEAR SEISMIC PERFORMANCE OF SELF-CENTERING ECCENTRICALLY BRACED FRAME STRUCTURES WITH REPLACEABLE HYSTERIC DAMPER

by

Arshia Keivan Esfahani

Dissertation submitted to the Faculty of the Graduate School of the
University of Maryland, College Park, in partial fulfillment
of the requirements for the degree of
Doctor of Philosophy
2018

Advisory Committee:
Prof. Yunfeng Zhang, Chair
Prof. Amde M. Amde
Prof. Bilal M. Ayyub
Prof. Sung Lee
Prof. Chung C. Fu

Dedication

It is my genuine gratefulness and warmest regard that I dedicate this work to my always encouraging, ever faithful parents, and to my supportive, kind-hearted brothers and my beloved wife.

Acknowledgments

I would like to express my gratitude to my advisor, Professor Yunfeng Zhang for his patience, guidance and encouragement during this study. I learned a lot from him over the past four years, and it was my privilege to work under his supervision. Professor Zhang granted me an opportunity to work on numerous interesting research projects, and he taught me how to be a professional engineer and researcher which has been an exceptional and unforgettable experience for me. My Ph.D. program at University of Maryland at College Park has been as ideal as it can be, and I owe all of that to my supportive, intelligent advisor for which I am deeply thankful.

I gratefully acknowledge the efforts of my dissertation committee, Professor Amde M. Amde, Professor Bilal M. Ayyub, Professor Sung Lee and Professor Chung C. Fu for their contribution in my research studies and their insights and comments.

Furthermore, I want to thank my friend at University of Maryland, Heng Liu. It has been a wonderful experience for me to work and study with him and his friendship and support is deeply appreciated.

Finally, I appreciate all the support, love and encouragement from my beloved wife, my parents and my brothers without whom I would not be a person I am today. I am so blessed to have them in my life, and I am very grateful for all their support. Special thanks to my parents and my wife for inspiring me with a great passion for learning

and for doing everything possible to put me on the path to greatness. Words cannot express how important you are to me. I love you all!

Table of Contents

Dedication ii
Acknowledgements iii
Table of Contents v
List of Tables ix
List of Figures xi
List of Abbreviations xxiii
Chapter 1 Introduction 1
1.1 Introduction 1
1.2 Research Motivation 3
1.3 Research Objectives 5
1.4 Organization of the Dissertation 6
Chapter 2 Literature Review 10
2.1 Conventional Eccentrically Braced Frame 10
2.2 Self-Centering structures 12
2.2.1 Self-Centering Moment Resisting Frame (SCMRF) 12
2.2.2 Self-Centering Eccentrically Braced Frame (SCEBF) 13
2.2.3 Other Types of Self-Centering Structures 19
2.3 Replaceable Hysteric Damper 20
Chapter 3 Background 30
3.1 Conventional Eccentrically Braced Frame 30
3.2 Self-Centering structures 31
3.3 Experimental Test Verification 32
3.4 Finite Element Simulation 38

3.4.1 Shear Link Model of CEBF in SAP2000 38

3.4.2 Material and Loads 40

Chapter 4 Seismic Performance Evaluation of D-type SCEBF 59
4.1 Prototype SCEBF-D Type Buildings and Seismic Design 59

4.2 SCEBF-D Type Analytical Formula 61

4.3 Numerical Model of CEBF-D & SCEBF-D 68

4.4 Nonlinear Static Analysis 71

4.5 Nonlinear Time History Analysis 74

4.5.1 Global and Local Deformation Demand 74

4.5.2 Parametric Study 75

4.5.3 Typical Case 79

Chapter 5 Seismic Performance Evaluation of K-type SCEBF 110
5.1 Prototype SCEBF-K Type Buildings and Seismic Design 110

5.2 SCEBF-K Type Analytical Formula 112

5.3 Numerical Model of CEBF-K & SCEBF-K 119

5.4 Nonlinear Static Analysis 122

5.5 Nonlinear Time History Analysis 124

5.5.1 Global and Local Deformation Demand 125

5.5.2 Parametric Study 126

5.5.3 Typical Case 130

Chapter 6 Seismic Performance Evaluation of Y-type SCEBF 161
6.1 Analytical Formulation of SCEBF-Y Structural Property and Seismic Design

..... 161

6.1.1 Properties of SCEBF-Y Module Frame 161

6.1.2 Comparison of Finite Element Analysis and Analytical Results 167

6.1.3 Prototype SCEBF-Y Building 168

6.2 Numerical Modeling of SCEBF-Y Structure 172

6.3 Nonlinear Static Analysis 174

6.4 Nonlinear Time History Analysis: Results and Discussion 176

6.4.1 General Response 177

6.4.2 Parametric Study 177

6.4.3 Typical Case 181

Chapter 7 Parametric Study of Replaceable hysteric Damper 212

7.1 CVGM method for TPAD 213

7.2 Calibration of CVGM model 216

7.3 Analytical formula 217

7.4 Parametric study 218

7.4.1. Effect of TPAD length ($\boldsymbol{h}$) 220

7.4.2. Effect of TPAD plate thickness ($\boldsymbol{\beta}$) 221

7.4.3. Effect of TPAD tongue plate length ($\boldsymbol{k}$) 222

7.4.4. Effect of friction coefficient ($\boldsymbol{fs}$) 222

7.4.5. Effect of TPAD slope ratio ($\boldsymbol{\alpha}$) 223

7.4.6 Guideline for making optimal TPAD device based on parametric study 224

Chapter 8 Conclusions and Future Studies 254

8.1 Conclusions 254

8.2 Future Studies 257

Appendix 259
References 280

List of Tables

Table 3.1 Specimen labeling and features 45

Table 3.2 Calibrated plastic hardening parameters for Q345 steel and low yield steel Q225LY in finite element simulation 45

Table 3.3 Member dimensions and nominal first yield moment My and axial load capacity Ne..... 46

Table 4.1 Member sections of conventional 3-story D-type EBF (CEBF-D) 83

Table 4.2 Member sections and PT cables of 3-story self-centering D-type EBF (SCEBF-D) 83

Table 4.3 Earthquake ground motion records..... 84

Table 5.1 Member sections of conventional 4-story K-type EBF (CEBF-K) 133

Table 5.2 Member sections and PT cables of 4-story self-centering K-type EBF (SCEBF-K) 133

Table 5.3 Earthquake ground motion records..... 134

Table 6.1 Structural member sections of the prototype Y-type self-centering EBF building frame (unit: mm)..... 184

Table 6.2 Member sections of conventional 3-story D-type EBF (CEBF-D) 184

Table 6.3 Member section size of the 3-story Y-type self-centering EBF frame..... 185

Table 7.1 TPAD parametric study 225

List of Figures

Figure 2.1 Post-tensioned connection test setup (Ricles, Sause [24]) 21

Figure 2.2 Hysteresis force-displacement relationship (Ricles, Sause [24]) 21

Figure 2.3 Frame response to the Chi-Chi maximum considered earthquake (Rojas, Ricles [25])..... 22

Figure 2.4 SC-EBF test setup (Cheng, Hsu [28]) 22

Figure 2.5 Experiment hysteresis force-displacement (Cheng, Hsu [28])..... 23

Figure 2.6 Proposed self-centering link using PT composite tendons (Xu, Zhang [59]) 23

Figure 2.7 Prototype self-centering EBF (Xu, Zhang [59])..... 24

Figure 2.8 (a) Configuration of the proposed eccentrically bracing frame system, (b) Details of the proposed system, (c) The SMA wires in the SMA device (Massah and Dorvar [48]) 24

Figure 2.9 Schematic of the hysteresis behavior of the SMA wires in the SMA device (Massah and Dorvar [48])..... 25

Figure 2.10 Schematics of self-centering wall (Hu, Zhang [51]) 25

Figure 2.11 Self-Centering precast concrete wall systems (Seo and Sause 2005) 26

Figure 2.12 Schematics of the SC-CBF system (Sause et al. 2010)..... 26

Figure 2.13 ADAS damper performance during earthquake (units: mm) (Alehashem, Keyhani [54]) 27

Figure 2.14 TADAS damper performance during earthquake (units: mm) (Alehashem, Keyhani [54]) 27
Figure 2.15 TADAS in the device to brace connection (Tsai, Chen [1]) 28
Figure 2.16 Details of steel welded TADAS device (units: mm)-(Tsai, Chen [1]) 28
Figure 2.17 Force versus deformation relationship of typical welded TADAS devices (Tsai, Chen [1]) 29
Figure 2.18 Force-deformation relationship in a frame system with TADAS 29
Figure 3.1 Schematic view of experimental test for D-type SCEBF 46
Figure 3.2 Experimental test setup for SCEBF: (a) Picture; (b) Schematics of RHD devices installed to rocking link beam; pictures of vertical RHD and horizontal RHD; (c) Picture of PT cable anchoring fixture with PT force sensor mounted on the short protruding beam. (Tong, Zhang [50]) 48
Figure 3.3 Instrumentation layout of displacement transducers and strain gauges for Specimen SCEBF1 (Tong, Zhang [50]) 49
Figure 3.4 Loading history (Note: Figures in brackets represent the number of cycles at corresponding peak drift) (Tong, Zhang [50]) 49
Figure 3.5 Specimen SCEBF5 at 2.5% drift ratio: (a) Picture of rotated link beam and PT cables; (b) Picture of yielded RHD plates with flaked white wash (Tong, Zhang [50]) 50
Figure 3.6 Base shear versus lateral drift ratio curves of all test specimens subjected to cyclic loading (Tong, Zhang [50]) 51
Figure 3.7 Schematic view of shear link model 52

Figure 3.8 Force-deformation relationship for parallel translational springs 52

Figure 3.9 SAP2000 shear link modal 52

Figure 3.10 Finite element (FE) simulation of SCEBF2 under cyclic loading: (a) Meshed FE model; (b) push-over curve from nonlinear FE analysis (Tong, Zhang [50])..... 53

Figure 3.11 Experimental model in ANSYS 54

Figure 3.12 Experimental model in SAP2000 54

Figure 3.13 Pushover curve of experiment test (SCEBF1)..... 55

Figure 3.14 Pushover curve of experiment test (SCEBF2)..... 56

Figure 3.15 Link and fuse device configuration when gap opening happens..... 57

Figure 3.16 RHD device-Von misses stress at 2% drift ratio 57

Figure 3.17 RHD device Von Mises Plastic strain at 2% drift ratio..... 58

Figure 3.18 Von Mises Plastic strain at 2% drift ratio..... 58

Figure 4.1 Rocking link and PT cables in SCEBF test specimen with RHD devices 85

Figure 4.2 Floor plan of prototype SCEBF-D type buildings..... 86

Figure 4.3 Elevation view of prototype SCEBF-D type buildings 86

Figure 4.4 Configuration and dimensions of SCEBF-D structure 87

Figure 4.5 Rocking link beam configuration and dimension in SCEBF-D structure 87

Figure 4.6 Pushover curve of one-story SCEBF-D type..... 88

Figure 4.7 Pushover curve of one-story SCEBF-D type with RHD devices 88

Figure 4.8 Beam/link flexural stiffness component: Kf 89

Figure 4.9 RHD device-shear force effect on SCEBF-D type structure..... 89

Figure 4.10 Schematics of rocking link with RHD devices in SCEBF and corresponding ANSYS model 90
Figure 4.11 Schematics of rocking link with RHD devices in SCEBF and corresponding SAP2000 model 90
Figure 4.12 Mode shapes of prototype self-centering EBF-D type buildings 91
Figure 4.13 Pushover loading protocol for SCEBF-D type 92
Figure 4.14 Pushover curve of EBF-D type 93
Figure 4.15 Pushover curve of prototype SCEBF D-type 93
Figure 4.16 Peak roof drift ratio of prototype D-type EBFs 94
Figure 4.17 Residual roof drift ratio of prototype D-type EBFs 94
Figure 4.18 Configuration of parametric study cases for D-type EBFs 95
Figure 4.19 Hysteresis curves of prototype SCEBFs with varying PT cable initial stress and length for SCEBF-D type 96
Figure 4.20 Peak roof drift ratio from parametric study for SCEBF-D type 97
Figure 4.21 Residual drift ratio from parametric study for SCEBF-D type 97
Figure 4.22 Peak inter-story drift ratio from parametric study for D-type EBFs 98
Figure 4.23 Peak PT cable stress ratio from parametric study for SCEBF-D type 99
Figure 4.24 Roof drift time history for D-type EBFs 100
Figure 4.25 First-floor link shear force vs. link rotation angle hysteresis curve for D-type EBFs 101
Figure 4.26 First story drift time history for SCEBF-D type 102
Figure 4.27 Second story drift time history for SCEBF-D type 102

Figure 4.28 Third story drift time history for SCEBF-D type 103
Figure 4.29 First story inter-story drift ratio-time history for SCEBF-D type 103
Figure 4.30 Second story inter-story drift ratio-time history for SCEBF-D type..... 104
Figure 4.31 Third story inter-story drift ratio-time history for SCEBF-D type..... 104
Figure 4.32 Axial force time histories of link beam and PT cable for 1st story of SCEBF structures for SCEBF-D structure under La02 105
Figure 4.33 Axial force time histories of link beam and PT cable for 2nd story of SCEBF structures for SCEBF-D structures under La02..... 105
Figure 4.34 Axial force time histories of link beam and PT cable for 3rd story of SCEBF structures for SCEBF-D structures under La02..... 106
Figure 4.35 Column relative displacement for D-type SCEBF 107
Figure 4.36 Peak inter-story drift ratio for D-type SCEBF 108
Figure 4.37 Peak PT cable stress ratio for SCEBF-D type..... 108
Figure 4.38 Peak link rotation angle for SCEBF-D type..... 109
Figure 4.39 P-M interaction curve of rocking link beams for D-type SCEBF..... 109
Figure 5.1 Rocking link and PT cables in SCEBF test specimen with RHD devices 135
Figure 5.2 Floor plan of prototype SCEBF-K type building 136
Figure 5.3 Elevation view of prototype SCEBF-K type building..... 136
Figure 5.4 Configuration and dimensions of SCEBF-K structure..... 137
Figure 5.5 Rocking link beam configuration and dimension in SCEBF-K structure 137

Figure 5.6 Pushover curve of one-story SCEBF-K type..... 138
Figure 5.7 Pushover curve of one-story SCEBF-K type with RHD devices..... 138
Figure 5.8 Beam/link flexural stiffness component: Kf..... 139
Figure 5.9 RHD device-shear force effect on SCEBF-K type structure..... 139
Figure 5.10 Schematics of rocking link with RHD devices in SCEBF and corresponding ANSYS model..... 140
Figure 5.11 Schematics of rocking link with RHD devices in SCEBF and corresponding SAP2000 model..... 140
Figure 5.12 Mode shapes of prototype self-centering EBF-K type buildings..... 141
Figure 5.13 Pushover loading protocol for SCEBF-K type..... 142
Figure 5.14 Pushover curve of EBF-K type..... 143
Figure 5.15 Pushover curve of prototype SCEBF K-type..... 143
Figure 5.16 Peak roof drift ratio of prototype K-type EBFs..... 144
Figure 5.17 Residual roof drift ratio of prototype K-type EBFs..... 144
Figure 5.18 Configuration of parametric study cases for K-type EBFs..... 145
Figure 5.19 Hysteresis curves of prototype SCEBFs with varying PT cable initial stress and length for SCEBF-K type..... 146
Figure 5.20 Peak roof drift ratio from parametric study for SCEBF-K type..... 147
Figure 5.21 Residual drift ratio from parametric study for SCEBF-K type..... 147
Figure 5.22 Peak inter-story drift ratio from parametric study for K-type EBFs..... 148
Figure 5.23 Peak PT cable stress ratio from parametric study for SCEBF-K type..... 149
Figure 5.24 Roof drift time history for K-type EBFs..... 150

Figure 5.25 First-floor link shear force vs. link rotation angle hysteresis curve for K-type EBFs 151
Figure 5.26 First story drift time history for SCEBF-K type 152
Figure 5.27 Second story drift time history for SCEBF-K type 152
Figure 5.28 Third story drift time history for SCEBF-K type 153
Figure 5.29 Fourth story drift time history for SCEBF-K type 153
Figure 5.30 First story inter-story drift ratio-time history for SCEBF-K type 154
Figure 5.31 Second story inter-story drift ratio-time history for SCEBF-K type 154
Figure 5.32 Third story inter-story drift ratio-time history for SCEBF-K type 155
Figure 5.33 Fourth story inter-story drift ratio-time history for SCEBF-K type 155
Figure 5.34 Axial force time histories of link beam and PT cable for 1st story of SCEBF structures for SCEBF-K structures under La13 156
Figure 5.35 Axial force time histories of link beam and PT cable for 2nd story of SCEBF structures for SCEBF-K structures under La13 156
Figure 5.36 Axial force time histories of link beam and PT cable for 3rd story of SCEBF structures for SCEBF-K structures under La13 157
Figure 5.37 Axial force time histories of link beam and PT cable for 4th story of SCEBF structures for SCEBF-K structures under La13 157
Figure 5.38 Column relative displacement for K-type SCEBF 158
Figure 5.39 Peak inter-story drift ratio for K-type SCEBF 159
Figure 5.40 Peak PT cable stress ratio for SCEBF-K type 159
Figure 5.41 Peak link rotation angle for SCEBF-K type 160

Figure 5.42 P-M interaction curve of rocking link beams for K-type SCEBF 160

Figure 6.1 Schematic view of SCEBF-Y module structure without RHD devices (circle: simple connection)..... 186

Figure 6.2 SCEBF-Y: (a) Kdf; (b) Kr 187

Figure 6.3 SCEBF-Y rocking link shear force component: (a) Vl; (b) $VlFD$..... 188

Figure 6.4 Hysteresis loop of SCEBF-Y structure with replaceable energy dissipation devices..... 189

Figure 6.5 ANSYS model of prototype SCEBF-Y 190

(a) Figure 6.6 Validation of experimental test: Flag shaped curve of SCEBF-Y 191

Figure 6.7 Floor plan of 3-story eccentrically braced frame buildings for SCEBF-Y type..... 192

Figure 6.8 Elevation of 3-story eccentrically braced frame buildings for SCEBF-Y type..... 192

Figure 6.9 Floor plan of 3-story eccentrically braced frame buildings for CEBF-D type..... 193

Figure 6.10 Elevation of 3-story eccentrically braced frame buildings for CEBF-D type..... 193

Figure 6.11 PT cable design in a 3-story SCEBF-Y 194

Figure 6.12 RHD devices in SCEBF structure in finite element model 195

Figure 6.13 Picture of RHD device installed on one side of rocking link in SCEBF structure..... 195

Figure 6.14 Mode shapes of 3-story SCEBF-Y building..... 196
Figure 6.15 Pushover loading protocol for SCEBF-Y frame 196
Figure 6.16 Pushover curve of 3-story prototype SCEBF-Y building frame 197
Figure 6.17 Seismic response of SCEBF-Y and CEBF-D buildings under 20 seismic ground motions: (a) Peak roof drift ratio (b) Residual roof drift ratio..... 198
Figure 6.18 PT cable locations in SCEBF-Y models: (a) Case-A; (b) Case-B; (c) Case-C..... 199
Figure 6.19 Pushover curves of prototype SCEBF-Y frames with varying PT initial stress and length..... 200
Figure 6.20 Parametric study results of SCEBF-Y under 20 seismic ground motions: (a) Peak roof drift ratio; (b) Residual roof drift ratio..... 201
Figure 6.21 Parametric study results of SCEBF-Y under 20 seismic ground motions: (a) Peak inter-story drift ratio range with 68% confidence level ($\mu \pm \sigma$); (b) Peak PT cable stress ratio range with 68% confidence level 203
Figure 6.22 Parametric study results: Peak base shear range with 68% confidence level for SCEBF-Y..... 204
Figure 6.23 Typical time history response of SCEBF-Y and CEBF-D, Case-A under LA01 ground motion: (a) roof drift; (b) typical inter-story drift ratio in first story . 205
Figure 6.24 First story drift time history for SCEBF-Y type..... 206
Figure 6.25 Second story drift time history for SCEBF-Y type 206
Figure 6.26 Third story drift time history for SCEBF-Y type 207
Figure 6.27 First story inter-story drift ratio-time history for SCEBF-Y type 207

Figure 6.28 Second story inter-story drift ratio-time history for SCEBF-Y type 208
Figure 6.29 Third story inter-story drift ratio-time history for SCEBF-Y type 208
Figure 6.30 Peak inter-story drift ratio for Y-type SCEBF 209
Figure 6.31 Typical response of SCEBF-Y, Case-A under LA01 ground motion: (a) PT cable stress ratio; (b) Peak rocking link rotation angle 210
Figure 6.32 Link shear hysteresis curve of first story rocking links in SCEBF-Y, Case-A under LA01 ground motion 211
Figure 7.1 Schematic view of TADAS device in steel frame (Tsai, Chen [1]) 226
Figure 7.2 TPAD plate schematic view 226
Figure 7.3 ANSYS model of replaceable hysteric damper 227
Figure 7.4 Stress-strain curve for damage initiation and evolution (Amiri, Aghakouchak [2]) 227
Figure 7.5 Schematic view of the experimental bar test 228
Figure 7.6 Calibration of the hysteresis curve 228
Figure 7.7 TPAD plate parameters 229
Figure 7.8 Loading protocol for parametric study of TPAD 229
Figure 7.9 Pivot point location when rotational displacement in loading protocol is positive 230
Figure 7.10 Pivot point location when rotational displacement in loading protocol is negative 230
Figure 7.11 Meshed picture of TPAD plate 231
Figure 7.12 Damage counter for TPAD-1 at the onset of crack initiation 232

Figure 7.13 Von-mises stress counter for TPAD-1 at the onset of crack initiation.. 232
Figure 7.14 Damage counter for TPAD-2 at the onset of crack initiation..... 233
Figure 7.15 Von-mises stress counter for TPAD-2 at the onset of crack initiation.. 233
Figure 7.16 Damage counter for TPAD-3 at the onset of crack initiation..... 234
Figure 7.17 Von-mises stress counter for TPAD-3 at the onset of crack initiation.. 234
Figure 7.18 TPAD plate height parametric study: (a) $h<H$; (b) $h>H$..... 235
Figure 7.19 TPAD parametric study: height (h)..... 236
Figure 7.20 Effect of height (h) on ductility of TPAD..... 237
Figure 7.21 Damage counter for TPAD-4 at the onset of crack initiation..... 238
Figure 7.22 Von-mises stress counter for TPAD-4 at the onset of crack initiation.. 238
Figure 7.23 Damage counter for TPAD-5 at the onset of crack initiation..... 239
Figure 7.24 Von-mises stress counter for TPAD-5 at the onset of crack initiation.. 239
Figure 7.25 TPAD parametric study: beta (β)..... 240
Figure 7.26 Effect of beta (β) on ductility of TPAD..... 241
Figure 7.27 Damage counter for TPAD-6 at the onset of crack initiation..... 242
Figure 7.28 Von-mises stress counter for TPAD-6 at the onset of crack initiation.. 242
Figure 7.29 Damage counter for TPAD-7 at the onset of crack initiation..... 243
Figure 7.30 Von-mises stress counter for TPAD-7 at the onset of crack initiation.. 243
Figure 7.31 TPAD parametric study: rectangular height (k)..... 244
Figure 7.32 Effect of rectangular height (k) on ductility of TPAD..... 245
Figure 7.33 Damage counter for TPAD-8 at the onset of crack initiation..... 246
Figure 7.34 Von-mises stress counter for TPAD-8 at the onset of crack initiation.. 246

Figure 7.35 TPAD parametric study: friction coefficient (fs) 247

Figure 7.36 Effect of friction coefficient (fs) on ductility of TPAD 248

Figure 7.37 Damage counter for TPAD-9 at the onset of crack initiation..... 249

Figure 7.38 Von-mises stress counter for TPAD-9 at the onset of crack initiation.. 249

Figure 7.39 Damage counter for TPAD-10 at the onset of crack initiation..... 250

Figure 7.40 Von-mises stress counter for TPAD-10 at the onset of crack initiation 250

Figure 7.41 Damage counter for TPAD-11 at the onset of crack initiation..... 251

Figure 7.42 Von-mises stress counter for TPAD-11 at the onset of crack initiation 251

Figure 7.43 TPAD parametric study: alpha (α) 252

Figure 7.44 Effect of alpha (α) on ductility of TPAD 253

List of Abbreviations

EBF: Eccentrically Braced Frame

CEBF: Conventional Eccentrically Braced Frame

SCEBF: Self-Centering Eccentrically Braced Frame

MRF: Moment Resisting Frame

CBF: Concentrically Braced Frame

PT: Post-Tensioning

RHD: Replaceable Hysteric Damper

TPAD: Trapezoidal Added Damping Plate

DBE: Design Basis Earthquake

Chapter 1 Introduction

1.1 Introduction

Conventional Eccentrically braced frames (CEBF) have been used for over three decades as a ductile seismic load resisting system in buildings. CEBFs take advantage of moment resisting frame (MRF) and concentrically braced frame (CBF) which equip CEBF with high ductility and stiffness. The high ductility of CEBF is achieved through the plastic deformation of link beam located between two braces in K-type CEBF or between brace and column in D-type CEBF.

In CEBF, yielding of a link beam between eccentric braces provides ductility and energy dissipation under seismic loading. In other words, link beam act as passive fuse device which dissipates seismic energy through its plastic deformation. However, other structural members of CEBF such as columns, beams, and braces are designed to remain elastic through design base earthquake except for column base.

CEBFs has large elastic stiffness and exhibit very ductile deformation during a severe earthquake; nevertheless, they often suffer considerable damage during a strong earthquake because of the significant drift demand. After the strong earthquake, the plastic deformation of the links may lead to a permanently deformed frame, and large residual deformation not only compromises the appearance of the structure but also make the damaged structure with excessive drift too costly to repair and disrupt regular

occupancy. Thus, by concentrating the damage only in replaceable fuse devices, a high performance low-damage seismic resistant structure would be achieved, in which primary structural members remains damage free. This is very attractive to addressing the need for resilient civil infrastructure.

The overall goal of this study is to investigate an emerging EBF system that is more resilient to seismic hazards than CEBF. Different strategies have been considered to resolve noted problems associated with CEBF. First one is to use a replaceable link beams in CEBFs which can be removed after the verified occurrence of plastic deformation due to severe earthquake. The other one is to design EBFs in a way to keep all structural system damage free by using a new replaceable hysteric damper. Thus, damages would be concentrated only on the replaceable hysteric damper, and other structural members would remain elastic through DBE. Self-centering structure is a proper example of the second strategy.

Self-centering structures (SCEBF) have the potential to provide the economy, strength, and stiffness of traditional EBFs while sustaining less damage in primary structural members under strong earthquake due to special configurations with replaceable fuse members. The descriptor “self-centering” refers to the capacity to go through earthquake shaking without significant residual lateral drift (roof drift ratio < 0.2%).

To manage the high link rotation demand of replaceable fuse devices in SCEBF, the main energy dissipation plates in the adopted replaceable fuse devices termed TPAD are made of low yield steel Q225LY and carefully designed to accommodate the large rotation of the link beam in SCEBF at design basis earthquakes.

SCEBF systems are presumed to have these advantages over CEBF system: 1) residual deformation of the self-centering EBF are minimal; 2) All the earthquake-induced damages are concentrated on replaceable hysteric damper, thus, all the primary members of SCEBF such as columns, beams and braces would remain elastic through DBE; 3) in the SCEEBF system, the stiffness, strength, energy dissipation and ductility can be tuned with more flexibility than CEBF.

1.2 Research Motivation

For many years engineers designed EBF as a seismic load resisting system in buildings. The EBF is typically composed of columns, link beam, collector beam and bracing. The active links are designed to provide ductility and energy dissipation through yielding under design basis earthquakes, while all other structural members are designed to be stronger than the link and stay in elastic range. In CEBF, yielding of link beams provides ductility and energy dissipation under seismic loading. As a result, a properly designed EBF structure has large elastic stiffness and exhibits significant ductile deformation during intense seismic events [3-7].

However, though the EBFs can dissipate considerable energy under strong earthquakes through the plastic deformation of link beam, significant link damage can result in substantial residual distortion that increases the difficulty of repair after strong earthquakes and often make the damaged structure too costly to repair. Self-centering eccentrically braced frame (SCEBF) with replaceable hysteric damper is proposed with the expectation of overcoming the above-identified problems in the CEBF systems.

The self-centering systems have been developed to quickly bring a structural system back to a fully functional state following an earthquake, which can substantially reduce post-earthquake structural repair workload and thereby mitigate economic and functionality losses. However, no research on nonlinear time history analysis of SCEBFs systems has been reported.

To re-center a structural frame to its initial plumb position following a strong earthquake, self-centering systems have been developed in this study which can significantly minimize residual deformation of the structure.

Another challenge in implementing certain types of self-centering structural systems is the "gap-opening expansion" phenomenon which is the expansion of frame when gap opening at beam ends happens. However, no Y-type self-centering EBF structural system utilizing post-tensioned steel PT strands has been reported so far.

To permit gap opening to take place the frame must be accommodated by collector elements and PT frames to transfer inertial force from the floor system to the PT frame [8]. Special detailing like those proposed by Garlock et al. [27] can be applied to keep the columns of the SCEBF free of the floor slab and to prevent large axial force due to the restraint of the gap opening. Special design with vertical rocking links (SCEBF-Y) which is proposed in this study might also be applied to eliminate the gap-opening expansion phenomenon.

1.3 Research Objectives

This dissertation peruses the following two objectives with attention on implementing the design and knowledge base of self-centering eccentrically braced frame systems with replaceable hysteric damper specifically designed for sustaining large deformation demand.

The first objective is to develop self-centering eccentrically braced frames with replaceable hysteric damper. To address the needs to understand its system behavior, nonlinear seismic behavior of self-centering eccentrically braced steel frame (SCEBF) buildings with replaceable hysteretic damping devices (RHD devices) is studied. The prototype SCEBF design consists of an eccentrically braced steel frame with post-tensioning (PT) cables and RHD devices. Due to the rocking of the link beam, RHD devices are designed with a bracket configuration to take advantage of the rocking link beam's amplified rotation under lateral loading. This RHD device is intended to provide energy dissipation to the SCEBF in the form of replaceable fuse devices, which can be quickly replaced as evidenced in recent full-scale experiments [9]. The SCEBFs are designed in such a way that most of the damages will concentrate on the RHD devices, and the rocking link beam will remain undamaged. The residual drift of SCEBFs is found to be negligible compared to the CEBFs.

The second objective is to find a way to solve the issue of gap-opening expansion in SCEBF-K and D type. In this study, nonlinear seismic behavior of SCEBF-K, SCEBF-D and SCEBF-Y structural systems with replaceable hysteric steel devices termed as RHD devices are investigated through both analytical and numerical simulation study.

In the K-type and D-type SCEBF, the rocking of the link beam opens the interface between rocking link beam and the beam or column; thus, a gap-opening expansion would occur. The SCEBF-Y frame contains vertical rocking link beam mounted on chevron or V bracings while SCEBF-K and SCEBF-D have horizontal rocking link beam.

In SCEBF-Y, rocking link beam is connected to the frame beam through shear keys, which does not transfer the axial force to the rocking link. Rocking motion of the links in the SCEBF-Y frame thus does not cause gap-opening expansion phenomenon because the gap opening happens in the vertical direction only and an initial gap created between the rocking link beam and frame beam accommodates the vertical movement of the rocking link. RHD devices absorb most of the seismic energy and as such damages are confined to them while primary structural members would remain elastic under design basis earthquakes. Such RHD devices providing energy dissipation to SCEBF-Y, can be replaced quickly based on recent full-scale experiments [9].

1.4 Organization of the Dissertation

In this study, various finite element simulations are performed on different self-centering eccentrically braced frame systems including SCEBF-K, SCEBF-D, and SCEBF-Y frame. Full-scale experimental testing of a one-story one-bay D-type SCEBF module frame specimen conducted by Tong et al. [35] was used for validating the finite element models and analytical formulation. It is found that after severe cyclic loading the SCEBF module frames with replaced energy dissipation devices exhibits

almost identical stiffness, strength, re-centering ability, and energy dissipation capacity to that of the initial SCEBF structure before testing. The behavior of different SCEBF systems are investigated through both nonlinear static and nonlinear time history analysis.

Chapter 2 reviews prior research work on the conventional eccentrically braced frame and their benefits and draw backs in seismic resisting structure. Moreover, different self-centering structures with various hysteric dampers such as friction devices, shape memory alloy (SMA) bolts, etc. are also reviewed in this chapter.

Chapter 3 presents information regarding the overall behavior of concentrically braced frame whether they have short or long link. Moreover, the concept behind the self-centering structure is explained in detail in which the post-tensioned tendons are the main part of the system making it re-center. All the primary members of self-centering structures are designed to remain elastic through DBE, and only replaceable hysteric damper should suffer damage in a self-centering EBF. In this chapter, experimental test results of a one-story one-bay SCEBF-D module frame is also described thoroughly, which are used to calibrate the finite element model and verify the analytical formulas regarding the self-centering EBF module frame and replaceable hysteric damper. Furthermore, the finite element simulation detail of CEBF and SCEBF are presented.

Chapter 4 investigates the seismic performance of SCEBF-D type through finite element simulation and compare it with the conventional EBF-D type under static and time history analysis. Analytical formula is also presented for SCEBF-D type in order to predict design base shear force and initial stiffness and post-gap opening stiffness of

SCEBF-D type. Furthermore, a parametric study has been done on three different cases of SCEBF-D type with different PT length and initial stress to better understand the seismic performance of SCEBF-D type.

Chapter 5 involves the seismic performance studies of SCEBF-K and CEBF-K type through finite element simulation, and their behavior is investigated under static and time history analysis. Analytical formula is derived for SCEBF-K type to predict design base shear force, initial stiffness and post-gap opening stiffness of SCEBF-K type. Furthermore, a parametric study has been done on three different cases of SCEBF-K type with different PT length and initial PT stress to better understand the effecting factors on the seismic performance of SCEBF-K type.

Chapter 6 studies the self-centering EBF with vertical link through static and time history analysis in various finite element simulations. A prototype design of SCEBF-Y type is presented in this study to overcome the common issue of gap-opening expansion in SCEBF-K and D type. Moreover, analytical formula is also derived for SCEBF-Y type and verified with finite element simulation results. The numerical modeling techniques of SCEBF-Y is also presented in this chapter. Furthermore, parametric study of various SCEBF-Y system is also investigated.

Chapter 7 studies a replaceable hysteretic damper termed TPAD. The TPAD design is inspired by TADAS [1], which dissipates energy through yielding of tapered plate and has been used in real buildings requiring great energy dissipation. In this study, a new metallic hysteric damper introduced based on TADAS named TPAD. TPAD is a trapezoidal plate connected to a round rod. TPAD is designed and optimized base on

fracture investigation [2]. Crack initiation is analyzed based on CVGM method [10]. Moreover, cyclic loading has been applied to different TPAD plate based on their slope and thickness, and overall behavior of TPAD have been investigated

Chapter 8 presents the conclusions and summaries of this dissertation research and suggestions for worthy future research work.

Chapter 2 Literature Review

In this chapter, a literature review of relevant research over different areas of engineering is presented. At first, the concept of conventional eccentrically braced frame is discussed followed by the review of self-centering structure. Then, advantages of self-centering eccentrically braced frame as a new type of seismic resisting structure are reviewed, since they are primary motivations of this study. Then, replaceable hysteric damper is presented which is used as the fuse members of self-centering eccentrically braced frame.

2.1 Conventional Eccentrically Braced Frame

Eccentrically braced frames (EBF) has been considered as a ductile seismic lateral load resisting frames competitive for building applications in seismic-active regions. The EBF typically consists of bracing, columns, collector beam, and link beam. In conventional EBF (CEBF), active links are designed to dissipate energy through ductile plastic deformation, and a well-designed CEBF structure thus not only has large elastic stiffness but also displays remarkable ductility [3-7]. In order to dissipate great amount of energy during strong earthquakes, link beams would suffer from severe damage and have to be replaced afterward.

In the United States, the first study of EBF system was done in 1978 [3]. In the 1980s, several studies have been investigated the cyclic response of EBFs and provide

experimental verifications of EBF response [4, 11-14]. These studies developed the design provisions in the 1988 Uniform Building Code and later in AISC 341 (AISC2010).

Inelastic Behavior of short-wide flange link beam in EBF showed that using web stiffeners, not only can reduce unfavorable web buckling but also enhance energy dissipation capability of shear link [4]. ASCE Seismic Provision (2002) was found to underestimate the inelastic rotation capacity of shear link and is overly conservative. A new cyclic load testing recommended for shear links [15].

Eccentrically braced frames (EBF) have been considered as a ductile seismic lateral load resisting frames competitive for building applications in seismic-active regions. The EBF typically consists of bracing, columns, collector beam, and link beam. In conventional EBF (CEBF), active links are designed to dissipate energy through ductile plastic deformation, and a well-designed CEBF structure thus not only has large elastic stiffness but also displays remarkable ductility [3-7]. In order to dissipate great amount of energy during strong earthquakes, link beams would suffer from severe damage and have to be replaced afterward.

In the past two decades, several studies were conducted not only on buildings but also on bridge applications [16, 17]. In recent researches, researchers used built-up sections including I-shaped sections, boxed sections, and double C sections [18-20] and the emphasis on performance-based design of replaceable link has also investigated thoroughly [21-23].

Nabil et al. (2011) performed some tests on replaceable shear link which were bolted between the beams in EBF. They found out that replaceable shear link has similar behavior as conventional shear link. However, web reinforcement plates should carefully be designed to avoid connection failure and limit pinching in the link hysteresis response [22].

2.2 Self-Centering structures

2.2.1 Self-Centering Moment Resisting Frame (SCMRF)

In a conventional MRF (CMRF), seismic energy is dissipated by the plastic hinges formation at the ends of the beam causing permanent deformation at the beam end which may lead to permeant residual deformation in the CMRF under large earthquake loading. In the self-centering MRF (SCMRF), the post-tensioned (PT) strands compress the beams and columns to be in contact together forming rigid connections. Under low to moderate seismic load, SCMRF has similar behavior as CMRF before gap-opening happens. However, after gap-opening happens, the geometry of SCMRF changes since the gap between the beam and columns are not closed. In SCMRF system, all the primary members of the structure must remain elastic except for the fuse members through DBE. Thus, they can re-center themselves after the earthquake through the compression force of the PT strands. Performance of the SCMRFs were investigated inclusively by Ricles, Sause [24]. They used high strength steel strands to create a post-tensioned (PT) steel moment connections. Seat angles were used as fuse members between the floor beams and

columns to transfer shear forces. Figure 2.1 shows the test set up in the research conducted by Ricles, Sause [24] and the hysteresis force-displacement relationship of the test set up is presented in Figure 2.2. As shown in Figure 2.2, the SCMRF has high strength, stiffness and it can re-center itself throughout the test.

Numerical analysis on the performance of a six-story MRF with post-tensioned (PT) strands with friction damper (PFDC-MRF) under different earthquake ground motion was conducted by Rojas, Ricles [25]. They compared PFDC-MRF with a six-story special moment resisting frame with welded connections (FR-MRF) and concluded that PFDC-MRF has the same inter-story drift as the FR-MRF. However, the PFDC-MRF does not involve residual deformation after the test. The comparison response of the PFDC-MRF and FR-MRF is shown in Figure 2.3.

The design principle and behavior of self-centering moment resisting frame (SC-MRF) further studied by Garlock and Li [26] and Garlock and Li [27].

2.2.2 Self-Centering Eccentrically Braced Frame (SCEBF)

For many years engineers designed eccentrically braced frames (EBF) as a seismic load resisting system in buildings. The EBF is typically composed of columns, link beam, collector beam and bracing. The active links are designed to provide ductility and energy dissipation through yielding under design basis earthquakes, while all other structural members are designed to be stronger than the link and stay in elastic range. In conventional EBFs (CEBF), yielding of link beams provides ductility and energy dissipation under seismic loading. As a result, a properly designed EBF structure has

large elastic stiffness and exhibits significant ductile deformation during intense seismic events [3-7].

However, though the EBFs can dissipate considerable energy under strong earthquakes through the plastic deformation of link beam, significant link damage can result in substantial residual distortion that increases the difficulty of repair after strong earthquakes and often make the damaged structure too costly to repair. Recently, combining the concept of self-centering structures and EBFs have been investigated by researchers [28-30].

The self-centering systems have been developed to quickly bring a structural system back to a fully functional state following an earthquake, which can substantially reduce post-earthquake structural repair workload and thereby mitigate economic and functionality losses. To re-center a structural frame to its initial plumb position following a strong earthquake, self-centering systems have been developed which can significantly minimize residual deformation of the structure.

The re-centering forces in most self-centering structures are provided by either post-tensioned members (e.g., steel strands) or special metal alloys (e.g., shape memory alloys) [31-33]. Typical of such self-centering systems is a flag-shaped hysteresis loop, which can reduce (or even eliminate) residual structural deformation while dissipating a moderate amount of seismic energy. In most such self-centering systems, post-tensioned members (e.g., steel strands) or special metal alloys (e.g., shape memory alloys) are used to provide the restoring forces required to return the system to its original position. Moreover, energy-dissipating elements installed at the post-tensioned

beam-column connection are used to dissipate energy during loading. This concept was initially implemented in unbonded post-tensioned precast concrete walls and frames in the early 1990s [31-33] and later extended to post-tensioned steel moment resisting frames [34, 35]. The post-tensioned (PT) steel moment resisting frames typically consist of high-strength steel bars or strands placed within the depth of the beams and anchored to the outer flanges of the columns. This type of beam-to-column connections can be used to provide the frame with self-centering capacity and limit hysteretic damages to the replaceable energy dissipating elements during earthquakes [24, 25, 36-38]. Moreover, friction devices were also used to dissipate seismic energy in post-tensioned beam-to-column moment connections [25, 39-42]. Roke [43] extended the concept of self-centering by post-tensioning the whole structural system of multistory braced frames.

Qiu and Zhu [44] investigated the high modes effects on seismic performance of multi-story self-centering braced steel frame (SC-BFs). They improved the seismic performance of SC-BFs by increasing the post-yield stiffness ratio along with energy dissipation capacity. Moreover, two special types of bracing element named self-centering friction damping brace (SFDB) and self-centering steel frame with SMA braces (SMAB) were proposed [45, 46]. Cheng, Hsu [28] studied the possibility of applying the self-centering concept to the link-beam connection of eccentrically braced frames. At the interface between the central link and adjacent link, they formed a post-tensioned joint connection and friction devices were used to dissipate energy. The

prototype SCEBF frame test setup is shown in Figure 2.4 and the experiment hysteresis force displacement acquired from one test on SCEBF frame is presented in Figure 2.5. Xu, Zhang [29], [30] investigated the behavior of self-centering braced frames using shape memory alloy (SMA) bolts and post-tensioned tendons. They numerically studied the cyclic load behavior of SCEBF and a negligible residual drift observed in the prototype system which would not affect the overall self-centering behavior. They reported that even without using PT tendons, the SCEBF system using SMA bolts could exhibit self-centering capability. The proposed self-centering link using composite tendons is presented in Figure 2.6. The schematic test set up view of prototype SCEBF is shown in Figure 2.7.

Recently, full-scale experimental testing of a one-story one-bay D-type SCEBF module frame specimen was conducted by Zhou [9], and it is found that after severe cyclic loading the SCEBF module frames with replaced energy dissipation devices exhibits almost identical stiffness, strength, re-centering ability, and energy dissipation capacity to that of the original structure.

Regarding Y-type EBFs, Ghobarah and Elfath [47] investigated the rehabilitation of reinforced concrete frame structures using eccentrically braced frames with a vertical link. EBFs with vertical link demonstrated better seismic performance compared to a concentric bracing alternative [47]. Massah and Dorvar [48] used shape memory alloys (SMA) in EBFs with a vertical link to not only re-center the EBFs but also reduce the structural damage considerably. Configuration of prototype eccentrically bracing frame system is shown in Figure 2.8. Shape memory alloys also reduce the

maximum residual inter-story drift ratio significantly; as a result, the EBF with vertical link has more uniform drift distribution. Schematic view of the hysteresis behavior of the SMA wires in the SMA device is presented in Figure 2.9.

No Y-type self-centering EBF structural system utilizing post-tensioned steel PT strands has been reported so far.

One challenge in implementing certain types of self-centering structural systems is the "gap-opening expansion" phenomenon which is the expansion of frame when gap opening at beam ends happens. To permit gap opening to take place the frame must be accommodated by collector elements and PT frames to transfer inertial force from the floor system to the PT frame [8]. Special detailing like those proposed by Garlock, Sause [49] and Garlock and Li [26] can be applied to keep the columns of the SCEBF free of the floor slab and to prevent large axial force due to the restraint of the gap opening. Special design with vertical rocking links (SCEBF-Y) might also be applied to eliminate the gap-opening expansion phenomenon. However, no research on nonlinear time history analysis of SCEBF systems has been reported.

To address the needs to understand its system behavior, the nonlinear seismic behavior of self-centering eccentrically braced steel frame (SCEBF) buildings with replaceable hysteretic damping devices (RHD devices) is studied. The prototype SCEBF design consists of an eccentrically braced steel frame with post-tensioning (PT) cables and RHD devices. Due to the rocking of the link beam, RHD devices are designed with a bracket configuration to take advantage of the rocking link beam's amplified rotation under lateral loading. This RHD device is intended to provide energy dissipation to the

SCEBF in the form of replaceable fuse devices, which can be quickly replaced as evidenced in recent full-scale experiments [9, 50]. The SCEBFs are designed in such a way that most of the damages will concentrate on the RHD devices, and the rocking link beam will remain undamaged. The residual drift of SCEBFs is found to be negligible compared to the CEBFs.

In this study, nonlinear seismic behavior of SCEBF-K, SCEBF-D and SCEBF-Y structural systems with replaceable hysteric steel devices termed as RHD devices are investigated through both analytical and numerical simulation study. The SCEBF-Y frame contains vertical rocking link beam mounted on chevron or V bracings while SCEBF-K and SCEBF-D have horizontal rocking link beam.

In K and D type SCEBF, the rocking of the link beam opens the interface between rocking link beam and the beam or column; thus, a gap-opening expansion would occur.

In SCEBF-Y, the rocking link beam is connected to the frame beam through shear keys, which does not transfer the axial force to the rocking link. Rocking motion of the links in the SCEBF-Y frame thus does not cause gap-opening expansion phenomenon because the gap opening happens in the vertical direction only and an initial gap created between the rocking link beam and frame beam accommodates the vertical movement of the rocking link. RHD devices absorb most of the seismic energy and as such damages are confined to them while primary structural members would remain elastic under design basis earthquakes. Such RHD devices providing energy dissipation to SCEBF-Y, can be replaced quickly based on recent full-scale experiments [9, 50].

2.2.3 Other Types of Self-Centering Structures

Self-centering behavior can be applied to precast wall systems and concentrically braced frames (CBF) when the PT strands are post-tensioned along the vertical members of these structures. The re-centering mechanism is achieved through the post-tensioned force of the PT strands or tendons along with the structure's self-weight. Fuse members usually are installed between the column/wall bases and foundation or between the segregated walls.

The seismic behavior of reinforced concrete frame integrated with self-centering hybrid wall was investigated by Hu, Zhang [51]. Figure 2.10 shows the schematics of the self-centering wall with PT tendons. Hu, Zhang [51] confirmed that the yield strength of base hysteretic dampers and the total area of the PT tendons are the primary factors which affect the self-centering hybrid wall behavior.

Self-centering precast concrete walls behavior under seismic force was investigated by Seo and Sause [52] which is plotted in Figure 2.11. They verified that self-centering precast concrete wall could be designed to exhibit large ductility capacities, while the post-earthquake damage is little.

Sause, M Ricles [53] investigated the behavior of self-centering concentrically braced frame (SC-CBF). The schematic view of studied SC-CBF is presented in Figure 2.12. The experiment results further verified the self-centering behavior of the SC-CBF under DBE and MCE level ground motions.

2.3 Replaceable Hysteric Damper

In order to obtain economical earthquake-resistant building, building structures need to absorb and dissipate seismic energy. In recent days, various fuse devices have been designed and tested. Metallic dampers have some advantages over other fuse devices. They are easily manufactured, and no complex technology is needed for that. Moreover, they can be easily placed in the structure while showing stable behavior. One of these metallic dampers is the steel-plate added damping and stiffness (ADAS). ADAS devices are made of X-shaped steel plated, and they bend in double curvature as shown in Figure 2.13 [54]. The performance of these devices was thoroughly investigated in the buildings as promising fuse members [55-58]. Another type of metallic damper is triangular added damping and stiffness (TADAS) proposed by Tsai, Chen [1]. TADAS has a uniform curvature along its length thus all the TADAS surface yield simultaneously [1]. Thus, it is suitable to be used in building requiring great energy dissipation. TADAS dissipate energy through yielding of tapered plates, and they bend in single curvature as shown in Figure 2.14 [1, 54]. These metallic dampers efficiently reduce vibration response of buildings under DBE. The details of TADAS devices in steel frame are shown in Figure 2.15 and Figure 2.16 [1]. A typical force-deformation relationship of TADAS in a steel frame is shown in Figure 2.17 and Figure 2.18 [1].

In this study, TPAD which is a new metallic hysteric damper is proposed. TPAD design is inspired by TADAS design. TPAD is a trapezoidal plate connected to a round rod.

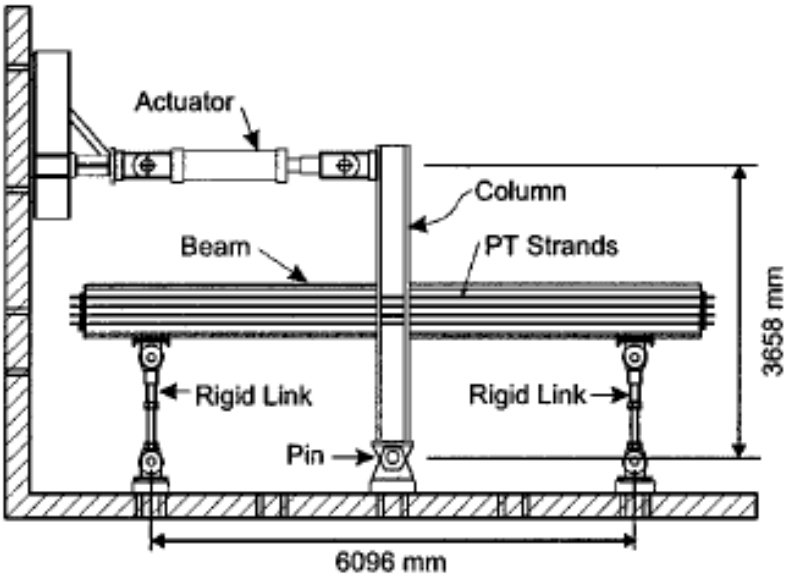

Figure 2.1 Post-tensioned connection test setup (Ricles, Sause [24])

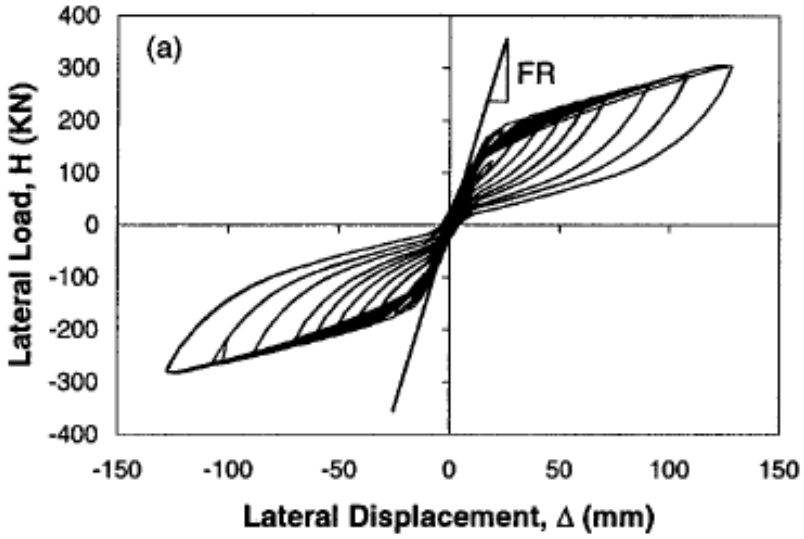

Figure 2.2 Hysteresis force-displacement relationship (Ricles, Sause [24])

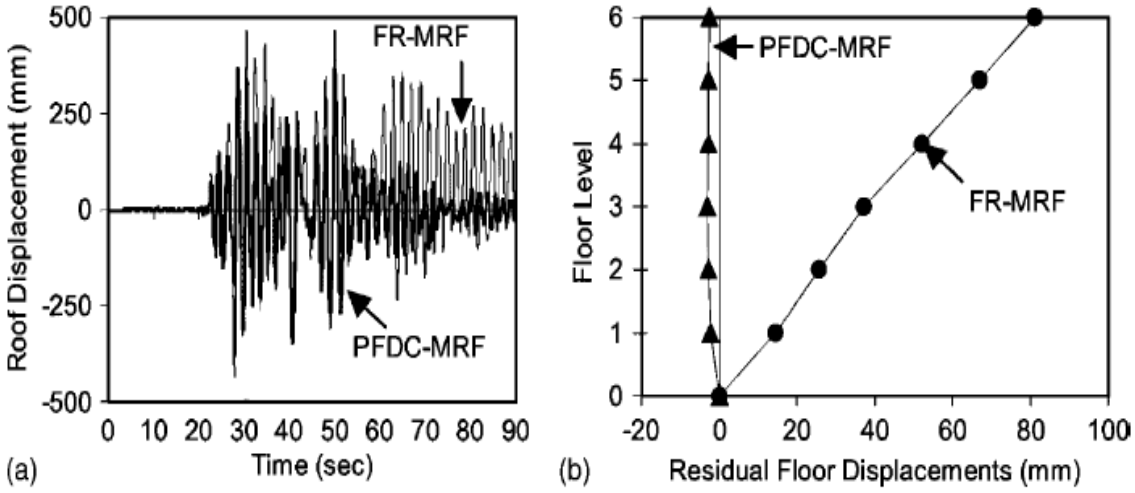

Figure 2.3 Frame response to the Chi-Chi maximum considered earthquake (Rojas, Ricles [25])

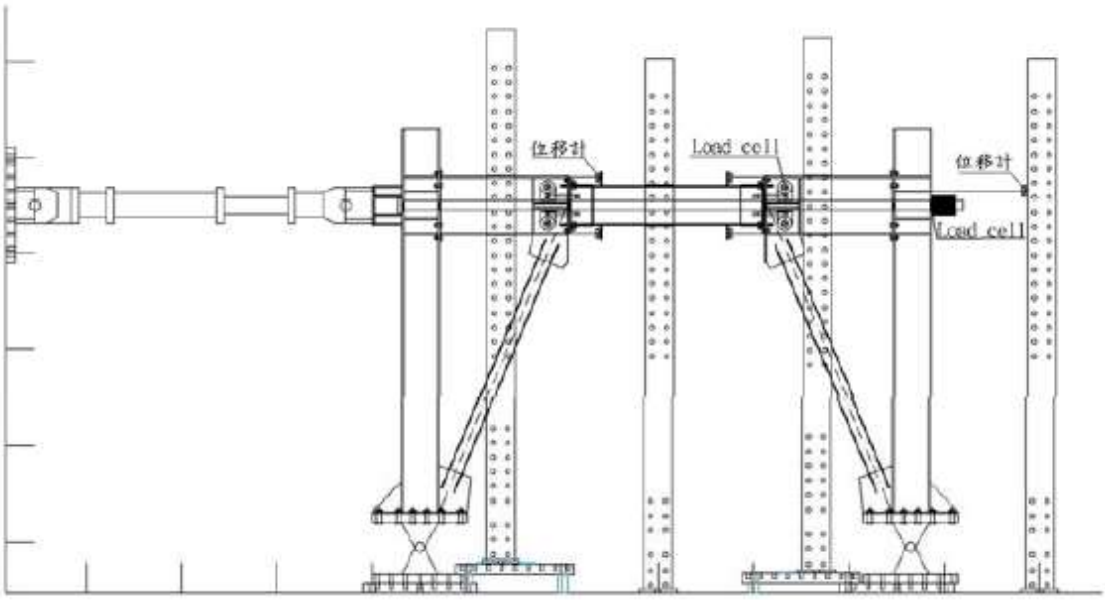

Figure 2.4 SC-EBF test setup (Cheng, Hsu [28])

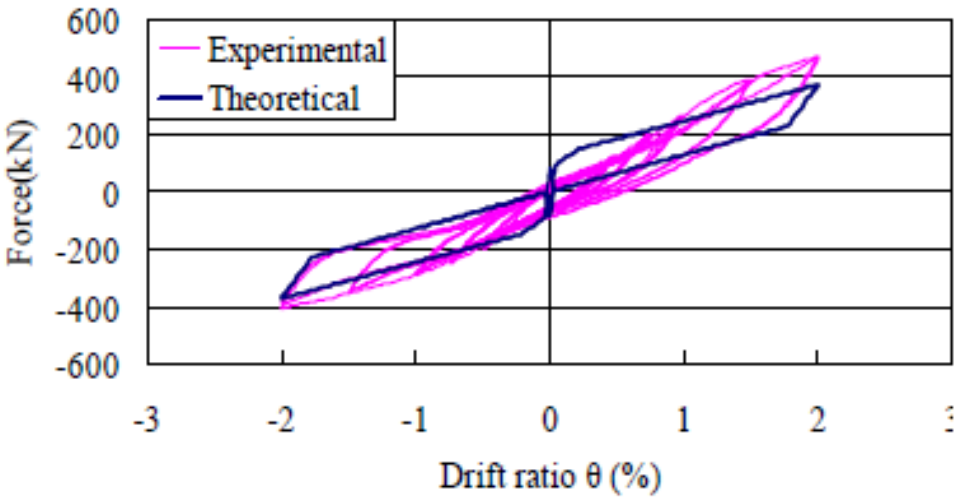

Figure 2.5 Experiment hysteresis force-displacement (Cheng, Hsu [28])

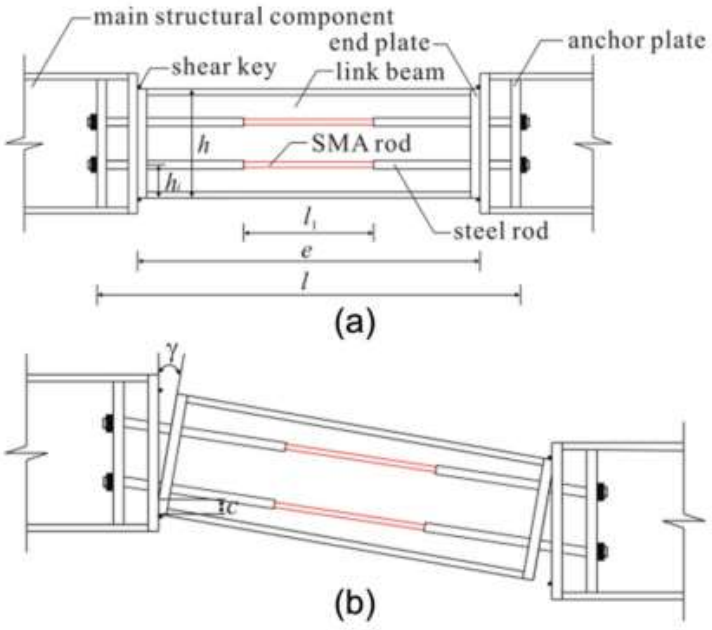

Figure 2.6 Proposed self-centering link using PT composite tendons (Xu, Zhang [59])

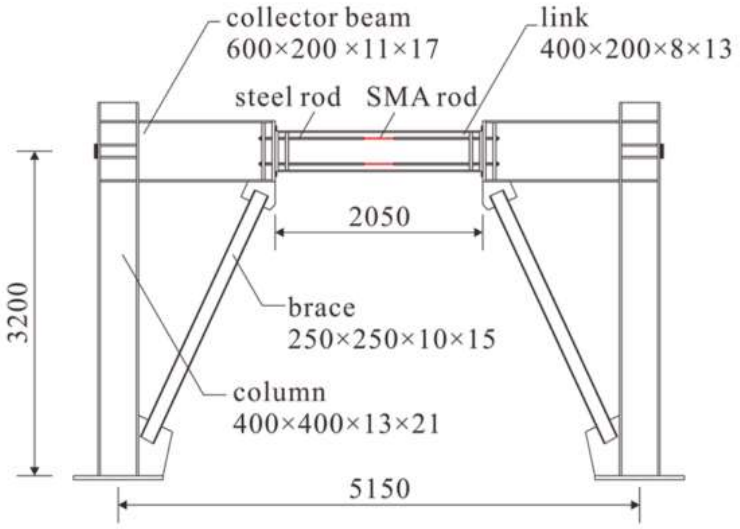

Figure 2.7 Prototype self-centering EBF (Xu, Zhang [59])

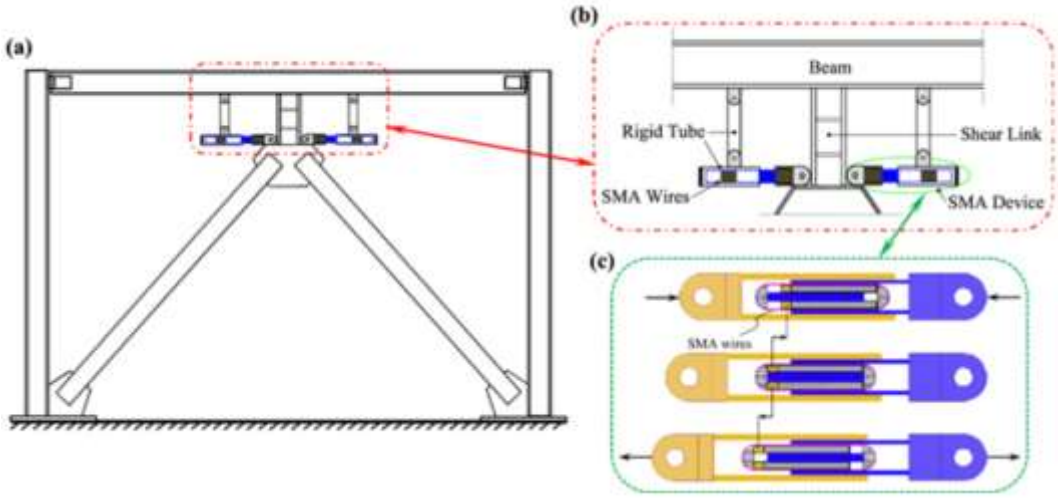

Figure 2.8 (a) Configuration of the proposed eccentrically bracing frame system, (b) Details of the proposed system, (c) The SMA wires in the SMA device (Massah and Dorvar [48])

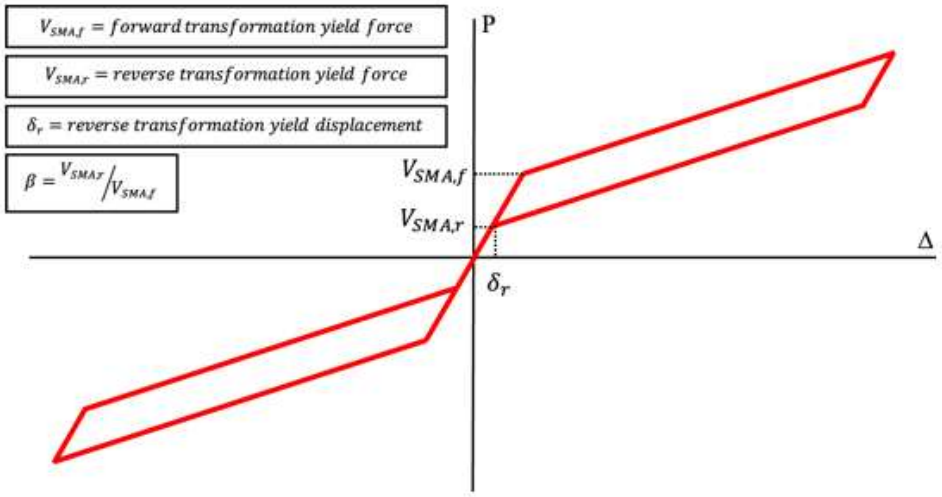

Figure 2.9 Schematic of the hysteresis behavior of the SMA wires in the SMA device (Massah and Dorvar [48])

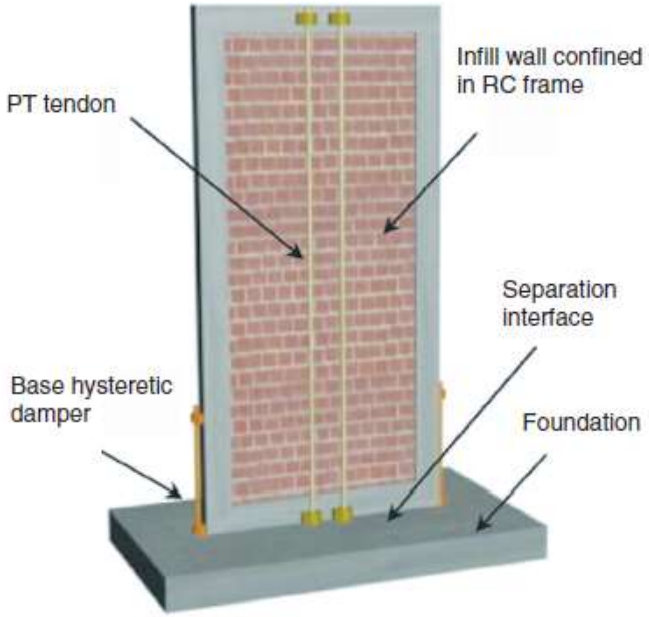

Figure 2.10 Schematics of self-centering wall (Hu, Zhang [51])

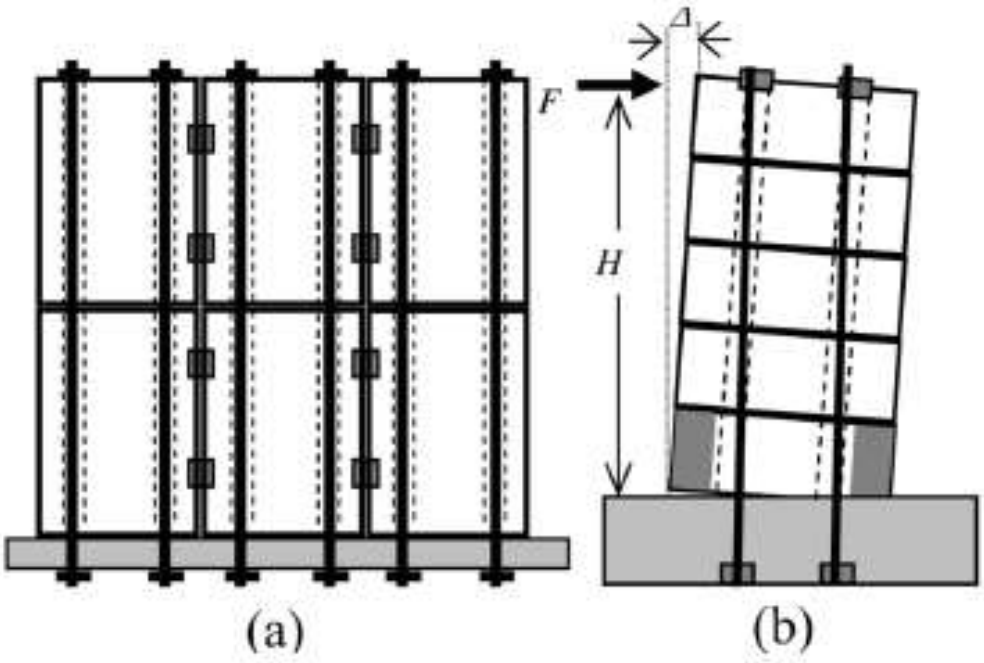

Figure 2.11 Self-Centering precast concrete wall systems (Seo and Sause 2005)

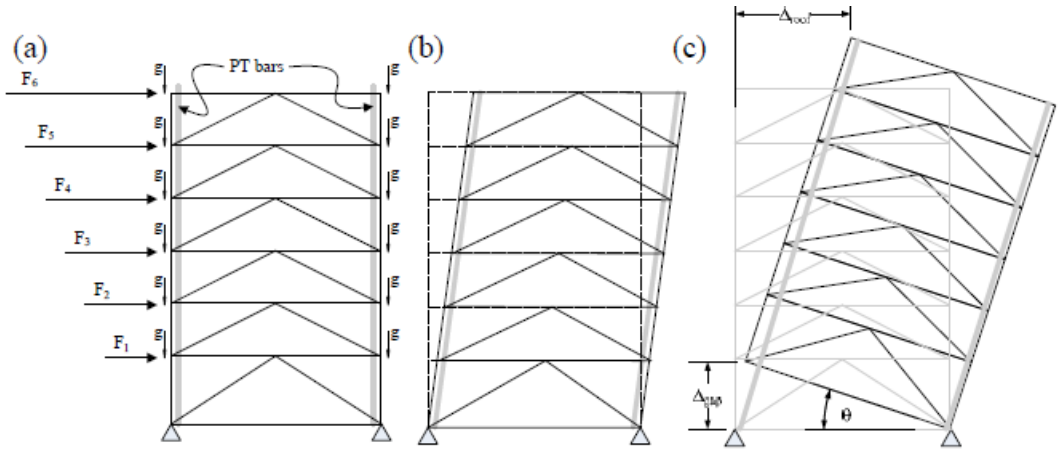

Figure 2.12 Schematics of the SC-CBF system (Sause et al. 2010)

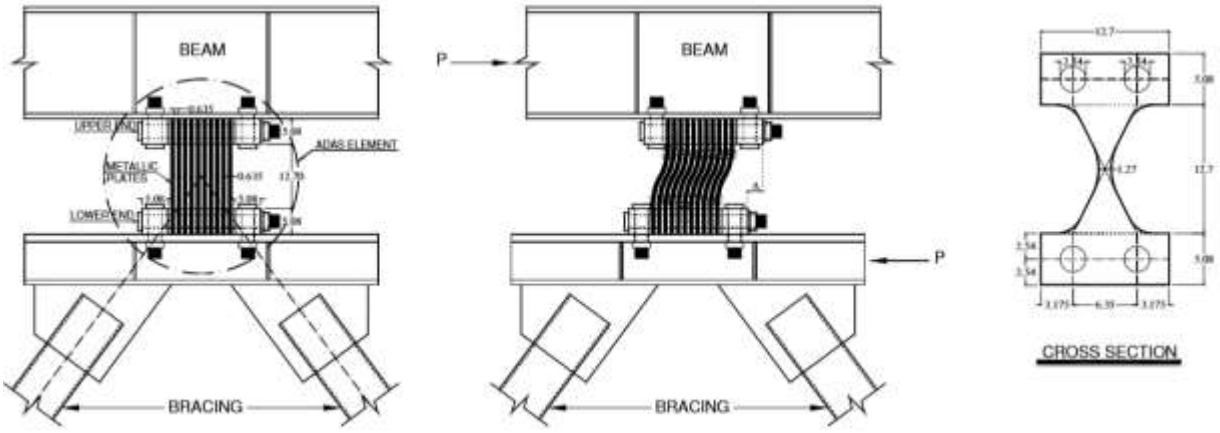

Figure 2.13 ADAS damper performance during earthquake (units: mm)

(Alehashem, Keyhani [54])

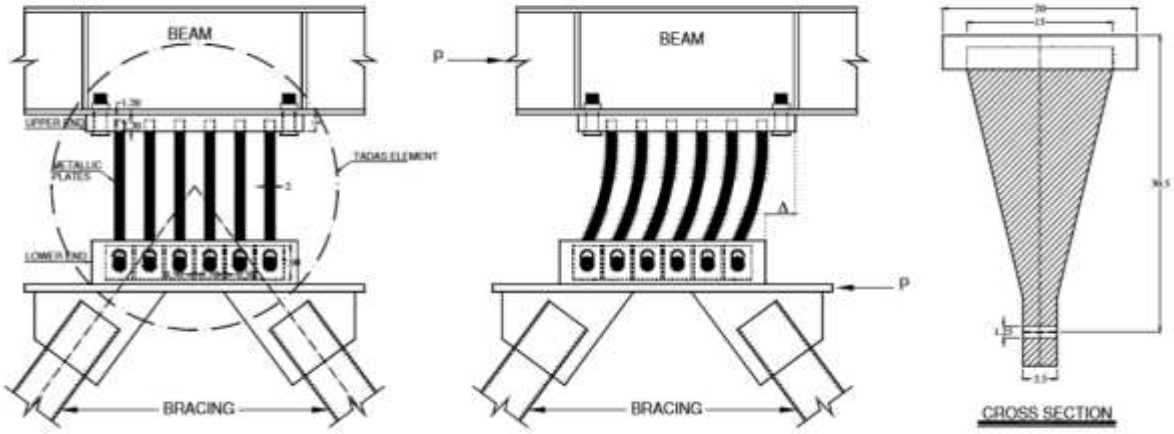

Figure 2.14 TADAS damper performance during earthquake (units: mm)

(Alehashem, Keyhani [54])

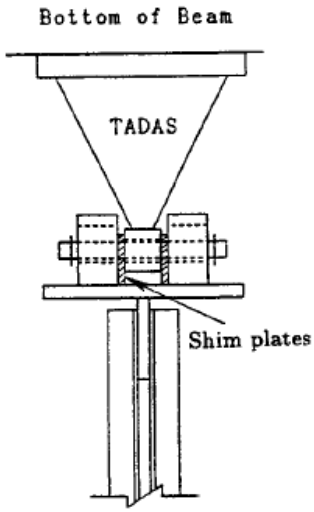

Figure 2.15 TADAS in the device to brace connection (Tsai, Chen [1])

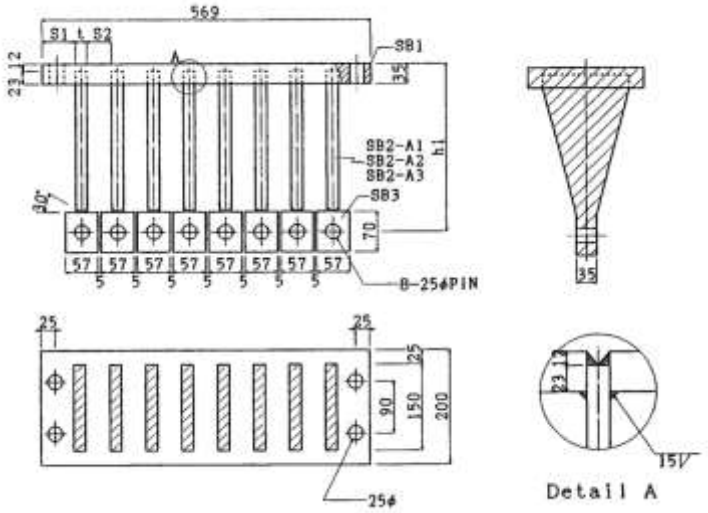

Figure 2.16 Details of steel welded TADAS device (units: mm)-(Tsai, Chen [1])

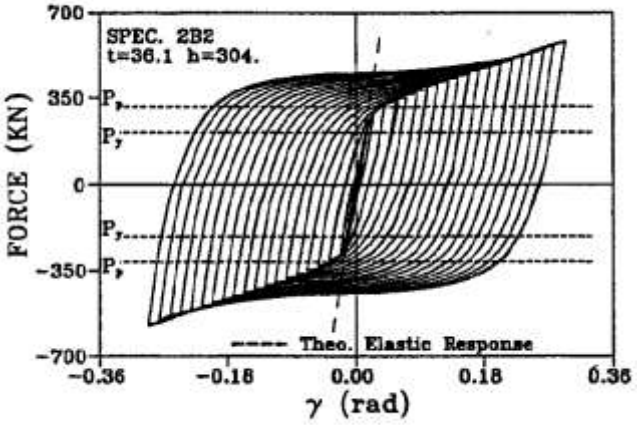

Figure 2.17 Force versus deformation relationship of typical welded TADAS devices (Tsai, Chen [1])

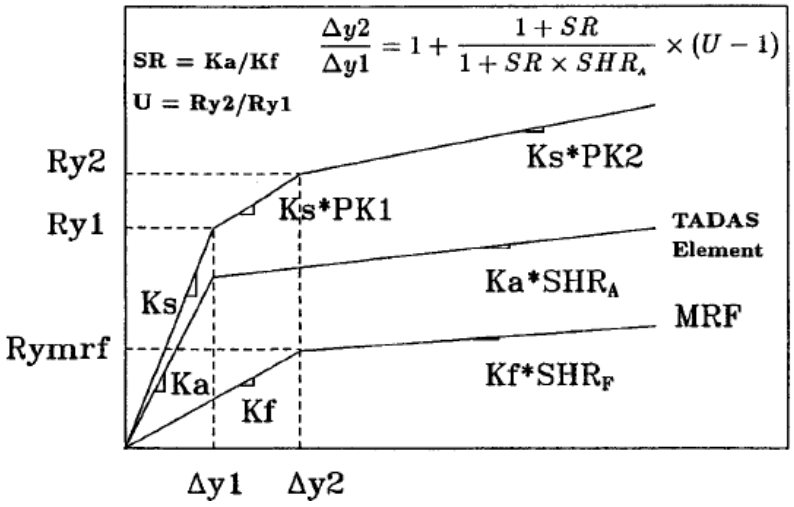

Figure 2.18 Force-deformation relationship in a frame system with TADAS

Chapter 3 Background

In this chapter, conventional eccentrically braced frame (CEBF), self-centering eccentrically braced frame (SCEBF) and replaceable hysteric dampers are explored in detail. Then experimental test and numerical analysis methods used in this dissertation are thoroughly discussed.

3.1 Conventional Eccentrically Braced Frame

An eccentrically braced frame (EBF) is a seismic lateral-force resisting structural system in which a critical beam segment known as “link beam” acts as a fuse device and dissipate energy through its yielding and plastic mechanism. In CEBF design, link length has a key role in determining the dominant deformation behavior and failure mode of the link [60]. When link length (e) is larger than 2.6Mp/Vp (long link), flexural yielding is dominant in the link response. When e is smaller than 1.6Mp/Vp (shear link), shear yielding will occur in the link web, so that shear yielding dominates the link response. If e is larger than 1.6Mp/Vp and it smaller than 2.6Mp/Vp it undergoes mixed web shear yielding and flange flexural yielding [7]. In short links, closely spaced stiffeners are generally needed to prevent shear buckling and to increase rotation capacity of the link.

3.2 Self-Centering structures

Self-centering EBF structures have the potential to provide the strength and stiffness of traditional EBFs while sustaining repairable damage under strong earthquakes due to special design considerations for enhanced resilience. The descriptor “self-centering” refers to the capacity to go through strong earthquake shaking with minimal residual lateral drift.

The initial tension force of Post-Tension strands provides a restoring force in EBF to re-center the structure. In self-centering structures, high strength post-tensioned steel strands connect beams and columns and provide a pre-compression force in the beam to enable self-centering behavior. For the system to be self-centered, the main structural member must remain undamaged and essentially linear elastic under earthquake loads and shear keys mostly used to prevent slip between link and adjacent structure component.

In SCEBF, before gap opens, it behaves like a CEBF; as a result, elastic deformation of the braced frame contributes to all the drift. However, as soon as the gap opens, the rocking link geometry changes. Nonlinear elastic behavior of self-centering structure is thus triggered by gap opening at link to beam or link to column interface.

In SCEBF, the post-gap opening stiffness is controlled by the number of PT strands and the depth of the shear link. By increasing the PT strands only, the post-gap opening stiffness increase but it does not affect the initial stiffness, because the SCEBF behave similarly to CEBF before gap opens.

In CEBF design, link length has a key role in determining the dominant deformation of the link through its failure mode, but in SCEBF the link should remain elastic under the design basis earthquakes.

In SCEBF, the only plastic deformation may occur at the end corner (i.e., rotating points of protruding link flanges) of link beam and column bases which would not affect the overall behavior of self-centering EBF system.

SCEBF with horizontal link (K and D type) has the following issues: 1) Issues with PT frame expansion in SCEBF, often referred to as "gap-opening expansion," arise from the opening of the rocking beam joint gap and link rotation. 2) another issue in SCEBF with horizontal link is the deformation discontinuity and incompatibility at higher levels; however, the design of all link to have same height diminish deformation discontinuity between floor significantly. To solve these issues of SCEBF with horizontal link, SCEBF with vertical link (Y type) is proposed and investigated in this dissertation. In SCEBF with vertical link, a vertical link which connects braces to the collector beam is used; as a result, gap-opening expansion issue and deformation discontinuity problem would be resolved.

3.3 Experimental Test Verification

In this chapter, experimental test results were verified engineering software. In the following section, the details of the prototype SCEBF-D module structure is also

presented.

In the experimental test done in China, D-type self-centering eccentrically braced frame designed and built [50]. All structure members are overdesigned including the rocking link beam to remain elastic through the entire test. The picture of the schematic view of experimental test for D-type SCEBF is shown in Figure 3.1. Picture and schematic drawings of the experimental test setup for cyclic loading test of SCEBF specimens are shown in Figure 3.2. The full-scale SCEBF specimen is a one-story one-bay module frame which measures 7,700 mm wide (from outer-edge-line of east-side column to end plate of the short protruding beam) and 3,620 mm in story height (from top-edge-line of collector beam to pin support center). The servo-hydraulic actuator used to load the specimen is positioned at a height of 3,155 mm above the center of the base pin support.

Short protruding beam and collector beam were welded to the corresponding columns, and beams were post-tensioned with PT strands after the entire frame is assembled but before cyclic loading tests. Bracing was welded to the gusset plate of the collector beam and column. Columns with welded base plate were connected to the base pin support by high-strength bolts. The pin supports at the column bases are bolted to the ground beam with high-strength bolts. The ground beam was anchored on the strong floor using strong ties while the ground beam was also secured to the reaction frame using threaded rods and concrete blocks to form a self-balanced loading system. Two pairs of lateral bracings were installed to prevent the out-of-plane displacement of the test specimen during the test, as shown in Figure 3.2(b).

During preliminary test of Specimen SCEBF1, sliding of the base pin support on the ground beam occurred and the base pin support plate was subsequently welded to the ground beam.

Figure 3.2(c) shows the schematics of rocking link beam with vertical RHD devices and horizontal RHD devices (at upper corners). The energy dissipation mechanism can be illustrated by using vertical RHD devices as an example. The vertical RHD devices are comprised of four trapezoidal-shaped energy dissipation steel plates welded to a base steel plate. This base plate is to be installed near the end sections of the rocking link beam as shown in Figure 3.2(c). Steel bracket holders with deep slots are installed to hold the vertical energy dissipation steel plates during link beam rotation. Before the test starts, steel energy dissipation plates are inserted into the deep slots with pre-specified initial gaps in the steel bracket holders. With increasing lateral drift, link beam would rotate, and the trapezoidal-shaped energy dissipation steel plates would deform in flexure and dissipate energy through plastic deformation. Based on the same operating principle, the horizontal RHD devices composed of two parallel energy dissipating plates welded to a base steel plate bolted to the sides of the end regions of link beam web. To achieve the required ductility of RHD devices without premature fracture failure, a highly ductile steel type Q225LY low yield point steel with a yield strength of 225 MPa was used for the trapezoidal shape energy dissipation steel plates.

Coupon tests were conducted on materials taken from the members which may yield during the tests to determine its monotonic uniaxial material behavior (see Table

3.2). The member material properties were taken as the averages of all the coupon tests for each member.

A total of five specimens, listed in Table 3.1, were tested to investigate the behavior of SC-EBF under cyclic loading. The first specimen, SCEBF1, has no RHD devices installed to validate its self-centering characteristics. The eccentrically braced steel frame and PT strands in SCEBF1 were reused in the following tests without replacement of any parts or tensioning of PT strands. The second type, SCEBF2, and SCEBF3 are the same as the SCEBF1 except for the installing of the vertical RHD devices, while SCEBF3 was designed to check the effectiveness and convenience of replacing the vertical RHD devices. The third type, SCEBF4 is the same as SCEBF1 except for the installing of the horizontal RHD devices. The last type, SCEBF5, has both vertical and horizontal RHD devices installed. Specimens SCEBF1-SCEBF5 used the same main frame because it remained elastic in all tests. There was no re-tensioning of the PT strands before each test. The tests were conducted in the order shown in Table 3.1.

The PT strands were typical 15.2-mm-diameter seven-wire strands with an ultimate tensile strength of 1,860 MPa. A total of 6 PT strands were used for the SCEBF specimen, which were all placed symmetrically about the center plane of the beams. As shown in Figure 3.2, these PT strands are anchored to the end plates of the short protruding beam and east-side column flange using PT anchoring fixtures. The PT strands are intended to remain elastic during the tests up to 2.5% drift ratio so that it could be reused in repeating tests without replacement, and thus a 1.5-m long short

protruding beam was included to increase the effective length of the PT strands and the PT strands were pre-tensioned to 41% of its yield strength. Horizontal stiffeners and end plates of beams and columns were added to protect against local failure due to large compressive forces acting on the flanges during the tests. Transverse stiffeners were also added near the ends of beams to prevent local buckling or potential damage from large forces exerted by the columns and bracing.

The short protruding beam, link beam, collector beam, and columns in these tests were made up of welded H-sections with a dimension of 350x350x14x20 mm, 350x250x30x40 mm, 630x330x20x30 mm, and 370x360x14x20 mm respectively. Their nominal section capacity and dimensions are shown in Table 3.3. These members are intended to remain elastic so that they can be reused without the need for repair throughout the experimental tests. The bracing was cold-formed hollow square-tube with a section size of 220x12 mm. Because the goal of these experimental tests was to investigate the lateral load behavior of SCEBF module frames under cyclic loading, no other gravity loads except for members' self-weight were applied to the test specimens.

Instrumentation equipment was installed to record the cyclic load response of the SCEBF specimens, as well as the responses of replaceable hysteretic damping devices. The applied load to the SCEBF specimen was measured directly with the actuator's load cell. Horizontal displacement transducers D1, D9 were placed at the mid-depth location of the collector beam and short protruding beam to measure the lateral drift of the SCEBF specimens during cyclic loading test. Due to gap opening at

PT connections, the measured displacements from transducers D1 and D9 were not equal. It should be noted that for SCEBF, the gap-opening expansion phenomenon still exists with the current design. Special detailing like those proposed by Garlock, Sause [49] can be applied to keep the columns of the SCEBF free of the floor slab and to prevent large axial force due to the restraint of the gap opening. Displacement transducers D2 to D5 were installed at the PT connections to measure the relative displacement between the link beam flange and the corresponding position of the west-side column and collector beam so that that gap opening angle can be derived in radians. Displacement transducers D12 to D17 were installed at the upper and lower plates of the base pin supports, and the ground beam to monitor if the two base pin supports slide due to insufficient friction. Horizontal displacement transducers D18 and D19 were placed at the upper flange of the link beam and the lower flange of the collector beam to monitor the out-of-plane displacements. A load cell is placed in the PT cable anchoring fixture to measure the total PT force.

Strain gauges were attached at selected sections along the rocking link beam, collector beam, bracing and columns to measure the axial forces and bending moments of each member during cyclic loading. Rosette strain gauges were also attached to the webs of the link beam and collector beam and the bracing-to-column joint to measure the local strain variation during the tests. The layout of displacement transducers and strain gauges for Specimen SCEBF1 was shown in Figure 3.3.
The target cyclic drift history (see Figure 3.4) for the test is referred to ANSI/AISC 341-10 (AISC 2010a). It is comprised of three cycles of 0.25% peak drift. After this,

the peak drift was increased to 0.4%, 0.8%, 1.2%, 1.6%, 2.0% and 2.5% each with two cycles of corresponding peak drift. In the cyclically symmetric loading protocol, an initial three cycles of pre-gap opening drift (0.25%) were imposed. It is noted that Specimen SCEBF1 was tested with a focus on observing the initial response behavior of the main SCEBF frame and verifying its self-centering ability. Therefore its loading program only reached a peak drift of 2.0%. The loading program of Specimen SCEBF4 has two additional cycles of 3.0% peak drift after the 2.5% drift.

Picture of rotated link beam and PT cables of specimen SCEBF5 at 2.5% drift ratio is shown in Figure 3.5(a) and picture of yielded RHD plates with flaked white wash is shown in Figure 3.5(b) [50]. Base shear versus lateral drift ratio curves of all test specimens subjected to cyclic loading are shown in Figure 3.6.

3.4 Finite Element Simulation

In this section finite element simulation techniques for modeling SCEBFs are reviewed along with experimental test result validation.

3.4.1 Shear Link Model of CEBF in SAP2000

In SAP2000, the approach proposed by Ghobarah and Ramadan [23] was employed for this study for modeling shear links. Shear link model consists of the following three elements: a beam element at the middle of the link to account for elastic axial, bending and shears deformations and yielding in bending, and two link elements at the two ends of the shear link to account for yielding in shear.

The middle beam element is a frame element with two plastic hinges at its end (M3). This element consists of three parts: a linear elastic region in the middle and two hinges at the ends. Schematics view of the shear link model is shown in

Figure 3.7.

Flexural hinges at the ends of the middle frame element are modeled with an auto plastic hinge assignment in SAP2000 based on the ASCE 41-13 equation 9-2.

$$M_p = 1.18\, Z_p F_{ye}\left(1 - \frac{P}{P_{ye}}\right) \leq Z_p F_{ye} \qquad \text{Equation 3.1}$$

Where M_p, Z_p, F_{ye}, P and P_{ye} represent expected flexural strength (Plastic moment), plastic section modulus, expected yield strength of material, axial force in the member at the target displacement for nonlinear static analyses, and expected axial yield force of the member ($A_g F_{ye}$).

Expected yield (F_{ye}) is the product of a code-prescribed factor and the expected strength of the material. This factor is typically around 1.1, as with FEMA 356 Table 5-3. These effective stress values represent the material response which occurs approximately halfway along the x-axis of the force-deformation relationship. FEMA 356 recommends using effective strength for deformation-controlled actions. Expected stress values are used to automatically generate hinge properties for P-M2-M3 and P-M3 hinges.

To define plastic hinges, plastic moment relative to yield moment and its rotation relative to yield rotation need to be calculated. The yield strength of the flexural hinges is defined as the plastic flexural capacity of the link beam using the expected yield

stress of 345MPa (50 Ksi). Since the shear links yield in shear, demand moment of the shear link should be lower than the link moment capacity.

Shear properties of the shear links in SAP2000 are defined by two link elements (shear hinge springs) at the ends of the shear link beam. The schematic view of shear hinge springs is shown in

Figure 3.7.

Shear forces (V) and stiffness in the link beam versus distance between internal and external nodes (δ) are shown in Figure 3.8. That curve can be divided into three distinct phases: 1) elastic range up to shear force of $V=1.1V_p$; 2) plastic phase before ultimate failure; 3) degradation phase due to excessive link rotation leads to web rupture of the link beam [61].

According to the AISC Seismic Provisions (2010), 0.08 rad is the link rotation limit for short links in CEBFs which can be considered as minimum limit value for required link deformation capacity.

To model shear hinges in SAP2000, one link element was used to have the behavior of four springs. SAP2000 link elements are used for these shear springs to simulate the piecewise-linear shear behavior of the shear link as shown in Figure 3.9.

3.4.2 Material and Loads

All columns, beams, braces, and links are modeled as frame elements, and braces are modeled as truss elements as braces primarily carry the axial load and moment in braces are negligible. Columns and braces are fixed at the base level. To consider gravity load,

two lean on columns used for SCEBF since it has gap-opening expansion issue and one lean on column used for CEBF. The lean on columns are connected through strong beam element to the main EBF frame, and they are pinned at the base level.

To design the structure load combination of 1.2DL+0.25LL used and to calculate seismic mass 1DL+0.2LL calculated and applied to the structure for modal, pushover and time history analysis [62]. Nodal masses are lumped into the lean on column nodes according to corresponding tributary areas. Gravity load of the structure was applied to lean on column and beam end nodes of EBF based on their tributary areas.

Nonlinear finite element (FE) analysis of the prototype SCEBF module structure was performed in ANSYS Academic ver. 18.2 and SAP2000. SCEBF1 and 2 are the cases chosen to be simulated in finite element software. In SCEBF2, four vertical TPADs were used on left side of the rocking link beam, and another 4 TPAD were placed on the right side of the rocking link beam, thus, in total eight vertical TPADs were utilized. The results from ANSYS are more accurate than SAP2000 but the computation time is more expensive than SAP2000. First, the finite element model of SCEBF1 and 2 of the experimental tests has been created in ANSYS to verify the experimental results, and then the same models in SAP2000 have been simulated afterward to compare the results between two simulation software. SAP2000 is preferred over ANSYS since the computation time of ANSYS is so expensive compared with SAP2000. Details of the prototype SCEBF (Specimen SCEBF2) module structure can be found in the following. The primary EBF frame members of the SCEBF module structure are made of Q345 steel, and the RHD devices' trapezoidal-shaped

energy dissipation plates are made of low yield steel Q225LY. The combined plasticity hardening model is employed to characterize the stress-strain relationship for both materials under cyclic loading. The calibrated material parameters of the combined hardening models for Q345 steel and low yield steel can be found in Table 3.2.

For finite element modeling, beam elements were adopted for modeling the SCEBF's columns, and portions of the beams and braces away from the rocking link beam. Solid elements were used for modeling the rocking link beam, the RHD device, and portions of the beam, column and brace that connect the rocking link beam, as shown in Figure 3.10(a). Beam elements are used for modeling the PT tendons. As the SCEBF structure is symmetric about the web planes of the EBF beam, only half model was built to represent the SCEBF structure in the ANSYS, but full model was simulated in SAP2000. Six post-tensioned strands with a cross-section area of 140 mm^2 were used in SCEBF with the initial stress level of 40% of its yield stress. Loading procedure adopted for the FE analysis of the SCEBF module structure in two steps: In the first phase, the initial pre-tensioning force was gradually applied to the PT strands before the time of one second when the pre-tensioning stress is 715 MPa. Following the first loading phase, starting from one second, a cyclic loading protocol shown in Figure 3.4 was applied to the SCEBF2 module structure for specimen design analysis. The corresponding load vs. displacement curve for ANSYS model is shown in Figure 3.10(b). For Specimen SCEBF1 without RHD devices, the gap-opening force V_{b0}, initial stiffness K_{b0} and post-gap-opening stiffness K_{bPGO} values

derived from finite element analysis are 420 kN, 99 kN/mm, and 3.7 kN/mm, respectively, which are in close agreement with the corresponding values (418 kN, 96 kN/mm, and 3.4 kN/mm respectively) predicted from the analytical formulas.

Experimental test model simulation in ANSYS and SAP2000 are shown in Figure 3.11 and Figure 3.12 respectively. The pushover curve comparison between SAP2000 results and experimental test for SCEBF-D type for SCEBF1 and 2 are shown in Figure 3.13 and Figure 3.14 respectively. Based on Figure 3.14, SAP2000 model can also accurately model the energy dissipation effect of the TPADs. The SAP2000 model was calibrated with both cases (SCEBF1 and SCEBF2) of experimental data of a full-scale SCEBF-D specimen.

The gap-opening behavior of SCEBF-D structure is shown in

Figure 3.15. RHD devices Von-misses stress at 2% roof drift ratio is shown in Figure 3.16, while in Figure 3.17 and Figure 3.18, Von-misses plastic strain of RHD devices is shown.

The target lateral force response of the SCEBF system subjected to seismically induced cyclic loading involves the limit states related to the PT tendons, fuse devices, and other structural components such as beams, columns, and braces. Potential limit states to consider in the design of the SCEBF structure include: 1) gap opening between the beams and the rocking link beam; 2) yielding of the fuse devices; 3) yielding of the SCEBF frame members, such as beams, rocking link beam, braces, and columns; 4) yielding of the PT cables; 5) ultimate failure of the SCEBF frame members, such as fuse fracture. Under the design basis earthquake, the

installed fuse devices should develop large plastic deformation for seismic energy dissipation. No damage such as inelastic action and buckling would occur to the frame members of the SCEBF structure, such as beams, columns, braces, and the rocking link beam. The building should remain fully operational and be available for immediate occupancy. Therefore, at 2% drift ratio, all SCEBF specimens are expected to remain elastic except for yielding in the corresponding RHD devices. Based on the FE analysis results, the SCEBF specimens are designed and tuned to achieve this goal before the test is terminated at 2% drift ratio. In this study, SAP2000 will be used for future modeling in this study to investigate the overall behavior of the SCEBF structures under design base earthquakes.

Table 3.1 Specimen labeling and features

Specimen	Descriptions
SCEBF1	Bare SCEBF module frame without RHD devices
SCEBF2	Bare SCEBF module frame with vertical RHD devices
SCEBF3	Same as SCEBF2, but RHD device replaced
SCEBF4	Bare SCEBF module frame with horizontal RHD devices
SCEBF5	Bare SCEBF module frame with both vertical and

Table 3.2 Calibrated plastic hardening parameters for Q345 steel and low yield steel Q225LY in finite element simulation

Steel Type	F_y (MPa)	$\boldsymbol{C}_1$ (MPa)	$\boldsymbol{\gamma}_1$	E_t(MPa)
Q345	345	7993	175	1500
Q225LY	235	900	10	47

Table 3.3 Member dimensions and nominal first yield moment My and axial load capacity Ne

Member	D (mm)	b (mm)	t_w (mm)	t_f (mm)	M_y (kN-m)	N_e (kN)
Link	350	250	30	40	2291	10764
Beam	630	330	20	30	1050	9695
Columns	370	360	14	20	821	6327
Bracing	220	220	12	12	227	3444

Note: D=section depth; b =section width; t_w and t_f are web and flange thickness respectively. $M_y = F_y*S_x$ is the bending moment at first yield of extreme fiber in flange; S_x is the elastic section modulus.

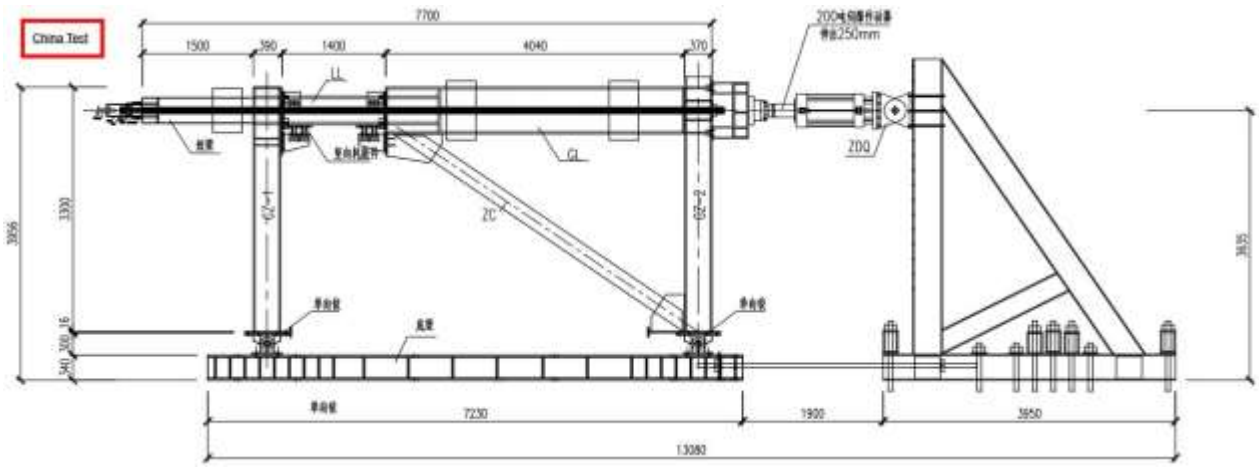

Figure 3.1 Schematic view of experimental test for D-type SCEBF

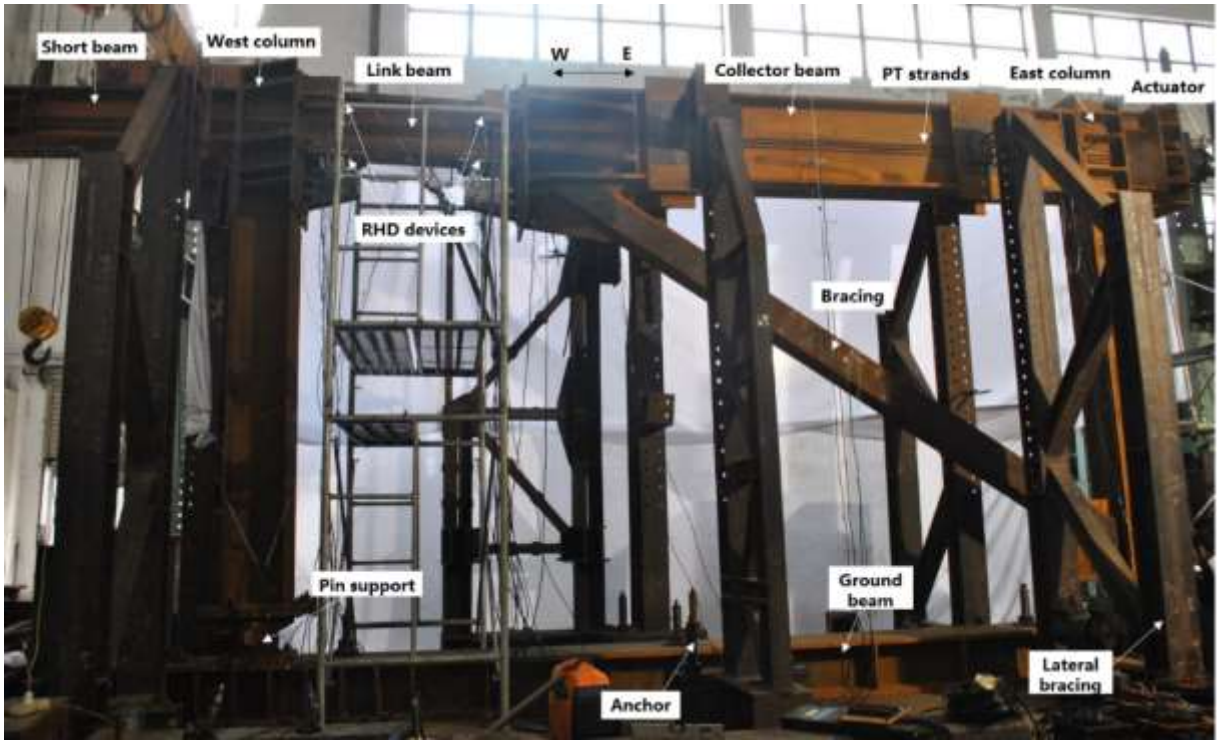
Short beam
West column
Link beam
W
E
Collector beam
PT strands
East column
Actuator
RHD devices
Bracing
Pin support
Ground beam
Lateral bracing
Anchor

(a)


Horizontal RHD devices
Rocking link
Bracket holder
Vertical RHD devices
Lateral load direction

(b)

(c)

Figure 3.2 Experimental test setup for SCEBF: (a) Picture; (b) Schematics of RHD devices installed to rocking link beam; pictures of vertical RHD and horizontal RHD; (c) Picture of PT cable anchoring fixture with PT force sensor mounted on the short protruding beam. (Tong, Zhang [50])

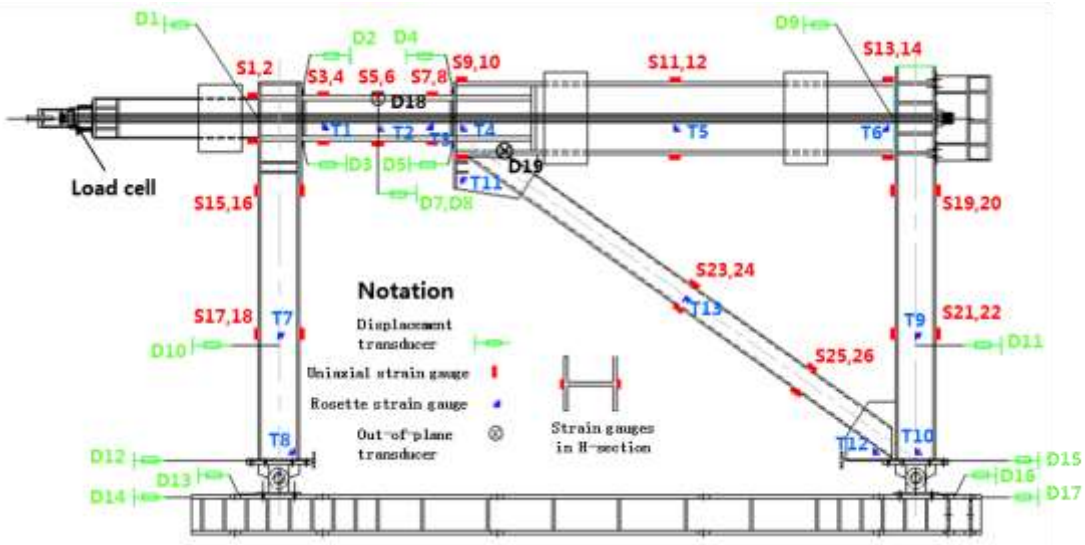

Figure 3.3 Instrumentation layout of displacement transducers and strain gauges for Specimen SCEBF1 (Tong, Zhang [50])

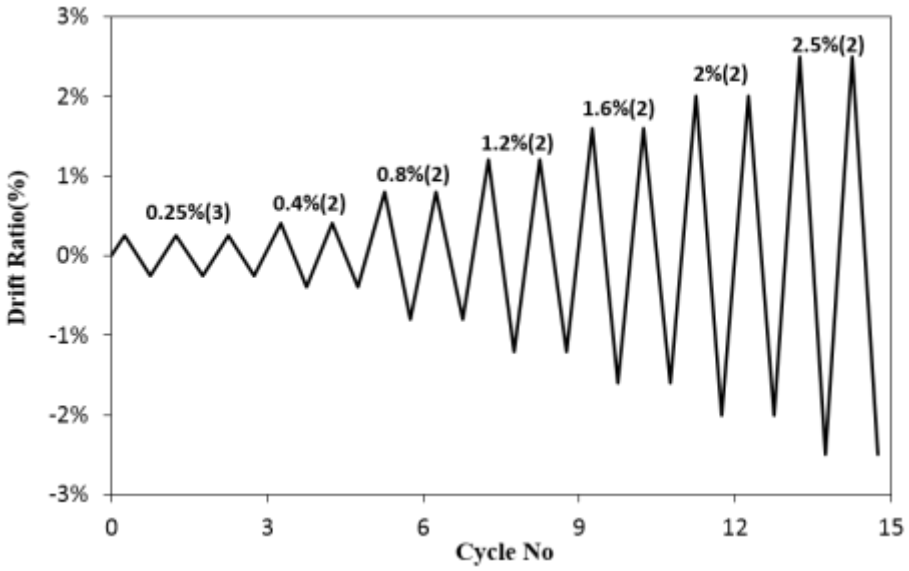

Figure 3.4 Loading history (Note: Figures in brackets represent the number of cycles at corresponding peak drift) (Tong, Zhang [50])

(a)

(b)

Figure 3.5 Specimen SCEBF5 at 2.5% drift ratio: (a) Picture of rotated link beam and PT cables; (b) Picture of yielded RHD plates with flaked white wash (Tong, Zhang [50])

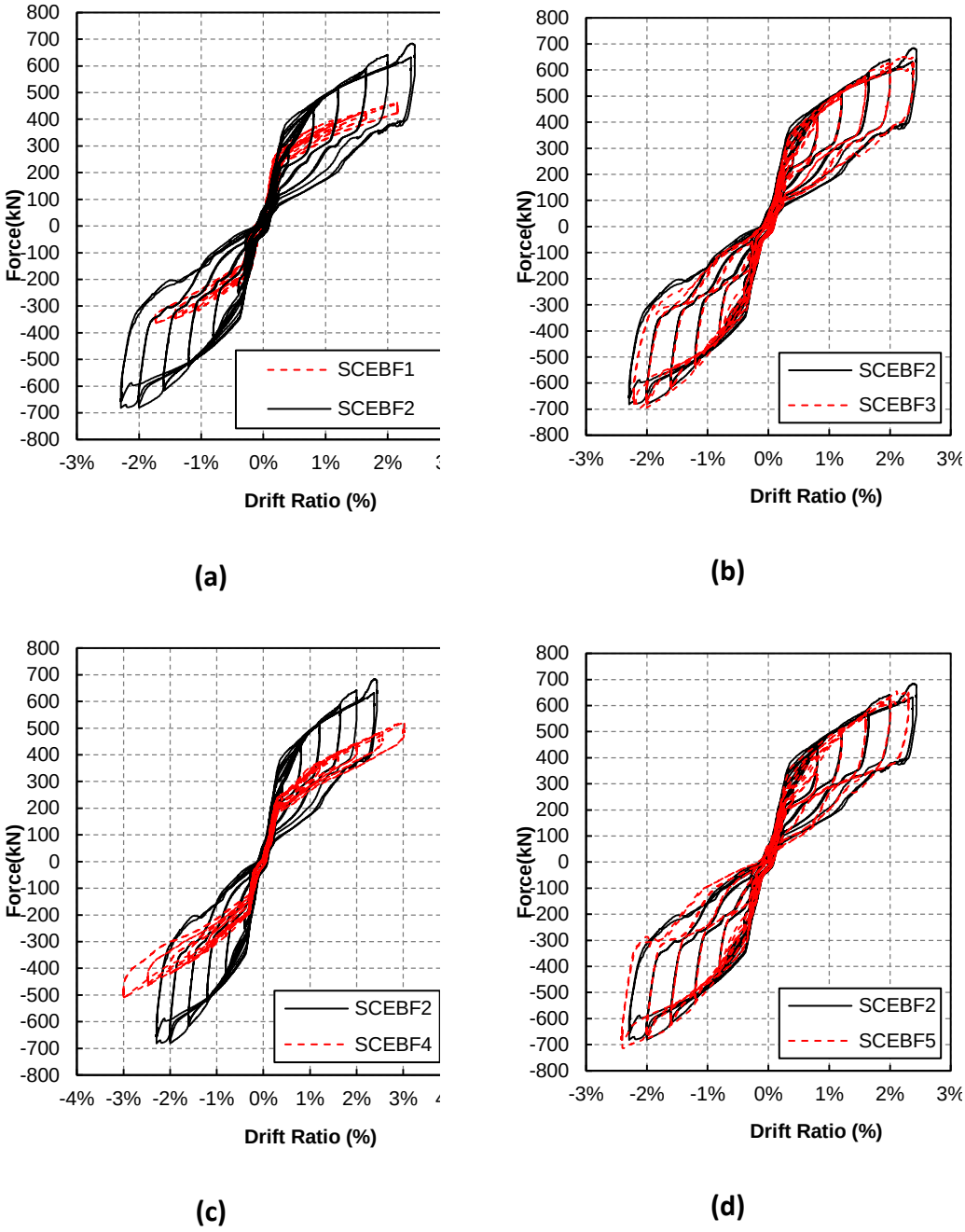

Figure 3.6 Base shear versus lateral drift ratio curves of all test specimens subjected to cyclic loading (Tong, Zhang [50])

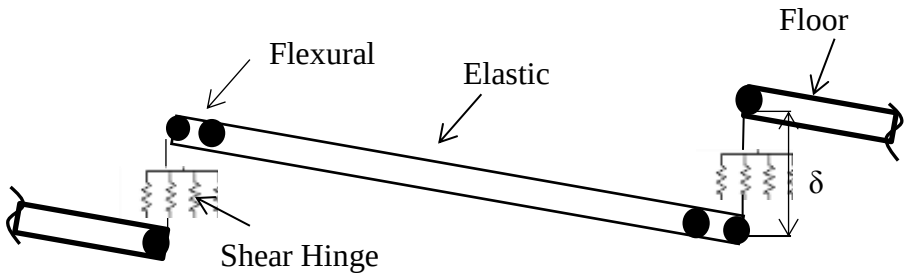

Figure 3.7 Schematic view of shear link model

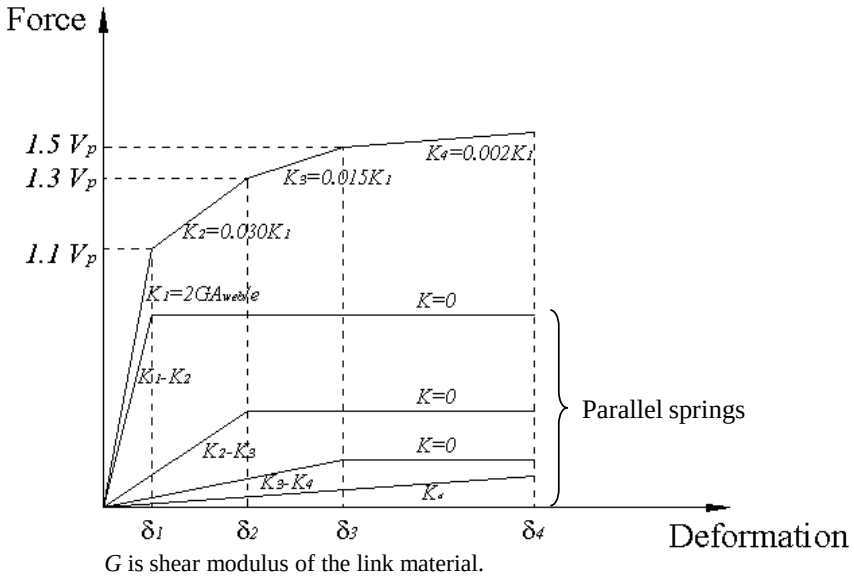

G is shear modulus of the link material.

Figure 3.8 Force-deformation relationship for parallel translational springs

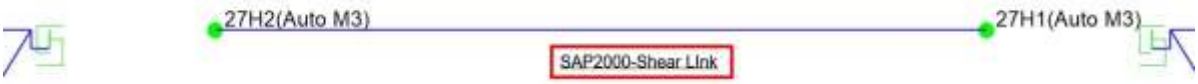

Figure 3.9 SAP2000 shear link modal

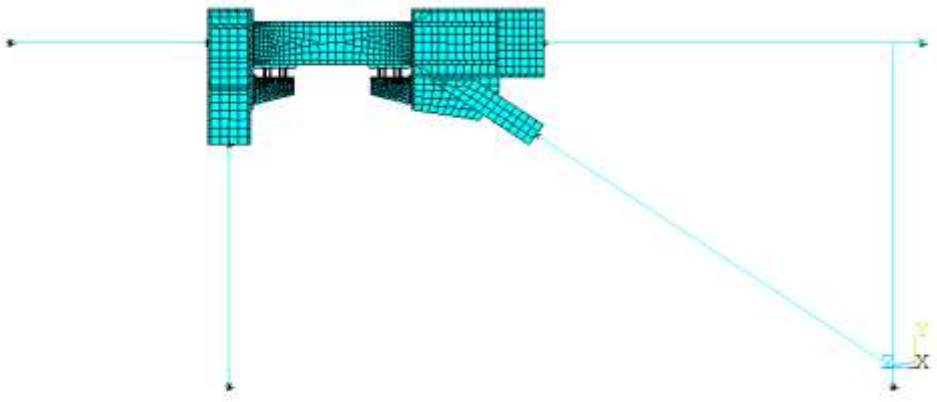

(a)

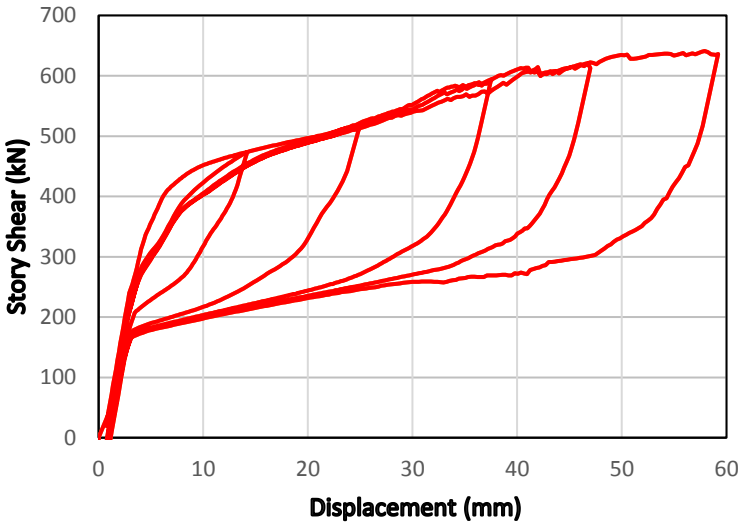

(b)

Figure 3.10 Finite element (FE) simulation of SCEBF2 under cyclic loading: (a) Meshed FE model; (b) push-over curve from nonlinear FE analysis (Tong, Zhang [50])

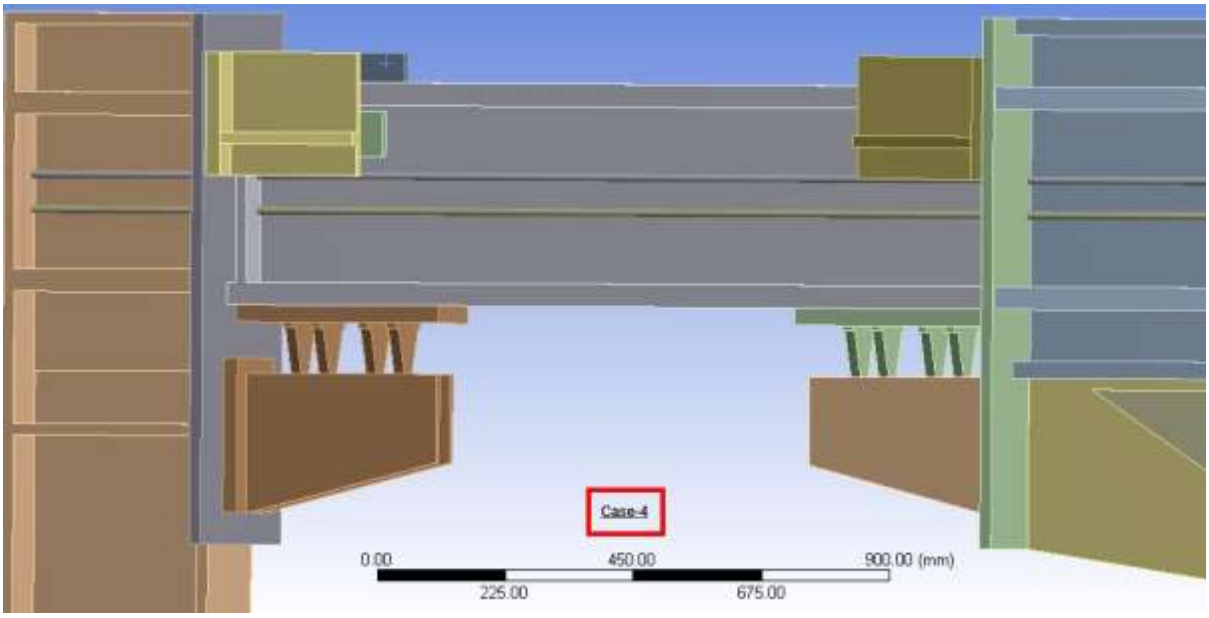

Figure 3.11 Experimental model in ANSYS

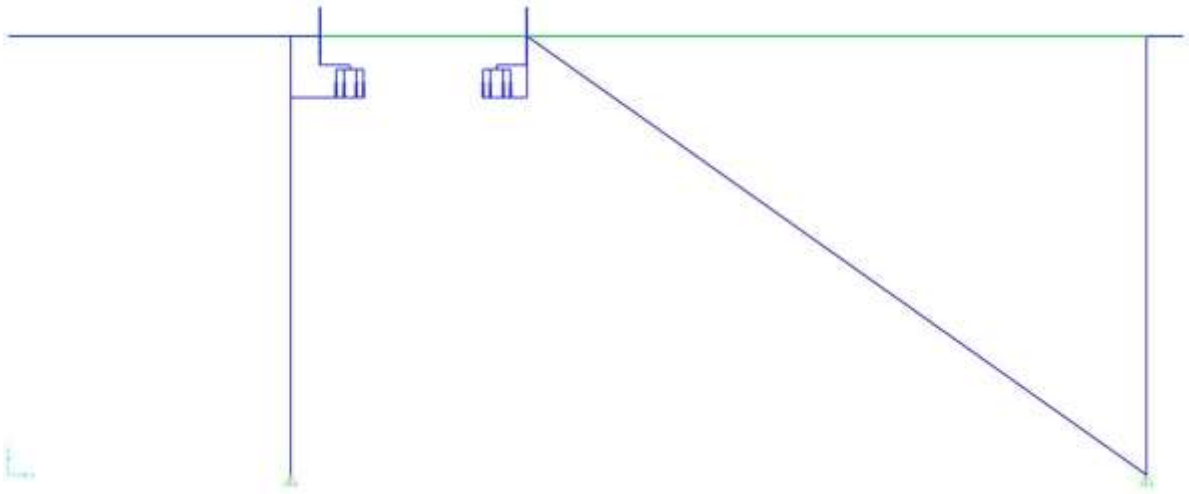

Figure 3.12 Experimental model in SAP2000

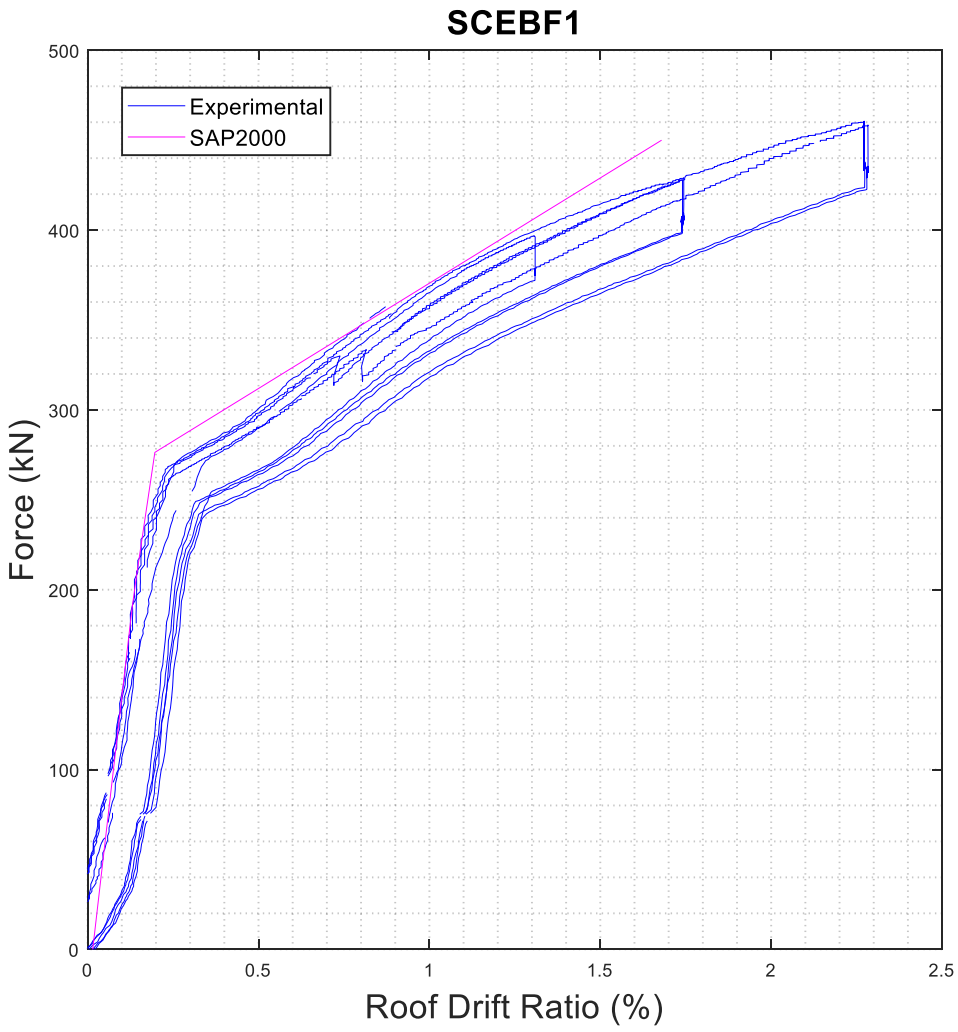

Figure 3.13 Pushover curve of experiment test (SCEBF1)

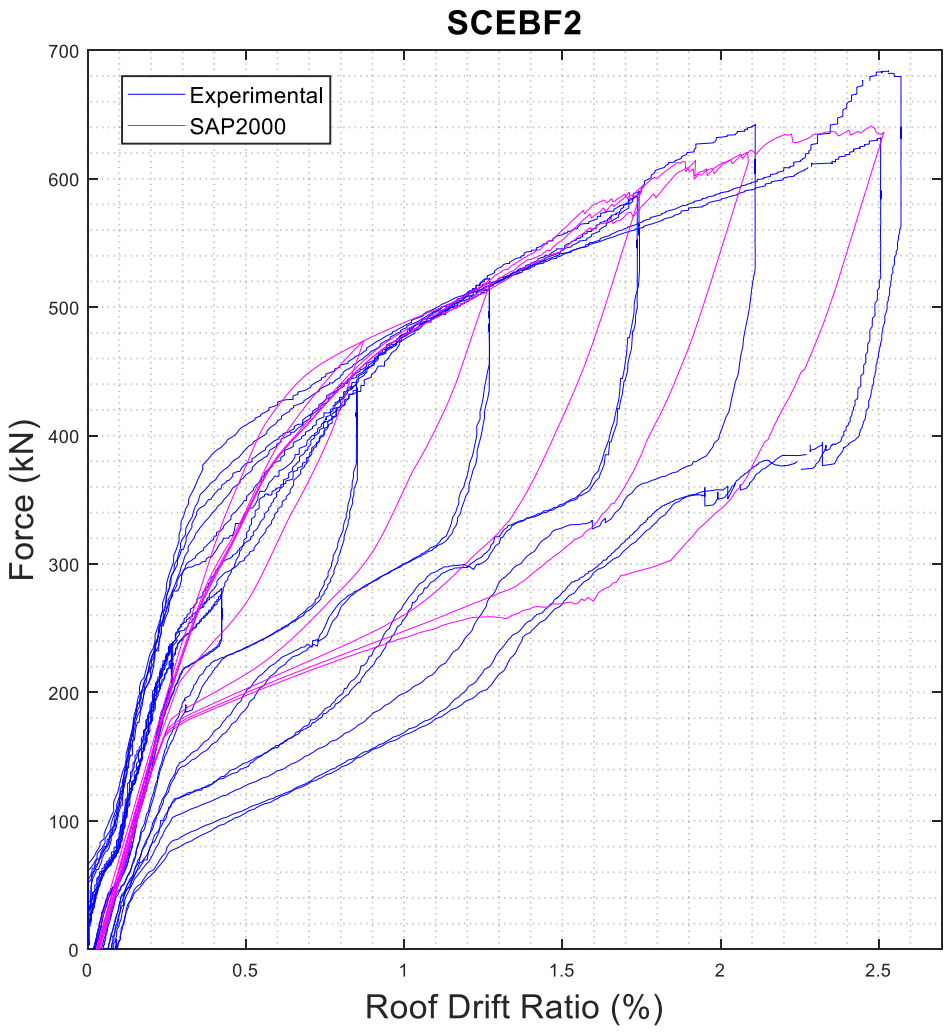

Figure 3.14 Pushover curve of experiment test (SCEBF2)

Figure 3.15 Link and fuse device configuration when gap opening happens

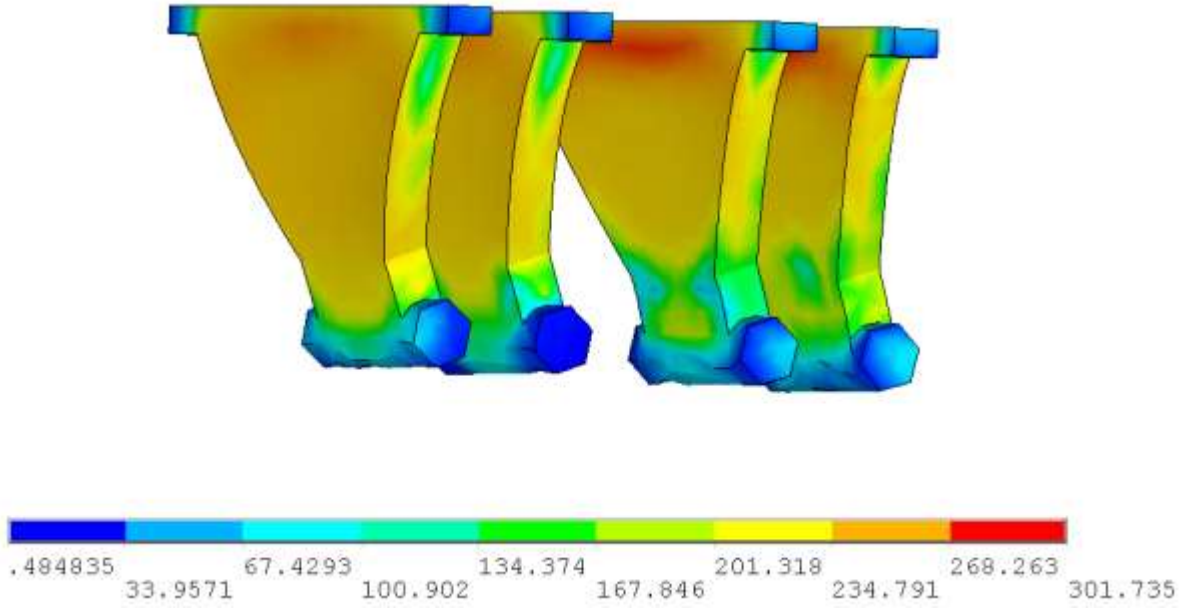

Figure 3.16 RHD device-Von misses stress at 2% drift ratio

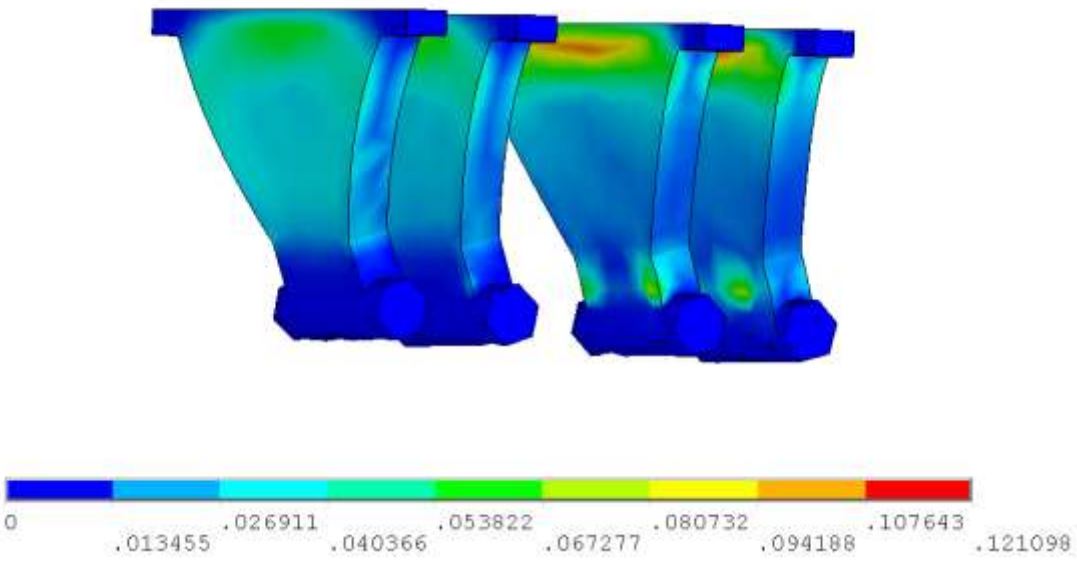

Figure 3.17 RHD device Von Mises Plastic strain at 2% drift ratio

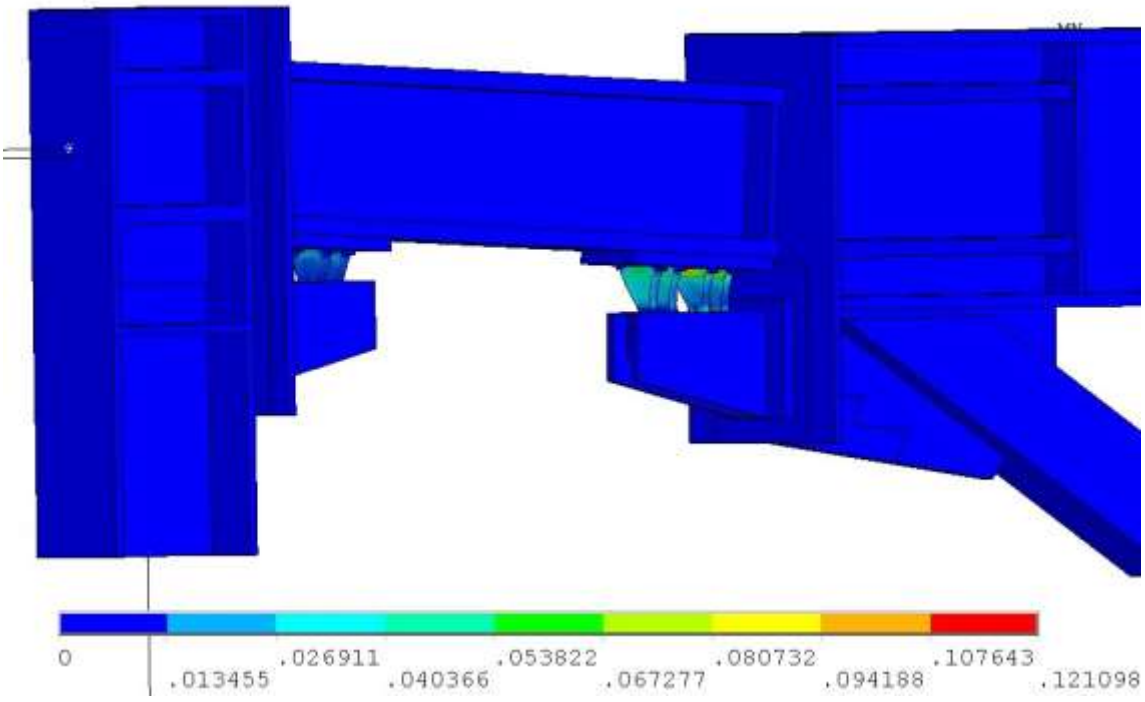

Figure 3.18 Von Mises Plastic strain at 2% drift ratio

Chapter 4 Seismic Performance Evaluation of D-type SCEBF

In this Chapter, the seismic performance evaluation of D-type SCEBF has been investigated and compared with D-type CEBF. Moreover, analytical formulas to design SCEBF-D type structure is also presented. Furthermore, D-type SCEBF has been investigated by nonlinear static analysis and nonlinear time history analysis.

4.1 Prototype SCEBF-D Type Buildings and Seismic Design

SCEBFs have the potential to provide the economy, strength, and stiffness of EBFs while sustaining less damage under design basis earthquakes. SCEBFs have columns, braces, rocking link beam, collector beam and RHD devices along with PT cables which connect all structural members through compression. The arrangement of PT cables, RHD devices and rocking link beam in a full-scale SCEBF test specimen [9, 50] are shown in Figure 4.1.

One prototype self-centering structure – a 3-story D-type (SCEBF-D) building is considered in this Chapter. For the conventional D-Type building, a modified design of three-story EBF originally inspired by Richards and Uang [63] was chosen to accommodate the replaceable links in the prototype EBF building. The 4x6 bay building is 11.9 m (39 ft.) tall and 36.6 x 54.9 m (120 x 180 ft.) in the plan as shown in Figure 4.2 and

Figure 4.3. The seismic weight of the 3-story EBF-D is 30,630 kN (6,886 kips) in total. The 1st, 2nd and 3rd floor weights are 9,901 kN (2,226 kips), 9,901 kN (2,226 kips) and 10,827 kN (2,434 kips) respectively. In the SCEBF-D building, eccentrically braced frames located along the North-South (N-S) direction is considered in this study. Table 4.1 and

Table 4.2 shows the member sizes of 3 story CEBF-D and SCEBF-D respectively.

In self-centering structures, high strength post-tensioning strands connect beams and columns and provide pre-compression force in the beam to enable the rocking action of the link. The tension force of post-tensioning cable (PT) thus provides the critical source to re-center the SCEBF structure. PT cable is made up of multiple PT strands, which are standard seven-wire ASTM A416Gr270 steel strand with an effective cross-section area around 140 mm2. In the SCEBF-D, 14, 12 and 8 PT strands are used in their PT cable for first, second and third floor respectively with the initial stress level set as 50% of its yield stress. For the system to be self-centered, the main structural member is expected to remain essentially linear elastic under earthquake loads. In the SCEBF structures concerned here, most of the damages are concentrated to fuse devices called RHD devices (Replaceable Hysteric Damper) which can be easily replaced with low costs.

4.2 SCEBF-D Type Analytical Formula

The design principle for a one-story D-type SCEBF is briefly discussed here. A schematic view of the one-story SCEBF-D module is shown in Figure 4.4, and the rocking link beam configuration in SCEBF-D is shown in Figure 4.5.

In Figure 4.4, the geometric properties of SCEBF-D type frame are demonstrated. Based on Figure 4.4, h, a, L_d, L, e and Δ show frame height, beam length, brace length, frame length, link length and frame horizontal displacement. In Figure 4.5 Rocking link beam configuration and dimension in SCEBF-D structure are presented.

In Figure 4.6 and Figure 4.7, pushover curves of bare frame SCEBF-D type and SCEBF-D type with TPAD fuse device is presented respectively. $K_{b_0}, V_{b_0}, K_{b_{PGO}}$ and $V_{b_{FD}}$ represent SCEBF-D type initial stiffness, Gap opening shear force, post gap opening stiffness and fuse device shear force effect on SCEBF-D type. Stiffness and shear force formulas for one-story SCEBF-D module are presented in the following section. K_{b_0} depends on geometric configuration of the SCEBF-D type while V_{b_0} and $K_{b_{PGO}}$ mostly depends on the properties of PT strands.

In the following equations, I_l and I_b express the moment of inertia of link and beam respectively. $A_d, A_b$and A_{wl} show section area of brace, section area of beam and section area of link web respectively. F_{PT_0}, A_{PT}, L_{PT} and E_{PT} present the PT strands initial force, area, length and young's modulus respectively, while t_{f_l} and d_l express link flange thickness and depth. E and G are young and shear modulus of steel. K_{l_0} is required to compute the link initial stiffness. K_{l_0} consists of four terms K_{da}, K_{ba}, K_v

and K_f. K_{da}, K_{ba}, K_v show brace axial stiffness, beam axial stiffness, link shear stiffness [64]. The K_f expression is formulated in this study using the principle of virtual work representing the flexural stiffness of link/beam.

$$K_{l_0} = (\frac{1}{K_{da}} + \frac{1}{K_{ba}} + \frac{1}{K_v} + \frac{1}{K_f})^{-1} \quad \text{Equation 4.1}$$

$$K_{da} = E(\frac{A_d}{L_d})(\frac{a}{L_d})^2 \quad \text{Equation 4.2}$$

$$\mathrm{K_{ba}} = \frac{EA_b}{a} \quad \text{Equation 4.3}$$

$$\mathrm{K_v} = \frac{GA_{wl}L(L-e)}{h^2 e} \quad \text{Equation 4.4}$$

$$\mathrm{K_f} = \frac{3EL^2}{ahe^2}(\frac{a}{I_b} + \frac{e}{I_l})^{-1} \quad \text{Equation 4.5}$$

$$K_{b_0} = K_{l_0} + K_c \quad \text{Equation 4.6}$$

Where K_c represents the columns stiffness which can be neglected for initial stiffness. In this study, K_f, K_{l_0} and K_{b_0} were derived representing the link/beam flexural stiffness due to link and beam flexural deformation, link initial stiffness and SCEBF-D type initial stiffness respectively.

Based on Figure 4.8, a force of 1* applies as the brace-vertical force to the beam. Thus, the link/beam flexural stiffness (K_f) would be calculated based on principal virtual work as follows:

$$1 \times \Delta^{*} = \int_{0}^{e} \frac{\left(\frac{1^{*} ax}{a+e}\right)\left(\frac{pax}{a+e}\right)}{EI_l} dx + \int_{e}^{a+e} \frac{\left(\frac{1^{*} e(a+e-x)}{a+e}\right)\left(\frac{pe(a+e-x)}{a+e}\right)}{EI_b} dx$$

$$\rightarrow \qquad K_f = \frac{3EL^2}{ahe^2}\left(\frac{a}{I_b} + \frac{e}{I_l}\right)^{-1}$$

In D-type SCEBF, for rocking link beam design, the primary goal is to make the rocking link beam remain elastic under DBE earthquakes and should also be stiff enough. In designing the PT cables, two primary factors considered are: (1) adjusting the gap opening force to the value desired for the design; (2) PT cable should not yield under DBE level seismic loading. Rocking link beam gap-opening shear force (V_{l_0}) and initial PT force (F_{PT_0}) are presented below. Then, the initial PT stress (σ_0) needs to be determined, therefore, the number of PT strands (N_{PT}) forming the PT cable is derived.

The compression force created by PT strands provides gap opening shear force.

$$V_{l_0} = \frac{F_{PT_0}(d_l - t_{f_l})}{e} = V_{b_0}\frac{h}{L} \qquad \text{Equation 4.7}$$

$$V_{b_0} = V_{l_0} + K_c\left(\frac{V_{l_0}}{K_{l_0}}\right) \qquad \text{Equation 4.8}$$

Where F_{PT_0} represents the initial pre-tension force of PT strand. V_{l_0} and V_{b_0} were derived in this study and represent the link gap opening shear force, and SCEBF-D type gap opening shear force.

$$F_{PT_0} = V_{l_0} \frac{e}{(d_l - t_{f_l})} \quad \text{Equation 4.9}$$

$$N_{PT} = \frac{F_{PT_0}}{\sigma_0 A_{PT}} \quad \text{Equation 4.10}$$

Where h, L, e and A_{PT} represent the frame height, bay width, rocking link beam length and cross-section area of one 7-wire PT strand respectively. PT cables must remain elastic through DBE; as a result, they should be properly designed to not yield at 2% inter-story drift ratio. Based on Figure 4.5, after the gap opens, rocking link beam rotates around center of rotation or pivot point P; therefore, PT cable extends by $[(\frac{(L-e)(d_l - t_{f_l})}{he}) \Delta]$ and its axial force increases accordingly. PT cable axial force after gap opening happens (F_{PT}) can be calculated as follows.

$$F_{PT} = F_{PT_0} + \frac{N_{PT} A_{PT} E_{PT}}{L_{PT}} \frac{(L-e)(d_l - t_{f_l})}{he} \Delta \quad \text{Equation 4.11}$$

$$L_{PT_{min}} \geq \frac{N_{PT} A_{PT} E_{PT} (L-e)(d_l - t_{f_l}) \Delta}{(F_{PT_{max}} - F_{PT_0}) he} \quad \text{Equation 4.12}$$

where F_{PT}, Δ, E_{PT} and $L_{PT_{min}}$ denote PT cable force, frame drift, Modulus of Elasticity and minimum length of PT cables respectively. As mentioned earlier, the PT cable must remain elastic through DBE, as a result, the required PT cable length ($L_{PT_{min}}$) should be calculated based on maximum allowable PT cable force ($F_{PT_{max}}$).

Based on Figure 4.5, link post-gap opening stiffness and shear force are derived. When gap opens, PT strands extends $[(\frac{a(d_l - t_{f_l})}{he}) \Delta]$; thus, its axial force increases accordingly. By increasing PT strands force, the link shear force also increases. Post-

gap opening stiffness of SCEBF-D ($K_{b_{PGO}}$) and shear force of the link ($V_{l_{PGO}}$)is calculated as follows:

$$K_{l_{PGO}} = \frac{a\,A_{PT}E_{PT}}{L_{PT}he^2}(d_l - t_{f_l})^2 \qquad \text{Equation 4.13}$$

$$K_{b_{PGO}} = \frac{aL\,A_{PT}E_{PT}}{L_{PT}h^2e^2}(d_l - t_{f_l})^2 + K_c \qquad \text{Equation 4.14}$$

$$V_{l_{PGO}} = V_{l_0} + K_{l_{PGO}}\,\Delta \qquad \text{Equation 4.15}$$

$$V_{b_{PGO}} = \frac{L}{h}\,V_{l_{PGO}} + K_c\,\Delta \qquad \text{Equation 4.16}$$

where $K_{l_{PGO}}, K_{b_{PGO}}$, $V_{l_{PGO}}$ and $V_{b_{PGO}}$ represents link post-gap opening stiffness, SCEBF-D type post-gap opening stiffness, link post-gap opening shear force and SCEBF-D assembly post-gap opening lateral force respectively.

Based on Figure 4.5, after the gap opens, link rotates around pivot point P. Thus, PT strand extends by $[(\frac{a(d_l - t_{f_l})}{he})\,\Delta]$; thus, link post-gap opening stiffness ($K_{l_{PGO}}$) and link post-gap opening shear force ($V_{l_{PGO}}$) would be calculated as follows:

$$\mathrm{F}_{PT} \times (d_l - t_{f_l}) = V_{l_{PGO}} \times e \rightarrow \begin{cases} V_{l_{PGO}} = V_{l_{GO}} + \frac{a\,A_{PT}E_{PT}}{L_{PT}he^2}(d_l - t_{f_l})^2\,\Delta \\ K_{l_{PGO}} = \frac{a\,A_{PT}E_{PT}}{L_{PT}he^2}(d_l - t_{f_l})^2 \end{cases}$$

The behavior of the SCEBF-D before a gap opens, mostly depends on link and beam flexural deformation and it is independent of PT strands. However, as soon as the gap opens, the geometry of SCEBF-D changes and rocking behavior of the link starts to dominate the frame deformation. As a result, the post-gap opening stiffness of the SCEBF-D is controlled by PT area and PT length along with the rocking link depth.

Based on Figure 4.9, the effect of fuse device on SCEBF-D is calculated in the

following section. fuse device has shear force of V_{FD} and axial force of P_{FD} which is directly apply to the Fuse holder connected to the link; as a result, fuse device shear force contribution and energy dissipation would be calculated as follows:

$$\left.\begin{matrix} V_{FD} = \dfrac{MP_{FD}}{h_{FD}} \\ V_{l_{FD}} = \sum M_A + \sum M_B \end{matrix}\right\} \rightarrow V_{l_{FD}} = \frac{V_{FD}(d_l + 2h_{FD}) + 2P_{FD}w}{e}$$

$$V_{l_{FD}} = \frac{V_{FD}(d_l+2h_{FD})+2P_{FD}w}{e} \qquad \text{Equation 4.17}$$

$$V_{b_{FD}} = \frac{V_{l_{FD}}L}{h} \qquad \text{Equation 4.18}$$

$V_{l_{FD}}$ and $V_{b_{FD}}$ represent fuse device effect on the link shear force and fuse device effect on the SCEBF-D shear force respectively. As shown in Figure 4.9, fuse device increases the gap-opening shear force of SCEBF-D type (V_{b_0}) by $V_{b_{FD}}$.

Based on the analytical formula, K_f is the dominant parameter controlling total frame initial stiffness which is related to moment of inertia of link and beam. However, post-gap opening stiffness mostly depends on PT cable area and length along with rocking link depth.

Three key parameters defining the SCEBF force-displacement relationship are as follows: (1) SCEBF initial stiffness before gap opening happens; (2) SCEBF post-gap opening stiffness; (3) gap opening shear force (yield strength). The stiffness and yield strength of SCEBF can be controlled and tuned by proper design of PT cable, RHD devices, and rocking link beam. In the SCEBF, before a gap opens, it behaves like a

CEBF; as a result, elastic deformation of the braced frame contributes to all the drift. However, as soon as the gap opens, the structure geometry changes and link rocking starts to contribute to system deformation. This nonlinear elastic behavior of the self-centering structure is triggered by the gap opening at the link to beam or link to column interface. For SCEBF with the current design, the gap-opening expansion phenomenon still exists, and the relative displacement between columns is not zero. Special detailing (e.g., those proposed by Garlock, Sause [49] and Garlock and Li [26]) needs to be applied to keep columns of the SCEBF free of the floor slab and to prevent large axial force due to the restraint of the gap opening. The restraint of gap-opening expansion due to column is considered in this study; however, the restraint caused by floor slab is not considered in this study and as an important issue, it needs to be further investigated in future study of SCEBFs.

In the SCEBF, the post-gap opening stiffness is controlled by the number of PT strands used in the PT cable and the depth of the rocking link beams. By increasing number of the PT strands only, the post-gap opening stiffness can be made to increase but, it does not affect the initial stiffness.

In CEBF design, link length has a key role in determining the dominant plastic behavior (web shear yielding or flexural yielding) of the link beam in terms of its failure mode. However, in the SCEBF structure, the rocking link beam is made very stiff and should remain elastic under the target design. The self-centering structure thus features significant initial stiffness due to rocking link beams with heavy sections while energy dissipation capability is offered by RHD devices. RHD device is the only part of the

SCEBF structures sustaining major earthquake-induced damage, and by its inelastic behavior it dissipates sufficient energy and would limit the drift of the structure. RHD devices can be replaced easily at low costs. Thus, the disruption time of such design would be considerably reduced for post-earthquake repair work.

The flag-shaped force-displacement of the SCEBFs is a combination of responses of SCEBF and RHD devices. The total stiffness of SCEBF with RHD devices is the sum of SCEBF stiffness and RHD devices. RHD device provides partial strength and stiffness and energy dissipation for the self-centering frame, and PT cables provide the re-centering capability of the frame. In SCEBF-D frame, 1st to 3rd-floor RHD device top width is 89 mm, 76 mm, and 47 mm respectively with the thickness of 25.4mm. For SCEBF-D type system, 12 RHD devices have been used for each floor.

This study investigates the overall seismic response behavior of SCEBF structures with D type configuration. The overall behavior of D-type self-centering EBF is investigated and compared it with a D-type CEBF.

4.3 Numerical Model of CEBF-D & SCEBF-D

A planar EBF model in the N-S direction of the building plan was conducted to simulate the seismic response behavior of the EBF frame using a general FE software SAP2000 [65]. A model has been created for D-type SCEBF, and another model has been created for D-type CEBF structures. In CEBF-D type, lighter sections with the length of 0.76 m (2.5 ft.) were considered for replaceable links.

Seismic performance of CEBFs during strong earthquake events largely depends on the inelastic hysteretic behavior of link beams, while, in SCEBFs the seismic performance depends on the rocking behavior of elastic link beams and associated fuse devices for energy dissipation. Therefore, accurate numerical simulation of rocking link beams is critical to the nonlinear seismic analysis of EBFs. In the nonlinear FE model CEBFs, the approach proposed by Ghobarah and Ramadan [23] for modeling shear links is employed. Shear forces and stiffness in the link beam versus distance between internal and external nodes can be divided into three distinct phases: 1) elastic range up to shear force of $V=1.1V_p$; 2) plastic phase before ultimate failure; 3) degradation phase due to excessive link rotation leads to web rupture of the link beam [66]. Flexural hinges at the ends of the shear links and column bases are modeled with an autoplastic hinge assignment based on the ASCE 41-13 Equation 9-2. In FE simulation of CEBF and SCEBF, all connections between frame elements are rigid connections except for braces which have pinned ends.

Schematic views of SCEBF, composed of the rocking link beam, PT cables, RHD devices, and other structural members are shown in Figure 4.10 and Figure 4.11. The pivot point of rocking link beam is also assumed to form at the mid-thickness line of rocking link's flanges. Thus, the depth of the rocking link would be equal to rocking link depth minus rocking link flange thickness. To simulate the gap opening behavior, a special link element in the FE model called "Gap element" is used. Gap elements are located at the pivot point of the rocking link. To model the RHD devices, a frame element with a tapered section along with 20 plastic hinges for each plate segment is

employed. RHD devices are connected to the lower fuse holder bracket through Gap element as shown in Figure 4.10 and Figure 4.11. Furthermore, PT cables are modeled with "Cable element" in the FE software which can sustain tension forces. It is important to mention that In FE software based on CSI Analysis Reference Manual, the linear effective damping for non-linear Link/Support elements such as Gap element would not be used for nonlinear direct-integration time history analysis [65].

Nonlinear beam-column elements were used to model columns and beams. Truss elements were used to model all braces. Moreover, the model does allow the SCEBF rocking link beam to yield in bending, axial force, or combined bending and axial force. However, the rocking link beams' sections are properly selected to avoid any yielding in the SCEBF rocking link beam through DBE. The material utilized for all columns, beams, rocking link beams, and braces are A992 Gr50 steel, and for RHD devices and PT cables, Q225LY and A416Gr270 were used respectively. A lean-on column along the height of the structure has been modeled in FE model to consider the p-delta effect which is connected through rigid truss element to EBF. First floor columns of EBF are fixed at their bases, but the lean on-columns are pinned at their bases. Floor masses are lumped into the lean-on column nodes at each floor level. For EBF-D type, only a quarter of the total seismic mass is considered for EBF-D type model since we have 4 EBFs in the N-S direction of EBF-D type building.

A 5% damping ratio for the first and second modes through Rayleigh damping is considered for the EBF in the FE model. The first three vibration periods of SCEBF-D

are 0.54 sec, 0.23 sec, 0.19 sec respectively. The first vibration period of CEBF-D frame is 0.67 sec. Figure 4.12 shows the first three mode shapes of SCEBF-D.

The first mode shape is the dominant mode shape in the EBFs based on FE results, thus, for pushover analysis, an inverted triangular vertical load profile [67] should be used to spread the base shear along the height of the eccentrically braced frames.

4.4 Nonlinear Static Analysis

The seismic performance of CEBF and SCEBF is thoroughly investigated by pushover and nonlinear time history analysis in FE model. Pushover analysis is a nonlinear static analysis providing information regarding elastic and inelastic behavior of structure such as ductility, key load levels and deflection of the structure until the ultimate condition is reached. The pushover analysis also shows the formation of plastic hinges at various locations as the lateral load increases. To perform the pushover analysis, first, appropriate plastic hinges need to be assigned to corresponding locations of members as needed. For CEBF, plastic hinges are created in shear links and column base, and for SCEBF, plastic hinges are set up in fuse members and column base but not rocking links because it is supposed to remain elastic through the design-basis earthquake. Moreover, material nonlinearities are also assigned to different hinge locations to capture plastic rotation behavior better.

Pushover analysis is essentially based on the assumption that the first mode shape dominates the response of the structure and first mode shape remains constant through

elastic and inelastic response of the structure. Based on FEMA2000, an inverted triangular load distribution was used to derive pushover forces as shown in Figure 4.13. Pushover force applied at the designated floor nodes forms an approximately inverted triangular profile. The control point of pushover analysis for the CEBF is the right column roof node but for SCEBF is the node in the mid-span of the rocking link to bypass the gap-opening expansion in self-centering structures. The lateral load was increased monotonically until the control point reaches 2% roof drift ratio. Roof drift ratio is defined as the horizontal roof displacement divided by the height of the EBF structure.

Figure 4.14 and Figure 4.15 shows the pushover curves of CEBF-D type and the flag-shaped curve of self-centering structure for D type EBF with RHD devices. Based on the flag-shaped curve, the residual drift is minimal meaning that the SCEBF can re-center itself after earthquake. Based on Figure 4.15 for CEBF, post-yield stiffness changes gradually which suggests the initiation of link shear yielding; however, for SCEBF, post-yield stiffness changes abruptly showing the gap opening behavior in self-centering structure. Pushover analysis also gives out information regarding the inelastic behavior and seismic energy dissipation of specific members in the structure such as a shear link in CEBF or RHD devices in SCEBF.

In Figure 4.15, number 1 denotes the point when gap opening happens, and number 2 shows plastic hinges formation of RHD device.

In SCEBF-D, gap opening happens at 0.15% roof drift ratio (number 1) and at 0.23% roof drift ratio, first-floor RHD devices form plastic hinges (number 2). The yield

strength of SCEBF-D would be at 0.232% roof drift ratio which lateral stiffness of SCEBF- D reduces significantly.

PT cables would not yield at 2% roof drift ratio for SCEBF-D type. For the SCEBF-D, some reduction in unloading stiffness is observed.

In Figure 4.15, it is also seen the difference of force-displacement hysteresis of SCEBF Vs. CEBF. SCEBF has a flag-shaped hysteresis which minimizes residual drift of the structure leading to the re-centering system. Nevertheless, CEBF has a bilinear force-displacement hysteresis with a considerable amount of residual drift due to yielding of shear links. The Beta factor in SCEBF-D frame is equal to 0.37 respectively [52]. Moreover, based on Figure 4.15, the initial stiffness of SCEBF is higher than CEBF. The initial stiffness of the SCEBF system is higher than the corresponding CEBF system. Since, in the SCEBF structure, the primary structural members including link beam, braces, beams, and columns are designed so that they should remain elastic under the design level earthquakes. The self-centering EBF structures thus feature larger initial stiffness compared with conventional structural systems. Plastic hinges in column base of the SCEBF-D will form at 1.5% roof drift ratio, which is in the late stage of pushover curve before the 2% drift limit. It is worth noting that replaceable fuse devices such as that proposed by Freddi, Dimopoulos [68] can be applied in order to make the column base plastic hinge easily to be repaired after strong earthquakes.

4.5 Nonlinear Time History Analysis

To evaluate seismic response of the structure under different earthquakes, nonlinear time history analysis has been used. In SAP2000, 20 scaled design base earthquakes record for downtown Los Angeles [69], California region with a probability of exceedance of 10% in 50 years has been used.

Details of earthquake ground motion records are presented in Table 4.3.

To better understand the overall seismic behavior of structures, nonlinear time history analysis is conducted in this study. An ensemble of 20 strong motion records scaled to design basis earthquake intensity (probability of exceedance of 10% in 50 years) in downtown Los Angeles [69], California region are used. Details of earthquake ground motion records can be found from Moghaddasi and Zhang [70]. In the following sections, the time history results such as maximum roof drift ratio and residual roof drift ratio are reported. The peak value of these seismic demand parameters refers to the maximum absolute value of the specified parameters over the time in time history analysis.

4.5.1 Global and Local Deformation Demand

Peak roof drift ratio and residual drift ratio of the prototype three-story CEBF-D and SCEBF-D under 20 different ground motions are shown in Figure 4.16 and Figure 4.17 respectively. Peak roof drift ratio is the ratio of the horizontal displacement of the roof divided by EBF height, and residual drift ratio is the ratio of residual drift measured in the last 5 seconds of time history analysis of roof drift divided by the EBF height.

The dashed lines in Figure 4.16 and Figure 4.17 denote the ensemble average value of the peak roof drift ratio. The ensemble average value of peak roof drift ratio of CEBF-D and SCEBF-D is 1.15% and 1.10% respectively. The maximum peak roof drift ratio for SCEBF-D occurs under La16, however, for CEBF-D it occurs under La15.

The average value of residual drift ratio for CEBF-D and SCEBF-D is 0.304% and 0.029% respectively. The maximum residual drift ratio of SCEBF-D is 0.08%. In SCEBF-D type, maximum residual drift ratio occurred under La16 as the maximum roof drift ratio also occurred under La16. On the other hand, for CEBFs, the ground motion with higher peak roof drift ratio does not necessarily have the higher residual drift ratio. As expected, the residual drift ratio in SCEBF-D type is negligible compared to the CEBF-D type. The average residual drift ratio in CEBF for D type is considerable because of plastic deformation of the shear link.

4.5.2 Parametric Study

SCEBF has the benefits to be tuned separately for stiffness, equivalent yield strength (gap opening force plus fuse member strength) and ductility in a more flexible way than conventional structural systems. To demonstrate how to adjust two key response parameters (equivalent yield strength and post-gap opening stiffness) of self-centering structures and resulting behavior, a parametric study of three cases of SCEBFs is conducted. These three cases use the same prototype EBF frames except for PT cable length and initial stress level (with three different cases of PT initial stress (40%, 50%,

60%) and different length) but with the same ultimate base shear force for D type EBF at 2% roof drift ratio. Specifically, a parametric study is performed as follows:

Case-A: PT cable initial stress= 40% yield stress, cable length =2 bay widths

Case-B: PT cable initial stress= 50% yield stress, cable length =3 bay widths (baseline case)

Case-C: PT cable initial stress= 60% yield stress, cable length=5 bay widths

To have the similar final base shear force, different PT cable length for various cases should be used. PT cable extending over 2, 3, and 5 bays are used for Case A, B, and C respectively, as shown in Figure 4.18. Therefore, they have cable length corresponding to respective distribution bay widths. Equivalent yield strength (gap opening force + fuse member strength) is defined as the base shear force where stiffness changes abruptly in the force-displacement curve, and it directly depends on the PT cable initial stress level. Case-A has the lowest equivalent yield strength since its PT cable initial stress is the lowest among all three cases; on the other hand, Case-C has the largest equivalent yield strength as it has the highest PT cable initial stress level.

The flag-shaped hysteresis curves of D type EBFs for Case A, B, and C are shown in Figure 4.19. Based on Figure 4.19, the equivalent yield strength of each case has approximately 220 kN difference, but the ultimate base shear force is almost the same. Post-gap opening stiffness of SCEBF is the stiffness of self-centering structure after gap-opening happens. Post-gap opening stiffness directly depends on PT cable length and cross-sectional area. If area is maintained constant, the shorter the PT cable length, the higher the post-gap opening stiffness would be. The post gap opening stiffness of

Case-A is larger than Case-B and Case-C since not only Case-A has the shortest length among all three cases, but also the ultimate based shear force is same for all three cases. Figure 4.20 shows the peak roof drift ratio for Case-A, Case-B, and Case-C for SCEBF-D type. Peak roof drift ratio in all three cases are very close to each other. The ensemble average of peak roof drift is about 1.117% for SCEBF-D. For all three cases of SCEBF-D type, peak roof drift ratio is less than 2% for all ground motions except for La16. In D-type SCEBF, La16 has the largest peak roof drift ratio. Case-C has the largest average value of maximum roof drift ratio among all three cases for D-type SCEBF, but Case-A and Case-B have the same average value of maximum roof drift ratio.

Figure 4.21 shows the residual drift ratio for D-type SCEBF and their three different cases. For the SCEBF-D, residual roof drift ratio is about 0.029%, which is still small. For D-type SCEBF, Case-C and Case-A have the largest and smallest average value of residual drift ratio respectively. The results of peak roof drift ratio and residual drift ratio further verify that D-type SCEBFs can re-center themselves after the earthquake and are almost damage free in primary structural frames except for RHD devices.

Peak inter-story drift ratio is a key seismic response demand parameter that can be related to building damages. Peak inter-story drift ratio is relative lateral displacement between two adjacent floors divided by the story height between these floors.

In Fig. 13, ensemble average values of peak inter-story drift ratio along the structure height has been shown for both SCEBFs and CEBFs. The horizontal lines show the range of peak inter-story drift ratio within one standard deviation with a confidence

level of 68.3%. Case-A and Case-C have the minimum and maximum peak inter-story drift ratio among all three cases for both SCEBFs respectively.

Based on Figure 4.22, D-type SCEBFs have a smaller average value of peak inter-story drift ratio than D-type CEBFs. Peak inters-story drift ratio is almost uniform along the height of the structure for D-type SCEBFs which means that there is not any concentration of deformation along the structure height.

Figure 4.23 shows the peak PT cable stress ratio for three cases of SCEBF-D type along structure height. The horizontal lines show the range of peak PT cable stress ratio within one standard deviation with a confidence level of 68.3%. Peak PT cable stress ratio is the ratio of the PT cable maximum stress during a ground motion duration over PT cable yield stress. The average value of Peak PT cable stress ratio among all floors for SCEBF-D for the Case-A, B, and C is 56%, 61%, and 66% respectively. Case-A has the smallest value of peak PT cable stress ratio for D-type SCEBFs; on the other hand, Case-C has the largest value of it. The maximum peak PT cable stress ratio which happens in Case-C is 72% for SCEBF-D. Thus, PT cables would not yield through whole earthquake ground motions even in Case-C.

All three cases of parametric study almost have a similar seismic performance; however, Case-A seems to be the better one compared to the other two cases due to the following reasons. First, not only Case-A has the overall lowest roof drift ratio and peak inter-story drift ratio among all three cases, but also it has the lowest residual drift ratio for D-type SCEBFs. Second, Case-A requires fewer PT strands compared to the other two cases. As a result, more cable material saving would be achieved, and the

costs become lower than Case-B and Case-C. However, even though Case-A has a smaller equivalent yield strength, it seems to have better seismic performance than the other two cases.

4.5.3 Typical Case

Due to space limitations, here only the detailed response results for one chosen ground motion in Case-B are presented. Typical case refers to the median response out of the ensemble of 20 ground motion cases in Case-B for SCEBF-D type. This typical case was selected based on the case closest to the ensemble median value of peak roof drift ratio, which is found to be ground motion La02 for SCEBF-D. Figure 4.24 shows the roof drift time history of EBF-D in La02. The maximum roof drift of La02 ground motion for SCEBF-D and CEBF-D is 135.75 mm and 105 mm respectively which is less than 1.2% roof drift ratio. The dotted line shows the residual roof drift for SCEBF and the dash-dot line shows the residual roof drift for CEBF. Residual roof drift for SCEBF-D and CEBF-D, it is 3 mm and 13 mm respectively. It is evident that SCEBF models have negligible residual drift value compared with CEBF models. Based on the ground motion data, Peak Ground Acceleration (PGA) happens at t=2.11 sec for La02. Figure 4.24 shows that peak roof drift happens at PGA for SCEBF-D.

Figure 4.25 shows link shear force of first-floor versus link rotation angle hysteresis of EBF-D in La02. Link shear force of SCEBFs is larger than CEBFs in D type; however, link rotation demand of SCEBFs is lower than CEBFs. SCEBFs have pinched hysteresis because of their self-centering behavior. On the other hand, CEBFs

hysteresis shows the significant amount of energy dissipation due to shear yielding of link beam. Based on Figure 4.25, SCEBFs have self-centering behavior since residual drift is negligible; however, CEBFs require a greater amount of energy dissipation than SCEBFs to achieve the same level of peak drift response.

Figure 4.26, Figure 4.27 and Figure 4.28 present first, second and third story drift time history for SCEBF-D type under La02 respectively.

Figure 4.29, Figure 4.30 and Figure 4.31 show the first, second and third-floor inter-story drift ratios of La02 for SCEBF-D type respectively. The peak inter-story drift ratios for SCEBF-D for the first, second and third floor are 0.87%, 1.32%, 1.29% respectively happening at peak ground acceleration (PGA) of La02.

Figure 4.32, Figure 4.33 and Figure 4.34 show the first, second and third-floor axial force-time history of the rocking link beam and PT cable of SCEBF-D under La02 ground motion respectively. It is seen that the axial force in the link beam is not equal to PT cable's axial force due to column restraint from gap-opening expansion. The column shear force is the difference between axial force of the rocking link beam and PT cable which is less than 5% of PT cable axial force for D-type SCEBF. The relative displacement between the columns of each floor depends on the gap-opening expansion of each floor. In SCEBF-D the peak column relative displacement of 1st to 3rd floor is 24 mm, 28 mm and 47 mm respectively as shown in Figure 4.35.

Figure 4.36 represents peak inter-story drift ratio for SCEBF-D type under La02 ground motion. It is seen that peak inter-story drift ratios for SCEBF-D type under La02 are between 0.85% and 1.35%.

Figure 4.37 shows the peak PT cable stress ratio distribution along the height of the structure for D-type SCEBF. The magenta line in Figure 4.37 shows the initial stress level of PT cables which is 50% for D-type SCEBF. For SCEBF-D, Peak PT cable stress ratio of La02 varies between 55% and 66%. Maximum peak PT cable stress ratio for SCEBF-D is 66% respectively. Thus, PT cables would remain elastic during the whole earthquake as expected.

Figure 4.38 shows the maximum link chord rotation angle response, which is defined as the ratio of vertical displacement between two ends of the link divided by the link length. Maximum rotation demand of link for SCEBF-D in La02 is between 0.05 rad and 0.09 rad. Rocking link beam will remain elastic through design basis earthquake in SCEBF-D. In D type, peak link rotation angle is less than 0.1 rad.

The good performance of SCEBFs depends on the elastic behavior of rocking link beams. The link beams' section should be designed in such a way to remain elastic through DBE earthquakes or even MCE earthquakes. Figure 4.39 shows the P-M interaction curve time history for first-floor link beam of SCEBF-D in La02. It is seen that the link beams of D-type SCEBF remain in the elastic range based on their P-M interaction curve.

The promising performance of SCEBF under strong ground motions can be explained by the fact that all primary structural members remain undamaged and it can re-center itself after the earthquake. RHD devices have a role of fuse device dissipating all earthquake energy to keep other members damage free. Recent full-scale experiments

of RHD devices [9, 50] has shown that one set of RHD devices can be replaced in 30 minutes.

Table 4.1 Member sections of conventional 3-story D-type EBF (CEBF-D)

Story	Member sections				
	Braces	Columns with Link Connection	Columns without Link Connection	Collector Beams	Link
1	W14x176	W14x132	W14x61	W18x86	W12x53
2	HSS 14x14x0.625	W14x132	W14x61	W14x82	W10x45
3	HSS 12x12x0.625	W14x132	W14x61	W10x68	W8x31

Table 4.2 Member sections and PT cables of 3-story self-centering D-type EBF (SCEBF-D)

Story	Member sections					PT Cables	
	Braces	Columns with Link Connection	Columns without Link Connection	Collector Beams	Rocking link beam	# of 7-wire Strands	Initial PT force (kN)
1	W14x176	W14x132	W14x61	W24x192	W12x120	14	1656
2	HSS 14x14x0.625	W14x132	W14x61	W21x93	W12x96	12	1419
3	HSS 12x12x0.625	W14x132	W14x61	W18x76	W12x58	8	946

Table 4.3 Earthquake ground motion records

Code	Original EQ. Record	EQ. Magnitude	Epicenter Distance (km)	Scale Factor	PGA (cm/s^2)	Vertical PGA (cm/s^2)
LA01	Imperial Valley, 1940, El Centro	6.9	10	3.02	678.05	494.25
LA02	Imperial Valley, 1940, El Centro	6.9	10	3.02	994.32	724.79
LA03	Imperial Valley, 1979, Array #05	6.5	4.1	1.52	579.06	422.09
LA04	Imperial Valley, 1979, Array #05	6.5	4.1	1.52	717.98	523.36
LA05	Imperial Valley, 1979, Array #06	6.5	1.2	1.26	443.54	323.31
LA06	Imperial Valley, 1979, Array #06	6.5	1.2	1.26	345.12	251.57
LA07	Landers, 1992, Barstow	7.3	36	4.80	619.47	665.59
LA08	Landers, 1992, Barstow	7.3	36	4.80	626.24	672.86
LA09	Landers, 1992, Yermo	7.3	25	3.26	764.55	821.47
LA10	Landers, 1992, Yermo	7.3	25	3.26	530.03	569.49
LA11	Loma Prieta, 1989, Gilroy	7	12	2.69	978.74	713.43
LA12	Loma Prieta, 1989, Gilroy	7	12	2.69	1426.40	1039.75
LA13	Northridge, 1994, Newhall	6.7	6.7	1.55	997.40	730.59
LA14	Northridge, 1994, Newhall	6.7	6.7	1.55	966.74	708.13
LA15	Northridge, 1994, Rinaldi RS	6.7	7.5	1.19	784.95	574.97
LA16	Northridge, 1994, Rinaldi RS	6.7	7.5	1.19	852.87	624.72

LA17	Northridge, 1994, Sylmar	6.7	6.4	1.49	837.65	613.57
LA18	Northridge, 1994, Sylmar	6.7	6.4	1.49	1202.16	880.57
LA19	North Palm Springs, 1986	6	6.7	4.46	1499.15	1092.78
LA20	North Palm Springs, 1986	6	6.7	4.46	1451.42	1057.99

Figure 4.1 Rocking link and PT cables in SCEBF test specimen with RHD devices

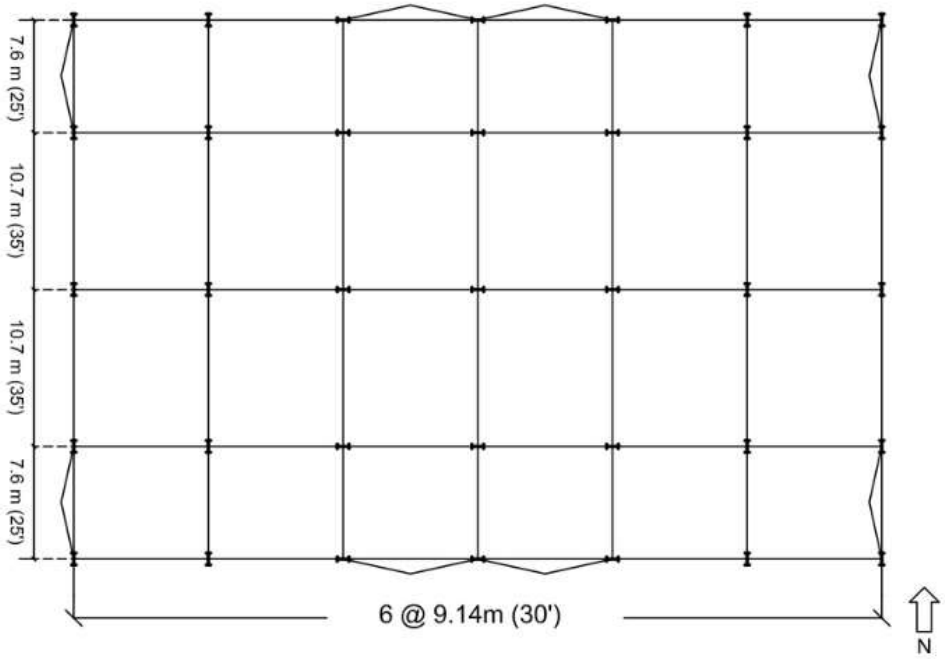

Figure 4.2 Floor plan of prototype SCEBF-D type buildings

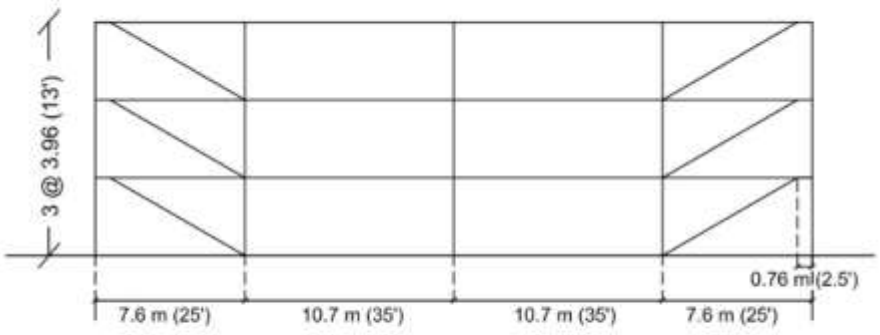

Figure 4.3 Elevation view of prototype SCEBF-D type buildings

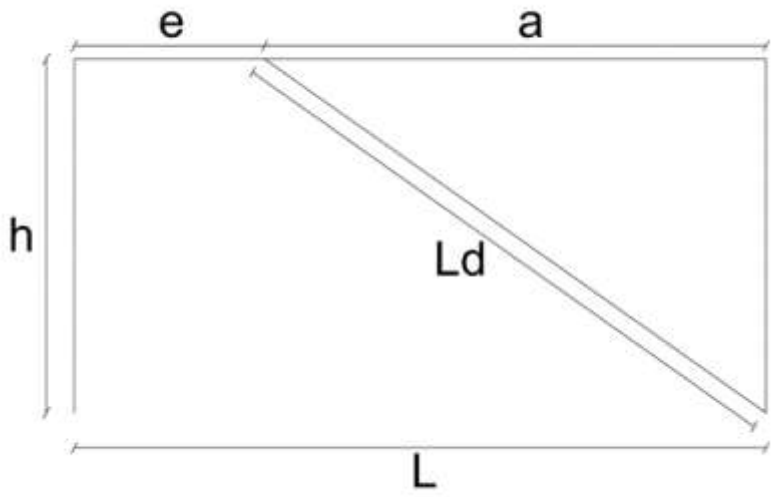

Figure 4.4 Configuration and dimensions of SCEBF-D structure

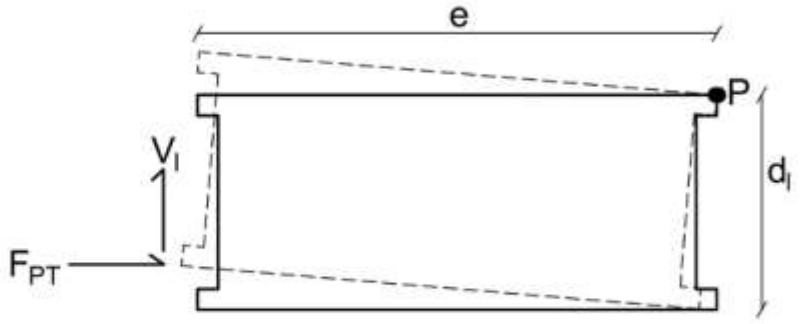

Figure 4.5 Rocking link beam configuration and dimension in SCEBF-D structure

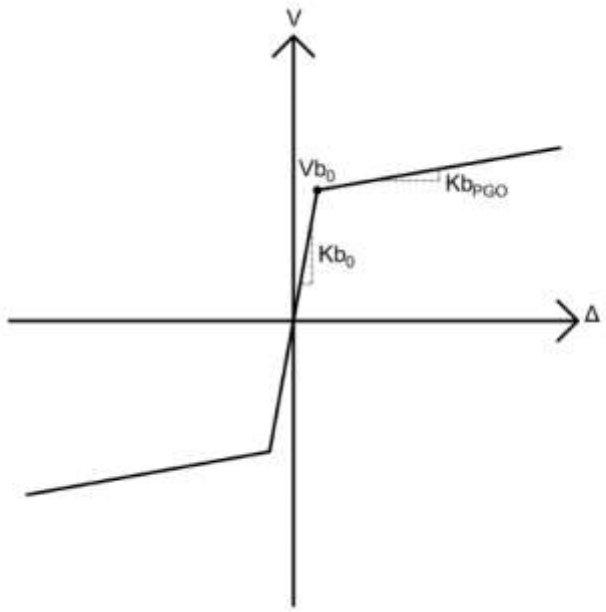

Figure 4.6 Pushover curve of one-story SCEBF-D type

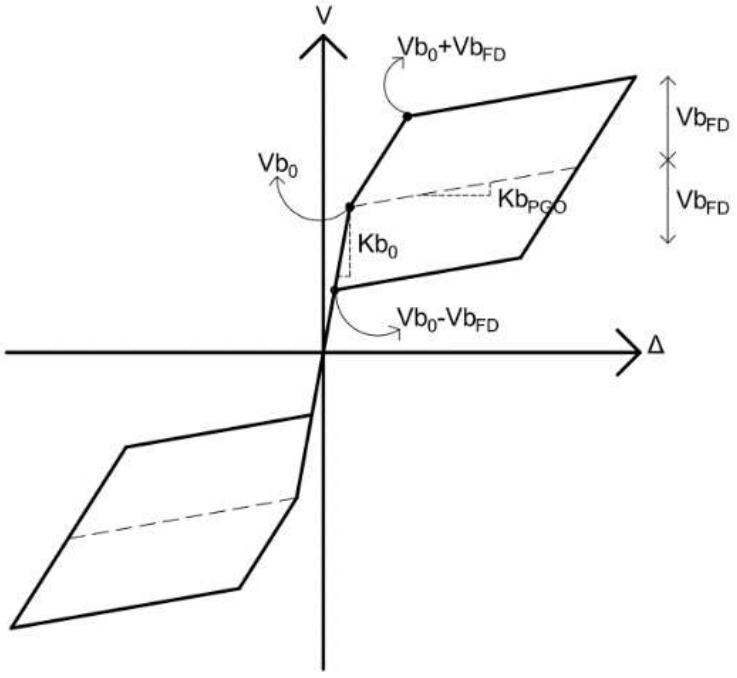

Figure 4.7 Pushover curve of one-story SCEBF-D type with RHD devices

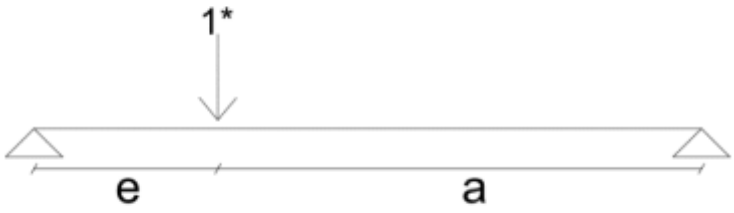

Figure 4.8 Beam/link flexural stiffness component: K_f

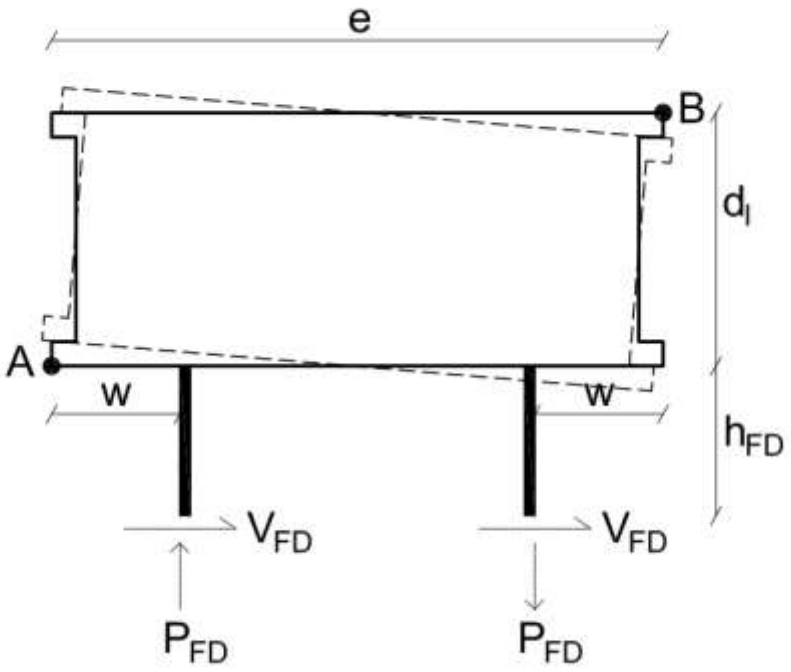

Figure 4.9 RHD device-shear force effect on SCEBF-D type structure

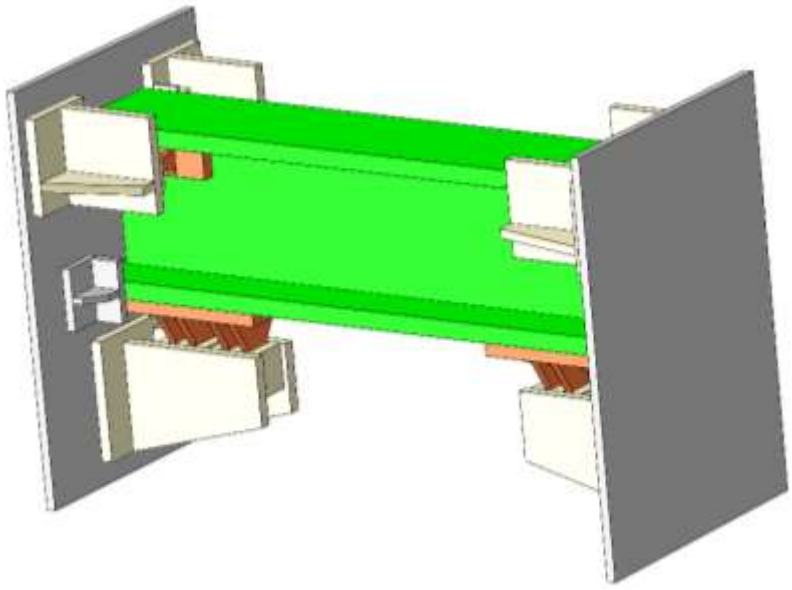

Figure 4.10 Schematics of rocking link with RHD devices in SCEBF and corresponding ANSYS model

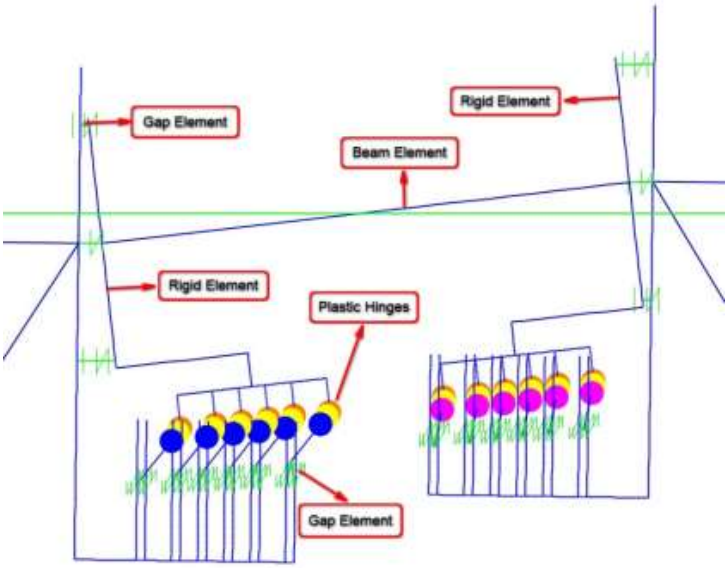

Figure 4.11 Schematics of rocking link with RHD devices in SCEBF and corresponding SAP2000 model

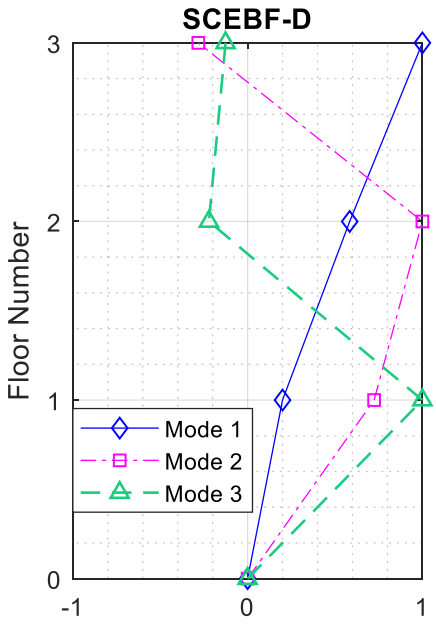

Figure 4.12 Mode shapes of prototype self-centering EBF-D type buildings

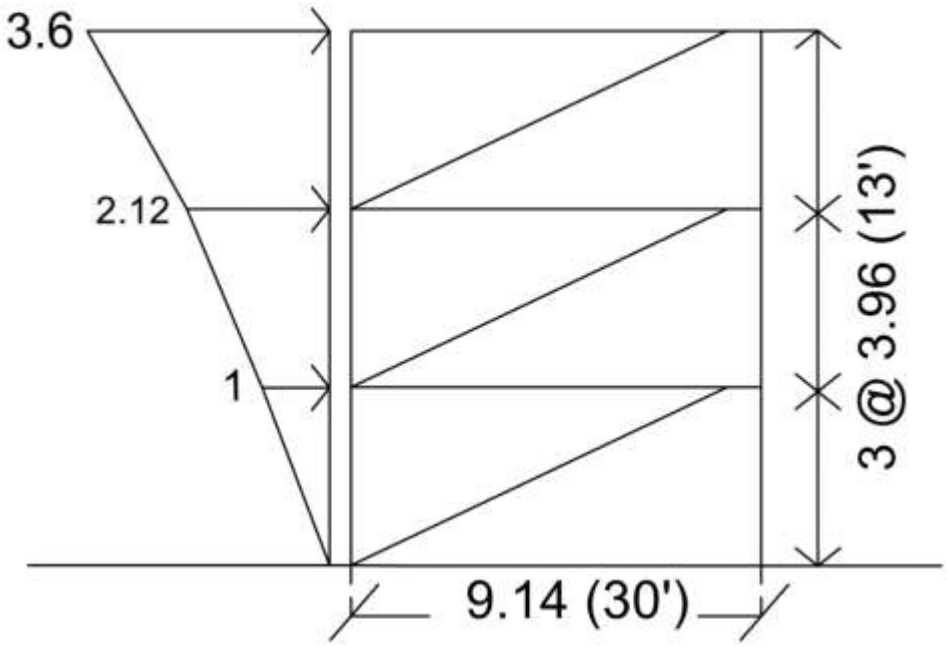

Figure 4.13 Pushover loading protocol for SCEBF-D type

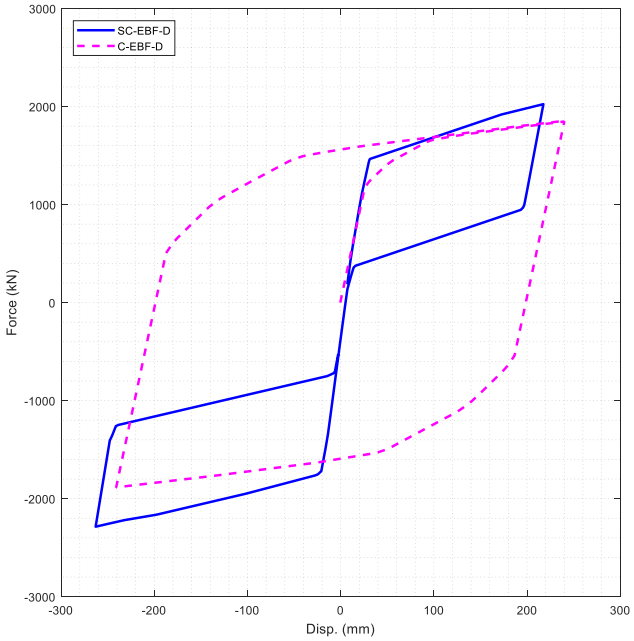

Figure 4.14 Pushover curve of EBF-D type

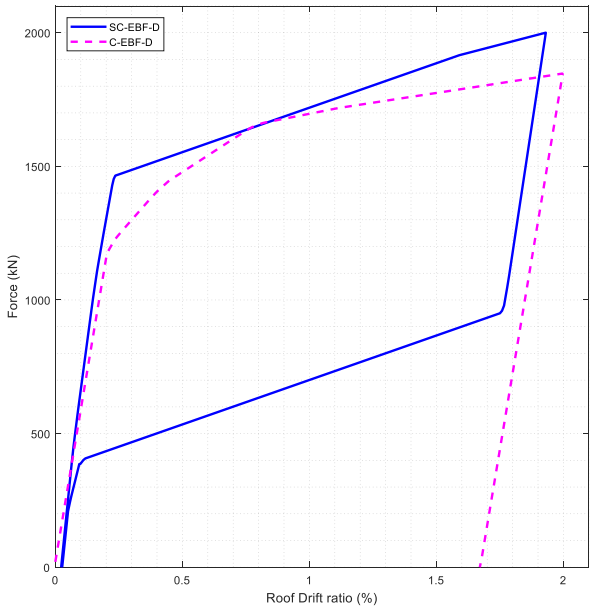

Figure 4.15 Pushover curve of prototype SCEBF D-type

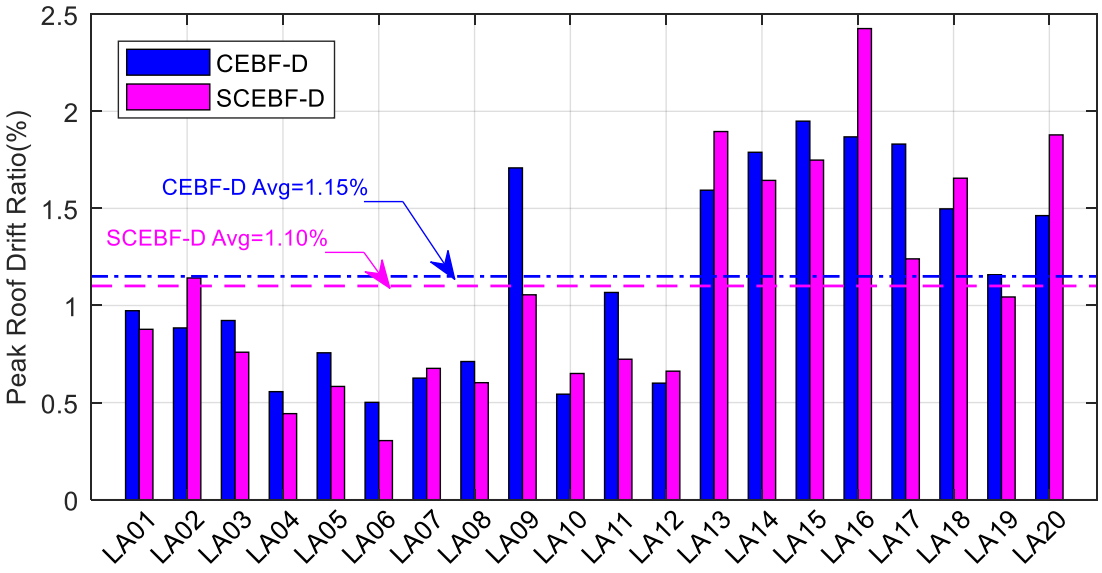

Figure 4.16 Peak roof drift ratio of prototype D-type EBFs

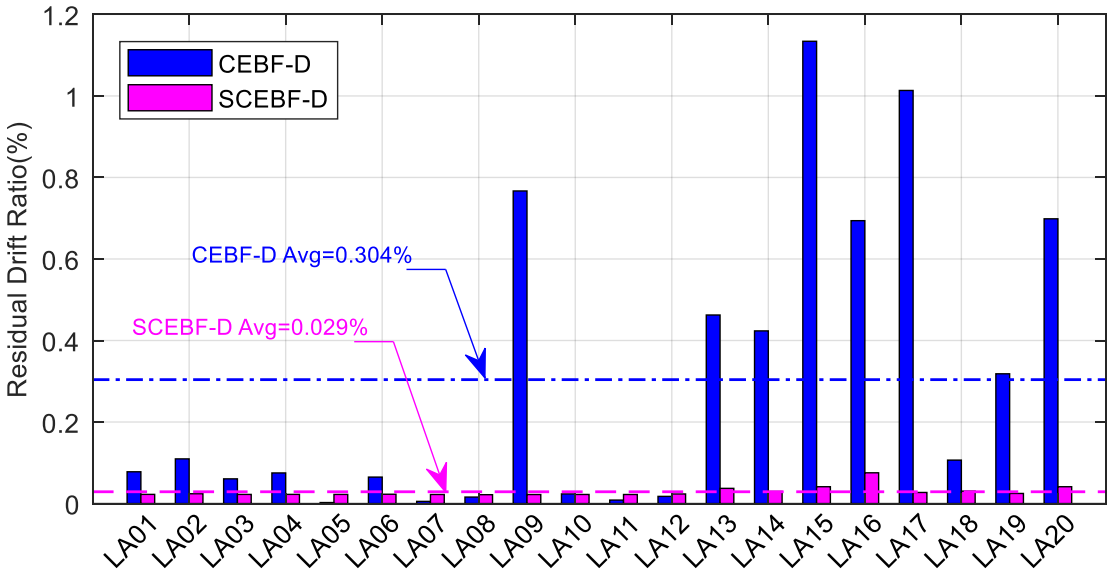

Figure 4.17 Residual roof drift ratio of prototype D-type EBFs

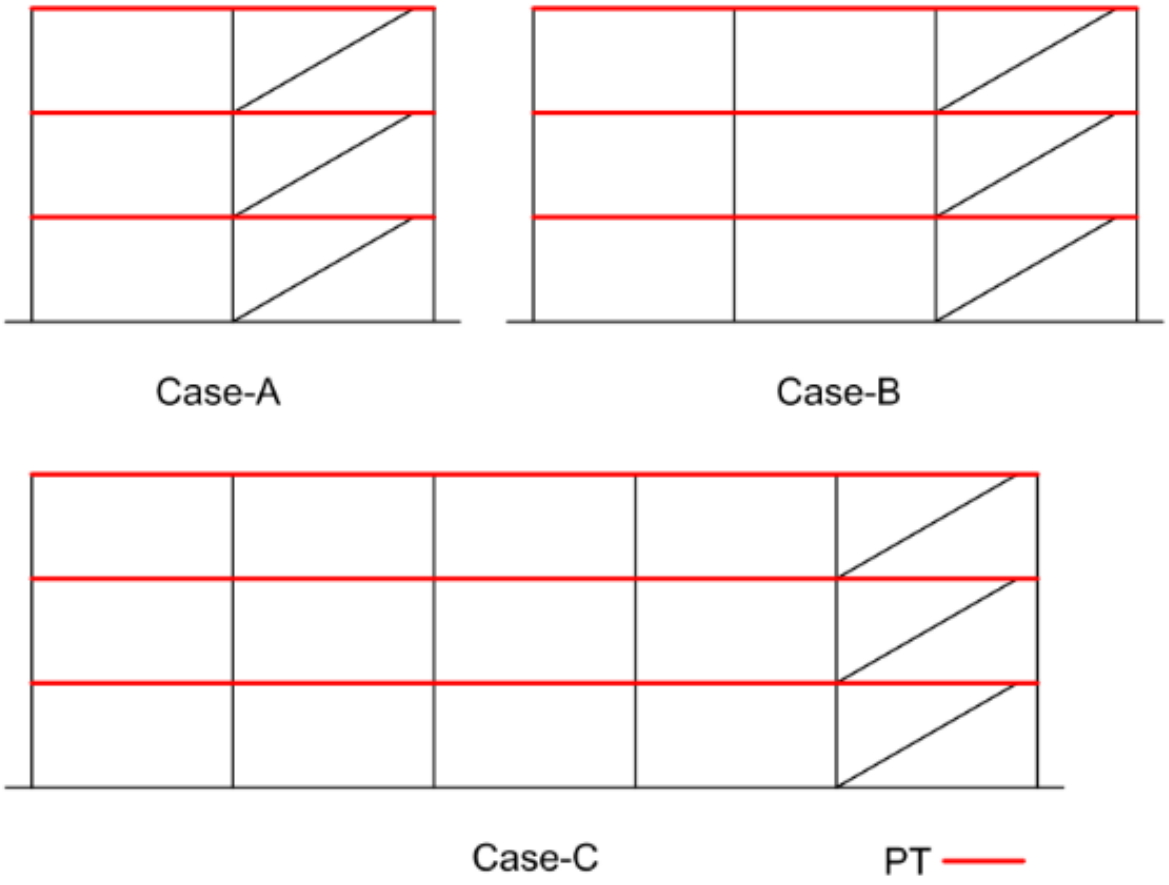

Figure 4.18 Configuration of parametric study cases for D-type EBFs

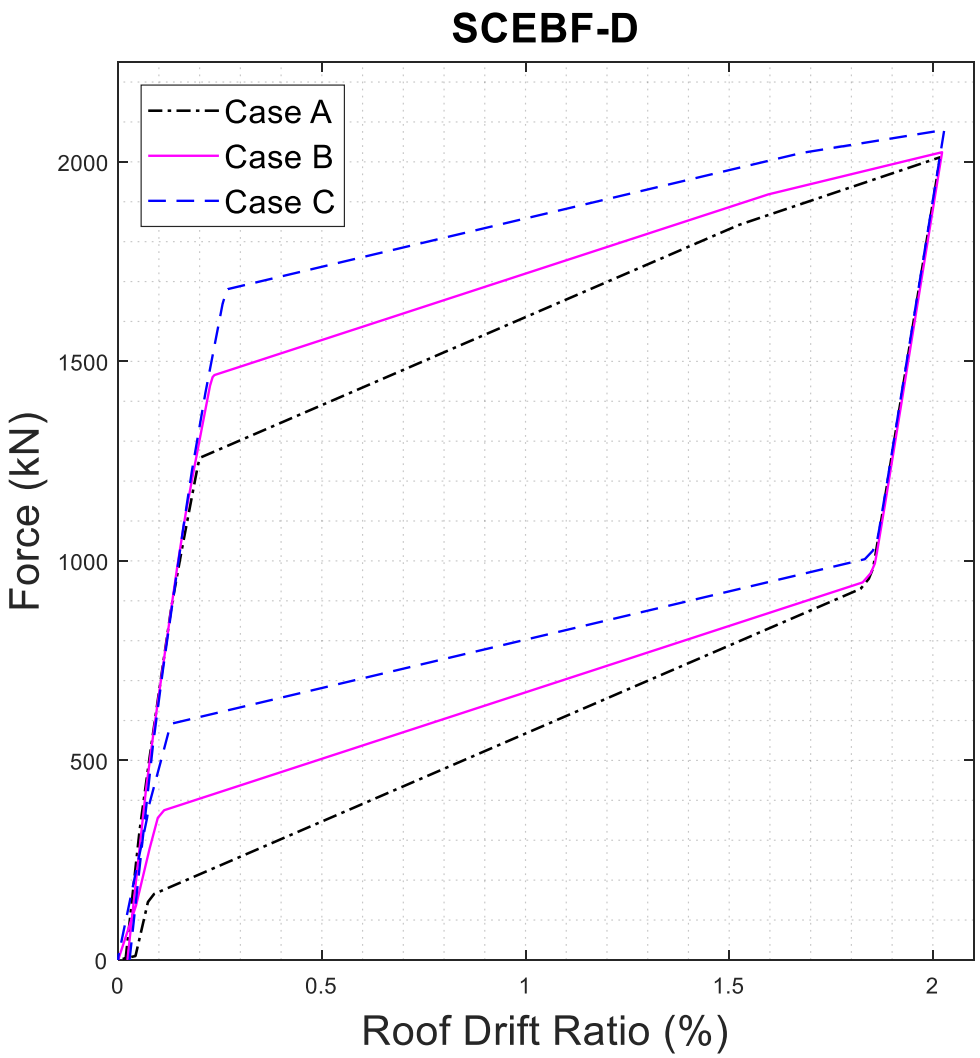

Figure 4.19 Hysteresis curves of prototype SCEBFs with varying PT cable initial stress and length for SCEBF-D type

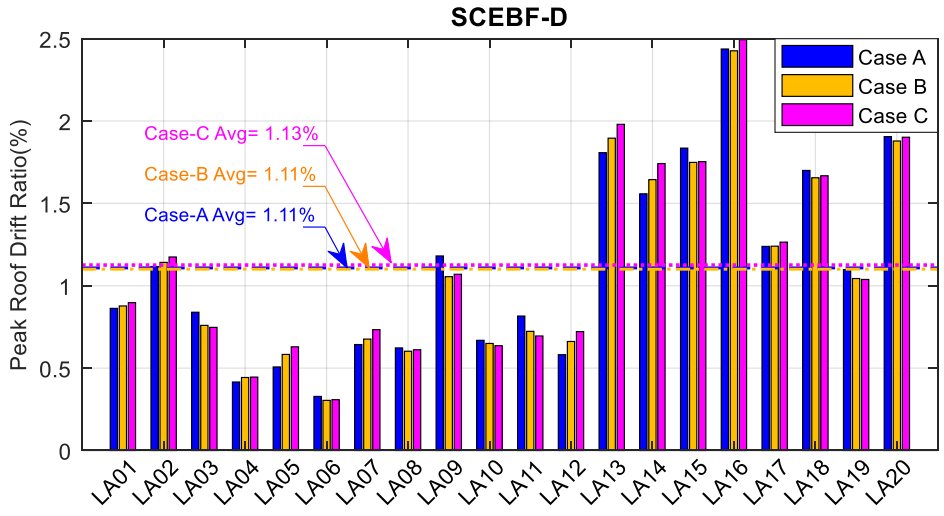

Figure 4.20 Peak roof drift ratio from parametric study for SCEBF-D type

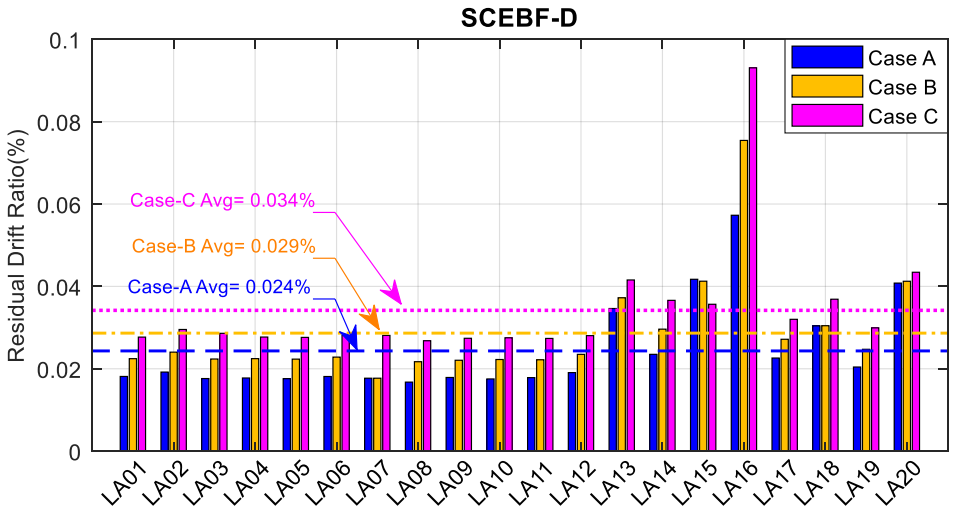

Figure 4.21 Residual drift ratio from parametric study for SCEBF-D type

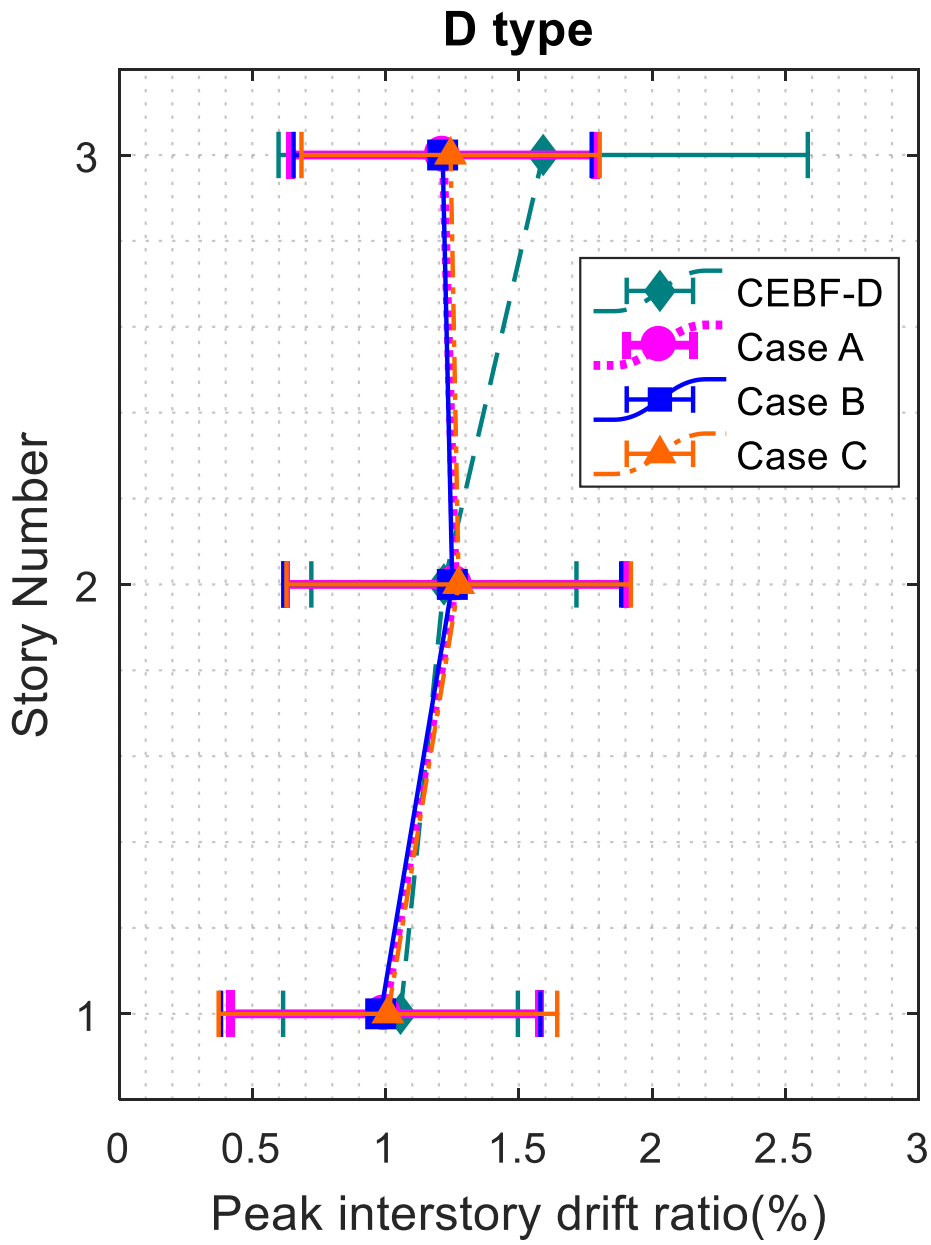

Figure 4.22 Peak inter-story drift ratio from parametric study for D-type EBFs

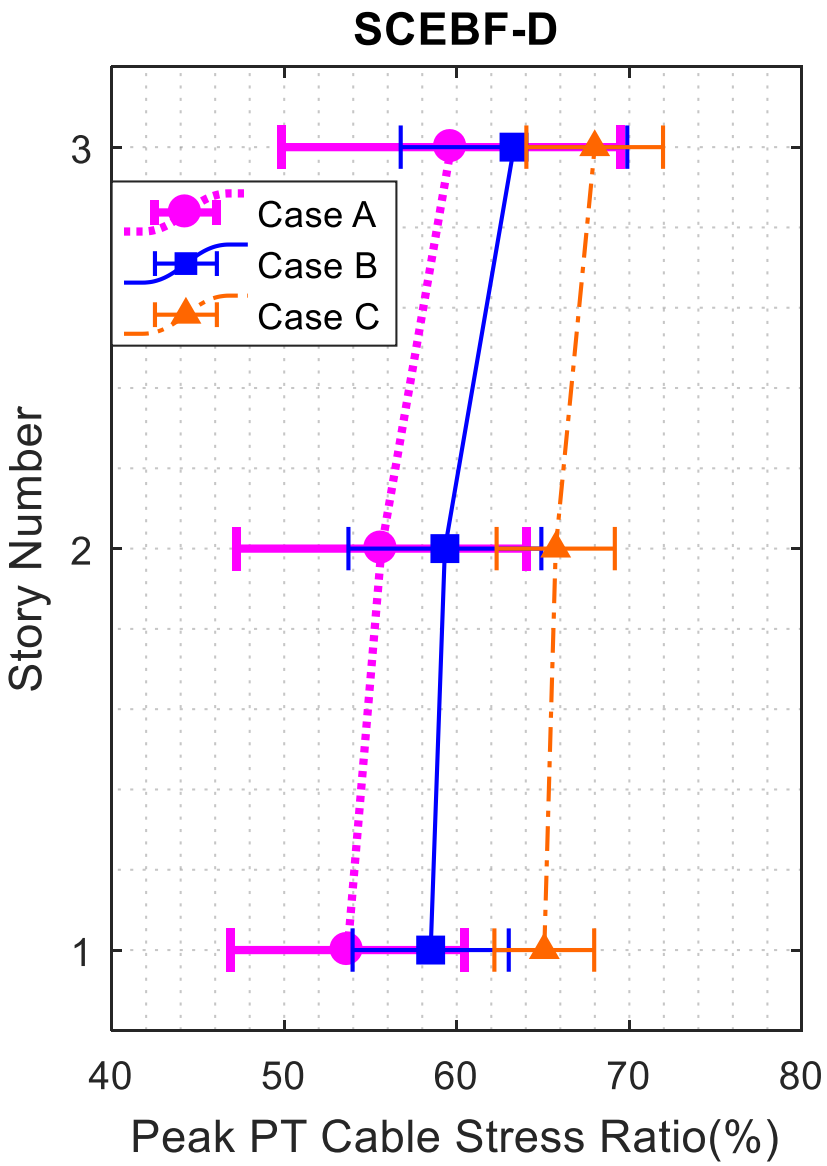

Figure 4.23 Peak PT cable stress ratio from parametric study for SCEBF-D type

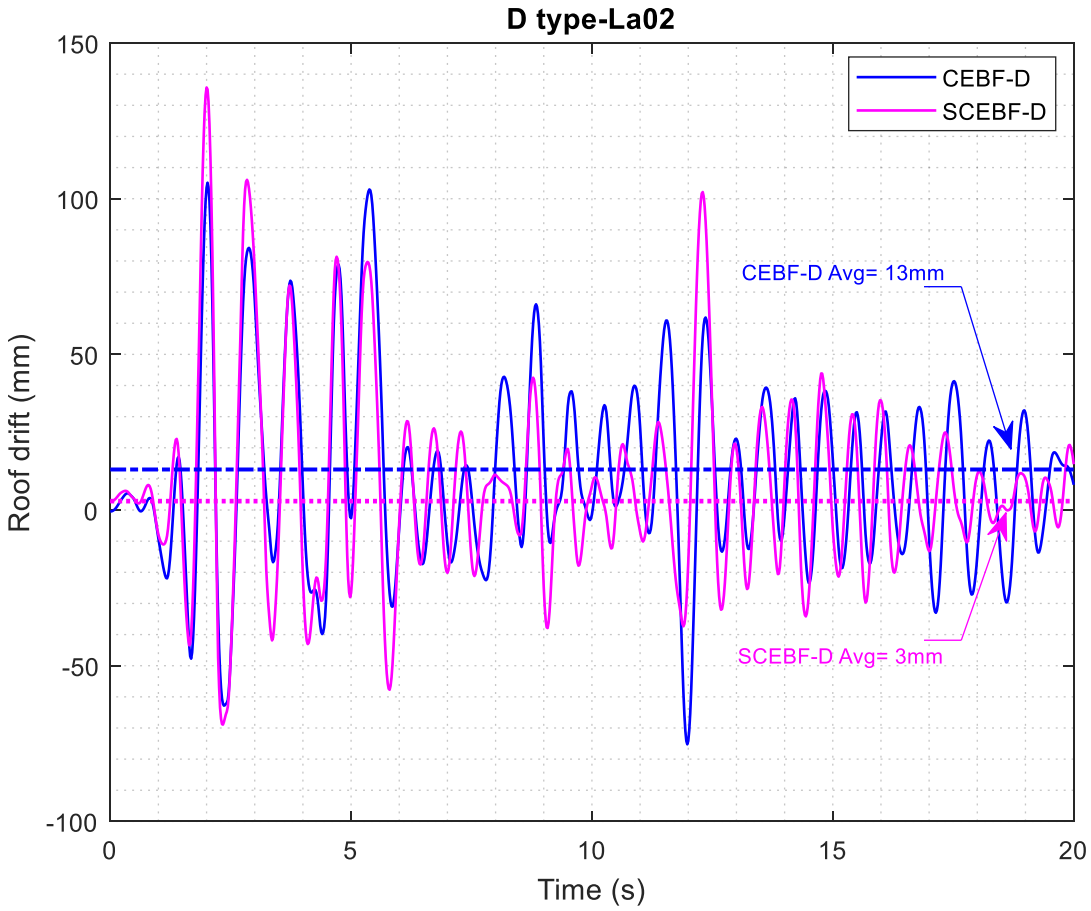

Figure 4.24 Roof drift time history for D-type EBFs

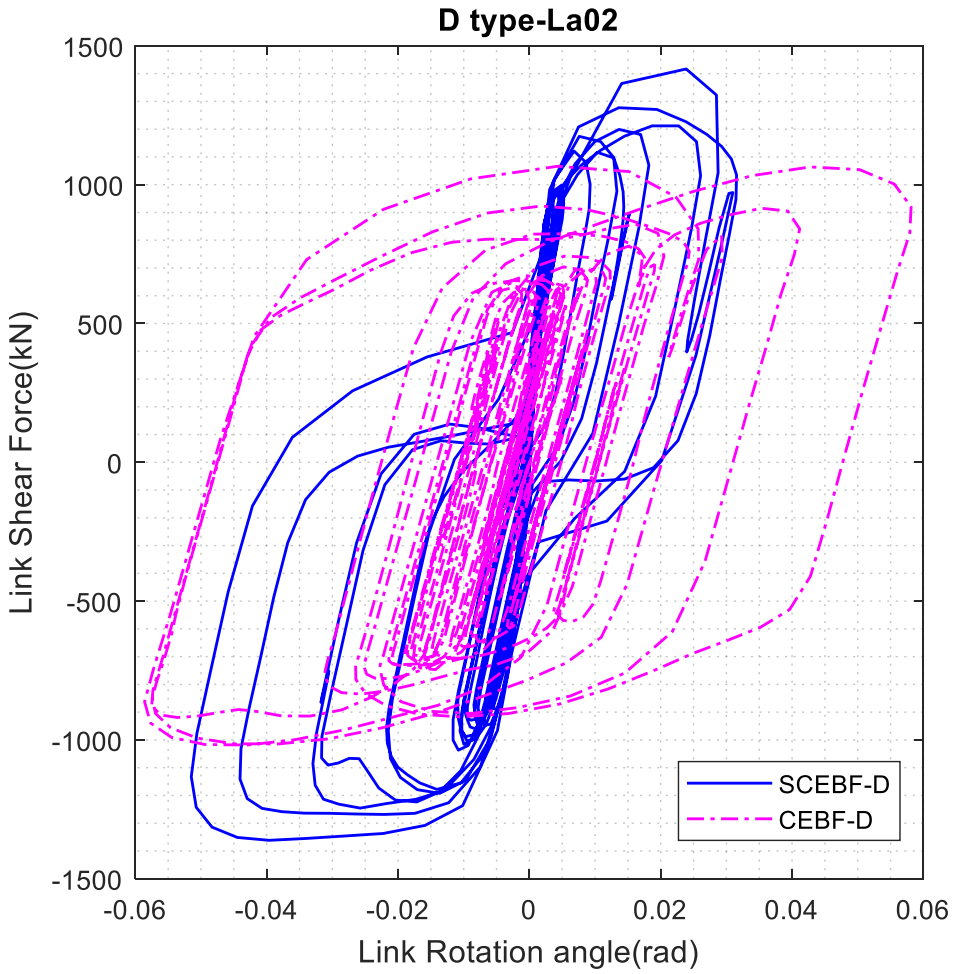

Figure 4.25 First-floor link shear force vs. link rotation angle hysteresis curve for D-type EBFs

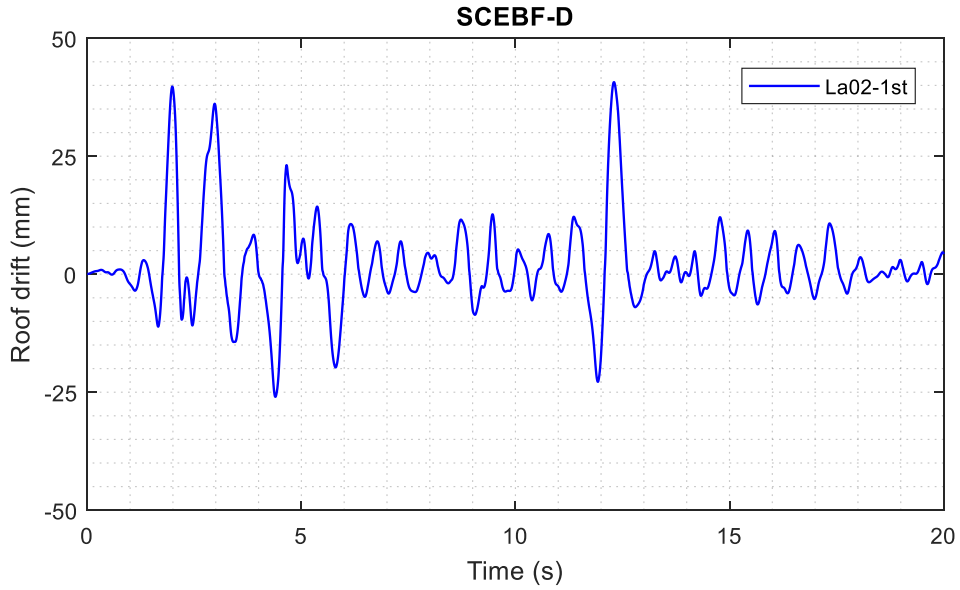

Figure 4.26 First story drift time history for SCEBF-D type

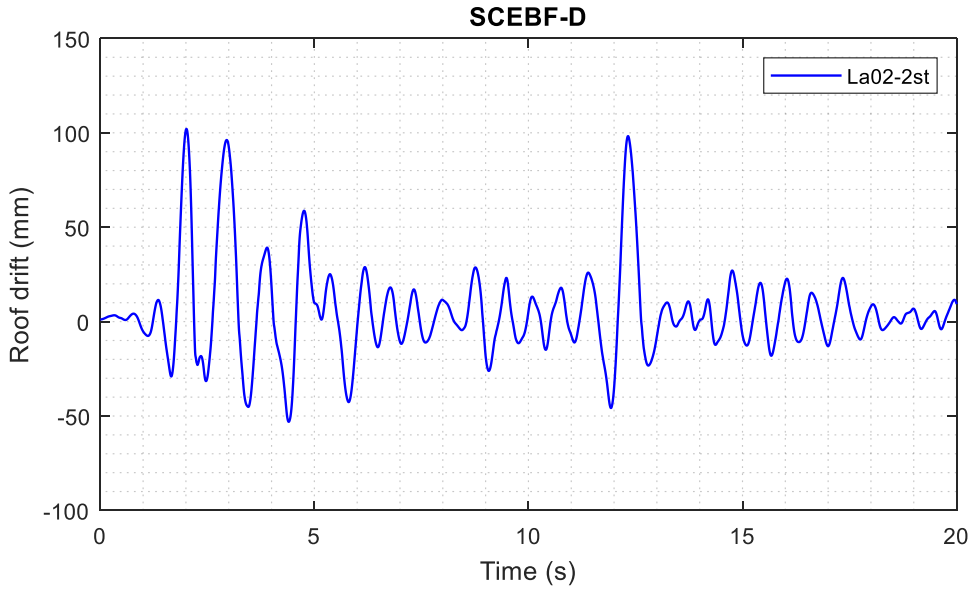

Figure 4.27 Second story drift time history for SCEBF-D type

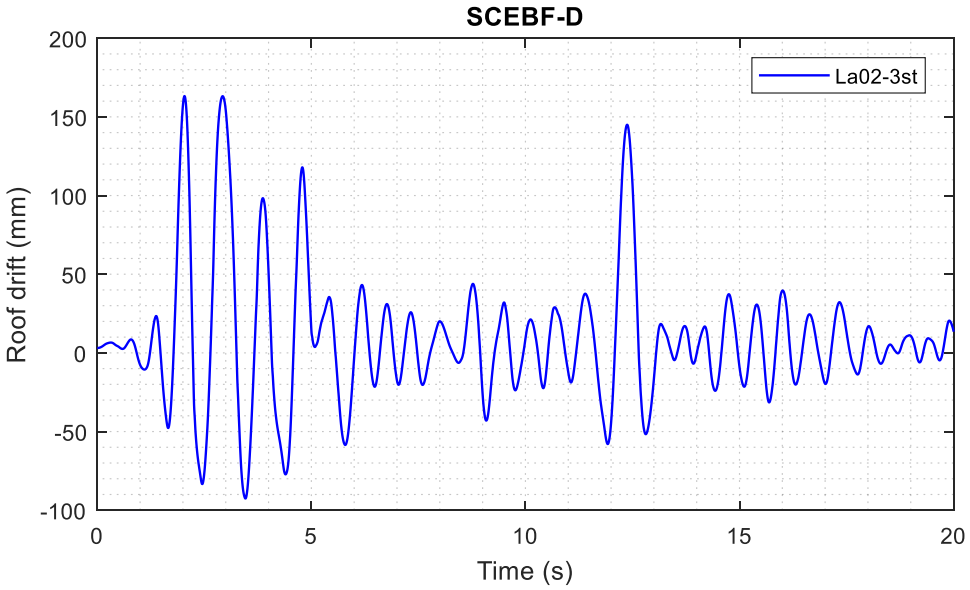

Figure 4.28 Third story drift time history for SCEBF-D type

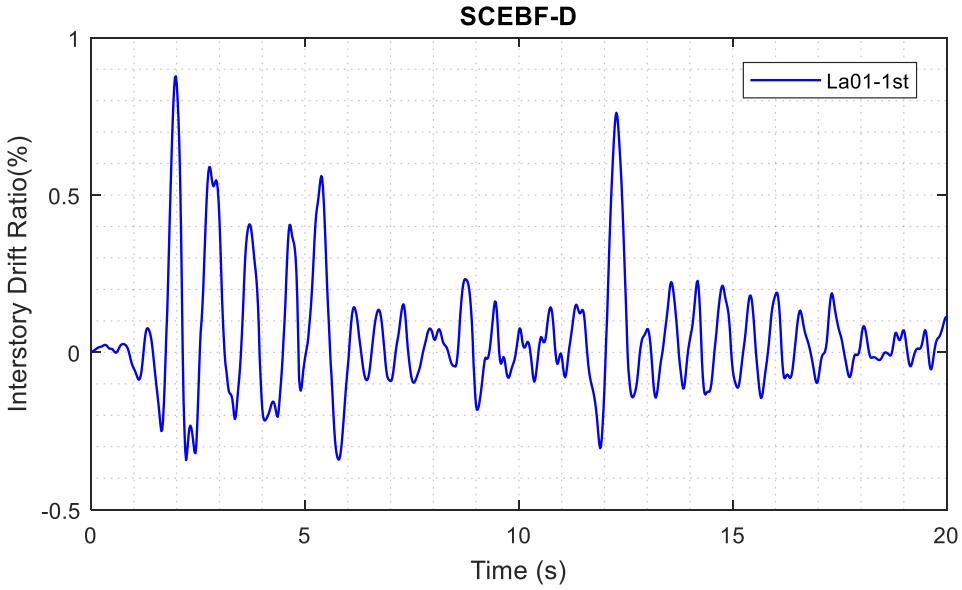

Figure 4.29 First story inter-story drift ratio-time history for SCEBF-D type

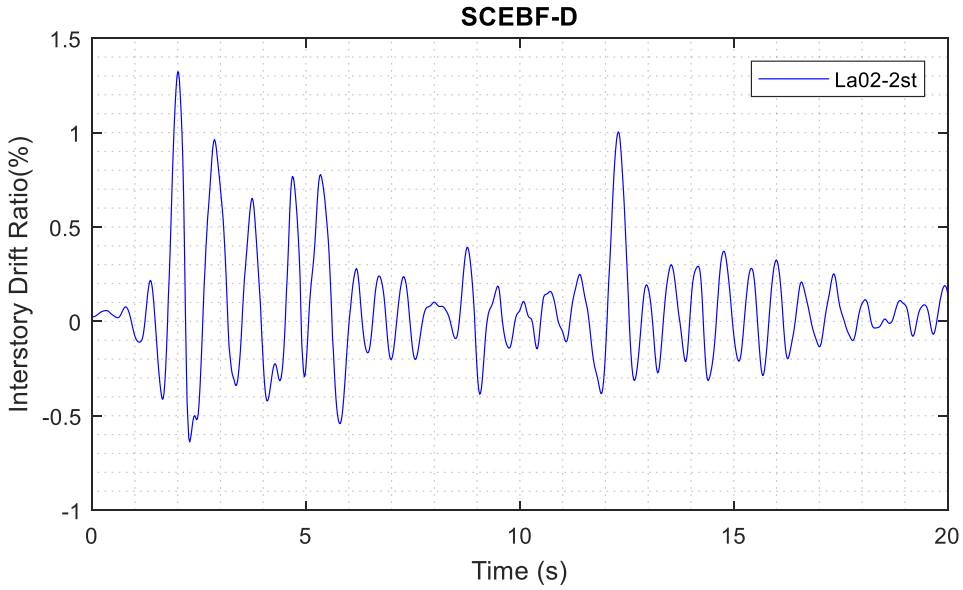

Figure 4.30 Second story inter-story drift ratio-time history for SCEBF-D type

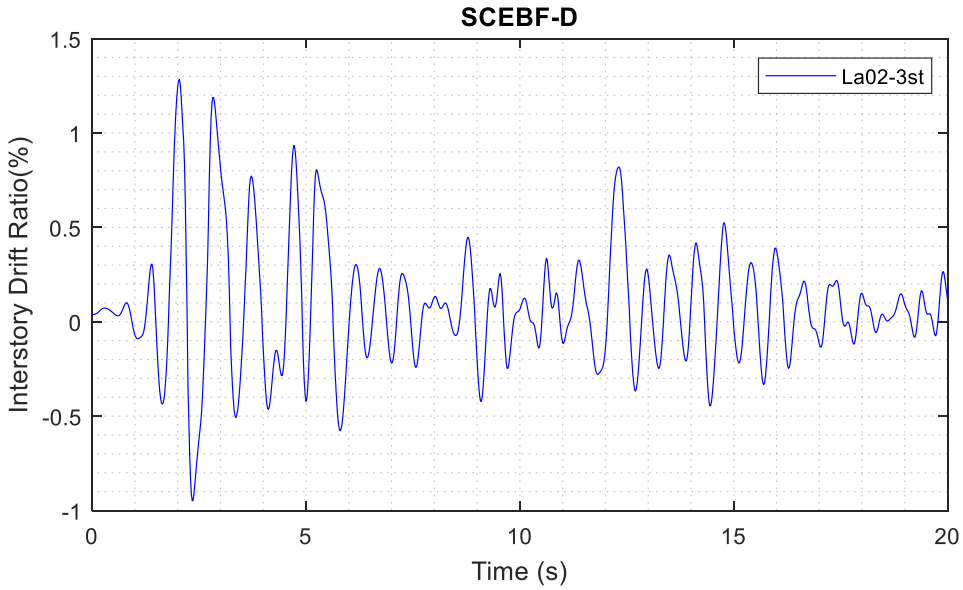

Figure 4.31 Third story inter-story drift ratio-time history for SCEBF-D type

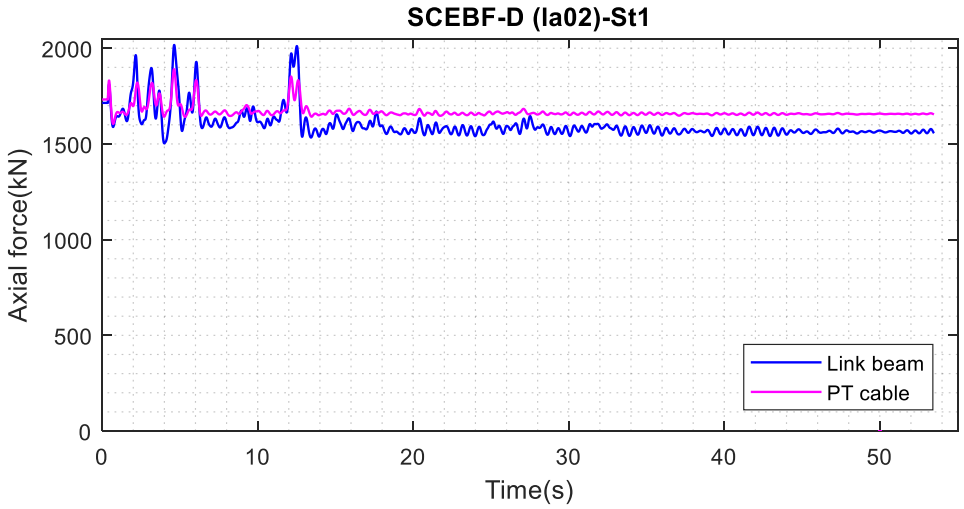

Figure 4.32 Axial force time histories of link beam and PT cable for 1st story of SCEBF structures for SCEBF-D structure under La02

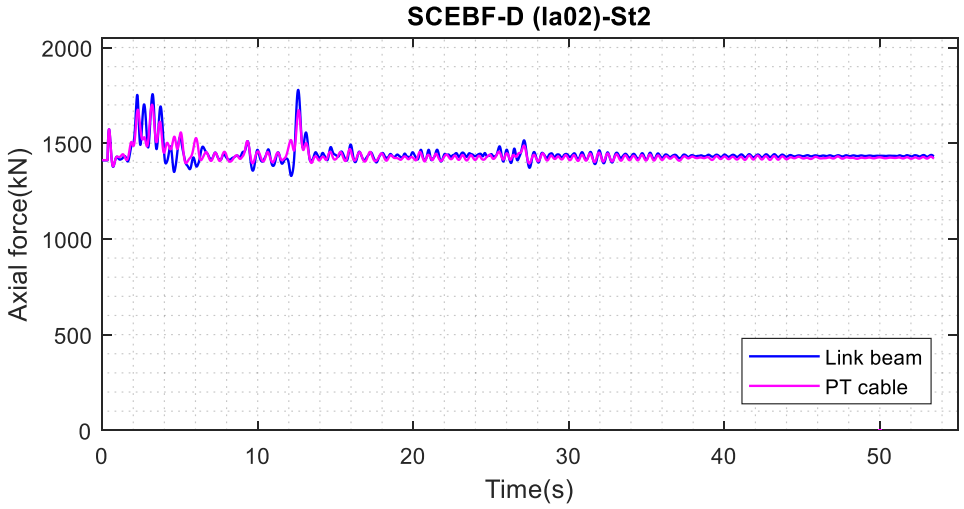

Figure 4.33 Axial force time histories of link beam and PT cable for 2nd story of SCEBF structures for SCEBF-D structures under La02

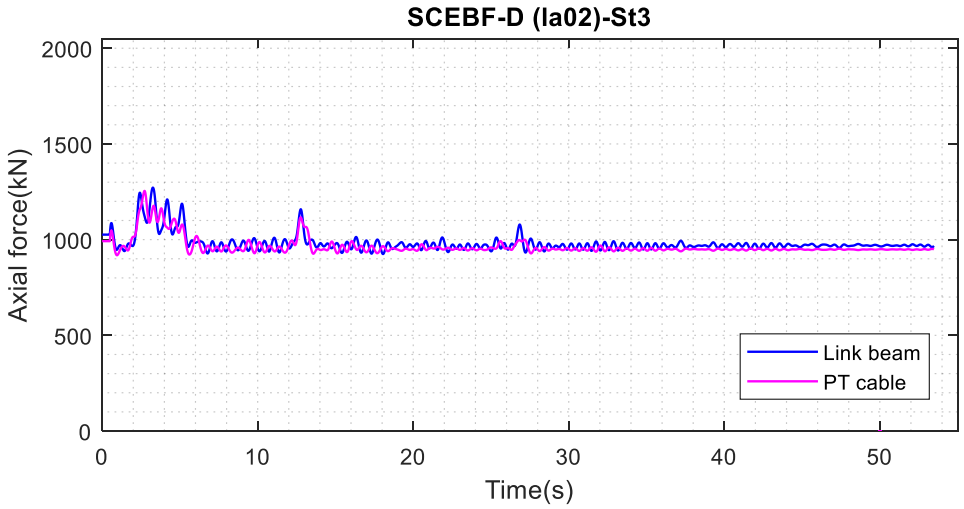

Figure 4.34 Axial force time histories of link beam and PT cable for 3rd story of SCEBF structures for SCEBF-D structures under La02

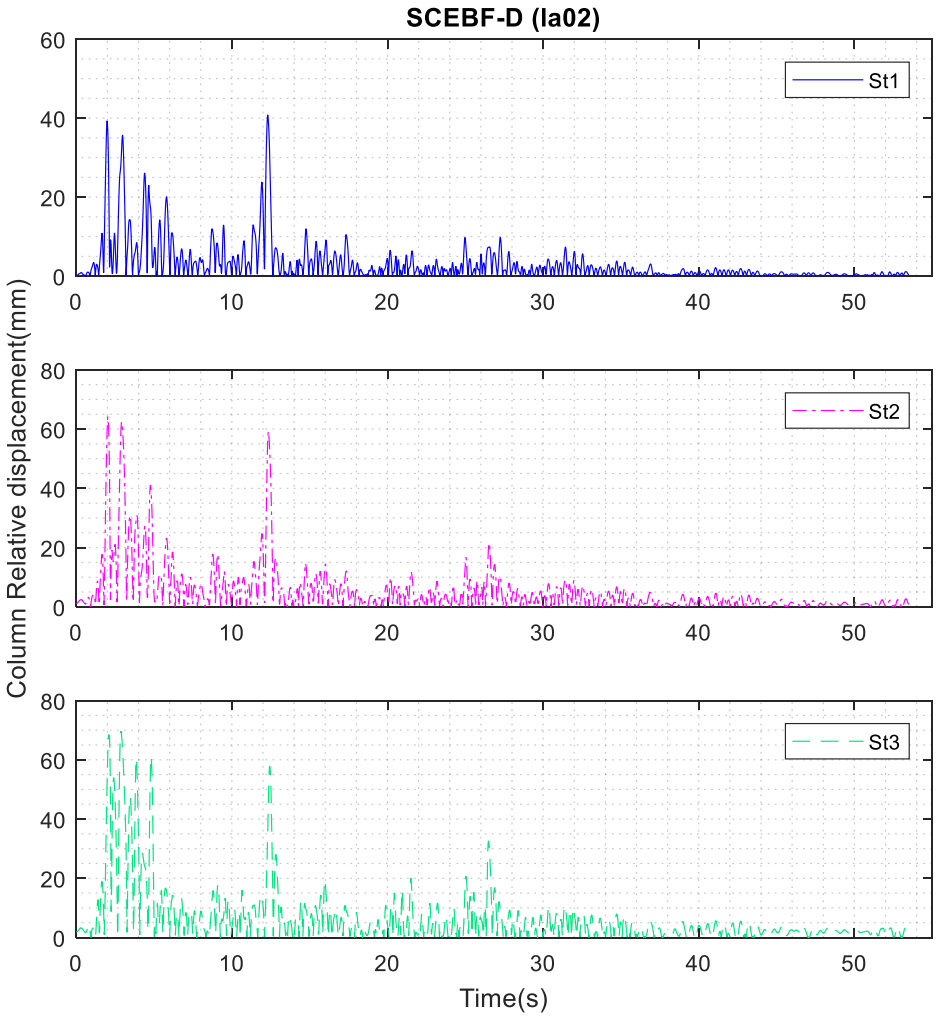

Figure 4.35 Column relative displacement for D-type SCEBF

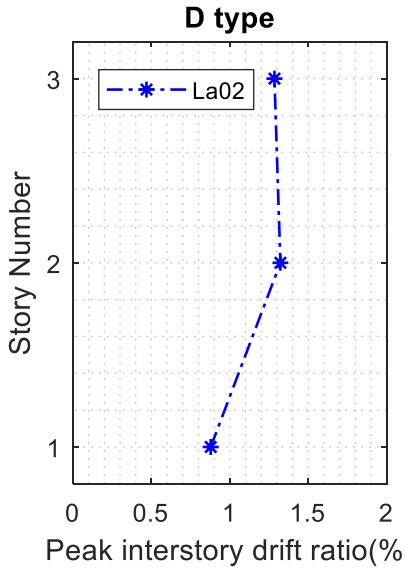

Figure 4.36 Peak inter-story drift ratio for D-type SCEBF

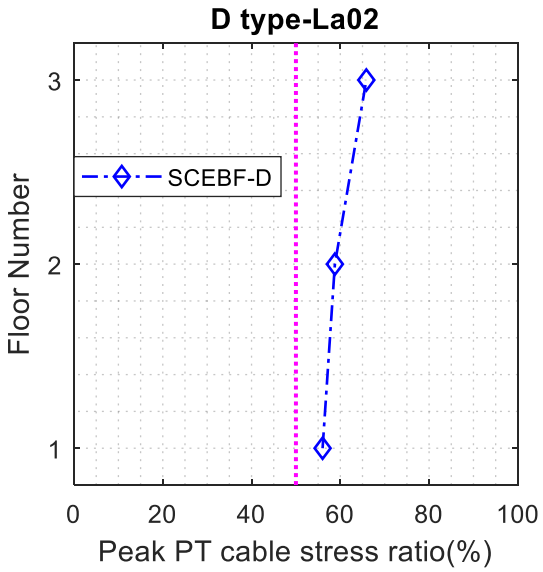

Figure 4.37 Peak PT cable stress ratio for SCEBF-D type

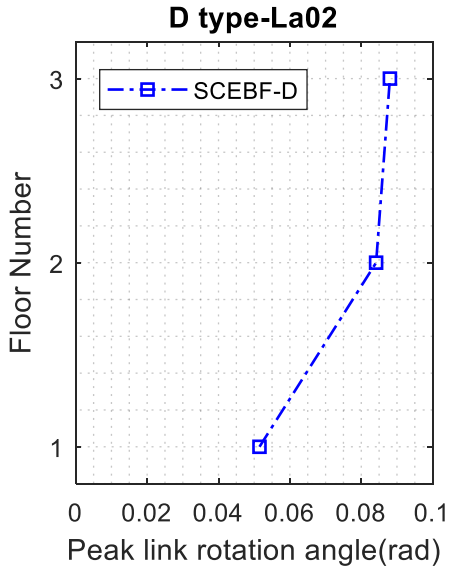

Figure 4.38 Peak link rotation angle for SCEBF-D type

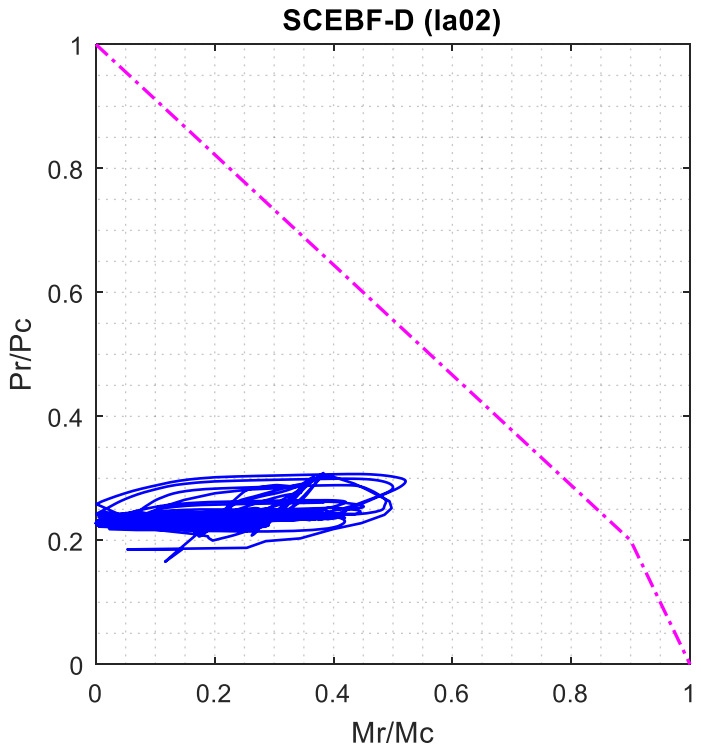

Figure 4.39 P-M interaction curve of rocking link beams for D-type SCEBF

Chapter 5 Seismic Performance Evaluation of K-type SCEBF

In this Chapter, the seismic performance evaluation of K-type SCEBF has been investigated and compared with K-type CEBF. Moreover, analytical formulas to design SCEBF-K type structure is also presented. Furthermore, K-type SCEBF has been investigated by nonlinear static analysis and nonlinear time history analysis.

5.1 Prototype SCEBF-K Type Buildings and Seismic Design

SCEBFs have the potential to provide the economy, strength, and stiffness of EBFs while sustaining less damage under design basis earthquakes. SCEBFs have columns, braces, rocking link beam, collector beam and RHD devices along with PT cables which connect all structural members through compression. The arrangement of PT cables, RHD devices and rocking link beam in a full-scale SCEBF test specimen [9, 50] are shown in Figure 5.1.

One prototype self-centering structure – a 4-story K-type (SCEBF-K) building is considered in this Chapter. To accommodate the replaceable links, the conventional K-type EBF design is derived from a four-story EBF design inspired by Speicher and Harris III [62] with slight modifications. The seismic design is for a location in the west coast of the United States based on AISC Seismic Provision (AISC 41). The 5x5 bay building plan measures 30.5 x 45.7 m (100 x 150 ft.) and is 18.3 m (60 ft) in height as shown in Figure 5.2 and

Figure 5.3. The seismic weight of the 4-story EBF-K building is 22,846 kN (5,136 kips). The 1st to 4th-floor weights are 6,063 kN (1,363 kips), 5,996 kN (1,348 kips), 5,956 kN (1,339 kips) and 4,831 kN (1,086 kips) respectively. For the SCEBF-K building, the eccentrically braced frames located along the North-South (N-S) direction is considered in this study. Table 5.1 and Table 5.2 show the member sizes of 4 story CEBF-K and SCEBF-K respectively.

In self-centering structures, high strength post-tensioning strands connect beams and columns and provide pre-compression force in the beam to enable the rocking action of the link. The tension force of post-tensioning cable (PT) thus provides the critical source to re-center the SCEBF structure. PT cable is made up of multiple PT strands, which are standard seven-wire ASTM A416Gr270 steel strand with an effective cross-section area around 140 mm2. In the SCEBF-K, the first, second, third and fourth floor, use 22, 16, 12 and 6 PT strands in their PT cable respectively with the initial stress level set as 50% of its yield stress. For the system to be self-centered, the main structural member is expected to remain essentially linear elastic under earthquake loads. In the SCEBF structures concerned here, most of the damages are concentrated to fuse devices called RHD devices (Replaceable Hysteric Damper) which can be easily replaced with low costs.

5.2 SCEBF-K Type Analytical Formula

The design principle for a one-story K-type SCEBF is briefly discussed here. A schematic view of the one-story SCEBF-K module is shown in Figure 5.4, and the rocking link beam configuration in SCEBF-K is shown in Figure 5.5.

In Figure 5.6 and Figure 5.7, pushover curves of bare frame SCEBF-K type and SCEBF-K type with TPAD fuse device is presented respectively. $K_{b_0}, V_{b_0}, K_{b_{PGO}}$ and $V_{b_{FD}}$ represent SCEBF-K type initial stiffness, Gap opening shear force, post gap opening stiffness and fuse device shear force effect on SCEBF-K type. Stiffness and shear force formulas for one-story SCEBF-K module are presented in the following section. K_{b_0} depends on geometric configuration of the SCEBF-K type while V_{b_0} and $K_{b_{PGO}}$ mostly depends on the properties of PT strands.

In the following equations, I_l and I_b express the moment of inertia of link and beam respectively. $A_d, A_b$and A_{wl} show section area of brace, section area of beam and section area of link web respectively. F_{PT_0}, A_{PT}, L_{PT} and E_{PT} present the PT strands initial force, area, length and young's modulus respectively, while t_{f_l} and d_l express link flange thickness and depth. E and G are young and shear modulus of steel. K_{l_0} is required to compute the link initial stiffness. K_{l_0} consists of four terms K_{da}, K_{ba}, K_v and K_f. K_{da}, K_{ba}, K_v show brace axial stiffness, beam axial stiffness, link shear stiffness [64]. The K_f expression is formulated in this study using the principle of virtual work representing the flexural stiffness of link/beam.

$$K_{l_0} = (\frac{1}{K_{da}} + \frac{1}{K_{ba}} + \frac{1}{K_v} + \frac{1}{K_f})^{-1}$$ Equation 5.1

$$K_{da} = 2E(\frac{A_d}{L_d})(\frac{a}{L_d})^2$$ Equation 5.2

$$\mathrm{K_{ba}} = \frac{2EA_b}{a}$$ Equation 5.3

$$\mathrm{K_v} = \frac{GA_{wl}L(L-e)}{h^2e}$$ Equation 5.4

$$\mathrm{K_f} = \frac{3EL^2}{2ahe^2}(\frac{a}{I_b} + \frac{e}{2I_l})^{-1}$$ Equation 5.5

$$K_{b_0} = K_{l_0} + K_c$$ Equation 5.6

Where K_c represents the columns stiffness which can be neglected for initial stiffness. In this study, K_f, K_{l_0} and K_{b_0} were derived representing the link/beam flexural stiffness due to link and beam flexural deformation, link initial stiffness and SCEBF-K type initial stiffness respectively.

Based on Figure 5.8, a force of 1* applies as the brace-vertical force to the beam. Thus, the link/beam flexural stiffness (K_f) for SCEBF-K type would be calculated based on principal virtual work similar to the K_f in SCEBF-D type.

In K-type SCEBF, for rocking link beam design, the primary goal is to make the rocking link beam remain elastic under DBE earthquakes and should also be stiff enough. In designing the PT cables, two primary factors considered are: (1) adjusting the gap opening force to the value desired for the design; (2) PT cable should not yield under DBE level seismic loading. Rocking link beam gap-opening shear force (V_{l_0}) and initial PT force (F_{PT_0}) are presented below. Then, the initial PT stress (σ_0) needs

to be determined, therefore, the number of PT strands (N_{PT}) forming the PT cable is derived.

The compression force created by PT strands provides gap opening shear force.

$$V_{l_0} = \frac{\mathrm{F}_{PT_0}(d_l - t_{f_l})}{e} = V_{b_0}\frac{h}{L} \quad \text{Equation 5.7}$$

$$V_{b_0} = V_{l_0} + K_c\left(\frac{V_{l_0}}{K_{l_0}}\right) \quad \text{Equation 5.8}$$

Where F_{PT_0} represents the initial pre-tension force of PT strand. V_{l_0} and V_{b_0} were derived in this study and represent the link gap opening shear force, and SCEBF-D type gap opening shear force.

$$\mathrm{F}_{PT_0} = V_{l_0}\frac{e}{(d_l - t_{f_l})} \quad \text{Equation 5.9}$$

$$N_{PT} = \frac{\mathrm{F}_{PT_0}}{\sigma_0 A_{PT}} \quad \text{Equation 5.10}$$

Where h, L, e and A_{PT} represent the frame height, bay width, rocking link beam length and cross-section area of one 7-wire PT strand respectively. PT cables must remain elastic through DBE; as a result, they should be properly designed to not yield at 2% inter-story drift ratio. Based on Figure 5.5, after the gap opens, rocking link beam rotates around center of rotation or pivot point P; therefore, PT cable extends by $[(\frac{(L-e)(d_l - t_{f_l})}{he})\ \Delta]$ and its axial force increases accordingly. PT cable axial force after gap opening happens (F_{PT}) can be calculated as follows.

$$\mathrm{F}_{PT} = \mathrm{F}_{PT_0} + \frac{N_{PT}A_{PT}E_{PT}}{L_{PT}}\frac{(L-e)(d_l-t_{f_l})}{he}\,\Delta \qquad \text{Equation 5.11}$$

$$L_{PT_{min}} \geq \frac{N_{PT}A_{PT}E_{PT}(L-e)(d_l-t_{f_l})\Delta}{(\mathrm{F}_{PT_{max}}-\mathrm{F}_{PT_0})he} \qquad \text{Equation 5.12}$$

where F_{PT},Δ, E_{PT} and $L_{PT_{min}}$ denote PT cable force, frame drift, Modulus of Elasticity and minimum length of PT cables respectively. As mentioned earlier, the PT cable must remain elastic through DBE, as a result, the required PT cable length ($L_{PT_{min}}$) should be calculated based on maximum allowable PT cable force ($\mathrm{F}_{PT_{max}}$).

Based on Figure 5.5, link post-gap opening stiffness and shear force are derived. When gap opens, PT strands extends $[(\frac{(L-e)(d_l-t_{f_l})}{he})\,\Delta]$; thus, its axial force increases accordingly. By increasing PT strands force, the link shear force also increases. Post-gap opening stiffness of SCEBF-K ($K_{b_{PGO}}$) and shear force of the link ($V_{l_{PGO}}$)is calculated as follows:

$$K_{l_{PGO}} = \frac{(L-e)\,A_{PT}E_{PT}}{L_{PT}he^2}(d_l - t_{f_l})^2 \qquad \text{Equation 5.13}$$

$$K_{b_{PGO}} = \frac{(L-e)L\,A_{PT}E_{PT}}{L_{PT}h^2e^2}(d_l - t_{f_l})^2 + K_c \qquad \text{Equation 5.14}$$

$$V_{l_{PGO}} = V_{l_0} + K_{l_{PGO}}\,\Delta \qquad \text{Equation 5.15}$$

$$V_{b_{PGO}} = \frac{L}{h}\,V_{l_{PGO}} + K_c\,\Delta \qquad \text{Equation 5.16}$$

where $K_{l_{PGO}}$,$K_{b_{PGO}}$, $V_{l_{PGO}}$ and $V_{b_{PGO}}$ represents link post-gap opening stiffness, SCEBF-K type post-gap opening stiffness, link post-gap opening shear force and SCEBF-K assembly post-gap opening lateral force respectively.

Based on Figure 5.5, after the gap opens, link rotates around pivot point P. Thus, PT strand extends by $[(\frac{a(d_l - t_{f_l})}{he})\ \Delta]$; thus, link post-gap opening stiffness ($K_{l_{PGO}}$) and link post-gap opening shear force ($V_{l_{PGO}}$) would be calculated as follows:

$$\mathrm{F}_{PT} \times (d_l - t_{f_l}) = V_{l_{PGO}} \times e \rightarrow \begin{Bmatrix} V_{l_{PGO}} = V_{l_{GO}} + \frac{(L-e)\,A_{PT}E_{PT}}{L_{PT}he^2}(d_l - t_{f_l})^2\ \Delta \\ K_{l_{PGO}} = \frac{(L-e)\,A_{PT}E_{PT}}{L_{PT}he^2}(d_l - t_{f_l})^2 \end{Bmatrix}$$

The behavior of the SCEBF-K before a gap opens, mostly depends on link and beam flexural deformation and it is independent of PT strands. However, as soon as the gap opens, the geometry of SCEBF-K changes and rocking behavior of the link starts to dominate the frame deformation. As a result, the post-gap opening stiffness of the SCEBF-K is controlled by PT area and PT length along with the rocking link depth. Based on Figure 5.9, the effect of fuse device on SCEBF-K is calculated in the following section. fuse device has shear force of V_{FD} and axial force of P_{FD} which is directly apply to the Fuse holder connected to the link; as a result, fuse device shear force contribution and energy dissipation would be calculated as follows:

$$\begin{Bmatrix} V_{FD} = \frac{MP_{FD}}{h_{FD}} \\ V_{l_{FD}} = \sum M_A + \sum M_B \end{Bmatrix} \rightarrow V_{l_{FD}} = \frac{V_{FD}(d_l + 2h_{FD}) + 2P_{FD}w}{e}$$

$$V_{l_{FD}} = \frac{V_{FD}(d_l+2h_{FD})+2P_{FD}w}{e}$$ Equation 5.17

$$V_{b_{FD}} = \frac{V_{l_{FD}}L}{h}$$ Equation 5.18

$V_{l_{FD}}$ and $V_{b_{FD}}$ represent fuse device effect on the link shear force and fuse device effect on the SCEBF-K shear force respectively. As shown in Figure 5.9, fuse device increases the gap-opening shear force of SCEBF-K type (V_{b_0}) by $V_{b_{FD}}$.

Based on the analytical formula, K_f is the dominant parameter controlling total frame initial stiffness which is related to moment of inertia of link and beam. However, post-gap opening stiffness mostly depends on PT cable area and length along with rocking link depth.

Three key parameters defining the SCEBF force-displacement relationship are as follows: (1) SCEBF initial stiffness before gap opening happens; (2) SCEBF post-gap opening stiffness; (3) gap opening shear force (yield strength). The stiffness and yield strength of SCEBF can be controlled and tuned by proper design of PT cable, RHD devices, and rocking link beam. In the SCEBF, before a gap opens, it behaves like a CEBF; as a result, elastic deformation of the braced frame contributes to all the drift. However, as soon as the gap opens, the structure geometry changes and link rocking starts to contribute to system deformation. This nonlinear elastic behavior of the self-centering structure is triggered by the gap opening at the link to beam or link to column interface. For SCEBF with the current design, the gap-opening expansion phenomenon still exists, and the relative displacement between columns is not zero. Special detailing (e.g., those proposed by Garlock, Sause [49] and Garlock and Li [26]) needs to be

applied to keep columns of the SCEBF free of the floor slab and to prevent large axial force due to the restraint of the gap opening. The restraint of gap-opening expansion due to column is considered in this study; however, the restraint caused by floor slab is not considered in this study, and as an important issue, it needs to be further investigated in a future study of SCEBFs.

In the SCEBF, the post-gap opening stiffness is controlled by the number of PT strands used in the PT cable and the depth of the rocking link beams. By increasing number of the PT strands only, the post-gap opening stiffness can be made to increase but, it does not affect the initial stiffness.

In CEBF design, link length has a key role in determining the dominant plastic behavior (web shear yielding or flexural yielding) of the link beam in terms of its failure mode. However, in the SCEBF structure, the rocking link beam is made very stiff and should remain elastic under the target design. The self-centering structure thus features significant initial stiffness due to rocking link beams with heavy sections while energy dissipation capability is offered by RHD devices. RHD device is the only part of the SCEBF structures sustaining major earthquake-induced damage, and by its inelastic behavior it dissipates sufficient energy and would limit the drift of the structure. RHD devices can be replaced easily at low costs. Thus, the disruption time of such design would be considerably reduced for post-earthquake repair work.

The flag-shaped force-displacement of the SCEBFs is a combination of responses of SCEBF and RHD devices. The total stiffness of SCEBF with RHD devices is the sum of SCEBF stiffness and RHD devices. RHD device provides partial strength and

stiffness and energy dissipation for the self-centering frame, and PT cables provide the re-centering capability of the frame. In SCEBF-K frame, 1st to 4th-floor RHD device top width is 178 mm, 160 mm, 125 mm and 66 mm respectively with the thickness of 25.4 mm. For SCEBF systems K type, 12 RHD devices have been used for each floor. This study investigates the overall seismic response behavior of SCEBF structures K type configuration. The overall behavior of K-type self-centering EBF is investigated and compared it with a K-type CEBF.

5.3 Numerical Model of CEBF-K & SCEBF-K

A planar EBF model in the N-S direction of the building plan was conducted to simulate the seismic response behavior of the EBF frame using a general FE software SAP2000 [65]. A model has been created for K-type SCEBF, and another model has been created for K-type CEBF structures. In CEBF-K type, beam section sizes increased, and instead of using W16 sections for the link, W14 was used.

Seismic performance of CEBFs during strong earthquake events largely depends on the inelastic hysteretic behavior of link beams, while, in SCEBFs the seismic performance depends on the rocking behavior of elastic link beams and associated fuse devices for energy dissipation. Therefore, accurate numerical simulation of rocking link beams is critical to the nonlinear seismic analysis of EBFs. In the nonlinear FE model CEBFs, the approach proposed by Ghobarah and Ramadan [23] for modeling shear links is employed. Shear forces and stiffness in the link beam versus distance between internal and external nodes can be divided into three distinct phases: 1) elastic range up to shear

force of $V=1.1V_p$; 2) plastic phase before ultimate failure; 3) degradation phase due to excessive link rotation leads to web rupture of the link beam [66]. Flexural hinges at the ends of the shear links and column bases are modeled with an autoplastic hinge assignment based on the ASCE 41-13 Equation 9-2. In FE simulation of CEBF and SCEBF, all connections between frame elements are rigid connections except for braces which have pinned ends.

Schematic views of SCEBF, composed of the rocking link beam, PT cables, RHD devices, and other structural members are shown in Figure 5.10 and

Figure 5.11. The pivot point of rocking link beam is also assumed to form at the mid-thickness line of rocking link's flanges. Thus, the depth of the rocking link would be equal to rocking link depth minus rocking link flange thickness. To simulate the gap opening behavior, a special link element in the FE model called "Gap element" is used. Gap elements are located at the pivot point of the rocking link. To model the RHD devices, a frame element with a tapered section along with 20 plastic hinges for each plate segment is employed. RHD devices are connected to the lower fuse holder bracket through Gap element as shown in Figure 5.10 and

Figure 5.11. Furthermore, PT cables are modeled with "Cable element" in the FE software which can sustain tension forces. It is important to mention that In FE software based on CSI Analysis Reference Manual, the linear effective damping for non-linear Link/Support elements such as Gap element would not be used for nonlinear direct-integration time history analysis [65].

Nonlinear beam-column elements were used to model columns and beams. Truss elements were used to model all braces. Moreover, the model does allow the SCEBF rocking link beam to yield in bending, axial force, or combined bending and axial force. However, the rocking link beams' sections are properly selected to avoid any yielding in the SCEBF rocking link beam through DBE. The material utilized for all columns, beams, rocking link beams, and braces are A992 Gr50 steel, and for RHD devices and PT cables, Q225LY and A416Gr270 were used respectively. A lean-on column along the height of the structure has been modeled in FE model to consider the p-delta effect which is connected through rigid truss elements to EBF. First floor columns of EBF are fixed at their bases, but the lean on-columns are pinned at their bases. Floor masses are lumped into the lean-on column nodes at each floor level. In EBF-K type, 2 EBFs are located in the N-S direction of the building, thus, because of symmetry only half of the total seismic mass is considered for EBF-K type model.

A 5% damping ratio for the first and second modes through Rayleigh damping is considered for the EBF in the FE model. The first three vibration periods of SCEBF-K are 0.88 sec, 0.34 sec, 0.21 sec respectively. The first vibration period of CEBF-K frame is 1.12 sec. Figure 5.12 shows the first three mode shapes of SCEBF-K.

The first mode shape is the dominant mode shape in the EBFs based on FE results, thus, for pushover analysis, an inverted triangular vertical load profile [67] should be used to spread the base shear along the height of the eccentrically braced frames.

5.4 Nonlinear Static Analysis

The seismic performance of CEBF and SCEBF is thoroughly investigated by pushover and nonlinear time history analysis in FE model. Pushover analysis is a nonlinear static analysis providing information regarding elastic and inelastic behavior of structure such as ductility, key load levels and deflection of the structure until the ultimate condition is reached. The pushover analysis also shows the formation of plastic hinges at various locations as the lateral load increases. To perform the pushover analysis, first, appropriate plastic hinges need to be assigned to corresponding locations of members as needed. For CEBF, plastic hinges are created in shear links and column base, and for SCEBF, plastic hinges are set up in fuse members and column base but not rocking links because it is supposed to remain elastic through the design-basis earthquake. Moreover, material nonlinearities are also assigned to different hinge locations to capture plastic rotation behavior better.

Pushover analysis is essentially based on the assumption that the first mode shape dominates the response of the structure and first mode shape remains constant through elastic and inelastic response of the structure. Based on FEMA2000, an inverted triangular load distribution was used to derive pushover forces as shown in Figure 5.13. Pushover force applied at the designated floor nodes forms an approximately inverted triangular profile. The control point of pushover analysis for the CEBF is the right column roof node but for SCEBF is the node in the mid-span of the rocking link to bypass the gap-opening expansion in self-centering structures. The lateral load was increased monotonically until the control point reaches 2% roof drift ratio. Roof drift

ratio is defined as the horizontal roof displacement divided by the height of the EBF structure.

Figure 5.14 and Figure 5.15 shows the pushover curves of CEBFs and the flag-shaped curve of self-centering structure for K type EBF with RHD devices. Based on the flag-shaped curve, the residual drift is minimal meaning that the SCEBF can re-center itself after earthquake. Based on Figure 5.15 for CEBF, post-yield stiffness changes gradually which suggests the initiation of link shear yielding; however, for SCEBF, post-yield stiffness changes abruptly showing the gap opening behavior in self-centering structure. Pushover analysis also gives out information regarding the inelastic behavior and seismic energy dissipation of specific members in the structure such as a shear link in CEBF or RHD devices in SCEBF.

In Figure 5.15, number 1 denotes the point when gap opening happens, and number 2 shows plastic hinges formation of RHD device. In SCEBF-K, initial gap opening happens at 0.16% roof drift ratio (number 1), and plastic hinges form at 0.28% roof drift ratio simultaneously for first and second-floor RHD devices (number 2). The yield strength of SCEBF-K would be at 0.282% roof drift ratio which lateral stiffness of SCEBF-K reduces abruptly.

PT cables would not yield at 2% roof drift ratio for SCEBF-K type. The unloading stiffness of SCEBF-K is the same as the loading stiffness.

In Figure 5.15, it is also seen the difference of force-displacement hysteresis of SCEBF Vs. CEBF. SCEBF has a flag-shaped hysteresis which minimizes residual drift of the structure leading to the re-centering system. Nevertheless, CEBF has a bilinear force-

displacement hysteresis with a considerable amount of residual drift due to yielding of shear links. The Beta factor in SCEBF-K frame is equal to 0.35 respectively [52]. Moreover, based on Figure 5.15, the initial stiffness of SCEBF is higher than CEBF. The initial stiffness of the SCEBF system is higher than the corresponding CEBF system. Since, in the SCEBF structure, the primary structural members including link beam, braces, beams, and columns are designed so that they should remain elastic under the design level earthquakes. The self-centering EBF structures thus feature larger initial stiffness compared with conventional structural systems. Plastic hinges in column base of the SCEBF-K will form at 1.63% roof drift ratio respectively, which are in the late stage of pushover curve before the 2% drift limit. It is worth noting that replaceable fuse devices such as that proposed by Freddi, Dimopoulos [68] can be applied in order to make the column base plastic hinge easily to be repaired after strong earthquakes.

5.5 Nonlinear Time History Analysis

To evaluate seismic response of the structure under different earthquakes, nonlinear time history analysis has been used. In SAP2000, 20 scaled design base earthquakes record for downtown Los Angeles [69], California region with a probability of exceedance of 10% in 50 years has been used.

Details of earthquake ground motion records are presented in Table 5.3.

To better understand the overall seismic behavior of structures, nonlinear time history analysis is conducted in this study. An ensemble of 20 strong motion records scaled to

design basis earthquake intensity (probability of exceedance of 10% in 50 years) in downtown Los Angeles [69], California region are used. Details of earthquake ground motion records can be found from Moghaddasi and Zhang [70]. In the following sections, the time history results such as maximum roof drift ratio and residual roof drift ratio are reported. The peak value of these seismic demand parameters refers to the maximum absolute value of the specified parameters over the time in time history analysis.

5.5.1 Global and Local Deformation Demand

Peak roof drift ratio and residual drift ratio of the prototype four-story CEBF-K and SCEBF-K under 20 different ground motions are shown in Figure 5.16 and Figure 5.17 respectively. Peak roof drift ratio is the ratio of the horizontal displacement of the roof divided by EBF height, and residual drift ratio is the ratio of residual drift measured in the last 5 seconds of time history analysis of roof drift divided by the EBF height.

The dashed lines in Figure 5.16 and Figure 5.17 denote the ensemble average value of the peak roof drift ratio. The average value of peak roof drift ratio of CEBF-K and SCEBF-K is 1.19% and 1.17% respectively. The maximum peak roof drift ratio for both SCEBF-K occurs under La16, however, for CEBF-K it occurs under La09.

Ensemble average value of roof residual drift ratio for CEBF-K and SCEBF-K is 0.236% and 0.003% respectively. The maximum residual drift ratio of SCEBF-K is 0.01%. In SCEBF-K type, maximum residual drift ratio occurred under La16 as the maximum roof drift ratio also occurred under La16. On the other hand, for CEBF-K

type, the ground motion with higher peak roof drift ratio does not necessarily have the higher residual drift ratio. As expected, the residual drift ratio in SCEBF-K type is negligible compared to the CEBF-K type. The average residual drift ratio in CEBF for K type is considerable because of plastic deformation of the shear link.

5.5.2 Parametric Study

SCEBF has the benefits to be tuned separately for stiffness, equivalent yield strength (gap opening force plus fuse member strength) and ductility in a more flexible way than conventional structural systems. To demonstrate how to adjust two key response parameters (equivalent yield strength and post-gap opening stiffness) of self-centering structures and resulting behavior, a parametric study of three cases of SCEBFs is conducted. These three cases use the same prototype EBF frames except for PT cable length and initial stress level (with three different cases of PT initial stress (40%, 50%, 60%) and different length) but with the same ultimate base shear force for K type EBF at 2% roof drift ratio. Specifically, a parametric study is performed as follows:

Case-A: PT cable initial stress= 40% yield stress, cable length =2 bay widths

Case-B: PT cable initial stress= 50% yield stress, cable length =3 bay widths (baseline case)

Case-C: PT cable initial stress= 60% yield stress, cable length=5 bay widths

To have the similar final base shear force, different PT cable length for various cases should be used. PT cable extending over 2, 3, and 5 bays are used for Case A, B, and C respectively, as shown in Figure 5.18. Therefore, they have cable length

corresponding to respective distribution bay widths. Equivalent yield strength (gap opening force + fuse member strength) is defined as the base shear force where stiffness changes abruptly in the force-displacement curve, and it directly depends on the PT cable initial stress level. Case-A has the lowest equivalent yield strength since its PT cable initial stress is the lowest among all three cases; on the other hand, Case-C has the largest equivalent yield strength as it has the highest PT cable initial stress level.

The flag-shaped hysteresis curves of K type EBFs for Case A, B, and C are shown in Figure 5.19. Based on Figure 5.19, the equivalent yield strength of each case has approximately 220 kN difference, but the ultimate base shear force is almost the same. Post-gap opening stiffness of SCEBF is the stiffness of self-centering structure after gap-opening happens. Post-gap opening stiffness directly depends on PT cable length and cross-sectional area. If area is maintained constant, the shorter the PT cable length, the higher the post-gap opening stiffness would be. The post gap opening stiffness of Case-A is larger than Case-B and Case-C since not only Case-A has the shortest length among all three cases, but also the ultimate based shear force is same for all three cases.

Post-gap opening stiffness of SCEBF is the stiffness of self-centering structure after gap-opening happens. Post-gap opening stiffness directly depends on PT cable length and cross-sectional area. If area is maintained constant, the shorter the PT cable length, the higher the post-gap opening stiffness would be. The post gap opening stiffness of Case-A is larger than Case-B and Case-C since not only Case-A has the shortest length among all three cases, but also the ultimate based shear force is same for all three cases.

Figure 5.20 shows the peak roof drift ratio for Case-A, Case-B, and Case-C for K-type SCEBF. Peak roof drift ratio in all three cases are very close to each other. The ensemble average of peak roof drift is about 1.18% for SCEBF-K. For all three cases of SCEBF-K type, peak roof drift ratio is less than 2% for all ground motions except for La16. In K-types SCEBF, La16 has the largest peak roof drift ratio. Case-C has the largest average value of maximum roof drift ratio among all three cases for K-type SCEBF, but Case-A and Case-B have the same average value of maximum roof drift ratio.

Figure 5.21 shows the residual drift ratio for K-type SCEBF and their three different cases. For three cases of SCEBF-K, residual drift ratio is minimal at about 0.0033%. For K-type SCEBFs, Case-C and Case-A have the largest and smallest average value of residual drift ratio respectively. The results of peak roof drift ratio and residual drift ratio further verify that K-type SCEBF can re-center themselves after the earthquake and are almost damage free in primary structural frames except for RHD devices.

Peak inter-story drift ratio is a key seismic response demand parameter that can be related to building damages. Peak inter-story drift ratio is relative lateral displacement between two adjacent floors divided by the story height between these floors. In Figure 5.22, ensemble average values of peak inter-story drift ratio along the structure height have been shown for K-type SCEBFs and CEBFs. The horizontal lines show the range of peak inter-story drift ratio within one standard deviation with a confidence level of 68.3%. Case-A and Case-C have the minimum and maximum peak inter-story drift ratio among all three cases for both SCEBFs respectively.

Figure 5.23 shows the peak PT cable stress ratio for three cases of K-type SCEBFs along structure height. The horizontal lines show the range of peak PT cable stress ratio within one standard deviation with a confidence level of 68.3%. Peak PT cable stress ratio is the ratio of the PT cable maximum stress during a ground motion duration over PT cable yield stress. The average value of Peak PT cable stress ratio among all floors for SCEBF-K for Case-A, B, and C is 59%, 63%, and 68% respectively. Case-A has the smallest value of peak PT cable stress ratio for K-type SCEBFs; on the other hand, Case-C has the largest value of it. The maximum peak PT cable stress ratio which happens in Case-C is 75% for SCEBF-K. Thus, PT cables would not yield through whole earthquake ground motions even in Case-C.

All three cases of parametric study almost have a similar seismic performance; however, Case-A seems to be the better one compared to the other two cases due to the following reasons. First, not only Case-A has the overall lowest roof drift ratio and peak inter-story drift ratio among all three cases, but also it has the lowest residual drift ratio for K-type SCEBFs. Second, Case-A requires fewer PT strands compared to the other two cases. As a result, more cable material saving would be achieved, and the costs become lower than Case-B and Case-C. However, even though Case-A has a smaller equivalent yield strength, it seems to have better seismic performance than the other two cases.

5.5.3 Typical Case

Due to space limitations, here only the detailed response results for one chosen ground motion in Case-B are presented. Typical case refers to the median response out of the ensemble of 20 ground motion cases in Case-B for SCEBF-K type. This typical case was selected based on the case closest to the ensemble median value of peak roof drift ratio, which is found to be ground motion La13 for SCEBF-K. Figure 5.24 shows the roof drift time history of EBF-K in La13. The maximum roof drift of La13 ground motion for SCEBF-K and CEBF-K is 208.25 mm, 151.5 mm respectively which is less than 1.2% roof drift ratio. The dotted line shows the residual roof drift for SCEBF and the dash-dot line shows the residual roof drift for CEBF. Residual roof drift for SCEBF-K, and CEBF-K is -0.3 mm and -11.1 mm respectively. It is evident that SCEBF models have negligible residual drift value compared with CEBF models. Based on the ground motion data, Peak Ground Acceleration (PGA) happens at t=5.8 sec for La13. Figure 5.24 shows that peak roof drift happens at PGA for SCEBF-K type.

Figure 5.25 shows link shear force of first-floor versus link rotation angle hysteresis of EBF-K in La13. Link shear force of SCEBFs is larger than CEBFs in K type; however, link rotation demand of SCEBFs is lower than CEBFs. SCEBFs have pinched hysteresis because of their self-centering behavior. On the other hand, CEBFs hysteresis shows the significant amount of energy dissipation due to shear yielding of link beam. Based on Figure 5.25, SCEBFs have self-centering behavior since residual drift is negligible; however, CEBFs require a greater amount of energy dissipation than SCEBFs to achieve the same level of peak drift response.

Figure 5.26, Figure 5.27, Figure 5.28 and Figure 5.29 present first, second, third and fourth story drift time history for SCEBF-K type under La13 respectively.

Figure 5.30, Figure 5.31, Figure 5.32 and Figure 5.33 show the first, second, third and fourth-floor inter-story drift ratios of La13 for SCEBF-K type respectively. The peak inter-story drift ratios for SCEBF-K for the first, second, third and fourth floor are 1.37%, 1.43%, 1.41%, 1.40% respectively happening at peak ground acceleration (PGA) of La13.

Figure 5.34, Figure 5.35, Figure 5.36 and Figure 5.37 show the first, second, third and fourth floor axial force-time history of the rocking link beam and PT cable of SCEBF-K under La13 ground motion. It is seen that the axial force in the link beam is not equal to PT cable's axial force due to column restraint from gap-opening expansion. The column shear force is the difference between axial force of the rocking link beam and PT cable which is less than 5% of PT cable axial force for both cases. The relative displacement between the columns of each floor depends on the gap-opening expansion of each floor. In SCEBF-K under La13, the peak column relative displacement of the 1^{st} to 4^{th} floor is 32 mm, 34 mm, 38 mm and 50 mm respectively as shown in Figure 5.38.

Figure 5.39 represents peak inter-story drift ratio for SCEBF-K type under La13 ground motion. It is seen that peak inter-story drift ratios for SCEBF-K type under La13 are between 1.3% and 1.5%.

Figure 5.40 shows the peak PT cable stress ratio distribution along the height of the structure for K-type SCEBF. The magenta line in Figure 5.40 shows the initial stress

level of PT cables which is 50% for K-type SCEBF. For SCEBF-K, Peak PT cable stress ratio of La13 is between 62% and 67% meaning that all floors PT cables have a similar contribution to the post-gap opening stiffness of the structure. Maximum peak PT cable stress ratio for SCEBF-K is 67%. Thus, PT cables would remain elastic during the whole earthquake as expected.

Figure 5.41 shows the maximum link chord rotation angle response, which is defined as the ratio of vertical displacement between two ends of the link divided by the link length. Maximum rotation demand of link in SCEBF-K for La13 is between 0.07 rad and 0.08 rad. Rocking link beam will remain elastic through design basis earthquake in SCEBF-K type. In K type, peak link rotation angle is less than 0.1 rad.

The good performance of SCEBFs depends on the elastic behavior of rocking link beams. The link beams' section should be designed in such a way to remain elastic through DBE earthquakes or even MCE earthquakes. Figure 5.42 shows the P-M interaction curve time history for first-floor link beam of SCEBF-K in La13. It is seen that the link beams of K-type SCEBF remain in the elastic range based on their P-M interaction curve.

The promising performance of SCEBF under strong ground motions can be explained by the fact that all primary structural members remain undamaged and it can re-center itself after the earthquake. RHD devices have a role of fuse device dissipating all earthquake energy to keep other members damage free. Recent full-scale experiments of RHD devices [9, 50] has shown that one set of RHD devices can be replaced in 30 minutes.

Table 5.1 Member sections of conventional 4-story K-type EBF (CEBF-K)

Story	Member sections			
	Braces	Columns	Beams	Link
1	HSS 9x9x0.5	W14x132	W18x97	W14x120
2	HSS 8x8x0.5	W14x132	W18x65	W14x74
3	HSS 6x6x0.5	W14x48	W18x50	W14x53
4	HSS 6x6x0.5	W14x48	W18x40	W14x43

Table 5.2 Member sections and PT cables of 4-story self-centering K-type EBF (SCEBF-K)

Story	Member sections				PT Cables	
	Braces	Columns	Beams	Rocking link beam	# of 7-wire Strands	Initial PT cable force (kN)
1	HSS 10x10x0.625	W14x211	W18x143	W14x233	22	2602
2	HSS 9x9x0.625	W14x211	W18x97	W14x145	16	1893
3	HSS 8x8x0.5	W14x82	W18x76	W14x120	12	1419
4	HSS 8x8x0.5	W14x82	W18x50	W14x74	6	712

Table 5.3 Earthquake ground motion records

Code	Original EQ. Record	EQ. Magnitude	Epicenter Distance (km)	Scale Factor	PGA (cm/s^2)	Vertical PGA (cm/s^2)
LA01	Imperial Valley, 1940, El Centro	6.9	10	3.02	678.05	494.25
LA02	Imperial Valley, 1940, El Centro	6.9	10	3.02	994.32	724.79
LA03	Imperial Valley, 1979, Array #05	6.5	4.1	1.52	579.06	422.09
LA04	Imperial Valley, 1979, Array #05	6.5	4.1	1.52	717.98	523.36
LA05	Imperial Valley, 1979, Array #06	6.5	1.2	1.26	443.54	323.31
LA06	Imperial Valley, 1979, Array #06	6.5	1.2	1.26	345.12	251.57
LA07	Landers, 1992, Barstow	7.3	36	4.80	619.47	665.59
LA08	Landers, 1992, Barstow	7.3	36	4.80	626.24	672.86
LA09	Landers, 1992, Yermo	7.3	25	3.26	764.55	821.47
LA10	Landers, 1992, Yermo	7.3	25	3.26	530.03	569.49
LA11	Loma Prieta, 1989, Gilroy	7	12	2.69	978.74	713.43
LA12	Loma Prieta, 1989, Gilroy	7	12	2.69	1426.40	1039.75
LA13	Northridge, 1994, Newhall	6.7	6.7	1.55	997.40	730.59
LA14	Northridge, 1994, Newhall	6.7	6.7	1.55	966.74	708.13
LA15	Northridge, 1994, Rinaldi RS	6.7	7.5	1.19	784.95	574.97
LA16	Northridge, 1994, Rinaldi RS	6.7	7.5	1.19	852.87	624.72

LA17	Northridge, 1994, Sylmar	6.7	6.4	1.49	837.65	613.57
LA18	Northridge, 1994, Sylmar	6.7	6.4	1.49	1202.16	880.57
LA19	North Palm Springs, 1986	6	6.7	4.46	1499.15	1092.78
LA20	North Palm Springs, 1986	6	6.7	4.46	1451.42	1057.99

Figure 5.1 Rocking link and PT cables in SCEBF test specimen with RHD devices

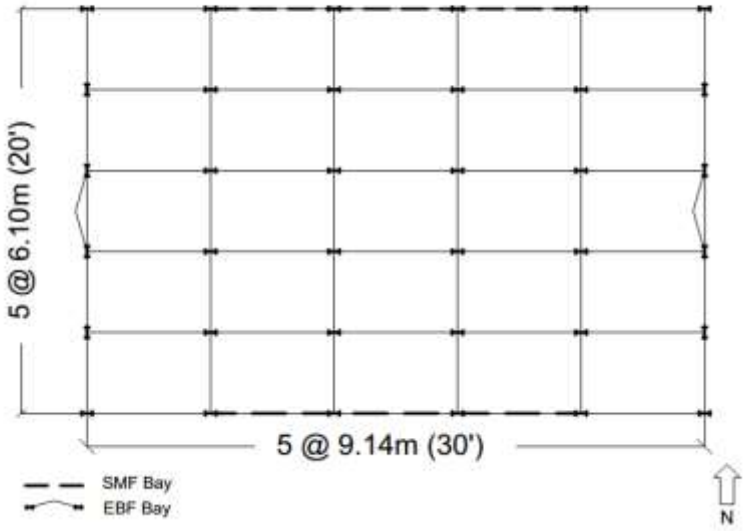

Figure 5.2 Floor plan of prototype SCEBF-K type building

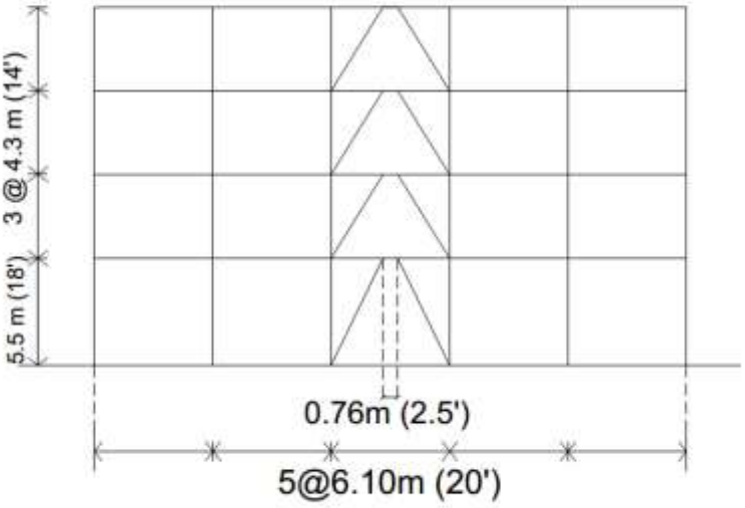

Figure 5.3 Elevation view of prototype SCEBF-K type building

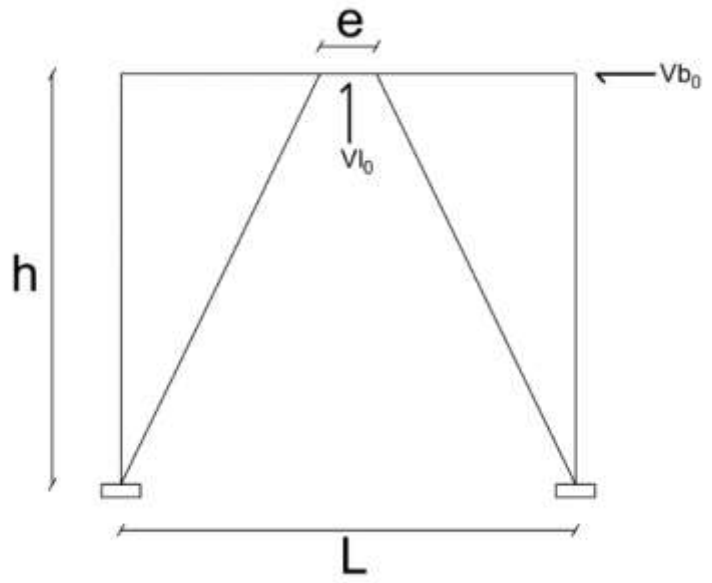

Figure 5.4 Configuration and dimensions of SCEBF-K structure

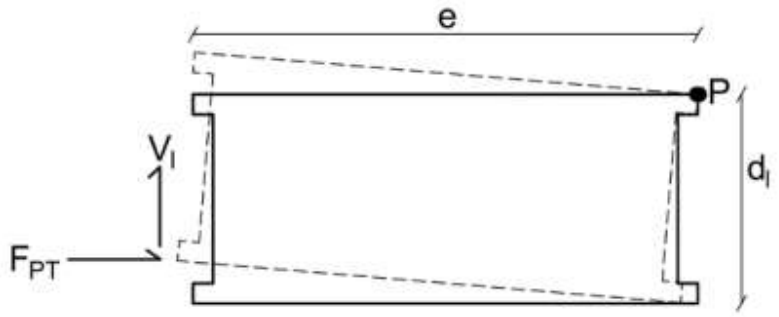

Figure 5.5 Rocking link beam configuration and dimension in SCEBF-K structure

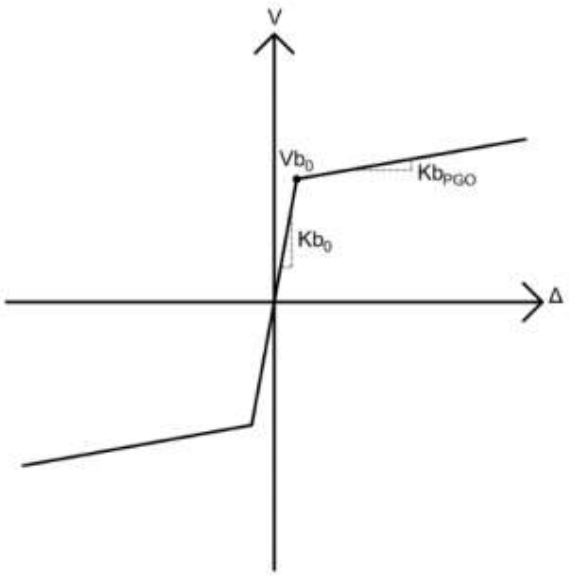

Figure 5.6 Pushover curve of one-story SCEBF-K type

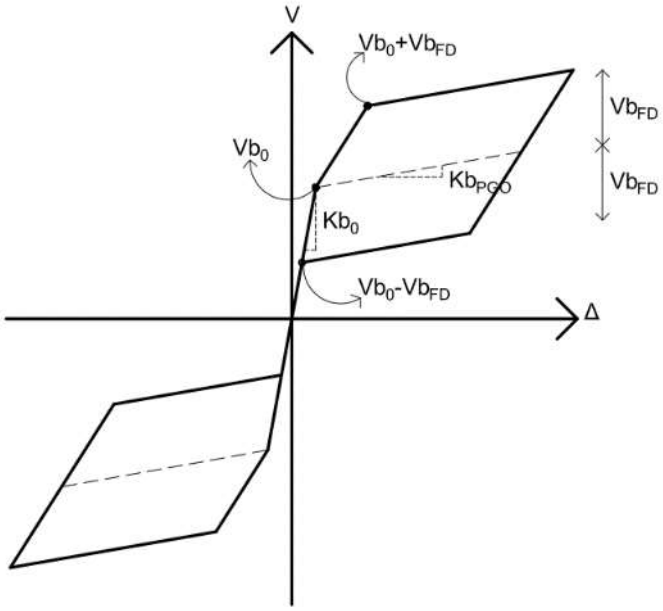

Figure 5.7 Pushover curve of one-story SCEBF-K type with RHD devices

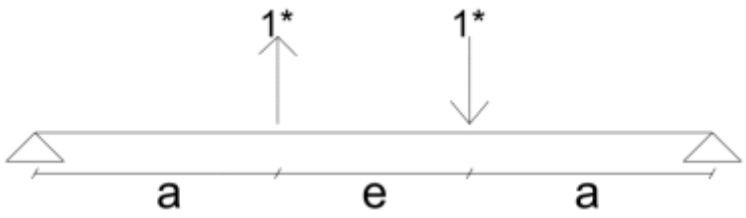

Figure 5.8 Beam/link flexural stiffness component: K_f

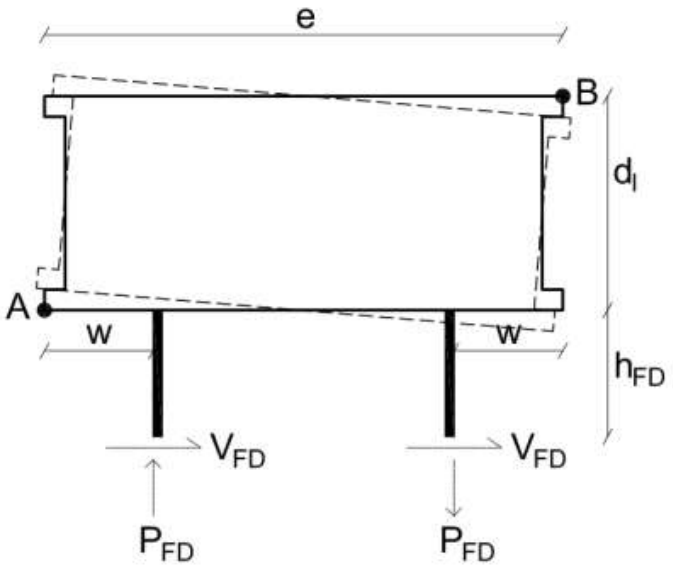

Figure 5.9 RHD device-shear force effect on SCEBF-K type structure

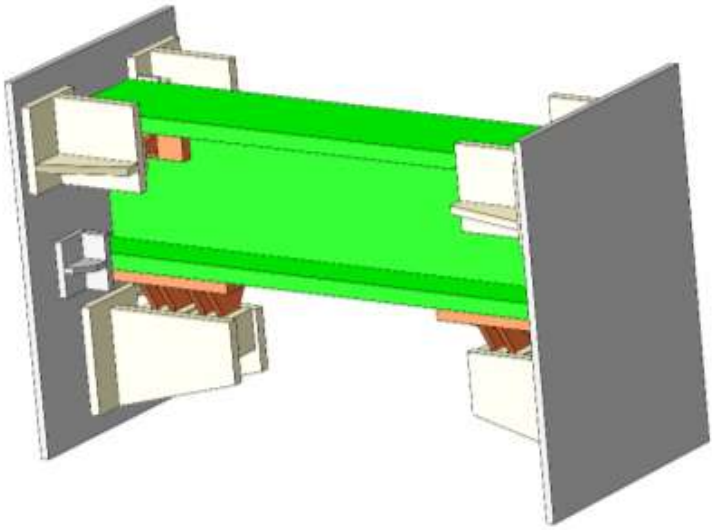

Figure 5.10 Schematics of rocking link with RHD devices in SCEBF and corresponding ANSYS model

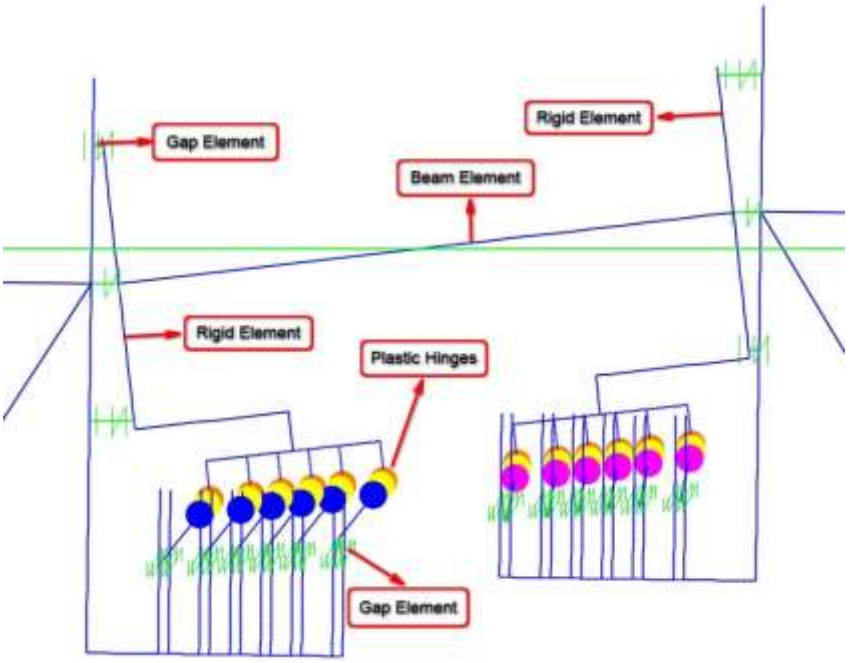

Figure 5.11 Schematics of rocking link with RHD devices in SCEBF and corresponding SAP2000 model

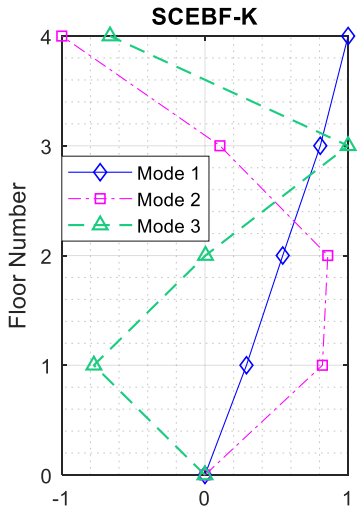

Figure 5.12 Mode shapes of prototype self-centering EBF-K type buildings

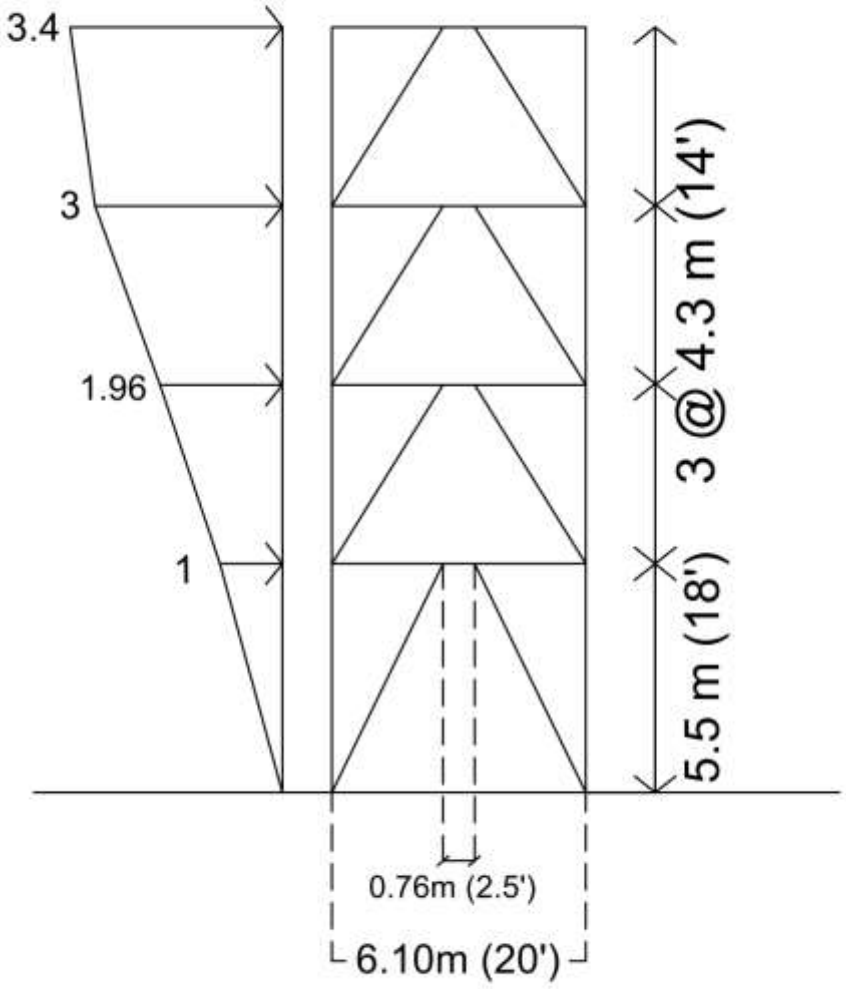

Figure 5.13 Pushover loading protocol for SCEBF-K type

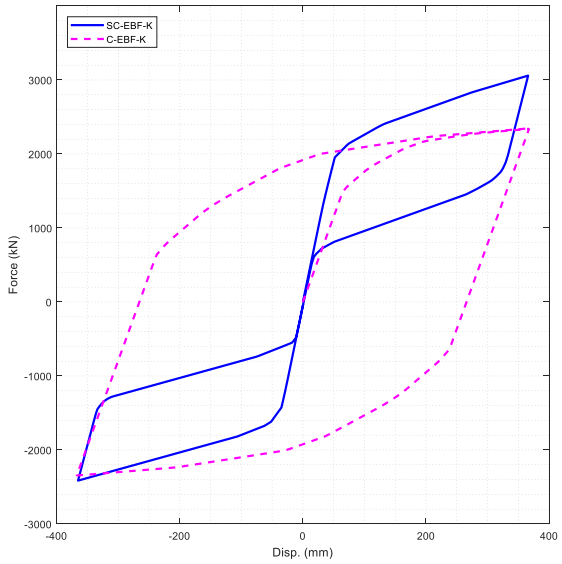

Figure 5.14 Pushover curve of EBF-K type

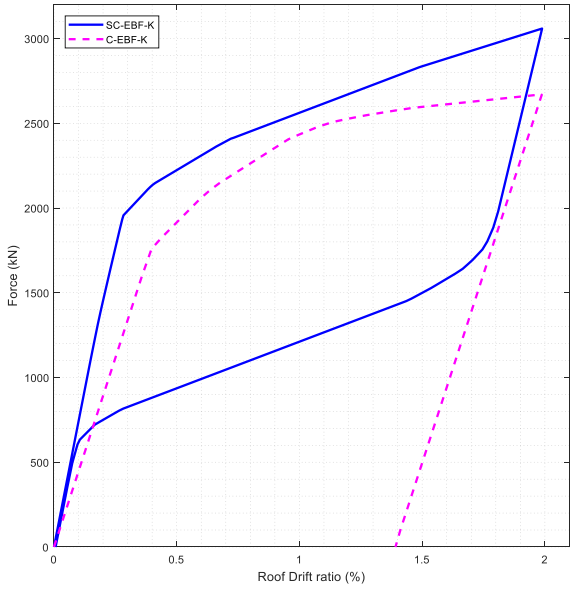

Figure 5.15 Pushover curve of prototype SCEBF K-type

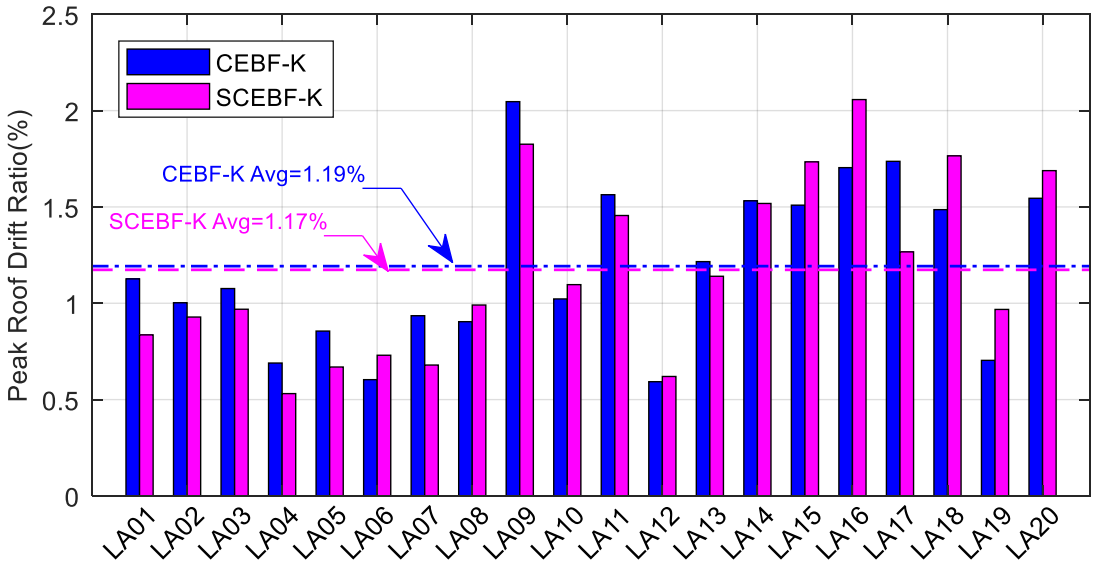

Figure 5.16 Peak roof drift ratio of prototype K-type EBFs

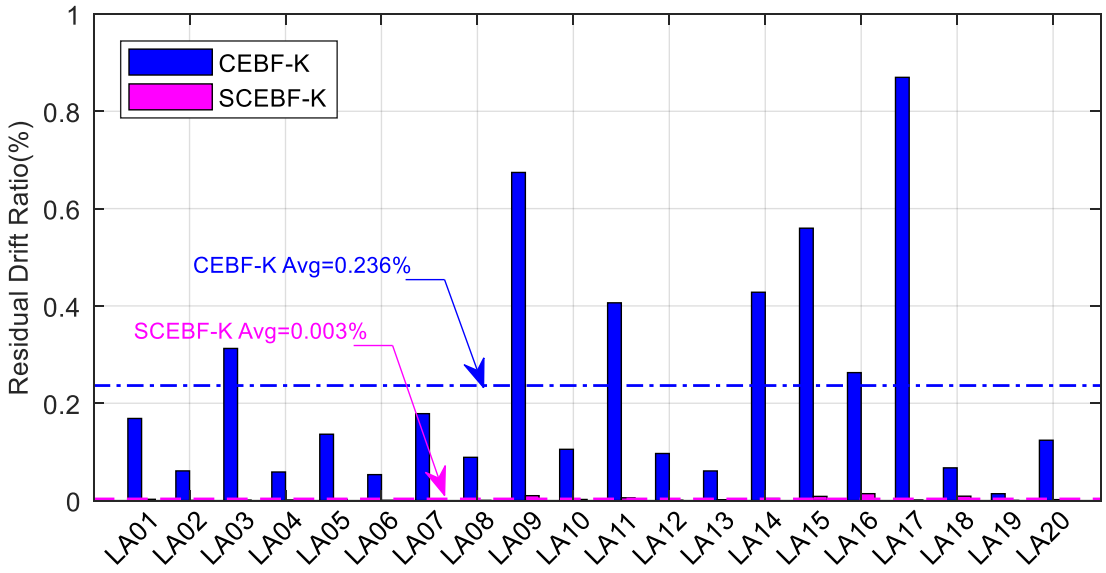

Figure 5.17 Residual roof drift ratio of prototype K-type EBFs

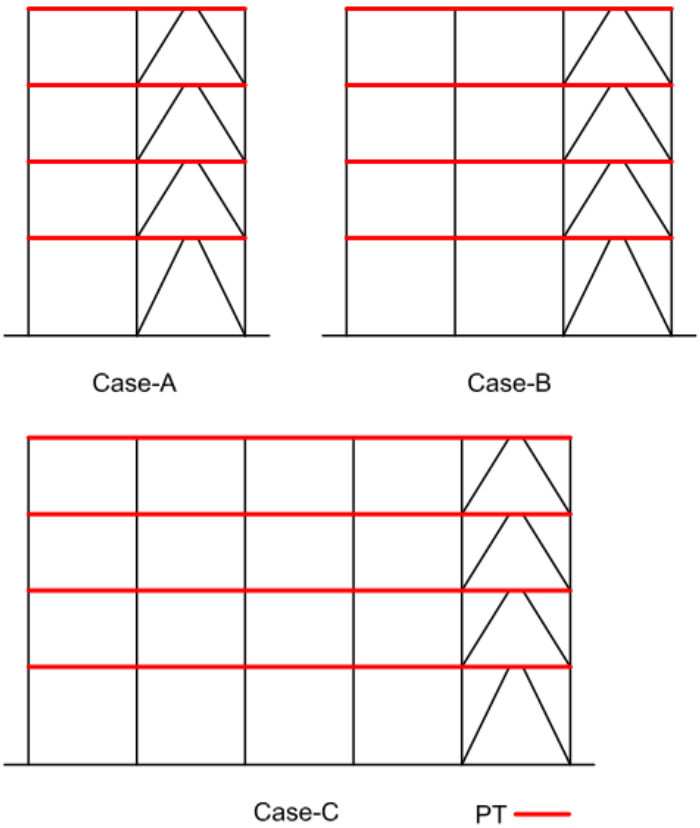

Figure 5.18 Configuration of parametric study cases for K-type EBFs

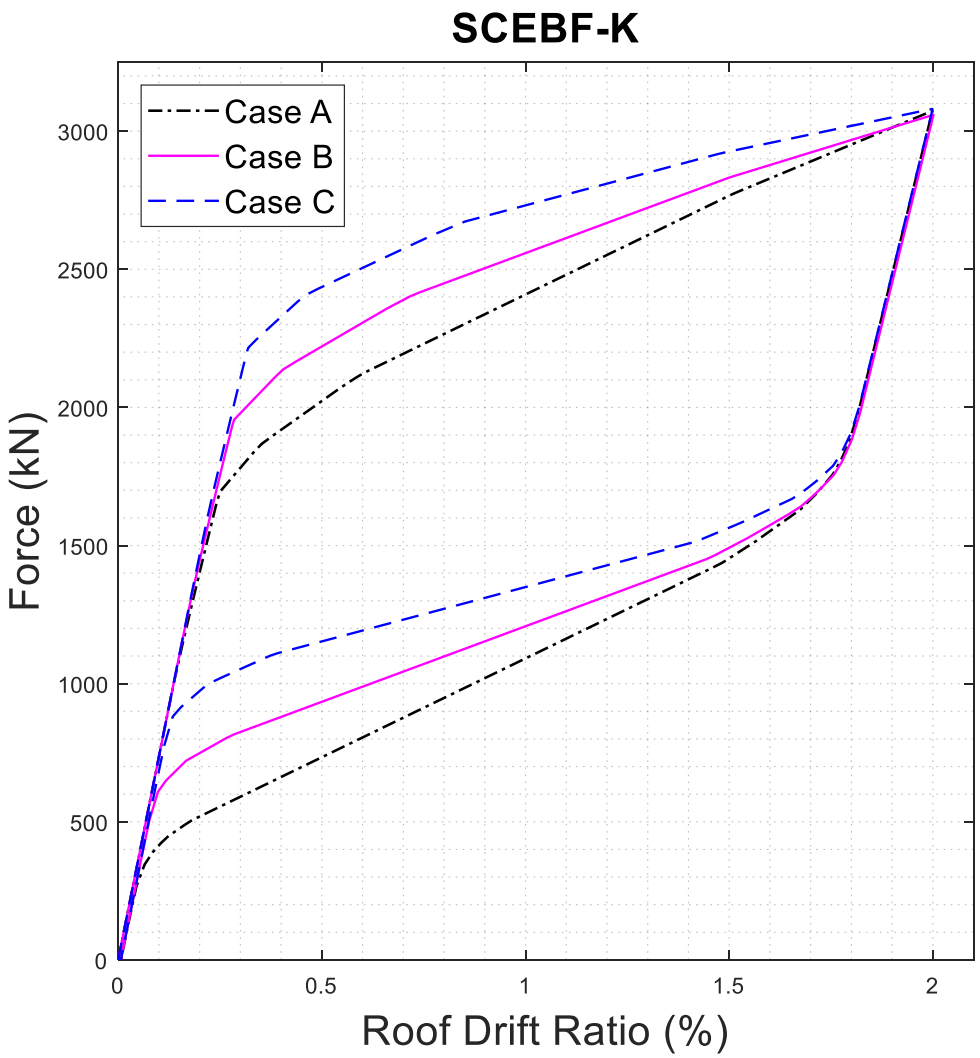

Figure 5.19 Hysteresis curves of prototype SCEBFs with varying PT cable initial stress and length for SCEBF-K type

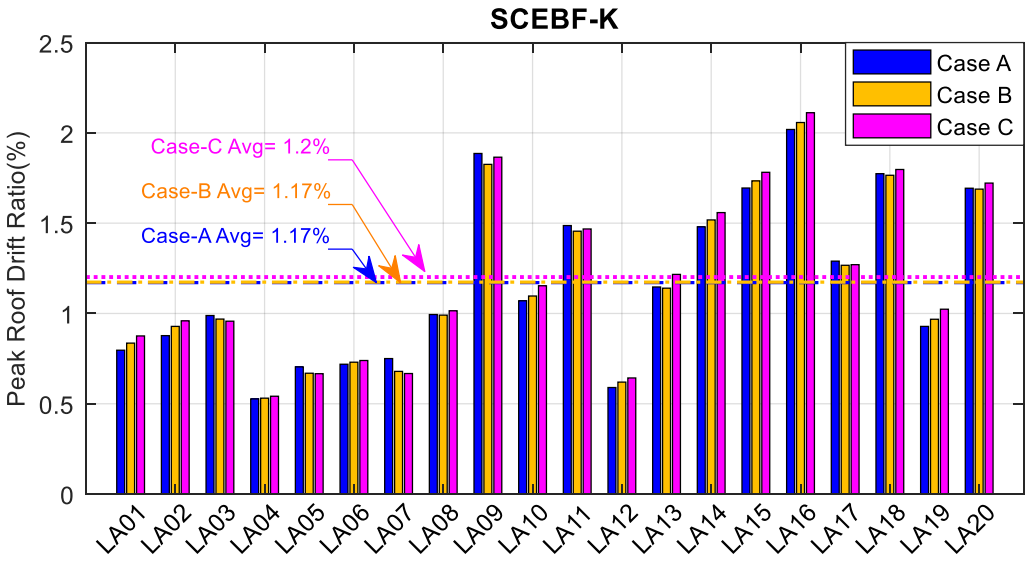

Figure 5.20 Peak roof drift ratio from parametric study for SCEBF-K type

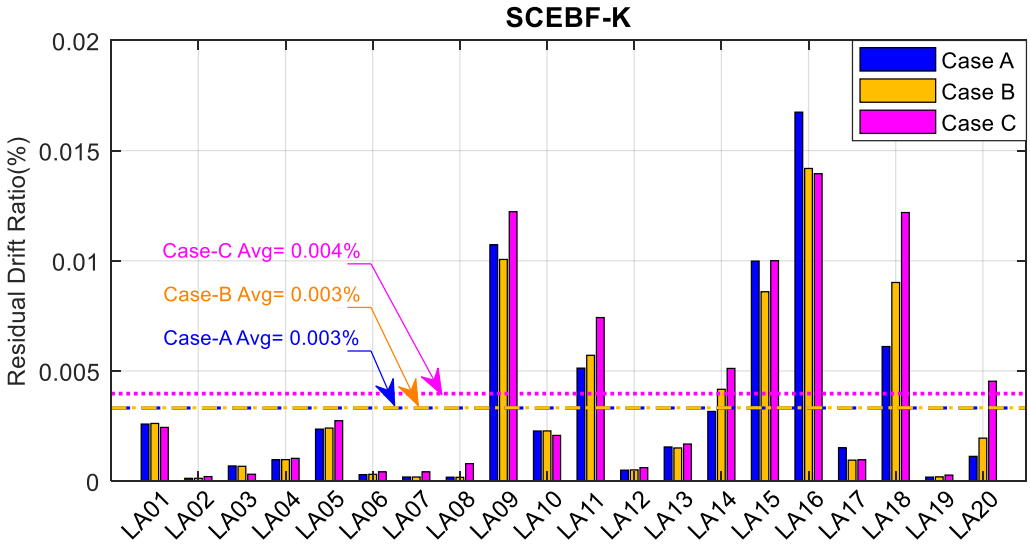

Figure 5.21 Residual drift ratio from parametric study for SCEBF-K type

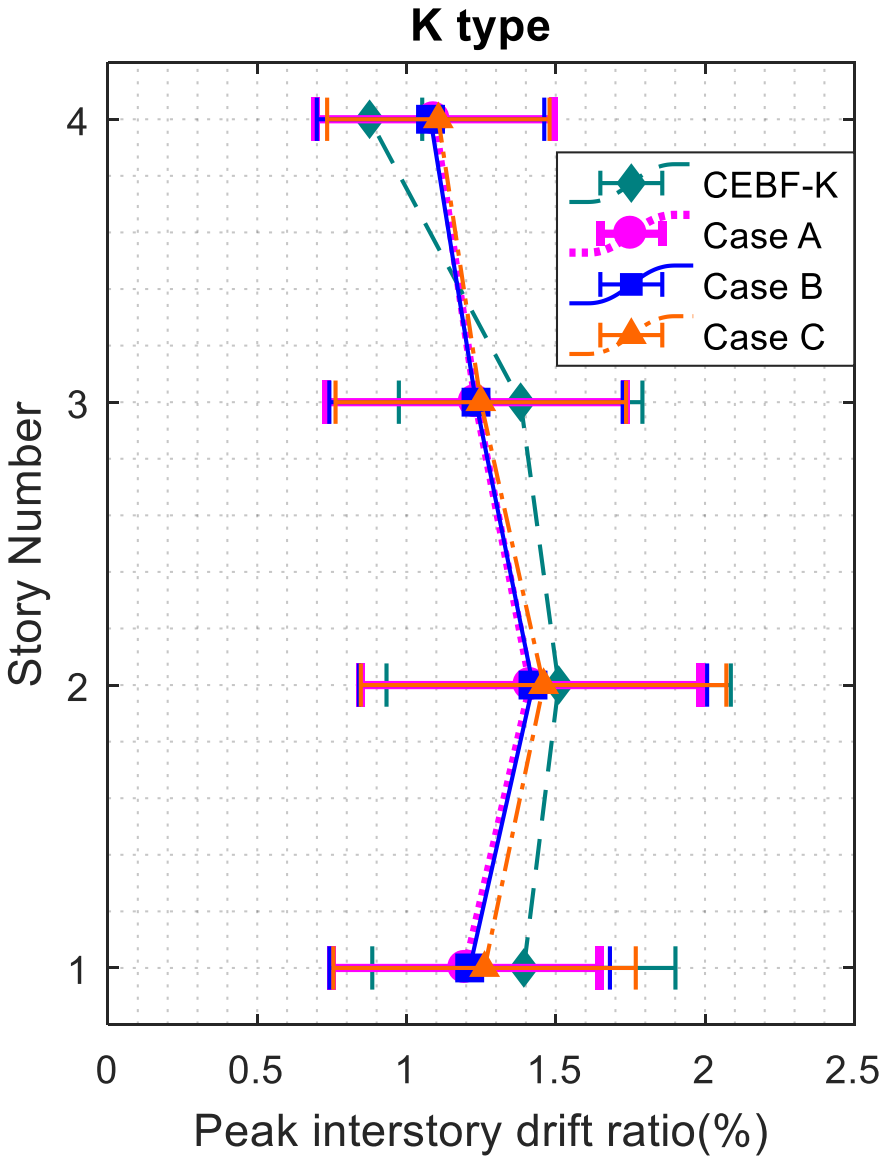

Figure 5.22 Peak inter-story drift ratio from parametric study for K-type EBFs

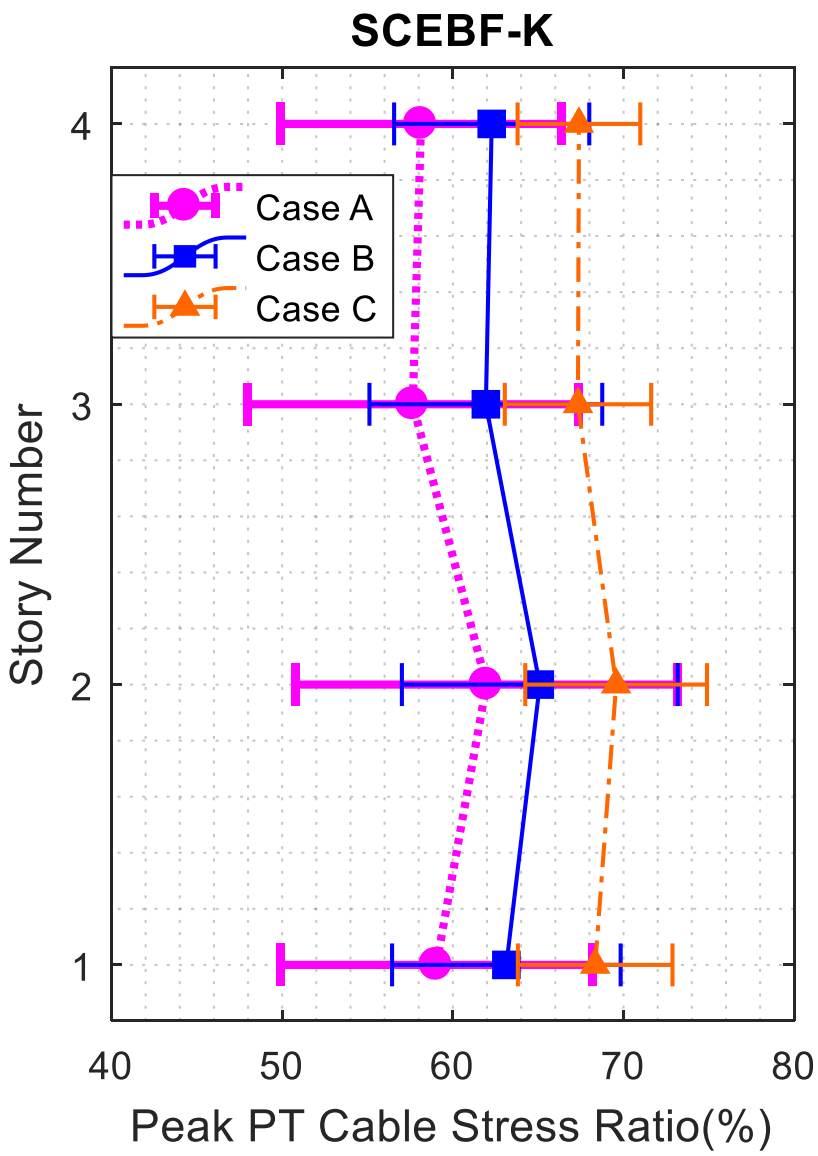

Figure 5.23 Peak PT cable stress ratio from parametric study for SCEBF-K type

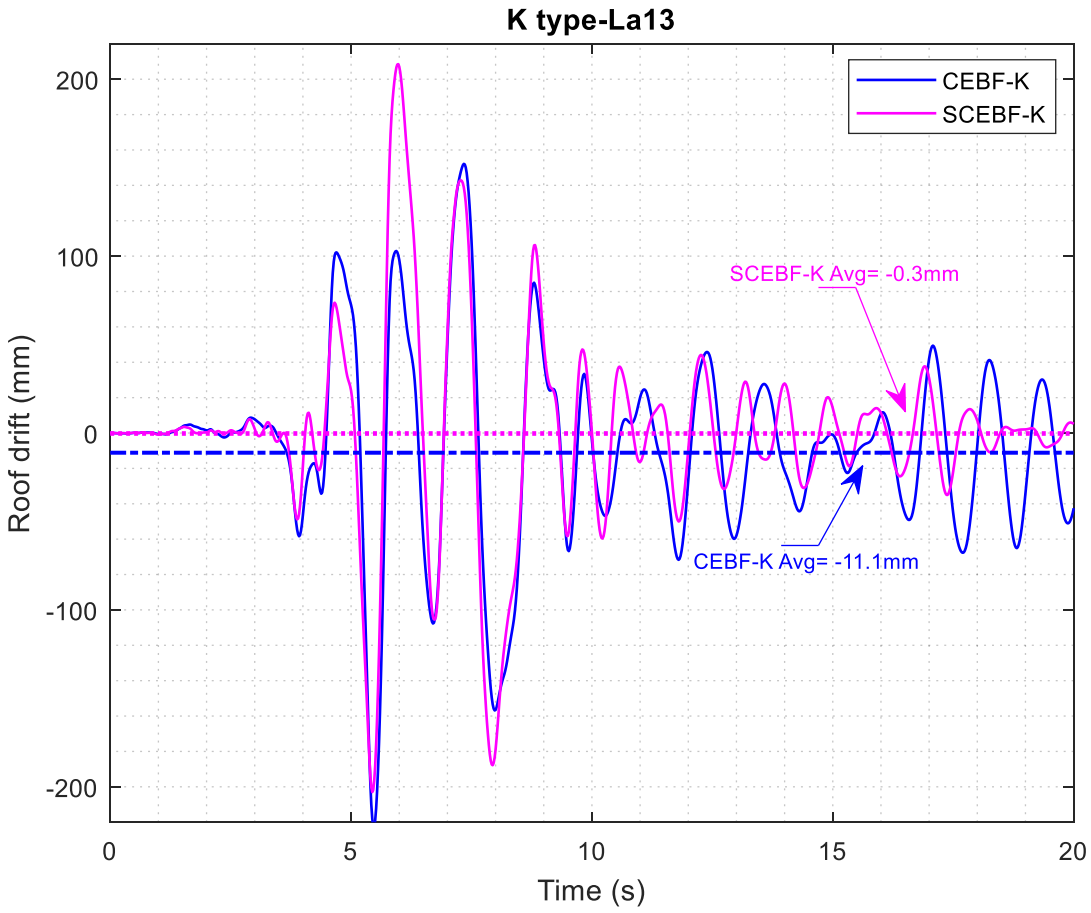

Figure 5.24 Roof drift time history for K-type EBFs

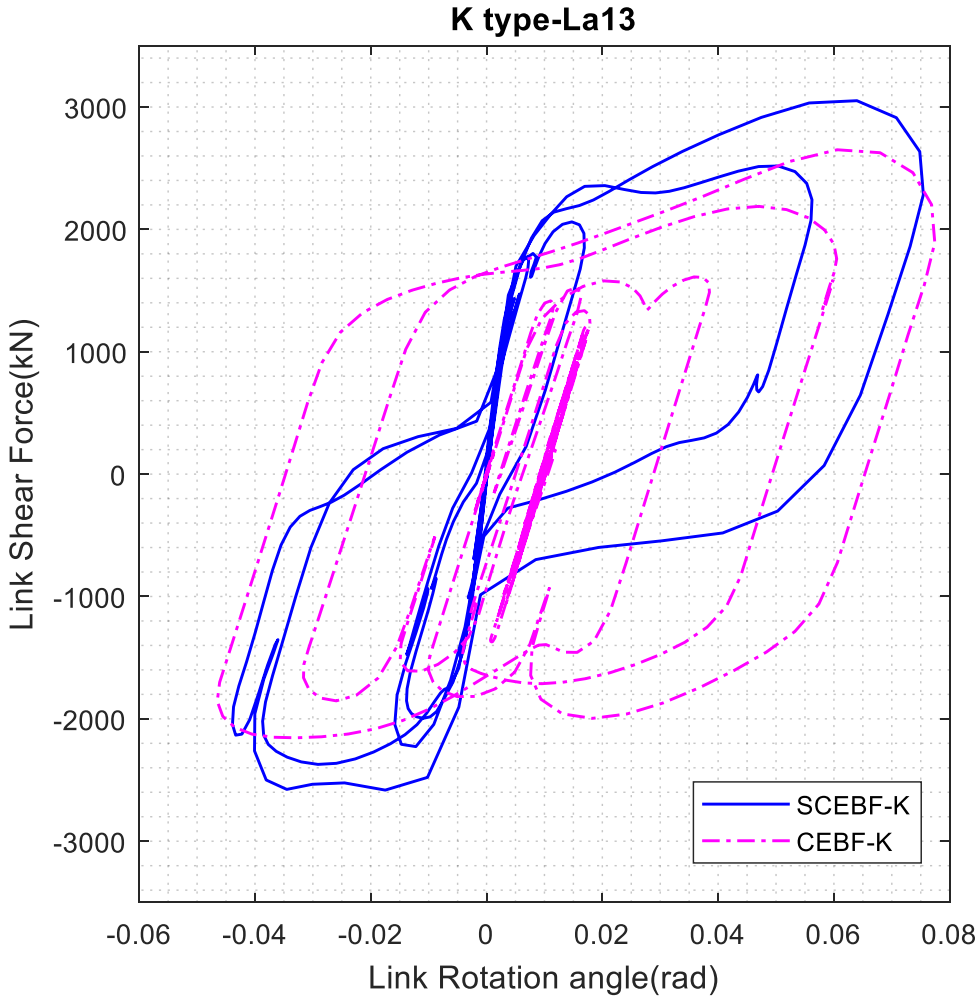

Figure 5.25 First-floor link shear force vs. link rotation angle hysteresis curve for K-type EBFs

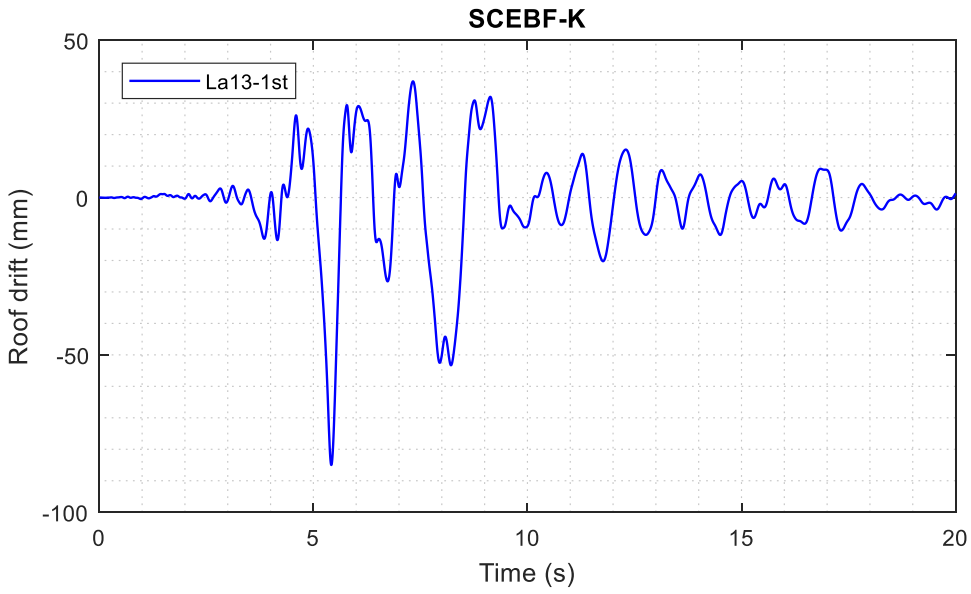

Figure 5.26 First story drift time history for SCEBF-K type

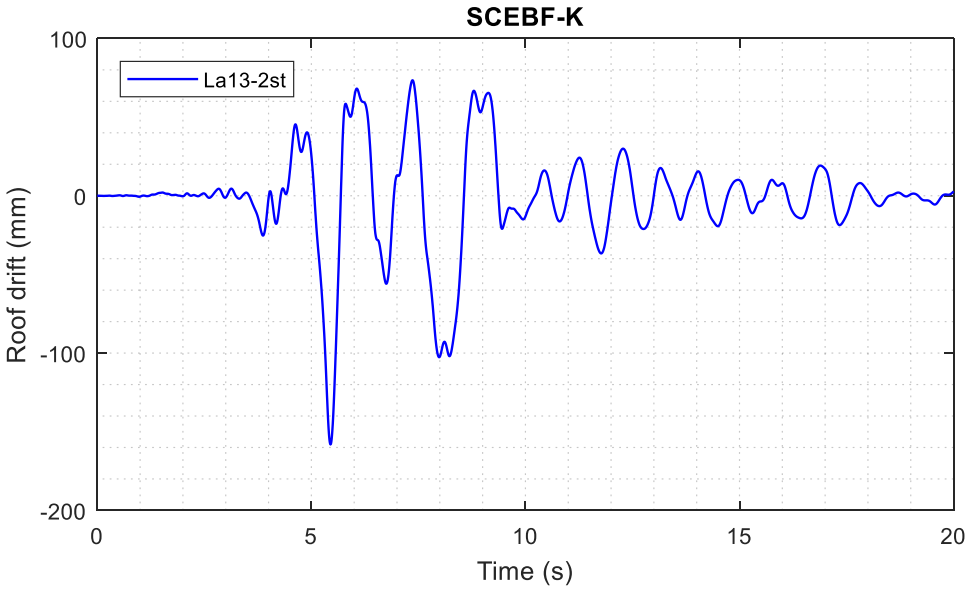

Figure 5.27 Second story drift time history for SCEBF-K type

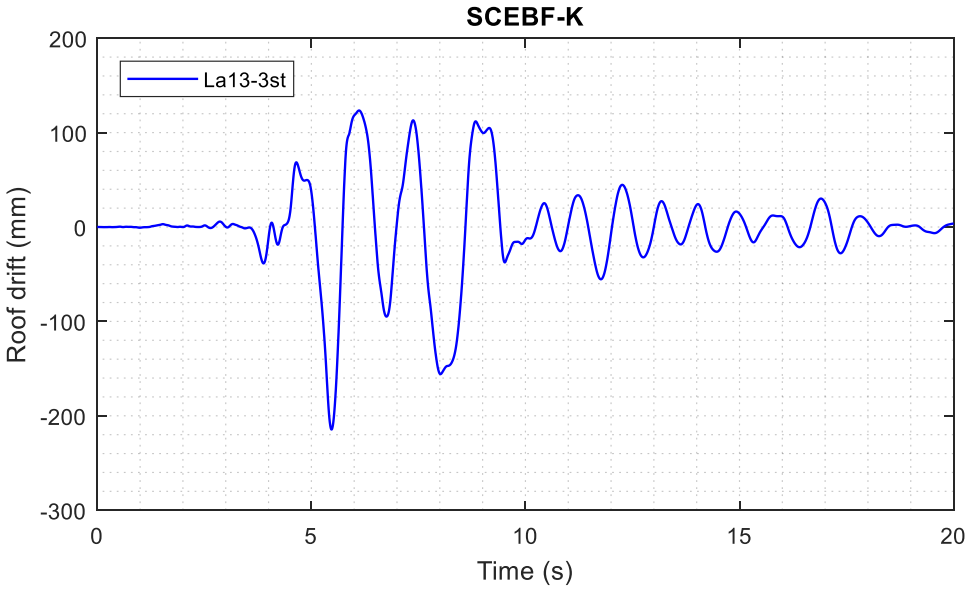

Figure 5.28 Third story drift time history for SCEBF-K type

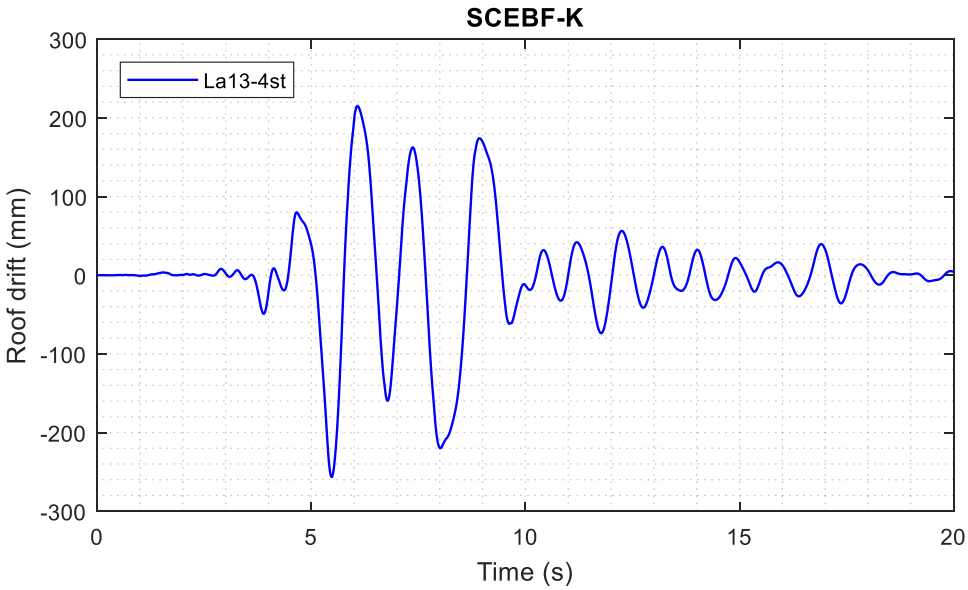

Figure 5.29 Fourth story drift time history for SCEBF-K type

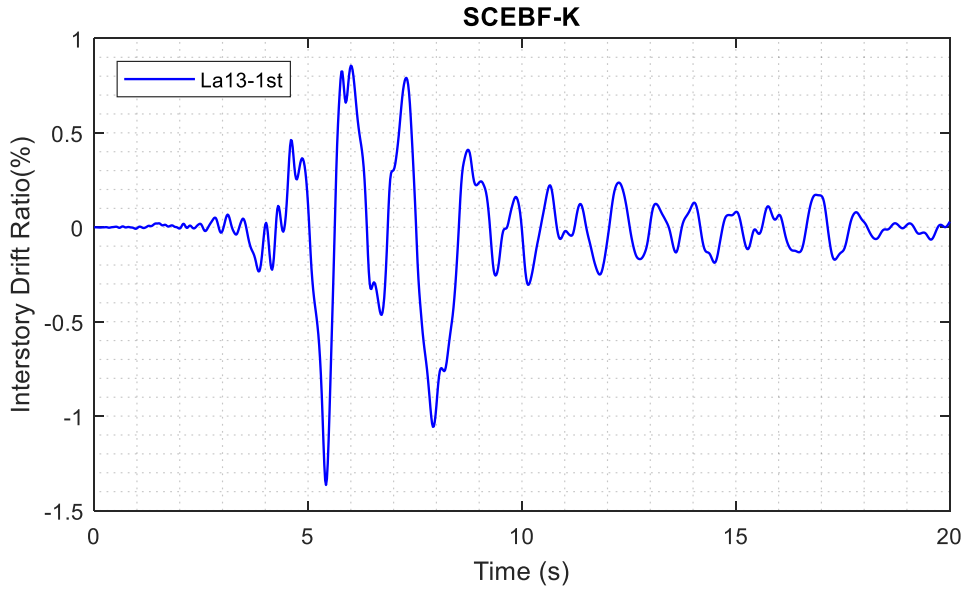

Figure 5.30 First story inter-story drift ratio-time history for SCEBF-K type

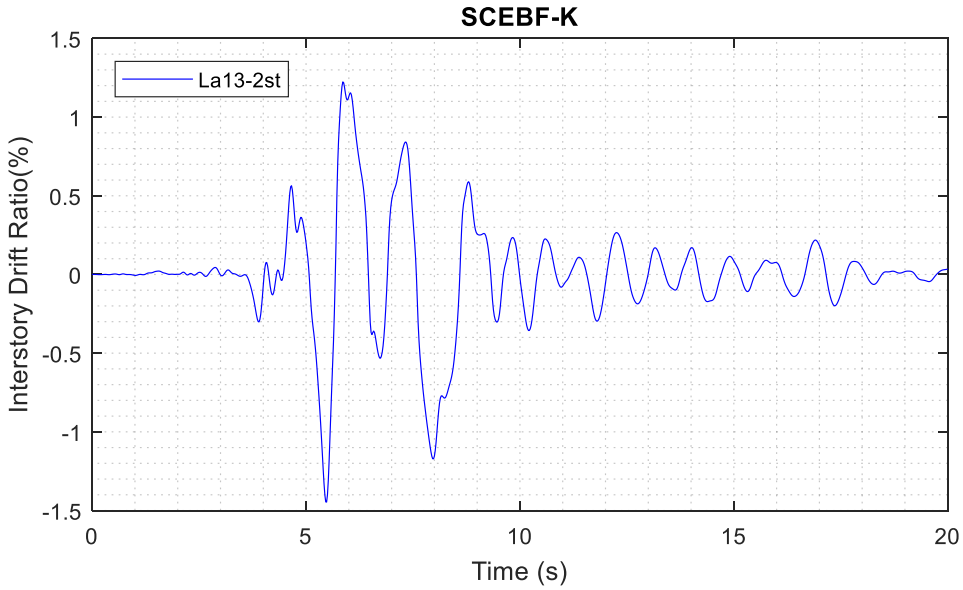

Figure 5.31 Second story inter-story drift ratio-time history for SCEBF-K type

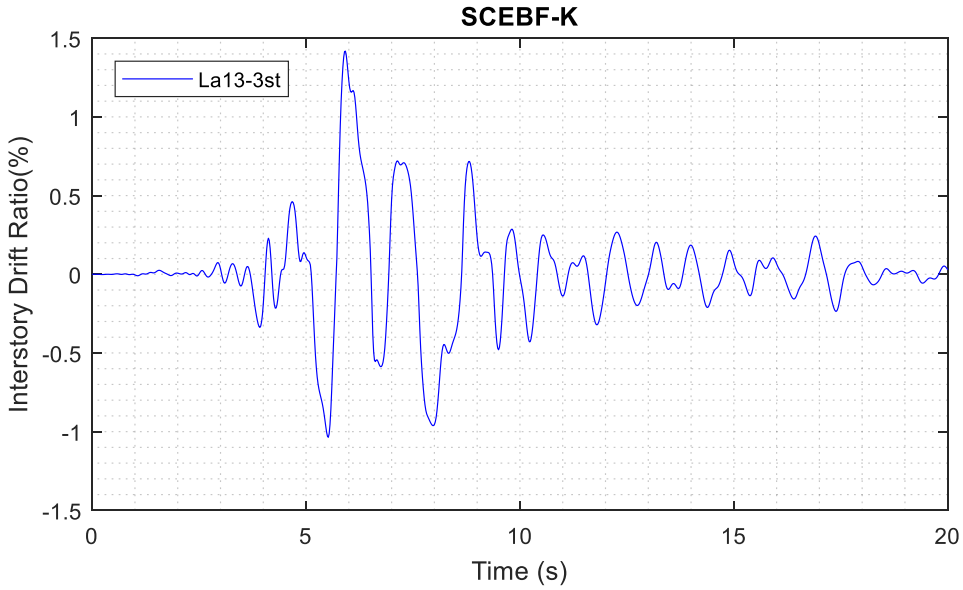

Figure 5.32 Third story inter-story drift ratio-time history for SCEBF-K type

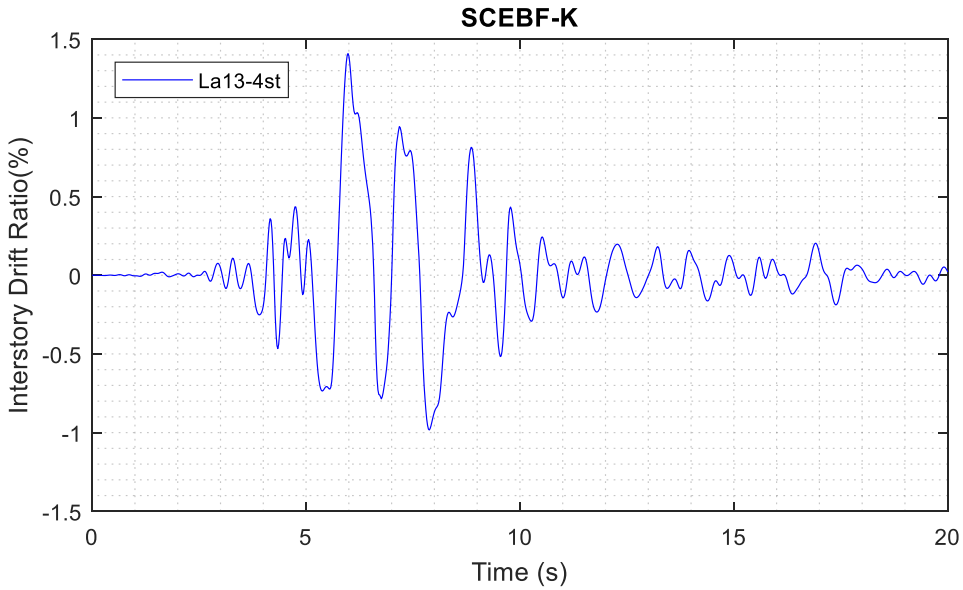

Figure 5.33 Fourth story inter-story drift ratio-time history for SCEBF-K type

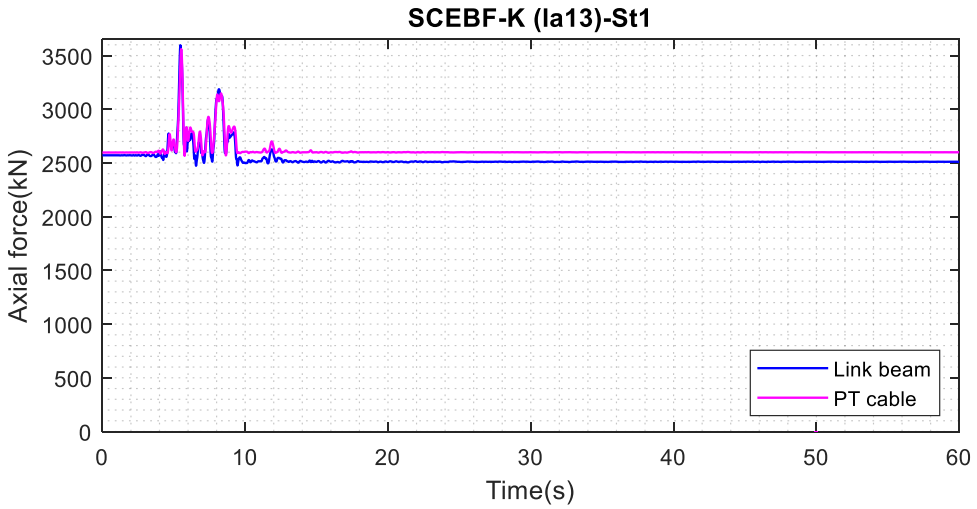

Figure 5.34 Axial force time histories of link beam and PT cable for 1st story of SCEBF structures for SCEBF-K structures under La13

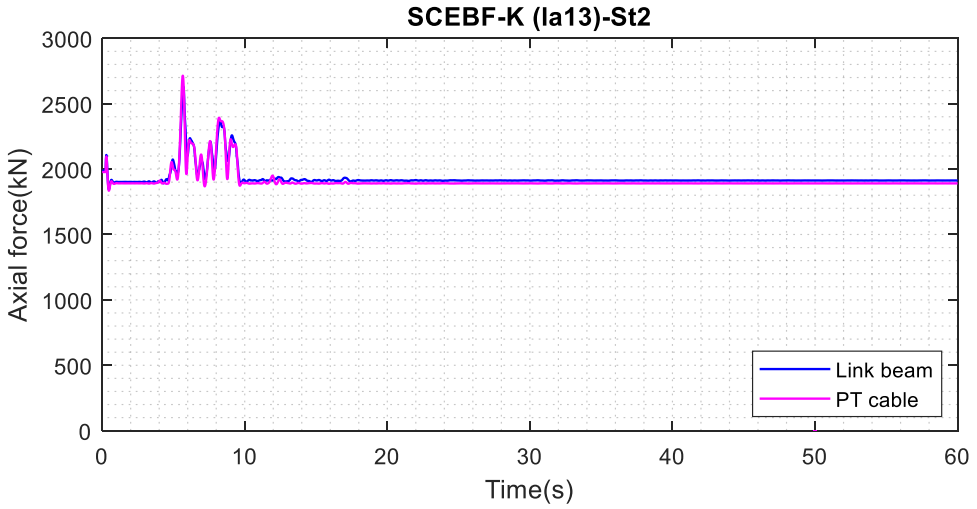

Figure 5.35 Axial force time histories of link beam and PT cable for 2nd story of SCEBF structures for SCEBF-K structures under La13

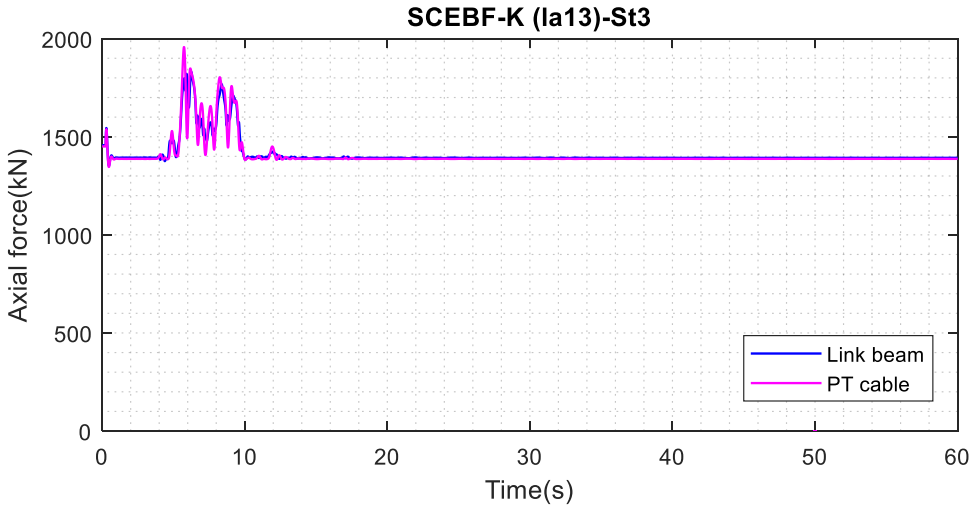

Figure 5.36 Axial force time histories of link beam and PT cable for 3rd story of SCEBF structures for SCEBF-K structures under La13

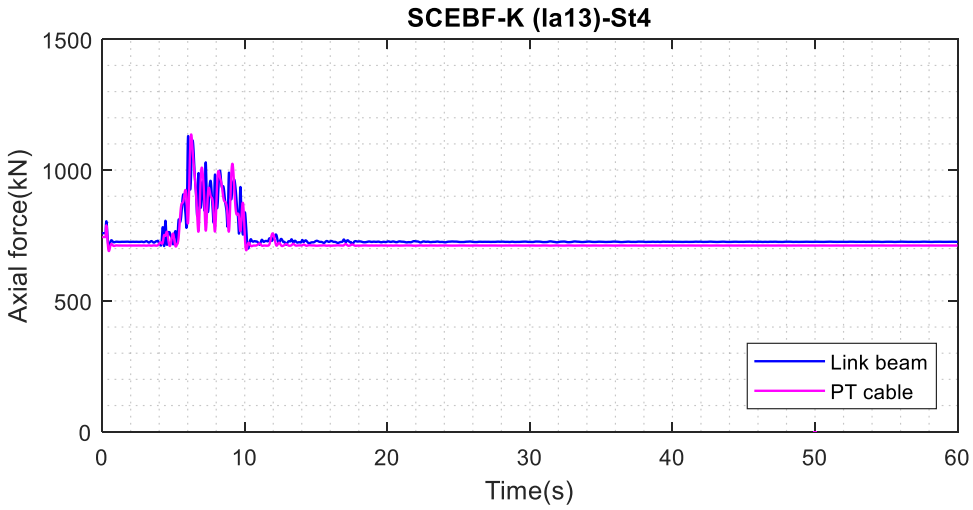

Figure 5.37 Axial force time histories of link beam and PT cable for 4th story of SCEBF structures for SCEBF-K structures under La13

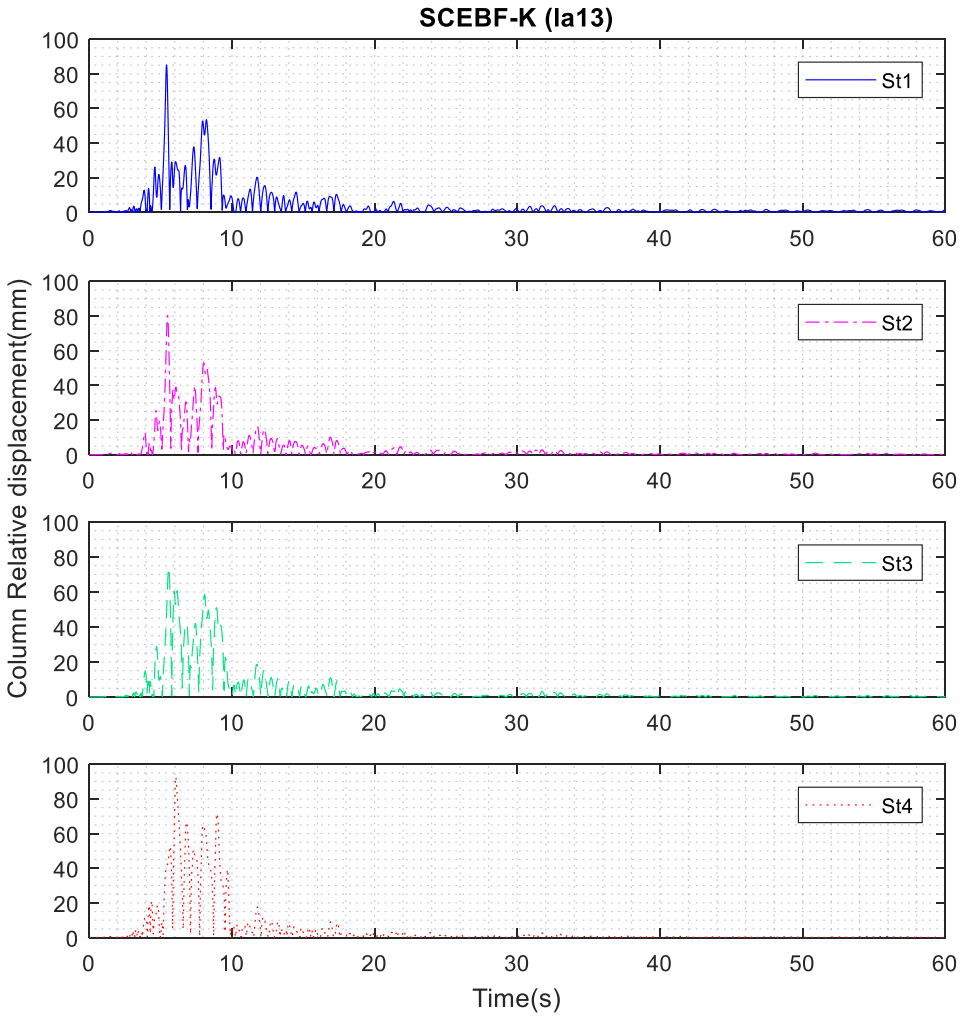

Figure 5.38 Column relative displacement for K-type SCEBF

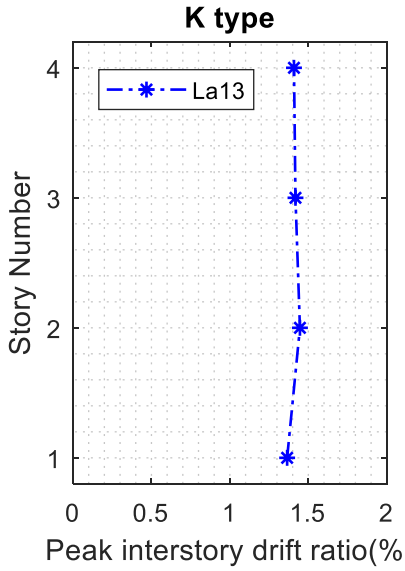

Figure 5.39 Peak inter-story drift ratio for K-type SCEBF

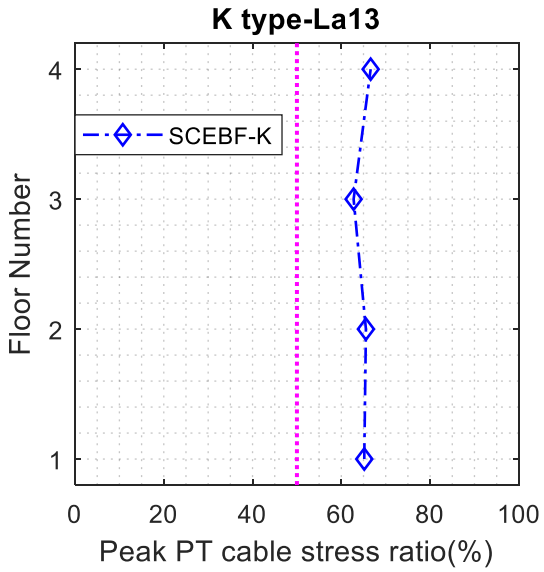

Figure 5.40 Peak PT cable stress ratio for SCEBF-K type

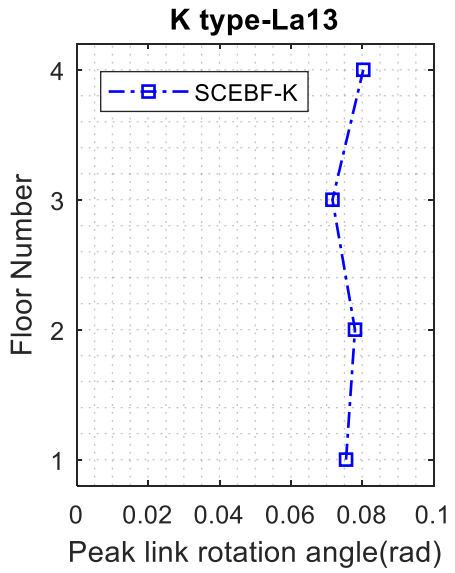

Figure 5.41 Peak link rotation angle for SCEBF-K type

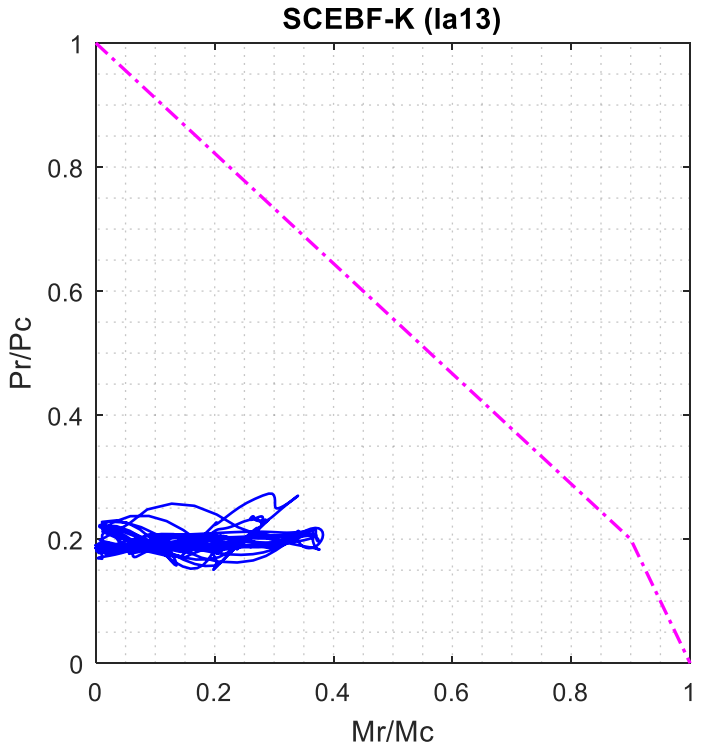

Figure 5.42 P-M interaction curve of rocking link beams for K-type SCEBF

Chapter 6 Seismic Performance Evaluation of Y-type SCEBF

In this Chapter, the seismic performance evaluation of Y-type SCEBF has been investigated and compared with D-type CEBF. Moreover, analytical formulas to design SCEBF-Y type structure is also presented. Furthermore, Y-type SCEBF has been investigated by nonlinear static analysis and nonlinear time history analysis.

6.1 Analytical Formulation of SCEBF-Y Structural Property and Seismic Design

Design of a SCEBF-Y prototype building is described in this section. The analytically derived structural properties and seismic design of SCEBF-Y module frames are presented in the following section.

6.1.1 Properties of SCEBF-Y Module Frame

SCEBF-Y consists of an eccentrically braced frame connected to the primary frame through a rocking link. The skeleton force vs. displacement curve of the SCEBF-Y frame can be defined by three key parameters: (1) initial stiffness of SCEBF-Y before gap opening happens, K_{b_0}; (2) post-gap-opening stiffness of SCEBF-Y, $K_{b_{PGO}}$; (3) gap opening shear force, V_{b_0}. Since SCEBF-Y module frame can be inserted into EBFs, stiffness and story shear expressions of a one-story SCEBF-Y module frame are formulated below. Figure 6.1 shows the dimensions of this one story SCEBF-Y module

frame. In this SCEBF-Y module frame, beam's end moments are released by using simple connections to eliminate the stiffness contribution of the primary frame. However, in practical design, the beam end connections do not need to be simply connected.

As shown in Figure 6.1, h, a, L_d, L, e and Δ denote the frame height, beam half-length, brace length, beam length, rocking link length and frame lateral drift. In the following formulation, I_c, I_d, I_l express the moment of inertia of column, brace and rocking link respectively. A_{wd}, A_{wl} and A_d also show the web cross-sectional area of the brace, web cross-sectional area of rocking link and cross-section area of the brace respectively. F_{PT_0}, A_{PT}, L_{PT} and E_{PT} denote the post-tensioning (PT) cable's initial force, cross-section area, length and Young's modulus respectively, while t_{f_l} and d_l express the rocking link flange thickness and section depth. E and G are the Young's modulus and shear modulus of steel. The initial stiffness of the SCEBF-Y module frame (K_{b_0}) in Figure 6.1 can be expressed as,

$$K_{b_0} = K_f + K_{l_0} \qquad \text{Equation 6.1}$$

where K_f represents the primary frame stiffness. K_{l_0}, which consists of three terms K_d, K_l and K_r, denotes the rocking link initial stiffness.

$$K_{l_0} = \left(\frac{1}{K_d} + \frac{1}{K_l} + \frac{1}{K_r}\right)^{-1} \quad \text{Equation 6.2}$$

$$K_d = \frac{1}{\frac{1}{K_{da}} + \frac{1}{K_{df}}} \quad \text{Equation 6.3}$$

$$K_{da} = 2E\left(\frac{A_d}{L_d}\right)\left(\frac{a}{L_d}\right)^2 \quad \text{Equation 6.4}$$

$$K_{df} = \frac{2a^2 E A_d}{e(h-e)L_d} \quad \text{Equation 6.5}$$

$$K_l = \frac{1}{\frac{1}{K_{l_s}} + \frac{1}{K_{l_f}}} \quad \text{Equation 6.6}$$

$$K_{l_s} = \frac{GA_{wl}}{e} \quad \text{Equation 6.7}$$

$$K_{l_f} = \frac{3EI_l}{e^3} \quad \text{Equation 6.8}$$

$$K_r = \left(\frac{e(h-e)L_d}{2a^2 E A_d} + \frac{e^2(h-e)^2}{2a^2 E A_d L_d} + \frac{e^2 L_d}{6EI_d} + \frac{e^2}{2L_d G A_{wd}}\right)^{-1} \quad \text{Equation 6.9}$$

K_{l_s} and K_{l_f} represent the rocking link shear and flexural stiffness respectively, while K_l denotes the frame stiffness due to rocking link deformation. K_r and K_d expressions represent the brace/link assembly's rotational stiffness and brace stiffness respectively. Bracing-link assembly refers to a strut beam element extending the PT cable from the rocking link. K_{df} denotes the module frame's stiffness contributed by brace flexural deformation, while K_{da} denotes brace axial stiffness. K_{da}, K_{df} and K_r can be developed based on principal virtual work theory as shown in Figure 6.2.

The gap-opening story shear of the SCEBF-Y module frame (see Figure 6.4 for V_{b_0} location in hysteresis curve) is expressed as,

$$V_{b_0} = V_{l_0} + K_f\left(\frac{V_{l_0}}{K_{l_0}}\right)$$ Equation 6.10

V_{l_0} is derived to represent the rocking link's gap opening shear force, and $\left(\frac{V_{l_0}}{K_{l_0}}\right)$ denotes the SCEBF-Y module frame's drift when gap opening occurs. Usually the first term in Equation 6.10 is much greater than $K_f\left(\frac{V_{l_0}}{K_{l_0}}\right)$, thus $K_f\left(\frac{V_{l_0}}{K_{l_0}}\right)$ can be neglected in calculating V_{b_0} value.

$$V_{l_0} = \frac{\mathrm{F}_{PT_0}(d_l - t_{f_l})}{2e}$$ Equation 6.11

where F_{PT_0} denotes the initial pre-tensioning force of PT cable. From Figure 6.3(a), gap opening occurs when tension stress (σ_T) in the link flange created by overturn moment $V_{l_0} \times e$ reaches the compressive stress (σ_C) created by the PT cable pre-tensioning force. Since only the rocking link flanges are in contact with the supporting surface (by removing part of the link web material), rocking link section area (A_l) is assumed to be equal to rocking link flange section area (A_{lf}), i.e., $A_{lf} \approx A_l$; similarly, for calculating gap opening force purpose only, moment of inertia of the rocking link can be calculated as,

$I_l \approx 2(\frac{A_{lf}}{2})(\frac{d_l - t_{f_l}}{2})^2$

Rocking link post-gap opening shear force is also derived based on Figure 6.3(a). PT cable would extend by $[(\frac{d_l - t_{f_l}}{2})\frac{\Delta}{e}]$ at gap opening, and its axial force would also increase correspondingly. By increasing the PT cable force, the rocking link's shear

force would also increase. Post-gap-opening stiffness of the SCEBF-Y ($K_{b_{PGO}}$)is calculated as,

$$K_{b_{PGO}} = K_{l_{PGO}} + K_f \quad \text{Equation 6.12}$$

and

$$K_{l_{PGO}} = \frac{A_{PT}E_{PT}}{L_{PT}e^2}\left(\frac{d_l - t_{f_l}}{2}\right)^2 \quad \text{Equation 6.13}$$

$$V_{l_{PGO}} = V_{l_0} + K_{l_{PGO}}\,\Delta \quad \text{Equation 6.14}$$

$$V_{b_{PGO}} = V_{l_{PGO}} + K_f\,\Delta \quad \text{Equation 6.15}$$

where $K_{l_{PGO}}, K_{b_{PGO}}, V_{l_{PGO}}$ and $V_{b_{PGO}}$ denote the rocking link post-gap-opening stiffness, SCEBF-Y post-gap-opening stiffness, rocking link post-gap opening shear force and SCEBF-Y assembly post-gap opening lateral force respectively.

Three critical design parameters mentioned above can be adjusted by appropriate design of rocking link, and PT strands. The behavior of the SCEBF-Y before the gap opens, mostly depends on brace axial and flexural deformation and it is independent of PT cables. However, as soon as the gap opens, the geometry of SCEBF-Y changes and rocking behavior of the link starts to dominate the frame deformation. As a result, the post-gap opening stiffness of the SCEBF-Y is controlled by PT cable area and length along with the rocking link height and depth.

Failure mode of conventional EBF which is related to plastic behavior of link depends on link length. However, in SCEBFs, links must remain elastic through design basis earthquake. In SCEBF-Y, the only part of the structure dissipating earthquake energy

is the fuse device - RHD devices. RHD devices limit frame lateral drift and dissipate energy through their inelastic behavior. After earthquake, they can be replaced rapidly.

In Figure 6.3(b), RHD device has shear force of V_{FD} and axial force of P_{FD} which is directly applied to the rocking link; as a result, RHD device's shear force contribution to the story shear of SCEBF-Y module frame can be calculated as,

$$V_{b_{FD}} = V_{l_{FD}} = \frac{V_{FD}(d_l+2h_{FD})+2P_{FD}w}{e} \quad \text{Equation 6.16}$$

Based on Figure 6.3(b), the effect of RHD devices on SCEBF-Y is mostly depended on plastic shear force of fuse devices (V_{FD}) which is directly applied to the fuse holders connected to the link (see Figure 6.13).

The idealized lateral force versus displacement response of SCEBF-Y (Figure 6.4) is a combination of responses of bare frame SCEBF-Y and replaceable hysteretic damping devices (RHD devices), which is characterized by a flag-shaped hysteresis curve that is typical of self-centering systems. The RHD devices provide partial strength to the SCEBF-Y module frame and the primary energy dissipation, whereas the PT connections provide the re-centering capabilities. After gap opening (Event 1 in Figure 6.4), the vertical RHD devices continue to resist additional load until its yielding (Event 2), after which the lateral stiffness is greatly reduced. Upon unloading (Event 3), the gap closes again.

The self-centering eccentrically braced frame has a flag-shaped force-displacement hysteresis curve which is a combination of responses of the SCEBF and RHD devices. The sum of the SCEBF-Y stiffness and RHD devices stiffness is the total stiffness of

SCEBF-Y with RHD devices. Partial stiffness, strength, and energy dissipation for the self-centering frame are also provided by RHD devices, and the re-centering capability of the SCEBF-Y frame is achieved by PT strands.

6.1.2 Comparison of Finite Element Analysis and Analytical Results

To validate the above-derived analytical formulas which define the hysteresis curve of a SCEBF-Y module frame, two finite element models have been built in both SAP2000 and ANSYS software respectively. It is worth noting that the finite element models have been calibrated using the experimental test data for a similar one-story D-type SCEBF module frame specimen with RHD devices [9, 50]. The ANSYS model of this SCEBF-Y module frame is shown in Figure 6.5. The red circle denotes the gap opening story shear of the SCEBF-Y module frame. The details of the structural section's properties of this SCEBF-Y module structure can be found in Table 6.1. In Table 6.1, $d,\ w,\ t_f, t_w$ represents I-section depth, flange width, flange thickness and web thickness respectively. For simplicity, column bases are pinned at their bases and support beam (the beam member connecting braces to rocking-link) is assumed to be rigid. PT tendons and all primary members except for rocking link were modeled using beam elements while for the rocking-link, support beam and RHD devices, solid elements were utilized. Moreover, eight PT strands each with a cross-section area of 140 mm^2 were considered, and their initial stress level is 45 percent of its yield stress. Each RHD device is comprised of four 18-mm-thick trapezoidal-shaped energy dissipation steel plates (300 mm at a larger width and 200 mm for total length) welded

to a base steel plate. This base plate is bolted to the rocking link beam as shown in Figure 6.13. Steel bracket holders with deep slots are installed to hold the vertical energy dissipation steel plates during link beam rotation.

Primary members of the SCEBF-Y module structure are made of Q345 steel, and the RHD devices' trapezoidal-shaped energy dissipation plates are made of low yield steel Q225LY. For both materials under cyclic loading, the combined plasticity hardening model is defined for the stress-strain relationship based on material coupon test data. The corresponding load versus displacement curve for this SCEBF-Y module frame is presented in Figure 6.6. It shows that the SCEBF-Y's gap-opening shear force (V_{b_0}), initial stiffness (K_{b_0}), post-gap-opening stiffness ($K_{b_{PGO}}$) and fuse devices effect on SCEBF-Y shear force ($V_{b_{FD}}$) from both FE models are in close agreement with the corresponding values predicted from analytical formulas. For this SCEBF-Y module frame without RHD devices, the gap opening force V_{b_0}, initial stiffness K_{b_0} and post-gap opening stiffness $K_{b_{\mathrm{PGO}}}$ values derived from finite element analysis are 194 kN, 51.1 kN/mm, and 2.05 kN/mm for the SAP2000 model, and 205 kN, 43 kN/mm, and 1.8 kN/mm for the ANSYS model respectively, which are in close agreement with the corresponding values (197.8 kN, 54.9 kN/mm, and 2.01 kN/mm respectively) predicted from the analytical formulas in the previous section.

6.1.3 Prototype SCEBF-Y Building

The SCEBF-Y frame seismic design is briefly described here. The target lateral force response of the SCEBF system subjected to seismically induced cyclic loading involves

the limit states related to the PT tendons, fuse devices, and other structural components such as beams, columns, and braces. Potential limit states to consider in the design of the SCEBF-Y structure include: 1) gap opening between the support beam and the rocking link beam; 2) yielding of the fuse devices; 3) yielding of the SCEBF frame members, such as beams, rocking link beam, braces, and columns; 4) yielding of the PT cables; 5) ultimate failure of the SCEBF-Y frame members, such as fuse fracture. Under the design basis earthquake, the installed fuse devices should develop large plastic deformation for seismic energy dissipation. No damage such as inelastic action and buckling would occur to the frame members of the SCEBF structure, such as beams, columns, braces, and the rocking link beam. The building should remain fully operational and be available for immediate occupancy. Therefore, at 2% drift ratio, SCEBF-Y structures are expected to remain elastic except for yielding in the corresponding RHD devices. Based on the FE analysis results, the SCEBF buildings are designed to achieve this goal before the test is terminated at 2% drift ratio.

A 3-story SCEBF-Y steel framed building is designed in this study as the prototype SCEBF building. To compare the seismic responses of 3-story SCEBF-Y and 3-story D-type conventional EBF (CEBF-D) structures, a 3-story CEBF-D building is modified from the original design of the three-story EBF building by Richards and Uang [63] to accommodate the replaceable links in the prototype EBF building, in which braced bay width is reduced to 25 ft in the N-S direction. The same seismic weight value and height of the CEBF-D building are considered in the design of the corresponding SCEBF-Y prototype building since they have the same total floor area; however, the braced bay

width in the N-S direction is reduced to 20 ft. in the SCEBF-Y. SCEBF-Y design is a 6x6 bay building with a total height of 11.9 m (39 ft.) and 36.6 x 54.9 m (120 x 180 ft.) in the building plan, as shown in Figure 6.7 and Figure 6.8. CEBF-D design is shown in Figure 6.9 and Figure 6.10. The seismic weight of the 1st, 2nd and 3rd floor is 9,901 kN (2,226 kips), 9,901 kN (2,226 kips) and 10,827 kN (2,434 kips) respectively. The total seismic weight of the 3-story SCEBF-Y building is thus 30,630 kN (6,886 kips). For simplicity, only the eccentrically braced frames located along the North-South (N-S) direction is considered in this study.

Member sections of the 3-story SCEBF-Y frame in the prototype building and 3-story CEBF-D frame are listed in Table 6.2 and Table 6.3 respectively. Bracing-link assembly refers to a strut member that extends the PT cable from the rocking link. The pre-compression force enabling the rocking action of the link is provided by post-tensioning (PT) cables which are made up of a number of strands (26, 22 and 14 PT strands used for first, second and third story PT cables respectively). Each standard-size PT strand made of ASTM A416GR270 steel has a cross-section area of 140 mm^2. PT cables in each story are connected from the bottom end of rocking link to the top surface of the bracing-link assembly. Bottom surface of the bracing-link assembly is fixed to the intersection of bracings while the top surface of it is free. In the SCEBF-Y structure, PT cables have an initial stress level set to be 35% of its yield stress. Rocking link length is 914.4 mm. Two RHD devices each containing five trapezoidal-shaped low yield steel plates are used for every rocking link. The trapezoidal-shaped low yield

steel plates used in the 1st to 3rd story of SCEBF-Y have their top widths of 152 mm, 130 mm and 84 mm respectively and they all have a thickness of 25.4 mm (1 inch).

A key step in the seismic design of SCEBF-Y structures is designing the PT cable. In designing the PT cables, three primary factors considered are: (1) adjusting the gap opening force to the value desired for the design; (2) PT cable should not yield; (3) PT strands must remain elastic through design level earthquakes; as a result, they should be properly designed to not yield at 2% inter-story drift ratio. The initial PT stress ranges from 35% to 60% of yield stress depending on the adopted PT cable length. Thus, the size of PT cables in each story is calculated mainly based on the gap opening shear force of each rocking link's design story shear as shown in Figure 6.11. For a three-story structure the gap opening shear force of rocking links is calculated as follows derived above:

$$V_{l_{0_i}} = (\sum_{i}^{3} F_i) = \frac{\mathrm{F}_{PT_{0_i}}(d_l - t_{f_l})}{2e}$$

$$\mathrm{F}_{PT_{0_i}} = \frac{2e(\sum_{i}^{3} F_i)}{(d_l - t_{f_l})}$$

where $\mathrm{F}_{PT_{0_i}}$ represent the initial PT cable force of i^{th} story. The size of PT cable in the i^{th} story shall be determined based on $\mathrm{F}_{PT_{0_i}}$ and desired PT strands' initial stress level.

All members of the SCEBF-Y structures such as columns, beams, braces, PT cables and rocking links should be designed in such a way to remain elastic up to the DBE level. Then initial stiffness of SCEBF-Y (K_{b_0}) and post-gap opening stiffness of SCEBF-Y ($K_{b_{PGO}}$) should be examined for drift control. Then, RHD devices need to

be designed in such a way that dissipate a favorable amount of energy and the sum of the SCEBF-Y gap openings force and RHD devices yield load would be equal to corresponding design story shear force. In the self-centering structure concerned here, RHD devices have the role in dissipating energy under seismic excitation and thus concentrate most of the damages to themselves.

6.2 Numerical Modeling of SCEBF-Y Structure

In the following sections, the overall seismic behavior of Y-type self-centering EBF is investigated and compared to a D-type conventional-EBF. In the North-South direction of the building plan, a planar EBF model was established in a general Finite Element analysis software SAP2000 to simulate the nonlinear seismic response behavior of the SCEBF-Y frame. Two separate SAP2000 models have been created and used in this study, first model for the SCEBF Y-type and second one for the CEBF D-type structure. As mentioned earlier, the SAP2000 model was calibrated with both ANSYS model with solid elements for rocking links and RHD devices as well as experimental data of a full-scale SCEBF-D specimen.

Inelastic hysteretic behavior of the link beams controls the seismic performance of conventional EBF-D type (CEBF-D) during a severe earthquake event, while, the seismic performance of self-centering EBF-Y type (SCEBF-Y) mostly depends on the behavior of rocking link and associated RHD devices for energy dissipation. As a result, link beams should accurately be simulated to investigate the nonlinear seismic analysis of EBFs. For modeling the shear links of conventional EBF-D type in

nonlinear FE model, the approach proposed by Ghobarah and Ramadan [23] was used in this study. Schematic view of nonlinear SCEBF-Y FE model composed of the rocking link beam, RHD devices, PT cable is shown in Figure 6.12. It is also presumed that the rotation point of rocking link beam forms at the mid-thickness line of the rocking link's flanges. Therefore, the effective depth of the rocking link would be equal to rocking link depth minus one rocking link flange thickness. A special link element called "gap element" is used to simulate the gap opening behavior of rocking link. Gap elements are located at the rotation point of the rocking link. Moreover, to simulate the plastic behavior of RHD devices, a nonlinear beam element with tapered section and 20 plastic hinges for each segment of the element is employed, as shown in Figure 6.12.

Nonlinear beam-column elements were used to model braces, columns, and beams of SCEBF-Y frame. A992 Gr50 steel was used to model braces, columns, and beams; and A416Gr270 and Q225LY steel were utilized for PT strands and RHD devices, respectively. A lean-on column along the height of the structure has been modeled and connected through rigid link element to the SCEBF-Y frame. At each floor level, floor masses are lumped onto the corresponding lean-on column nodes. In the SCEBF-Y frame, the lean-on columns are pinned at their bases, however, first story columns are fixed at their bases. The beams' end moments are released but braces' end moments only released at their top not at their bottom, because the rotation of rocking link creates moments needed to be transferred through braces.

A total of eight EBF bays are placed in the N-S direction of the prototype 3-story SCEBF-Y building. Therefore, one-eighth of the total seismic mass is considered for the single frame SCEBF-Y model. Rayleigh damping with 5% damping ratio assigned to the first and second mode is used in the FE model. The first three vibration periods of the prototype SCEBF-Y building are 0.52 sec, 0.21 sec, and 0.13 sec respectively. First mode vibration response is found to be dominant in the prototype 3-story SCEBF-Y building based on FE analysis results. Therefore, to distribute the base shear along the height of the SCEBF-Y frame for pushover analysis, an inverted triangular vertical load profile [67] is adopted here. Mode shapes of SCEBF-Y are shown in Figure 6.14.

6.3 Nonlinear Static Analysis

The seismic performance of the prototype SCEBF-Y building is investigated through both nonlinear static analysis (i.e., pushover analysis) and nonlinear time history analysis using the afore-mentioned FE model. Pushover analysis provides the elastic and inelastic behavior information regarding deformation, critical load capacity, failure modes, and ductility. Furthermore, pushover analysis also reveals plastic formation pattern at various locations of the structure as the lateral load increases. Performing the pushover analysis requires the proper simulation of plastic hinges at intended locations of structural members. Moreover, to capture plastic hinge behavior, material nonlinearity needs to be assigned to various plastic hinges. Plastic hinges are assigned in shear links and columns bases of CEBF-D, while for SCEBF-Y, plastic deformation in fuse devices and column bases are expected at design basis earthquake.

Lateral loads are applied to the control point of the structure. The control point of the SCEBF-Y and CEBF-D frame are mid-span point of the roof beam and right column roof node respectively. As shown in

Figure 6.15, an approximately inverted triangular shaped lateral load profile was imposed when pushover forces are applied at the designated floor nodes. Horizontal roof displacement divided by the total height of the EBF building is denoted as the roof drift ratio. In the pushover analysis, the lateral load is increased progressively until the control point of EBF structure reaches the 2% roof drift ratio.

The flag-shaped curve of the prototype SCEBF-Y building frame with RHD devices and pushover curve of CEBF-D frame for all braced bays in N-S direction of the building are shown in Figure 6.16. Based on the flag-shaped curve of the SCEBF-Y, residual drift is found to be negligibly small, meaning that the SCEBF-Y structure can re-center itself after earthquake. For CEBF-D structure, post-yield stiffness changes gradually which suggests the initiation of link shear yielding; however, in the SCEBF-Y structure, curved transition from initial stiffness to post-yield stiffness derives from the gap opening behavior of self-centering structures. Pushover analysis also produces information regarding the inelastic behavior and seismic energy dissipation of RHD devices in SCEBF-Y structures. In Figure 6.16, it is also seen the difference of force-displacement hysteresis of SCEBF-Y Vs. CEBF-D. SCEBF-Y has a flag-shaped hysteresis which minimizes residual drift of the structure leading to the re-centering system. Nevertheless, CEBF-D has a bilinear force-displacement hysteresis with a considerable amount of residual drift due to yielding of shear links. Moreover, based

on Figure 6.16, the initial stiffness of the SCEBF-Y system is higher than CEBF-D system. Since, in the SCEBF-Y structure, the primary structural members including link beam, braces, beams, and columns are designed so that they should remain elastic under the design level earthquakes. In Figure 6.16, Label #1 represents the gap opening occurrence at 0.08% roof drift ratio, and Label #2 shows that second-story RHD device starts to yield plastically at 0.16% roof drift ratio. Then, plastic hinge formation of RHD devices in first-story and third-story happen at 0.23%, and 0.18% roof drift ratio respectively. The equivalent "yield" load of the prototype SCEBF-Y structure occurs at 0.19% roof drift ratio when the lateral stiffness of SCEBF-Y frame reduces abruptly. Based on this pushover curve, the Beta factor is about 0.44. Beta factor uses the same definition as that in Reference [52]. The unloading stiffness is the same as the lateral loading stiffness in SCEBF-Y frame, and PT strands are found not to yield even at 2% roof drift ratio in the pushover analysis.

6.4 Nonlinear Time History Analysis: Results and Discussion

Nonlinear time history analysis is conducted to study the seismic response behavior of EBF structures under earthquake ground motion excitation. An ensemble of 20 strong ground motion records scaled to the design basis earthquake level (probability of exceedance of 10% in 50 years) corresponding to downtown Los Angeles [69], California region, are utilized in this study. Details of these 20 earthquake ground motion records can be found from Moghaddasi and Zhang [70]. In time history

analysis, the peak value of the response quantities refers to the maximum absolute value of the corresponding parameters over the entire duration of the seismic record.

6.4.1 General Response

Peak roof drift ratio and residual drift ratio of the prototype three-story CEBF-D and SCEBF-Y structures under 20 earthquake ground motions are shown in Figure 6.17(a) and (b) respectively. The ratio of the peak roof lateral displacement divided by the building height is the peak roof drift ratio, and the residual drift is measured as the average value of the last five seconds response in the time history analysis. The dashed lines in Figure 6.17 denotes the ensemble average value of the peak roof drift ratio and residual drift ratio. The ensemble average value of peak roof drift ratio of the SCEBF-Y and CEBF-D buildings is 1.26% and 1.15% respectively. The ensemble average value of residual drift ratio of the SCEBF-Y and CEBF-D buildings is 0.0007% and 0.304% respectively. The maximum value of both the peak roof drift ratio and peak residual drift ratio for the SCEBF-Y and CEBF-D cases occur under ground motion records La16 and La15 respectively. As anticipated, the average residual drift ratio in SCEBF-Y is negligibly small.

6.4.2 Parametric Study

Self-centering structures can be adjusted separately for equivalent yield strength (gap opening force plus fuse member strength), initial stiffness, post-gap opening stiffness and ductility in a more flexible way than conventional structural systems. For example,

equivalent yield strength is related to the PT cable's initial stress level according to the equations in Section 2. The post-gap opening stiffness of SCEBF is directly related to the stiffness of PT cable. If PT cable section area is maintained constant, the longer the PT cable length, the lower the post-gap opening stiffness would be. To demonstrate the effect of the PT cable properties on the two key structural parameters (equivalent yield strength and post-gap opening stiffness) of the SCEBF-Y structures, a parametric study involving three distinct cases of SCEBF-Y structures is performed here. Using the same prototype SCEBF frames, three SCEBF-Y structures with different values of PT cable length and initial stress level are considered as following,

- Case-A: PT cable initial stress= 35% σ_y, cable length =3.35 m (baseline case)
- Case-B: PT cable initial stress= 50% σ_y, cable length =6.35 m
- Case-C: PT cable initial stress= 60% σ_y, cable length=12.45 m

where σ_y is the yield stress of PT cable, which is 1690 MPa for standard high strength steel strands for pre-stressing applications. Schematic view of the PT cable arrangement in these three cases is shown in Figure 6.18, in which the red lines denote the PT cable. PT cable length used in Case-A and Case-B are within the story height and thus can be pre-installed in a SCEBE-Y module frame. In Case-C, PT cables are connected from the rocking link beam to outer surface of columns. The pushover curves of the SCEBF-Y are shown in Figure 6.19 for Case A, B, and C respectively. Although the equivalent yield strength of each case has roughly 100 kN difference, the case with lowest equivalent yield strength has highest post-gap opening stiffness and vice versa.

Case-A has the lowest equivalent yield strength, thus for Case-A to have the highest post-gap opening stiffness, shortest PT cable length has been selected. On the other hand, Case-C has the highest equivalent yield strength; as a result, for Case-C to have the lowest post-gap opening stiffness, the longest PT cable length was adopted.

Parametric study results of peak roof drift ratio and residual drift ratio for Case-A, B, and C for SCEBF-Y are shown in Figure 6.20(a) and (b) respectively. In all three cases, peak roof drift ratio and residual drift ratio are very close to one another. However, Case-A has higher ensemble average value of peak roof drift ratio and residual drift ratio. Peak drift ratio for all three cases of SCEBF-Y is less than 2% for all 20 earthquake ground motions except for La16. Peak roof drift ratio and residual drift ratio from the time history analysis thus further confirm that SCEBF-Y has the re-centering capability and their damage is primarily confined to RHD devices.

Ensemble average values of the peak inter-story drift ratio along the building height for SCEBF-Y structures are presented in Figure 6.21(a), in which the variation of peak inter-story drift ratio within one standard deviation (correspond to a confidence level of 68.3%) is displayed with horizontal bars. All three cases give very close results.

Peak PT cable stress ratio for all three SCEBF-Y cases along the building height is shown in Figure 6.21 (b). The range of peak PT cable stress ratio within one standard deviation is displayed by the horizontal bars. For the SCEBF-Y structures, the mean value of peak PT cable stress ratio among all three stories is 65%, 65.3%, and 68% for Case-A, B, and C respectively. The largest peak PT cable stress ratio which happens in

Case-A is about 92%. Therefore, PT strands would remain elastic throughout entire design basis earthquake ground motion duration even in Case-A which has the shortest PT cable length.

Figure 6.22 shows the peak base shear force for all three SCEBF-Y cases. In SCEBF-Y, the ensemble average value of peak base shear force for Case-A, B, and C is 1,400 kN, 1,400 kN and 1,450 kN which is consistent with the pushover curves in Figure 6.16. The vertical bars indicate the range of peak base shear force within one standard deviation. Case-A has the widest range of peak base shear force since it has the largest post-gap-opening stiffness but smallest equivalent yield strength among all three cases. On the contrary, Case-C has the narrowest range of peak base shear force because it has the smallest post-gap-opening stiffness but largest equivalent yield strength of all three cases.

Parametric study results suggest that almost all three cases have a similar seismic performance even though they have different gap opening force levels. However, Case-A appears to be a very appealing design configuration for the following reasons. First, the length of PT cable of Case-A is within the story height. Thus it can be prefabricated as a modular infill frame in a steel shop and insert into the designated bays on site while the Case-C requires more site work such as pre-stressing. Second, Case-A demands a fewer number of PT strands and thus less cost compared to the other two cases. Third, initial PT cable stress level and yield strength are the lowest in Case-A among all three cases.

6.4.3 Typical Case

To show the detailed response behavior of SCEBF-Y buildings, time history results for one typical ground motion record in Case-A are presented here. Seismic ground motion La01 is selected for this purpose based on the median roof drift value among 20 ground motion records. The maximum roof drift is 143.9 mm and 115.7 mm for the SCEBF-Y and CEBF-D frames respectively. The roof drift time history of the Case-A SCEBF-Y and CEBF-D buildings under La01 ground motion is shown in Figure 6.23(a). The dotted line in Figure 6.23 (a) denotes the residual roof drift of the SCEBF-Y building, and the dash-dot line represents the residual roof drift of the CEBF-D building. Residual roof drift of SCEBF-Y is 0.2mm, and that of CEBF-D building is 9.27mm.

Based on the La01 ground motion data, peak ground acceleration (PGA) happens at time instant of 11.7 sec. Peak roof drift for both SCEBF-Y and CEBF-D buildings happens at almost the same time instant as the PGA of La01 ground motion. First-story inter-story drift ratio of SCEBF-Y for La01 ground motion is shown in Figure 6.23 (b).

Figure 6.24, Figure 6.25 and Figure 6.26 present first, second and third story drift time history for SCEBF-Y type under La01 respectively.

Figure 6.27, Figure 6.28 and Figure 6.29 show the first, second and third-floor inter-story drift ratios of La01 for SCEBF-Y type respectively. The peak inter-story drift ratios for SCEBF-Y for the first, second and third floor are 0.78%, 1.42%, and 1.6% respectively happening at peak ground acceleration (PGA) of La01.

Figure 6.30 represents peak inter-story drift ratio for SCEBF-Y type under La01 ground motion. It is seen that peak inter-story drift ratios for SCEBF-Y type under La01 are between 0.7% and 1.6%.

The peak inter-story drift ratio for SCEBF-Y is 0.76% which takes place at the PGA time instant of La01 ground motion. Peak PT cable stress ratio along the SCEBF-Y height is displayed in Figure 6.31(a). PT cable initial stress level is 35% for SCEBF-Y as shown by the magenta dot line in Figure 6.31 (a). Peak PT cable stress ratio for the La01 ground motion case varies from 50% in first-story to 71% in third-story cables. The maximum value of peak PT cable stress ratio is 71%; therefore, PT cables would not yield throughout the whole earthquake ground motion record as designed even for Case-A with the shortest cable length.

Figure 6.31(b) displays the peak rocking link chord rotation angle response of this SCEBF-Y building under La01 ground motion. It is seen that the maximum rotation demand of the rocking link varies from 0.03 rad to 0.07 rad. Figure 6.32 shows the first-story rocking link shear force versus rocking link chord rotation angle hysteresis loop of SCEBF-Y under La01 ground motion. Flag-shaped hysteresis loop of the rocking link reaffirms its self-centering behavior.

The seismic performance of the SCEBF-Y buildings under 20 DBE-scaled earthquake ground motions reveal that it has the capability of re-centering itself and RHD devices absorb most of the damages induced by earthquake ground motion while keeping rocking link and other primary structural members elastic (except for column bases

which develop plastic hinges after roof drift ratio exceeds 1.5%). This is appealing because RHD devices can be replaced quickly after strong earthquakes. It is worth noting that recent full-scale experiments on RHD devices demonstrate one set of RHD devices can be replaced in less than half an hour [9, 50].

Table 6.1 Structural member sections of the prototype Y-type self-centering EBF building frame (unit: mm)

Member sections	d	w	t_f	t_w
Beam	400	300	20	14
Column	180	300	20	14
Brace	300	200	15	14
Rocking-link	410	240	30	20
Strut beam	268	200	14	14

Table 6.2 Member sections of conventional 3-story D-type EBF (CEBF-D)

Story	Member sections				
	Braces	Columns with Link Connection	Columns without Link Connection	Collector Beams	Link
1	W14x176	W14x132	W14x61	W18x86	W12x53
2	HSS 14x14x0.625	W14x132	W14x61	W14x82	W10x45
3	HSS 12x12x0.625	W14x132	W14x61	W10x68	W8x31

Table 6.3 Member section size of the 3-story Y-type self-centering EBF frame

Story	Bracing	Column	Beam	PT Strut column	Rocking Link
1	W14x120	W14x132	W21x101	HSS16x16x0.625	W14x211
2	W14x120	W14x132	W21x83	HSS16x16x0.625	W14x193
3	W14x61	W14x132	W21x62	HSS16x16x0.625	W14x145

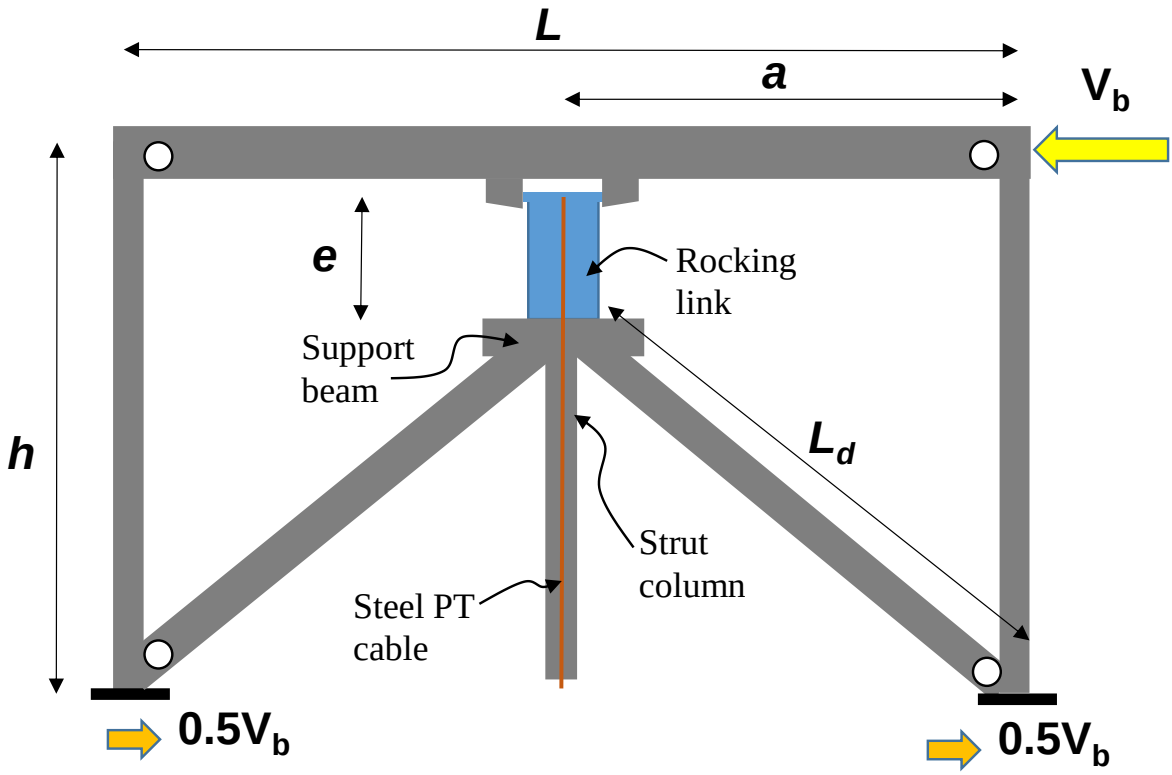

Figure 6.1 Schematic view of SCEBF-Y module structure without RHD devices (circle: simple connection)

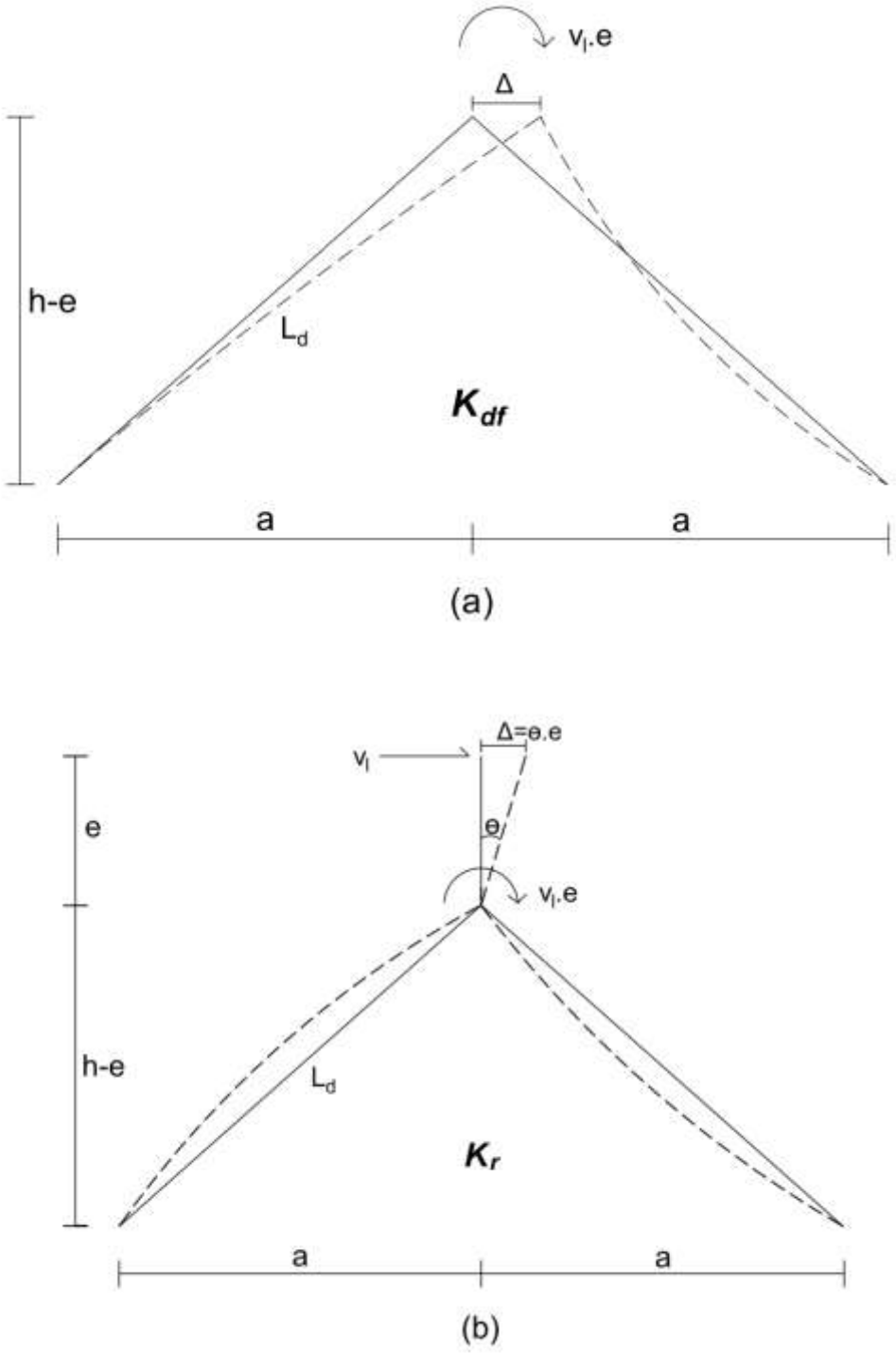

Figure 6.2 SCEBF-Y: (a) K_{df}; (b) K_r

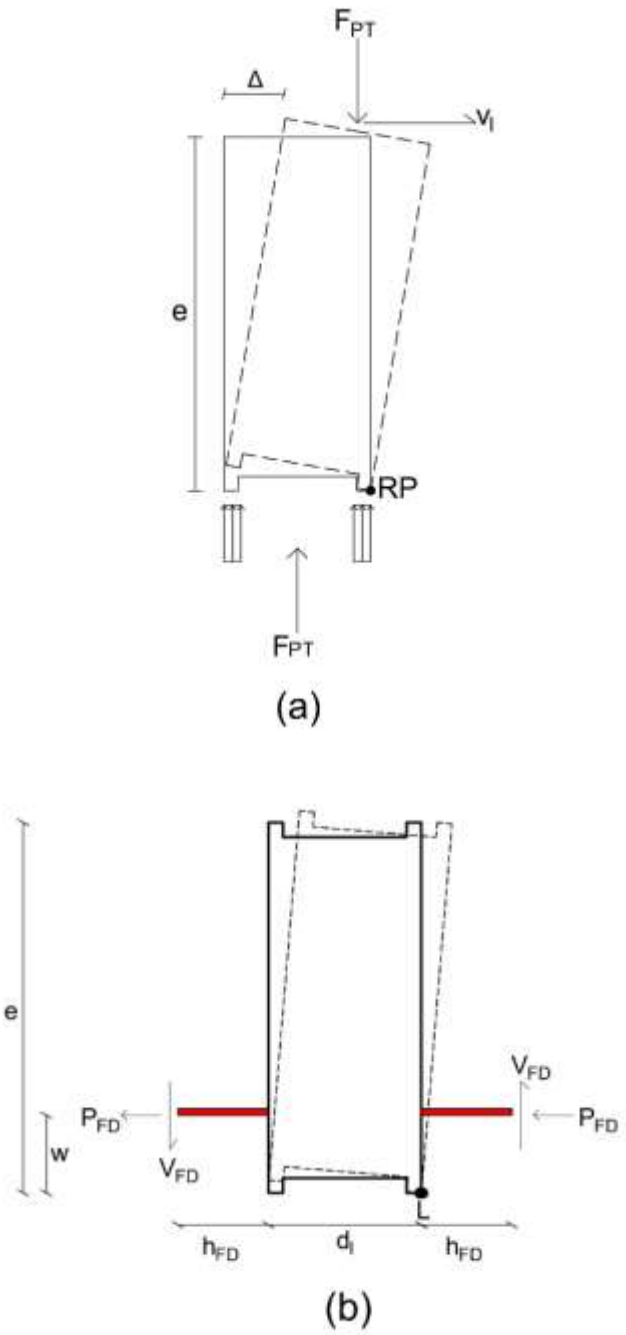

Figure 6.3 SCEBF-Y rocking link shear force component: (a) V_l; (b) $V_{l_{FD}}$

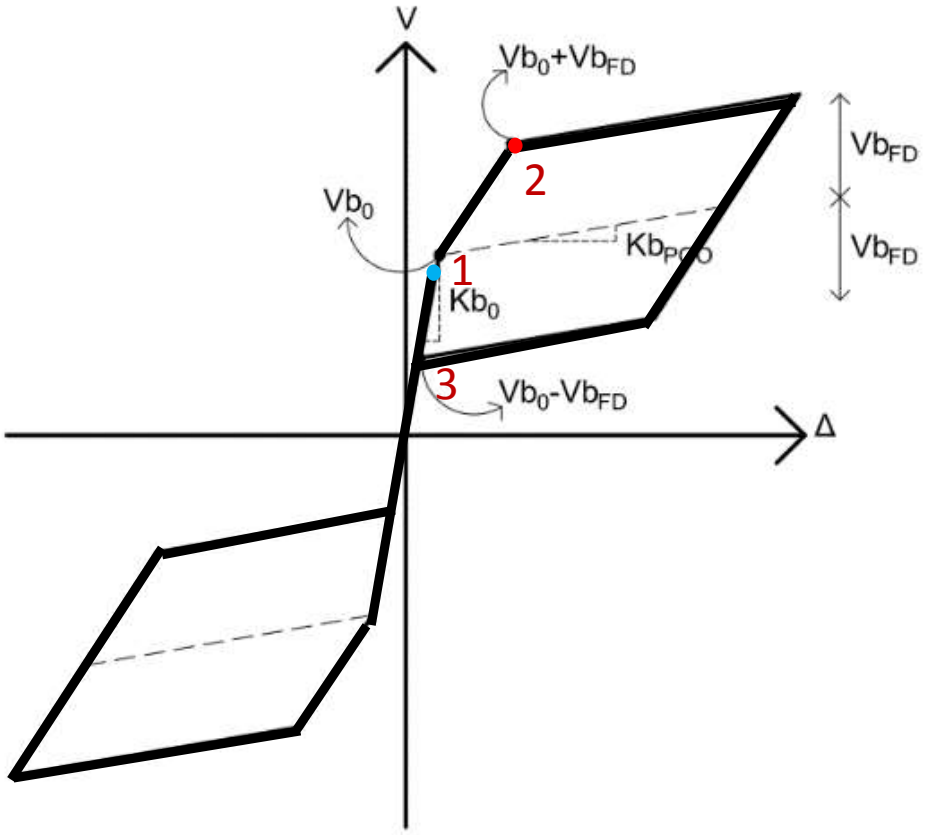

Figure 6.4 Hysteresis loop of SCEBF-Y structure with replaceable energy dissipation devices

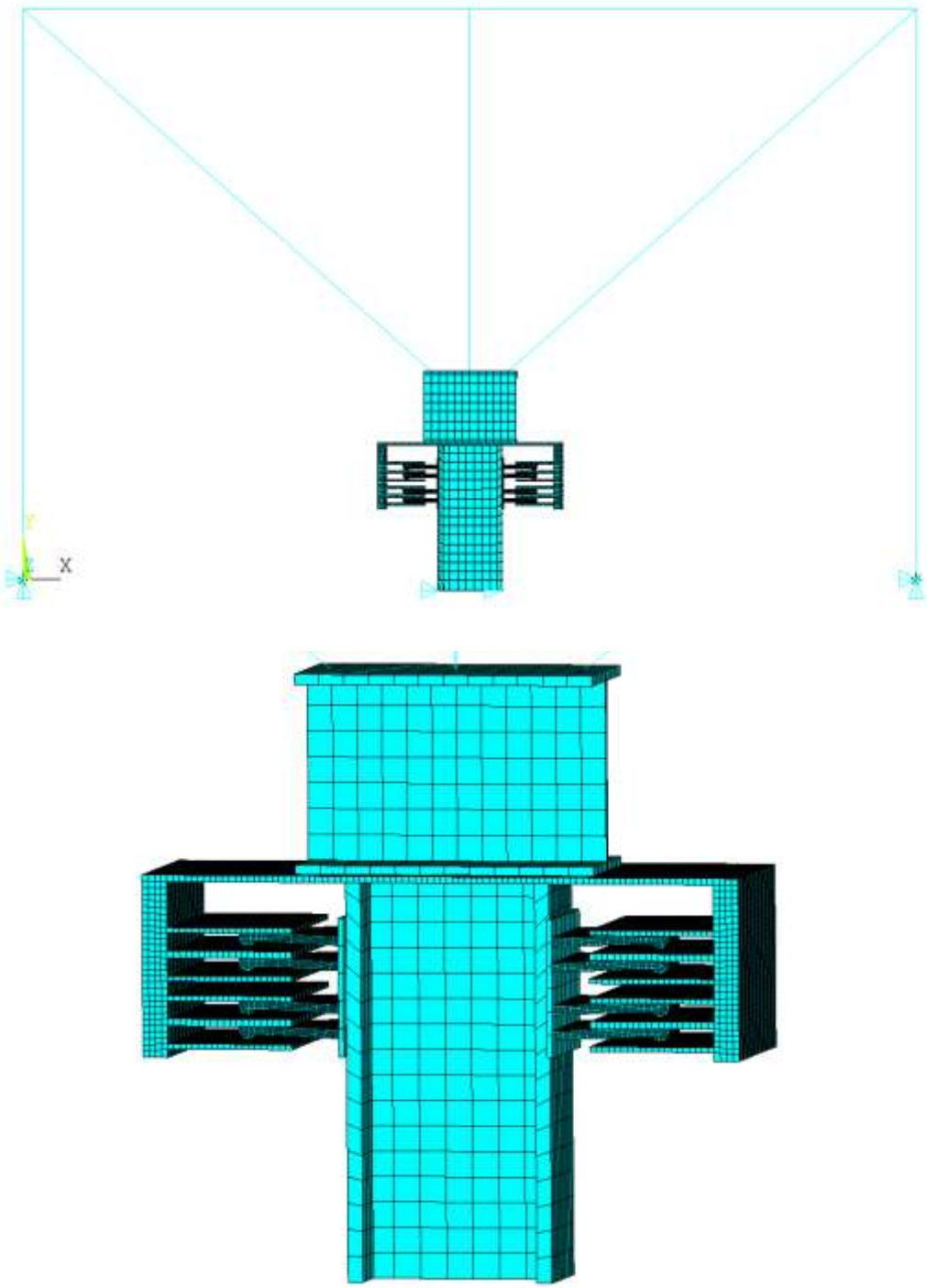

Figure 6.5 ANSYS model of prototype SCEBF-Y

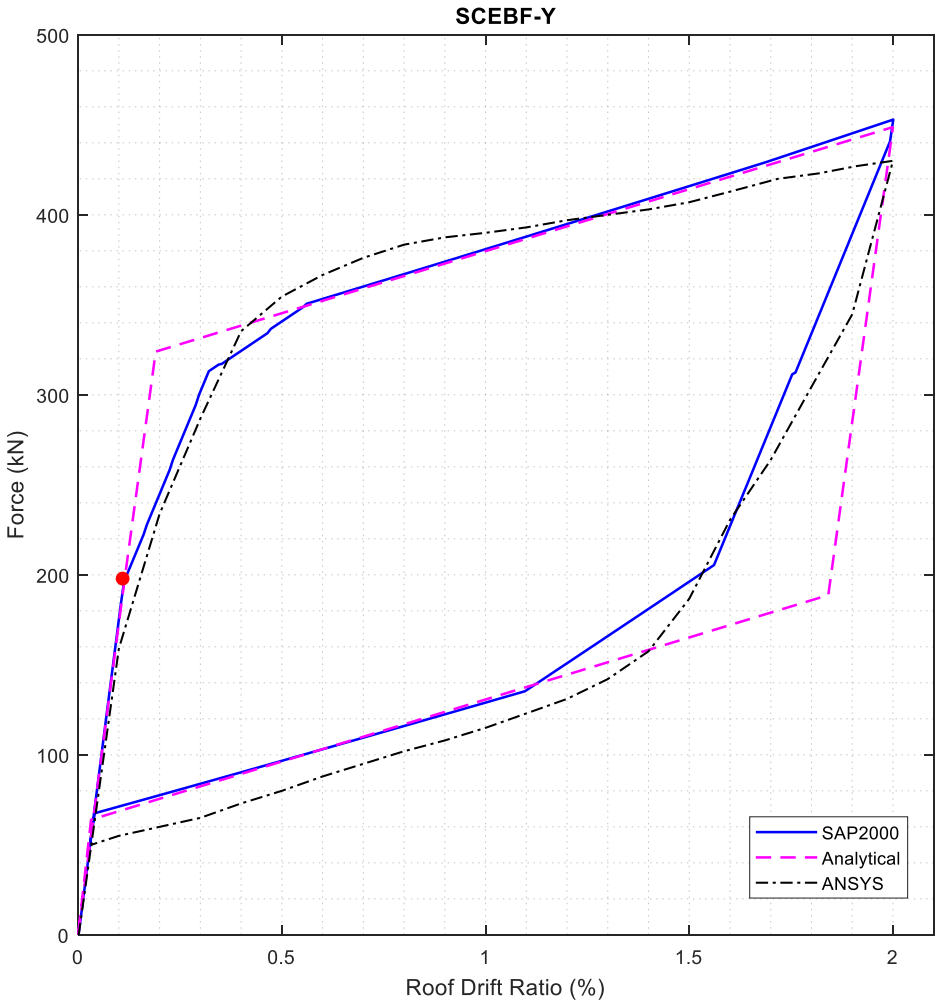

(a) Figure 6.6 Validation of experimental test: Flag shaped curve of SCEBF-Y

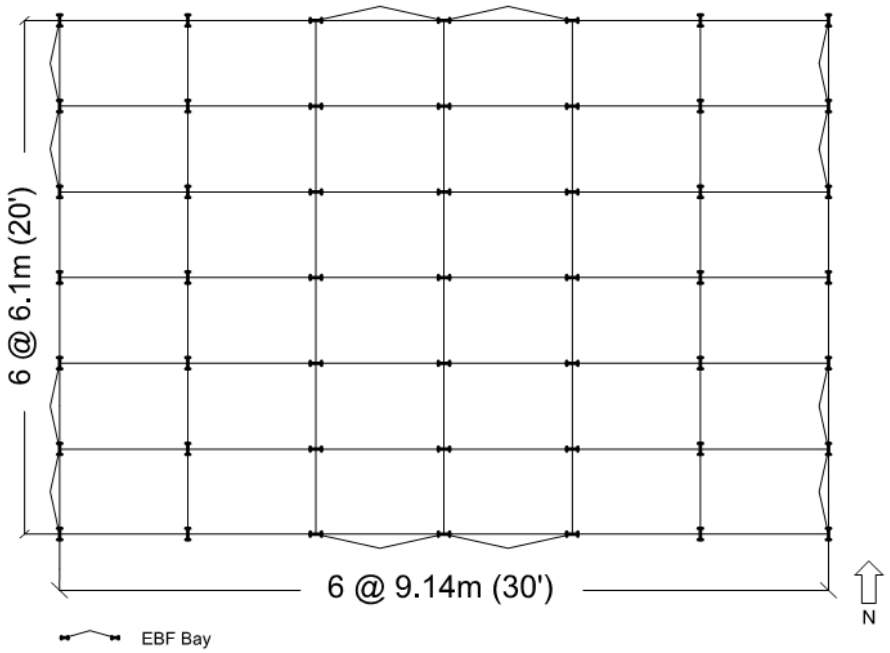

Figure 6.7 Floor plan of 3-story eccentrically braced frame buildings for SCEBF-Y type

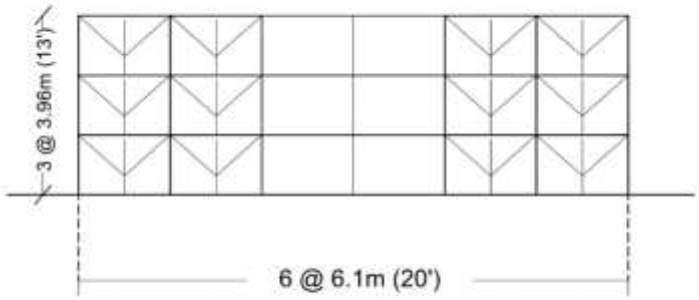

Figure 6.8 Elevation of 3-story eccentrically braced frame buildings for SCEBF-Y type

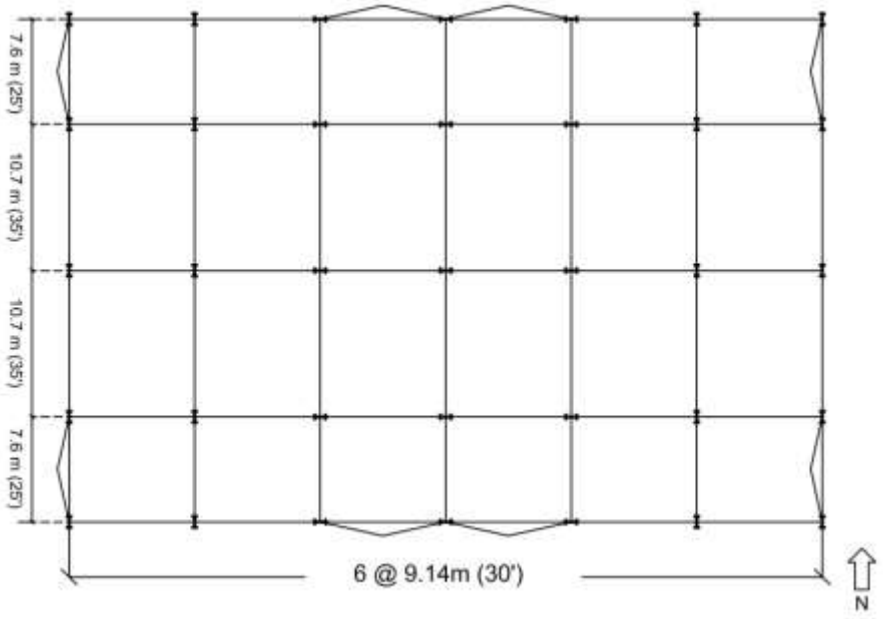

Figure 6.9 Floor plan of 3-story eccentrically braced frame buildings for CEBF-D type

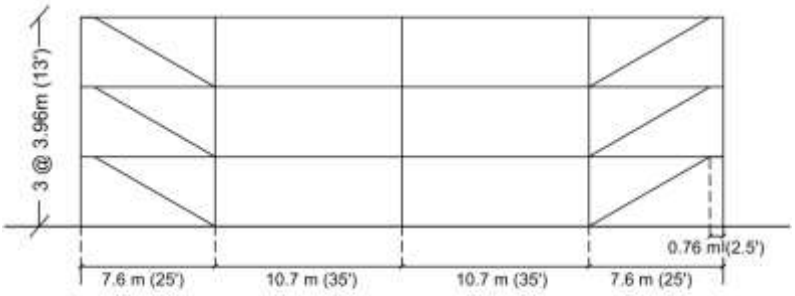

Figure 6.10 Elevation of 3-story eccentrically braced frame buildings for CEBF-D type

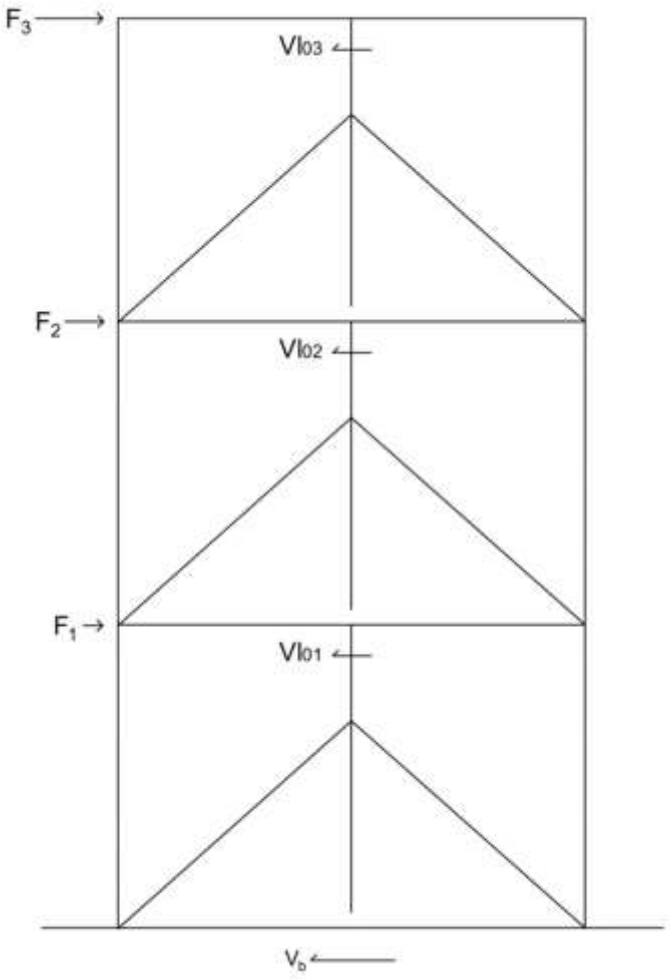

Figure 6.11 PT cable design in a 3-story SCEBF-Y

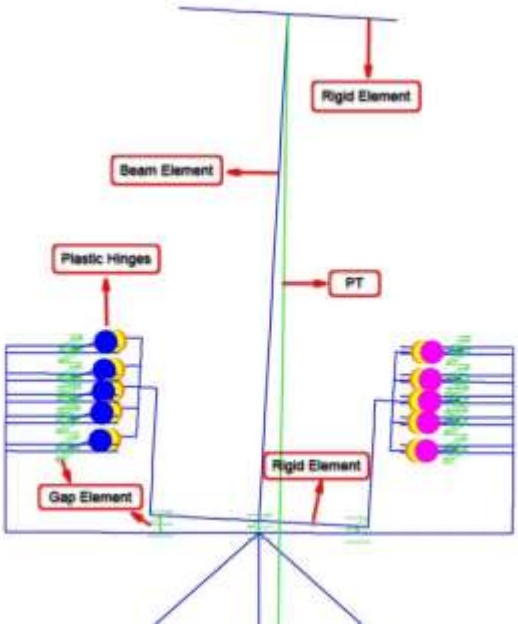

Figure 6.12 RHD devices in SCEBF structure in finite element model

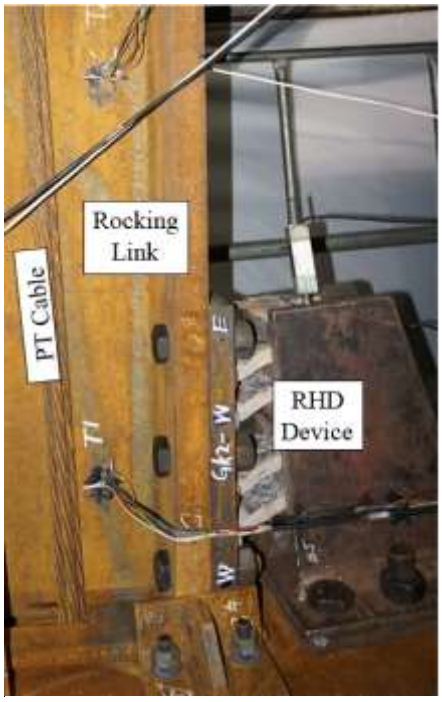

Figure 6.13 Picture of RHD device installed on one side of rocking link in SCEBF structure

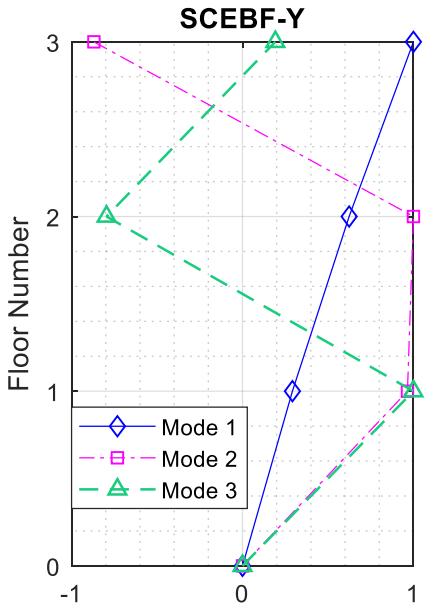

Figure 6.14 Mode shapes of 3-story SCEBF-Y building

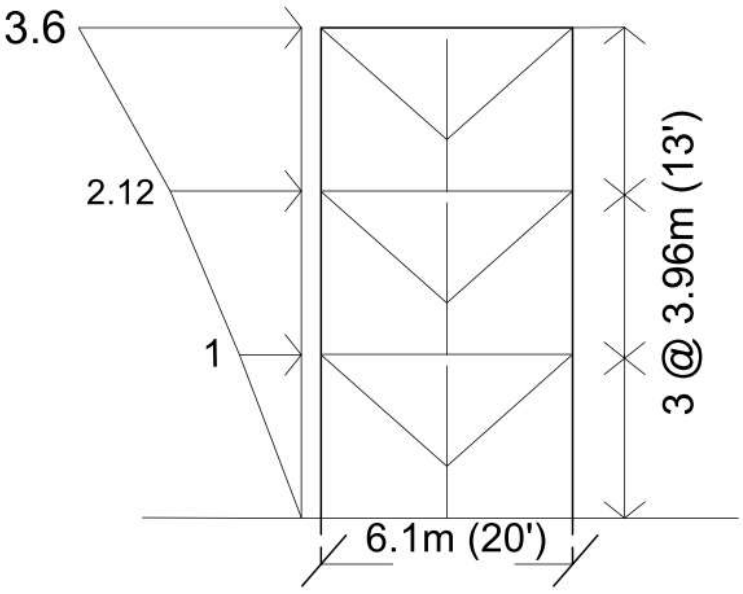

Figure 6.15 Pushover loading protocol for SCEBF-Y frame

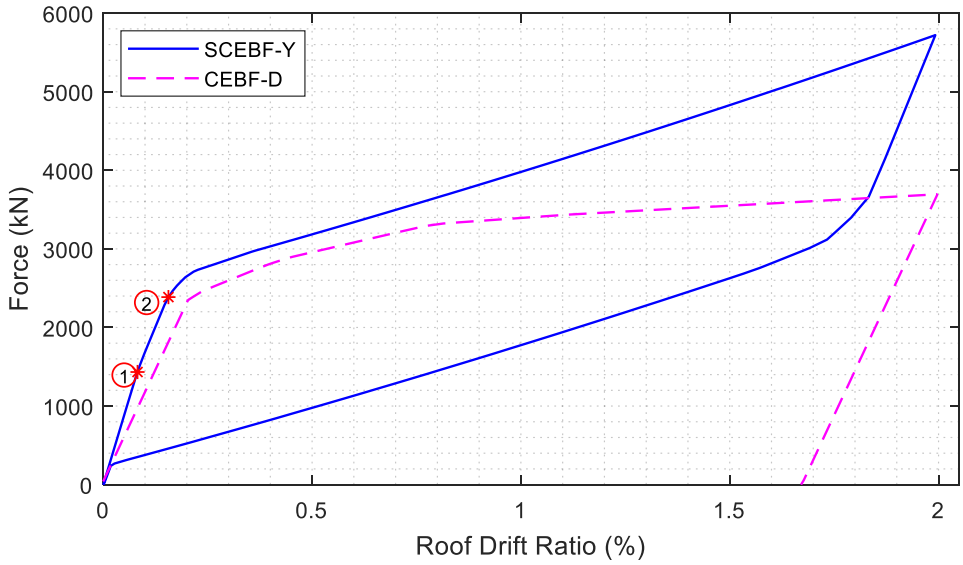

Figure 6.16 Pushover curve of 3-story prototype SCEBF-Y building frame

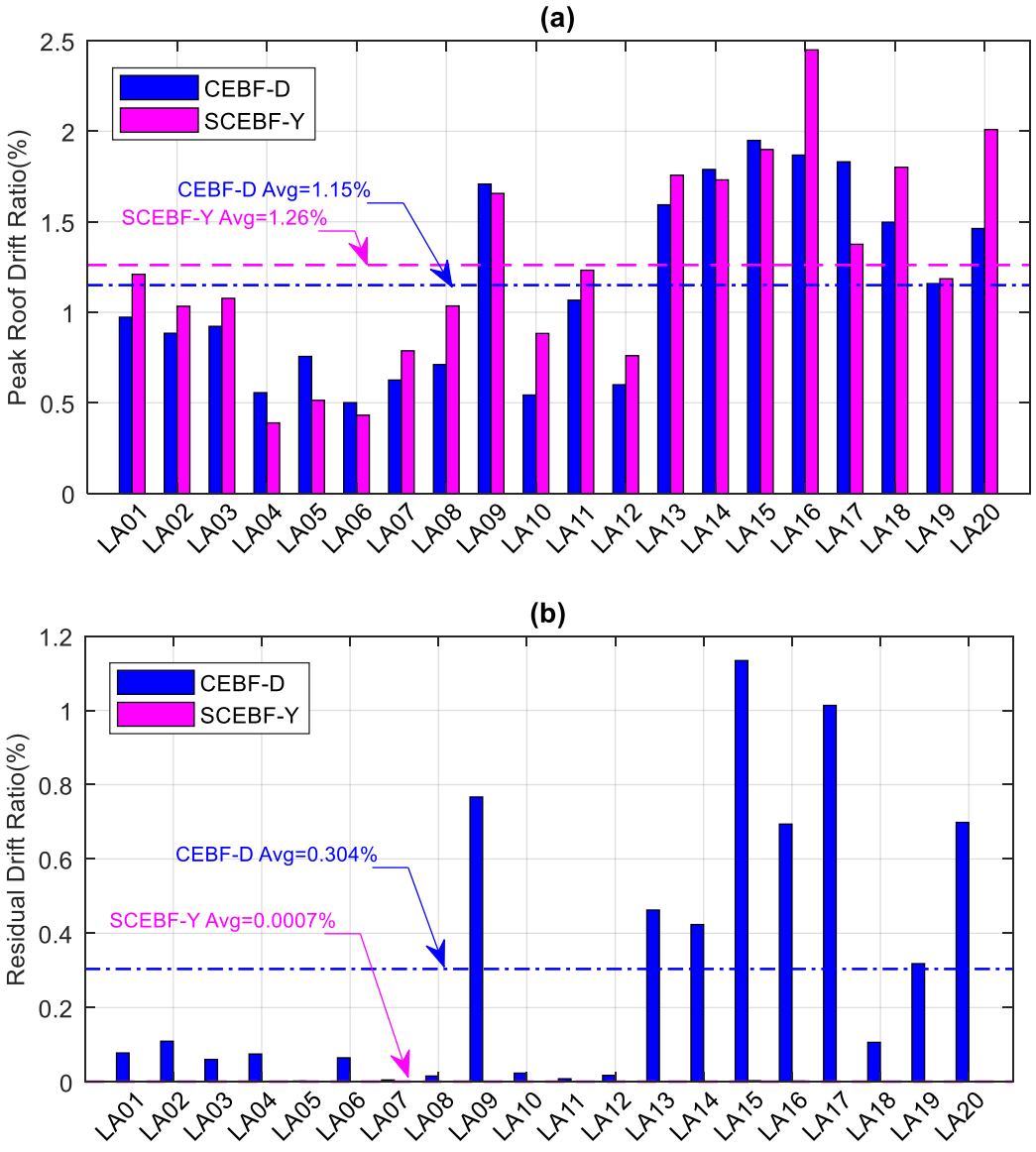

Figure 6.17 Seismic response of SCEBF-Y and CEBF-D buildings under 20 seismic ground motions: (a) Peak roof drift ratio (b) Residual roof drift ratio

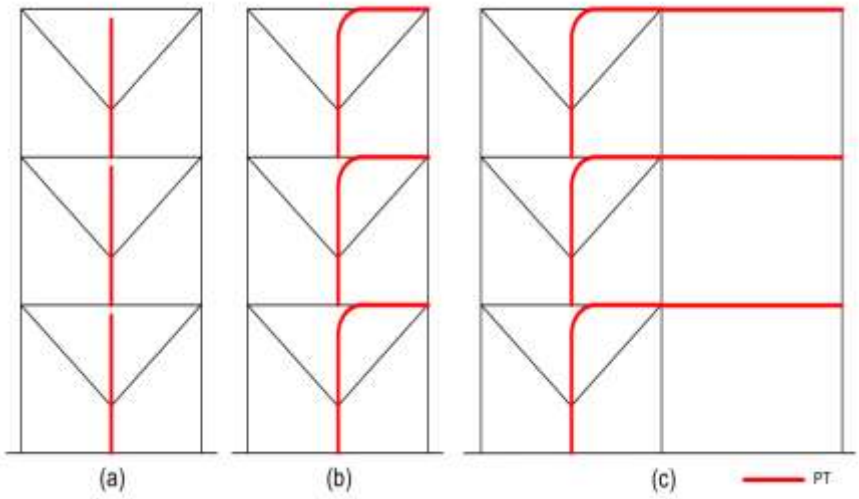

Figure 6.18 PT cable locations in SCEBF-Y models: (a) Case-A; (b) Case-B; (c) Case-C

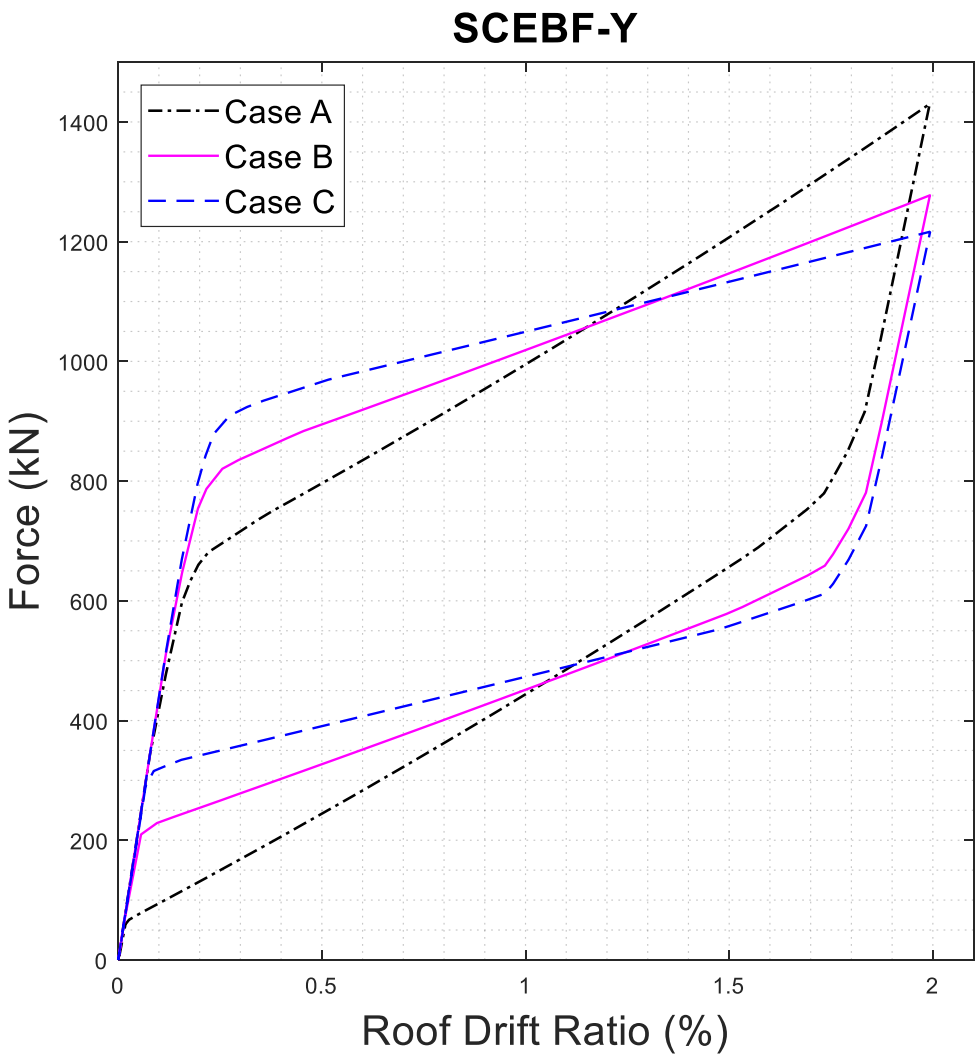

Figure 6.19 Pushover curves of prototype SCEBF-Y frames with varying PT initial stress and length

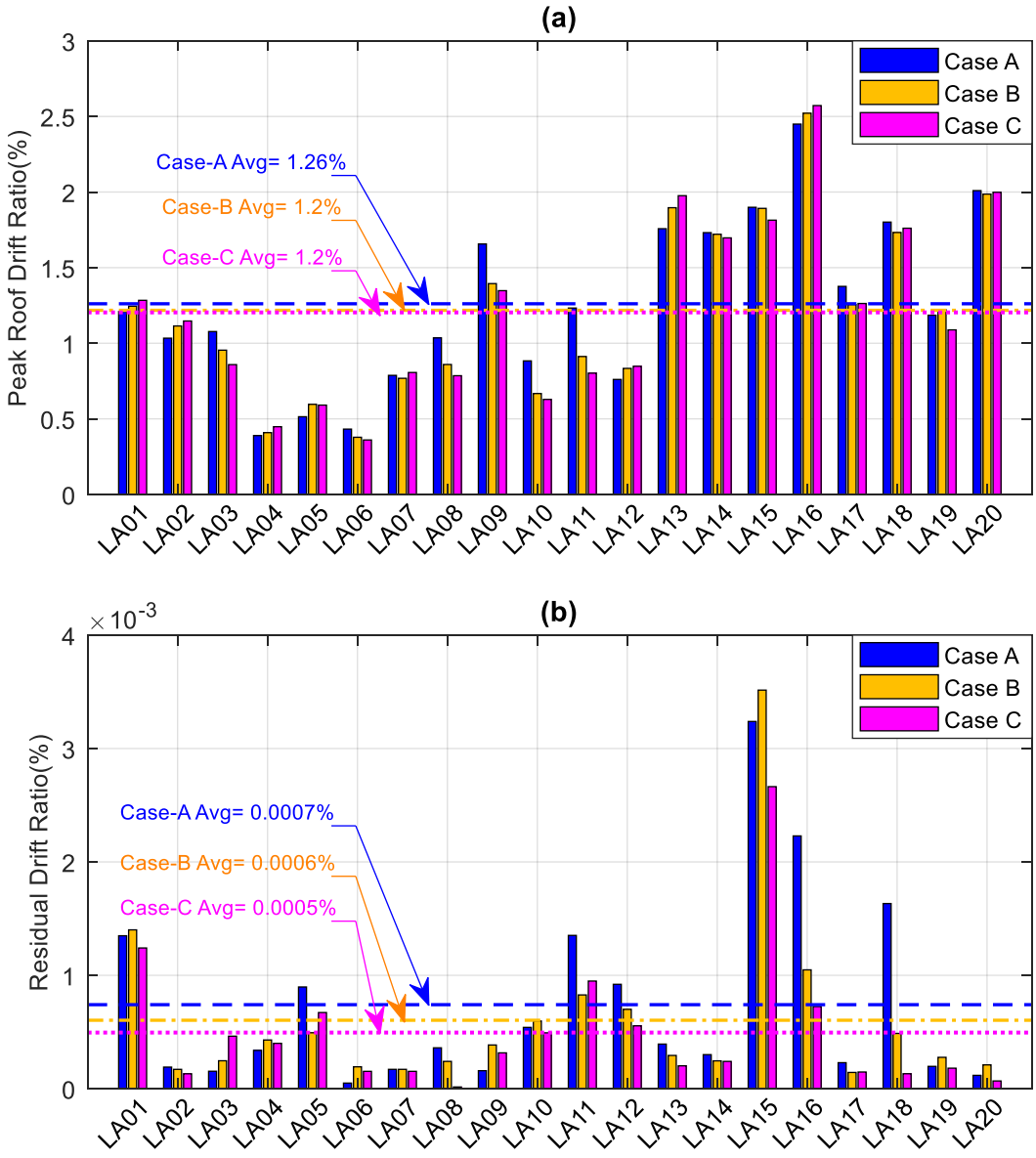

Figure 6.20 Parametric study results of SCEBF-Y under 20 seismic ground motions: (a) Peak roof drift ratio; (b) Residual roof drift ratio

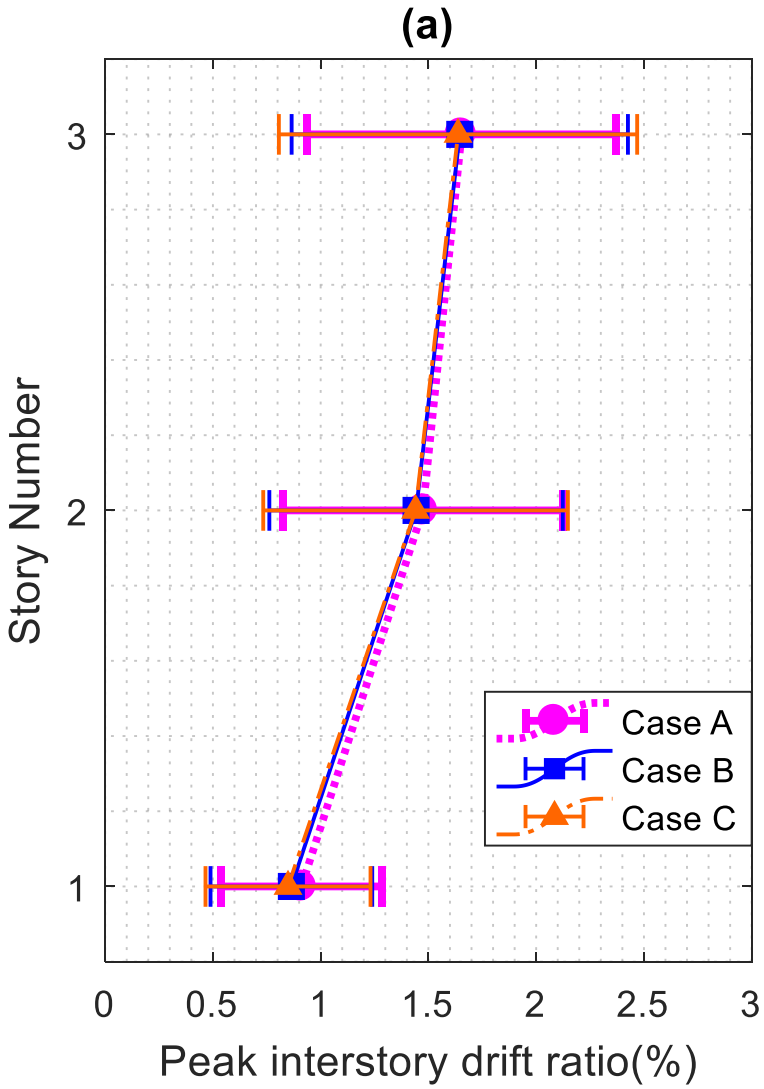
(a)
Story Number
Peak interstory drift ratio(%)
Case A
Case B
Case C
0
0.5
1
1.5
2
2.5
3
1
2
3

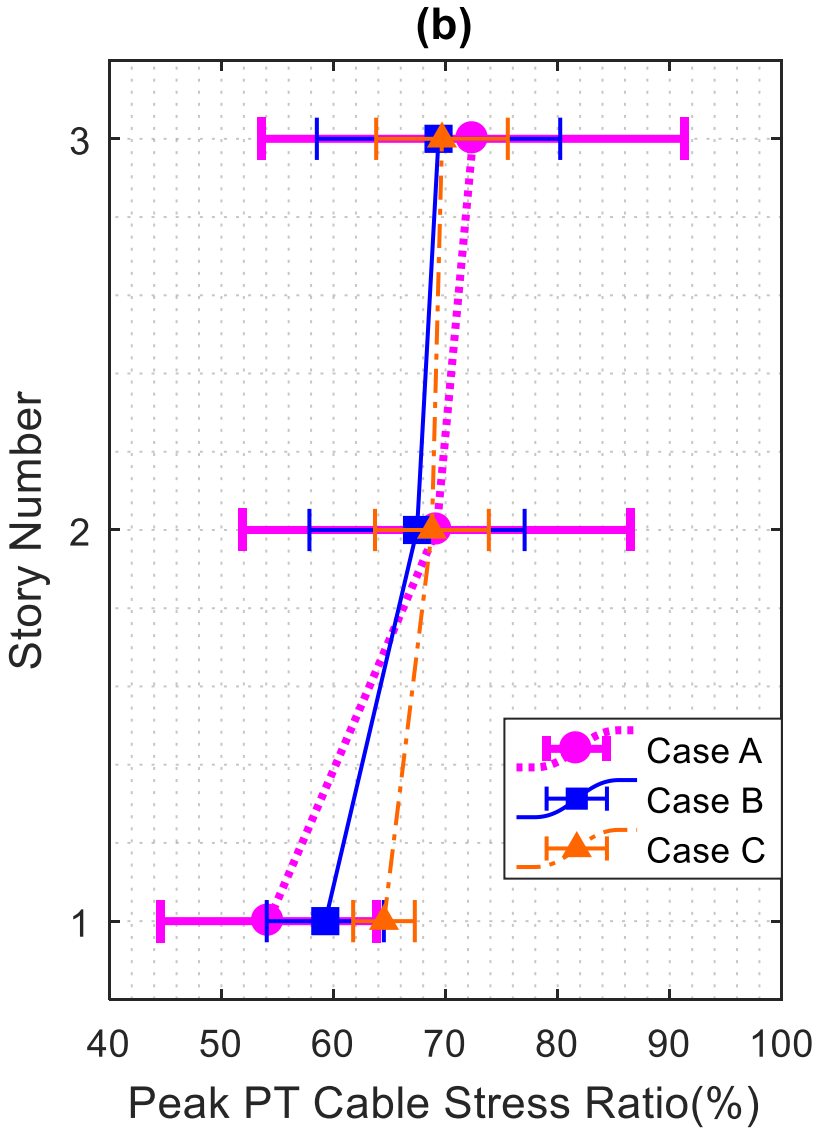

Figure 6.21 Parametric study results of SCEBF-Y under 20 seismic ground motions: (a) Peak inter-story drift ratio range with 68% confidence level (μ± σ); (b) Peak PT cable stress ratio range with 68% confidence level

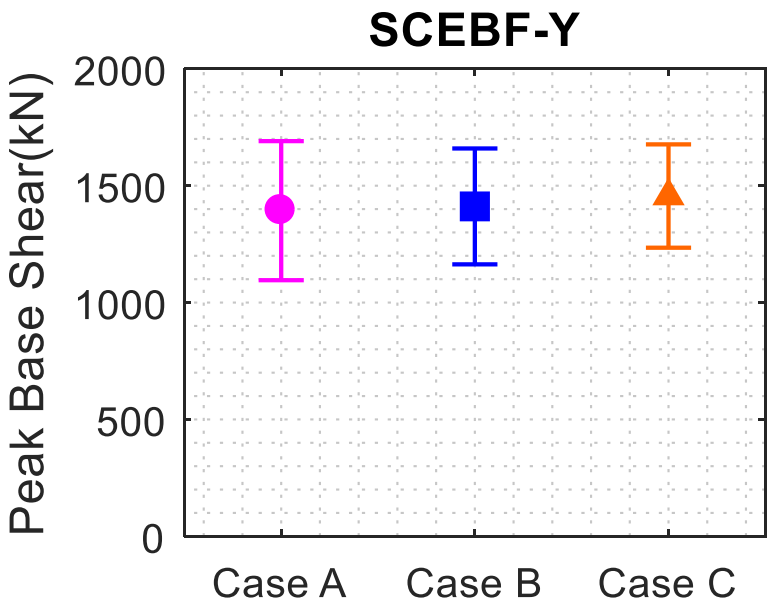

Figure 6.22 Parametric study results: Peak base shear range with 68% confidence level for SCEBF-Y

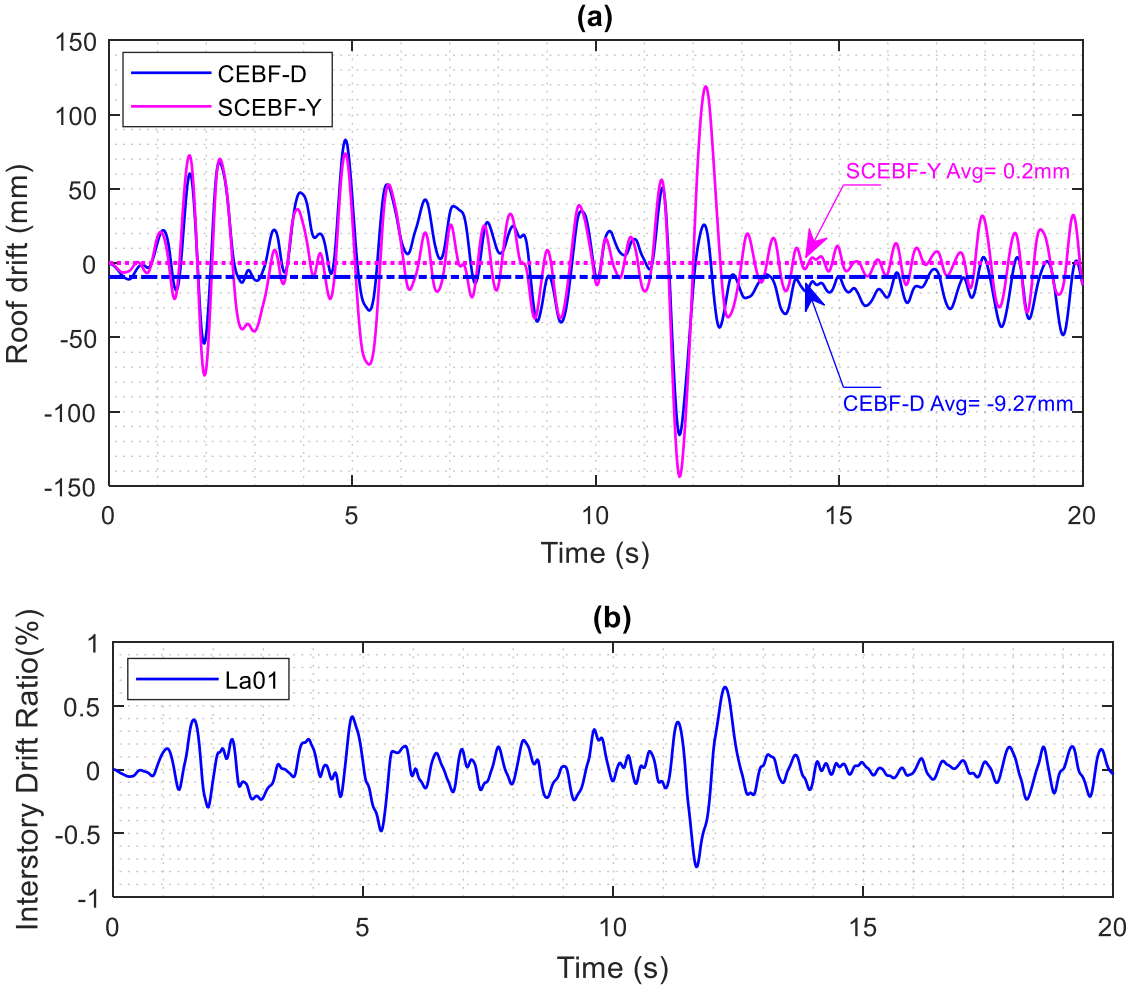

Figure 6.23 Typical time history response of SCEBF-Y and CEBF-D, Case-A under LA01 ground motion: (a) roof drift; (b) typical inter-story drift ratio in first story

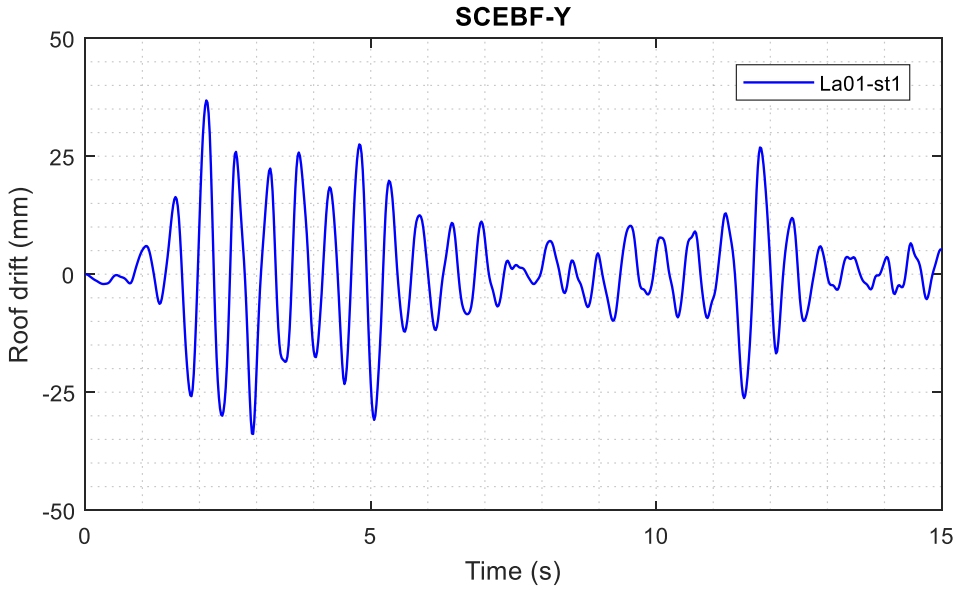

Figure 6.24 First story drift time history for SCEBF-Y type

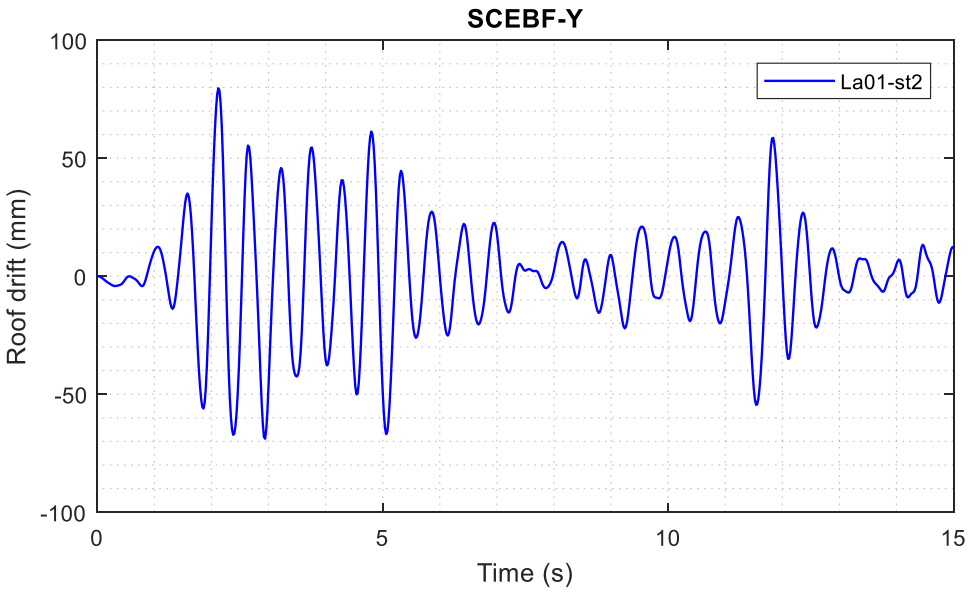

Figure 6.25 Second story drift time history for SCEBF-Y type

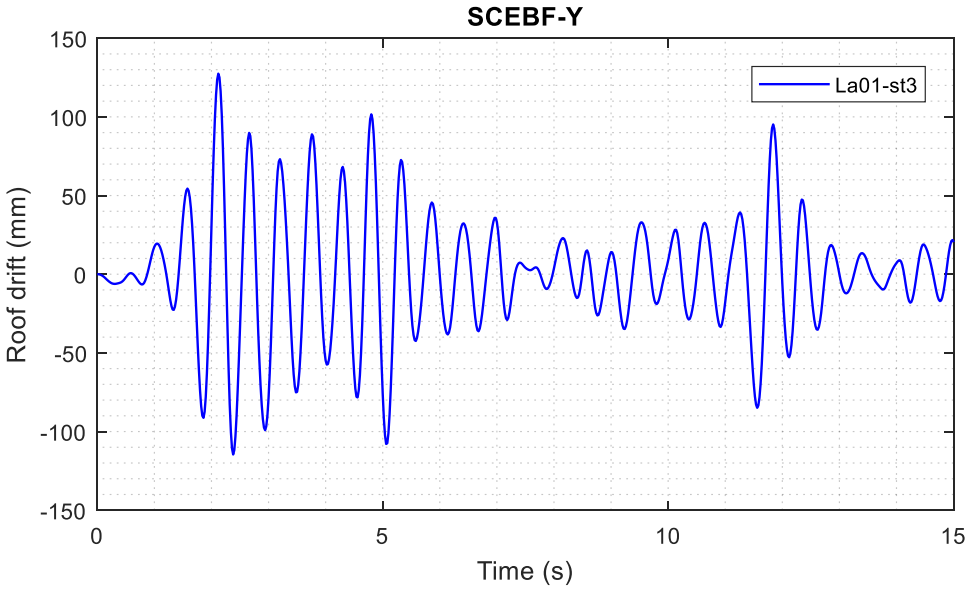

Figure 6.26 Third story drift time history for SCEBF-Y type

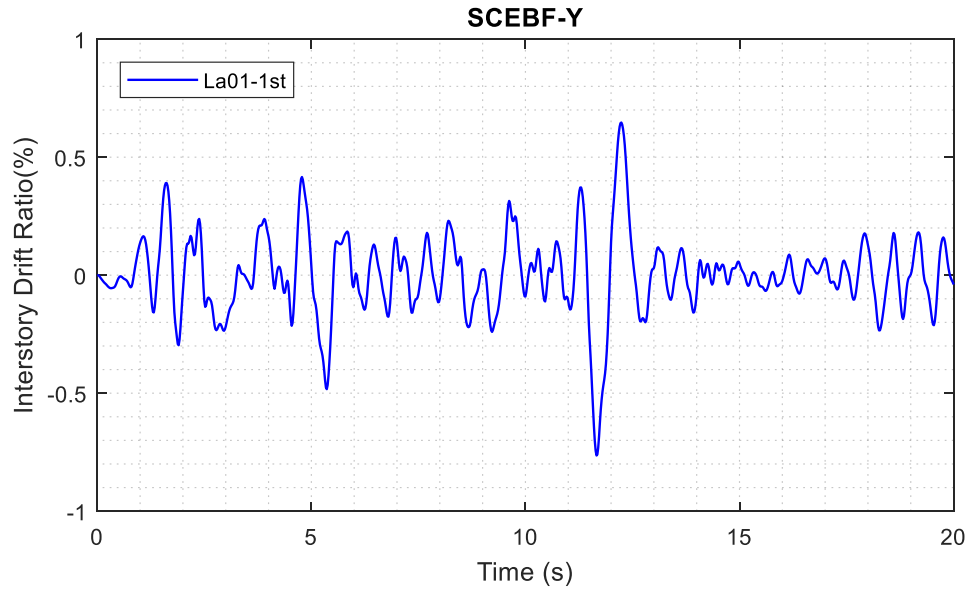

Figure 6.27 First story inter-story drift ratio-time history for SCEBF-Y type

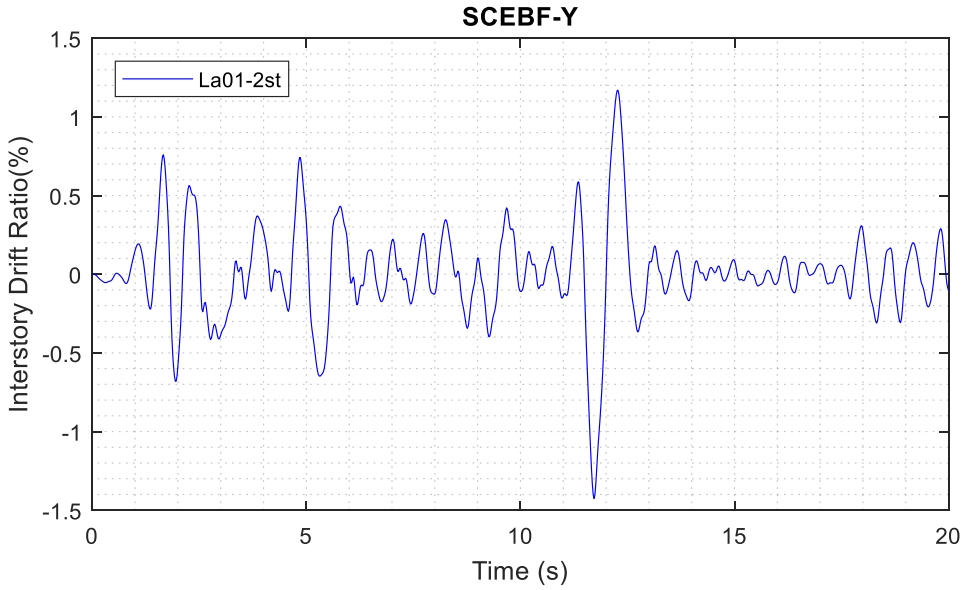

Figure 6.28 Second story inter-story drift ratio-time history for SCEBF-Y type

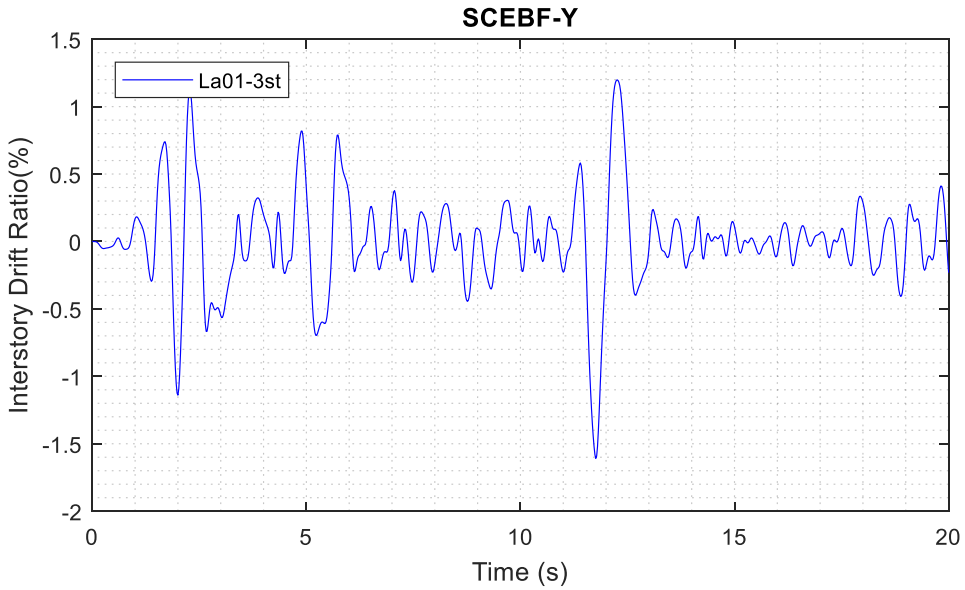

Figure 6.29 Third story inter-story drift ratio-time history for SCEBF-Y type

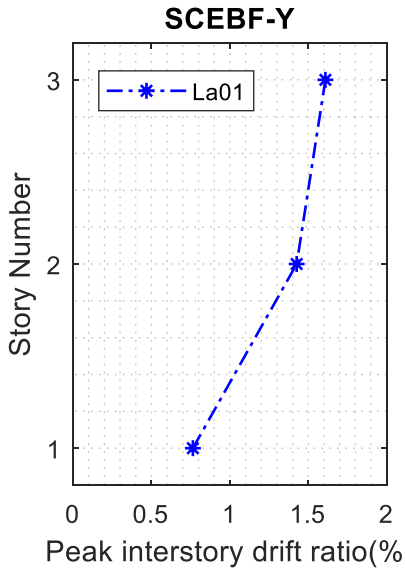

Figure 6.30 Peak inter-story drift ratio for Y-type SCEBF

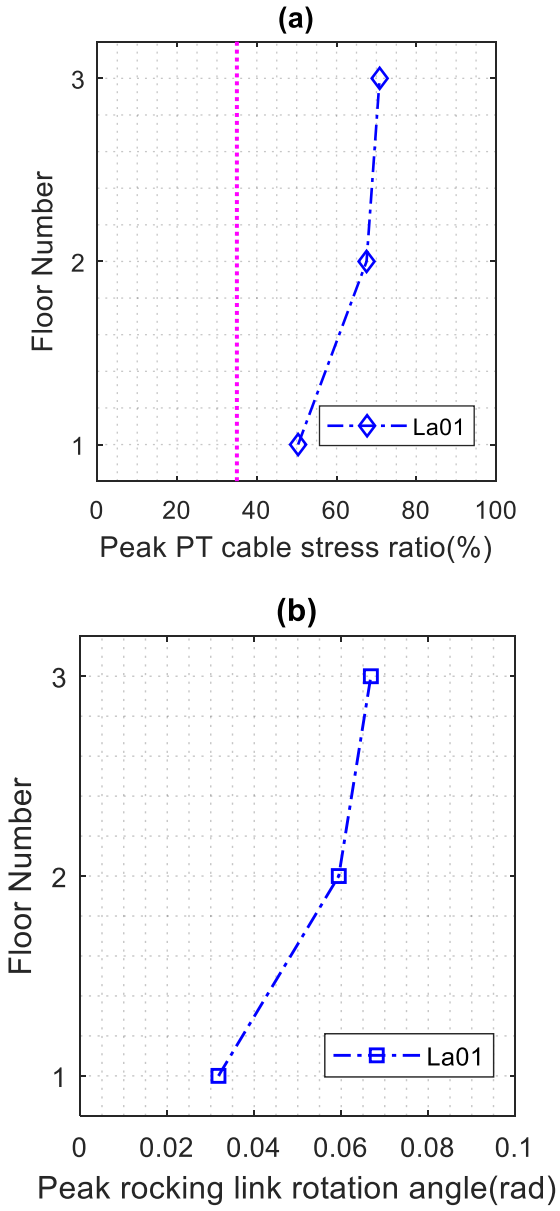

Figure 6.31 Typical response of SCEBF-Y, Case-A under LA01 ground motion: (a) PT cable stress ratio; (b) Peak rocking link rotation angle

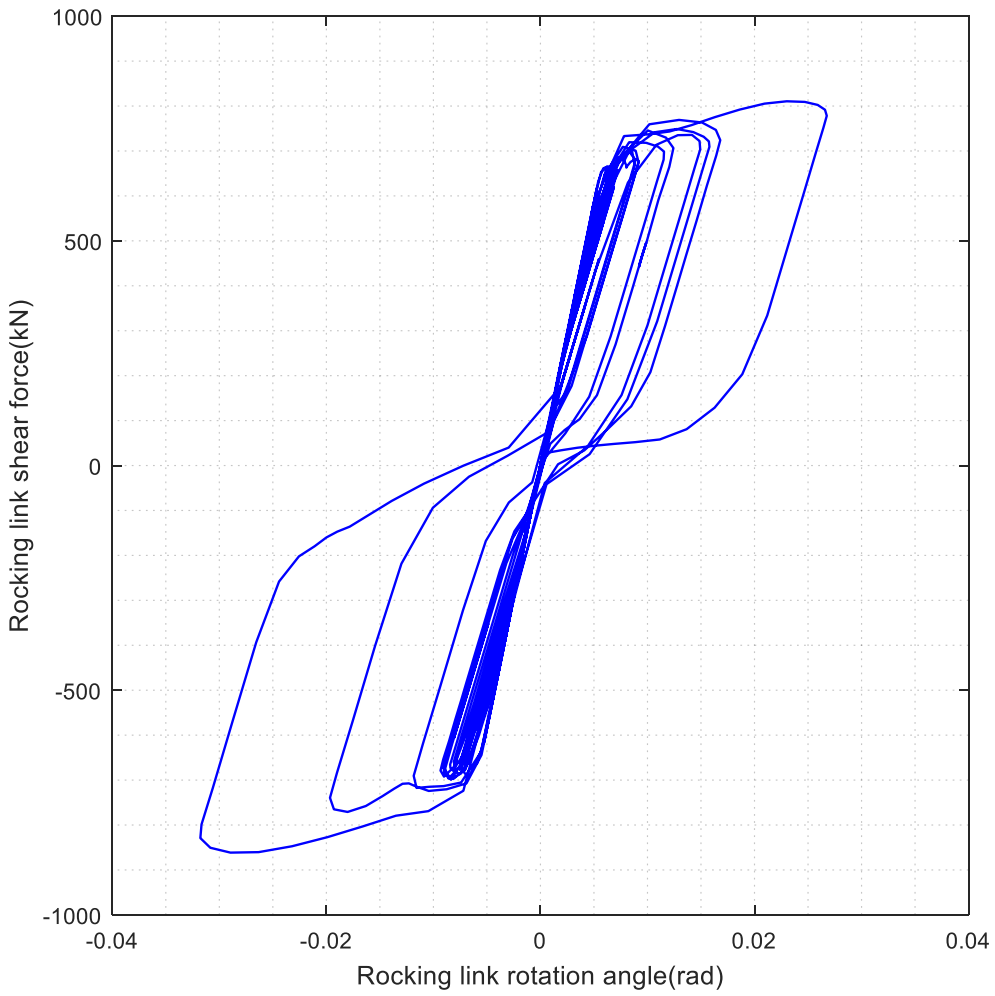

Figure 6.32 Link shear hysteresis curve of first story rocking links in SCEBF-Y, Case-A under LA01 ground motion

Chapter 7 Parametric Study of Replaceable hysteric Damper

In order to obtain seismic resilient buildings, structures are expected to behave in a ductile manner and dissipate seismic energy through replaceable fuse devices. In this study, a new replaceable hysteric damper (RHD) called TPAD has been developed and used for self-centering EBFs as reported in previous chapters. The design of this damper is inspired by the TADAS devices [1]. A schematic view of TADAS device in steel frame is shown in Figure 7.1. TPAD is a trapezoidal plate connected to a round rod at its free end so it can slide freely in the RHD holder slot. A schematic view of TPAD plate is shown in Figure 7.2.

In the proposed TPAD design, TPAD plate is connected to a round rod as shown in Figure 7.3. This rod is used in order to not only decrease the friction force when the TPAD plate slides inside the fuse holder but also to reduce the local bearing induced plastic deformation on TPAD plate. Moreover, by using the round rod, the initial gap between the TPAD plate and fuse holder can be easily fit, and TPAD plate surface would not touch the fuse holder's edges when it rotates with the link beam. Thus, fuse holder should be designed in a way to be able to hold the TPAD rod inside the fuse holder through DBE, so that TPAD plate would not slide out of the fuse holder. First, the CVGM and CDM method used to investigate the behavior of TPAD plate are presented, then the CVGM parameters are calibrated through the calibration of hysteresis curve of a low yield steel coupon test experiment. Analytical formula is

also presented for TPAD plate. Finally, a parametric study was done to obtain the optimum TPAD plate for a reduced scale specimen in order to reduce computation time.

7.1 CVGM method for TPAD

TPAD plate is designed and optimized based on the investigation of cracks initiation in TPAD plate. In order to predict cracks in TPAD plate, damages in the TPAD plate for ultra-low cycle fatigue (ULCF), were studied by the method proposed by Amiri, Aghakouchak [2]. CVGM method predicts [10] the initiation of micro-crack (Initiation of damage) over the characteristic length while CDM method anticipates the propagation of the cracks (damage evolution) [2, 71]. When VGI_{cyclic} gets greater than $VGI_{cyclic}^{critical}$ over a length larger than characteristic length, crack initiates. CVGM method is sensitive to mesh size that needs to be similar to the metallic material's characteristic length but CDM method can reduce the mesh size sensitivity, [2]. All these formulas are written to a user subroutine which is presented in the Appendix to be implemented in a general finite element simulation software - ANSYS. A brief review of CVGM and CDM formula is presented in the following.

$$T = \frac{\sigma_m}{\sigma_e} \qquad \text{Equation 7.1}$$

$$\varepsilon_{p,critical} = \alpha \exp(-1.5T) \qquad \text{Equation 7.2}$$

$$VGI_{cyclic} = \sum_{tensile\ cycles} \int_{\varepsilon_1}^{\varepsilon_2} \exp(|1.5T|) d\varepsilon_p -$$

$$\sum_{compressive\ cycles} \int_{\varepsilon_1}^{\varepsilon_2} \exp(|1.5T|) d\varepsilon_p \qquad \text{Equation 7.3}$$

$$VGI_{cyclic}^{critical} = VGI_{monotonic}^{critical} * \exp(-\lambda \varepsilon_p^{accumulated}) \qquad \text{Equation 7.4}$$

$$VGI_{monotonic}^{critical} = \int_0^{\varepsilon_{p,critical}} \exp(1.5T)\, d\varepsilon_p \qquad \text{Equation 7.5}$$

$VGI_{cyclic} > VGI_{cyclic}^{critical}$, $for\ l > l^* \longrightarrow$ Crack initiate

Where $T, \alpha, \lambda, \sigma_m, \sigma_e$ and l^* represent material stress triaxiality, toughness, material-dependent damageability coefficient, hydrostatic stress, von-mises stress and characteristic length respectively. $VGI_{monotonic}^{critical}$ represents the material parameter that quantifies the critical void ratio which is constant for each material. VGI_{cyclic}, and $VGI_{cyclic}^{critical}$ present cyclic void growth index and critical cyclic void growth index. $\varepsilon_p^{accumulated}$ is equivalent plastic strain (ε_p) that has accumulated up to the beginning of each tensile excursion of loading (this parameter is equal to zero for monotonic loading). ε_p shows the equivalent plastic strain increasing monotonically independent of loading history, thus, ε_p increases both in tension cycles and compression cycles while, $\varepsilon_{p,critical}$ is calculated based on stress triaxiality at each corresponding load. In this subroutine the peak stress of the material is considered as the time that crack initiates and after that crack propagates which means that damage starts increasing as shown in Figure 7.4. Subroutine steps are presented here [2, 10].

I. T & ε_p are monitored and recorded for each integration point. Then user subroutine calculates VGI_{cyclic} by using T & ε_p and $VGI_{cyclic}^{critical}$ by using $VGI_{monotonic}^{critical}$ & λ.

II. The equivalent plastic strain (ε_p) increases monotonically independent of loading history. It means that ε_p increases both in tension cycles and compression cycles. The VGI_{cyclic} increases and decreases during cyclic loading, reflecting growth and shrinkage of voids during tensile and compressive excursions. At the same time, $VGI_{cyclic}^{critical}$ is evaluated at the beginning of each tensile excursion based on $\varepsilon_p^{accululated}$ and remains constant throughout that excursion. If under cyclic loading, VGI_{cyclic} decreases to zero, it remains at zero until a subsequent "tensile" cycle increase its value above zero. The critical fracture initiation criterion is reached when VGI_{cyclic} exceeds $VGI_{cyclic}^{critical}$. This Explanation confirms that ULCF fracture can only be initiated during tensile loading excursions.

III. Then the subroutine triggers damage initiation (D=0) of the corresponding integration point in the ANSYS model as shown in Figure 7.4. The damage evolves based on the equivalent plastic displacement at the integration point by using energy balance approach (Hillerborg's crack growth method) [2, 71]. As damage propagates, stress value degrades up to the point that element has no stress (point B). At point B, the element will be removed from our analysis (D=1) as shown in Figure 7.4.

IV. At last, the fully damaged elements are deleted from the analysis.

V. Again, this procedure repeated ahead of the crack tip over a distance equal to a few multiples of the characteristic length, l^*.

The CDM approach is presented next. Based on the Hillerborg's fracture energy proposal, the G_f energy required to open a unit area of crack is defined as following [71]:

$$G_f = \int_{\bar{\varepsilon}_0}^{\bar{\varepsilon}_f} l^* \bar{\sigma}_y d\bar{\varepsilon} = \int_0^{\bar{u}_f} \bar{\sigma}_y d\bar{u} \quad \text{Equation 7.6}$$

$$\sigma_e = (1 - D) \cdot \bar{\sigma} \quad \text{Equation 7.7}$$

Exponential damage evolution rule:

$$D = 1 - \exp(-\int_0^{\bar{u}} \frac{\sigma_e}{G_f} d\bar{u}) \quad \text{Equation 7.8}$$

Where $G_f, \bar{u}, \bar{u}_f, \sigma_e$ and $\bar{\sigma}$ represent the threshold value of G (Hillerborg's fracture energy), equivalent plastic displacement, equivalent plastic displacement at failure, effective or damaged stress, and undamaged stress.

7.2 Calibration of CVGM model

In this section, the CVGM model parameters of low yield steel Q225LY are calibrated using the cyclic test data of a Q225LY coupon test as shown in Figure 7.5. The FE model of the bar test has been created in ANSYS software. To calibrate the CVGM parameters, several models with different parameters were tested. The force-displacement comparison graph between the FE simulation and experiment test results is shown in Figure 7.6. It is found that $VGI_{cyclic}^{critical}$=0.43 and λ=0.1 for the Q225LY material used in the TPAD plate. In Figure 7.6, number 1 shows the onset of

damage initiation (D=0) and number 2 presents complete fracture (D=1). To be conservative in the analysis of TPAD plate, number 1 (damage initiation) is considered as the critical point for the parametric study.

7.3 Analytical formula

TPAD plate plastic shear force is derived based on the plastic moment of TPAD plate top surface. Based on Figure 7.7, $t, h, w_1, w_2, k,$ and α represent TPAD thickness, height, top width, bottom width, rectangular height and slope ratio respectively. E, and F_y show TPAD-plate's young modulus, and yield stress while N represents the quantity of TPAD plate. TPAD yielding force (Vy_{TP}) is derive based on the plastic moment (MP_{TP}) of its top section while TPAD initial stiffness (K_{TP}) is related to TPAD top width (w_1), thickness (t), and height (h) [1]. TPAD plastic strength (P_p), yield strength (P_y), Elastic lateral stiffness (K_d), yield displacement (Δ_y), and yield rotational angle (γ_y) are presented below [1].

$$Vy_{TP} = \frac{MP_{TP}}{h_{TP}} = \frac{w_2 t^2 F_y}{4\mathrm{h}} \qquad \text{Equation 7.9}$$

$$K_{TP} = \frac{E w_2 t^3}{6h^3} \qquad \text{Equation 7.10}$$

$$P_p = \frac{w_2 t^2 F_y}{4h} \qquad \text{Equation}$$

7.11

$$P_y = \frac{w_2 t^2 F_y}{6h}$$ Equation 7.12

$$K_d = \frac{NEw_2 t^3}{6h^3}$$ Equation 7.13

$$\Delta_y = \frac{F_y h^2}{Et}$$ Equation 7.14

$$\gamma_y = \frac{F_y h}{Et}$$ Equation 7.15

7.4 Parametric study

To optimize the geometry for TPAD plate design, a parametric study has been conducted through finite element simulations. Cyclic loading has been applied to various TPAD plates, and overall behavior of TPADs have been investigated in this chapter.

Finite element model is created based on RHD design with TPAD plates in the full-scale experimental test of SCEBF-D module frame done in China as mentioned in Chapter 3. In order to simulate similar boundary conditions of the TPADs in a D-type self-centering EBF mentioned, a simple model has been created shown in Figure 7.3. Rotation is chosen based on the roof drift ratio of SCEBF-D type experimental test (Chapter 3). For instance, 1% roof drift ratio of SCEBF-D would be equal to 3% rotational angle for TPAD.

In the parametric study, a rotational displacement as shown in Figure 7.8 is applied to the pivot points for several cycles until the TPAD surface reaches to damage criteria

(number 1 in Figure 7.6) and the distribution of the plastic strain and stress on the surface of TPAD are derived.

Pivot points are connected to TPAD through rigid beam elements and a flexible plate. The rigid beam elements length is equal to link beam depth. For positive roof drift ratio, the pivot point shown in Figure 7.9 was used representing the top flange's edge of the link beam in experimental test of D type self-centering EBF. On the other hand, for negative roof drift ratio, the pivot point shown in Figure 7.10 was utilized, representing the bottom flange's edge of the link beam in experimental test of D type self-centering EBF.

TPAD is connected to a rigid rod which has a friction coefficient of 0.15 in contact with the fuse holder plates. It is required to use a uniform mesh size for TPAD since all nodes of it may yield simultaneously. In all analysis presented in this study, same mesh size of 0.25 mm has been used for different models of TPAD plate as shown in Figure 7.11. Mesh size of 0.25mm is used for TPAD plate since the characteristic length in metal for CVGM method is between 0.2mm and 0.3mm.

Based on Figure 7.7, TPAD can be optimized through the following parameters: w_1, t, k, h and α. TPAD top width (w_1) is limited to link's flange width while its bottom height (k) is limited to the max rotation of the link in a way that TPAD should not be pulled out of the fuse holder. TPAD bottom width (w_2) depends on (k) and TPAD height (h) is related to slope ratio (α). To be conservative, in the investigation done in this study, the critical point for the parametric study is considered when the damage initiation happens for the first time in TPAD plate (number 1 in Figure 7.6).

Thus, all the parametric studies for TPAD were done up to the point where damage initiation happens (D=0).

For the parametric study, 11 different models were studied as shown in Table 7.1. To reduce the computation time of the parametric study analysis in the ANSYS software, a 1/20-scale FE model of TPAD original size was adopted. TPAD-1 plate dimensions in the parametric study are as follows.

w_1=10 mm, h=6 mm, t =1mm, k =1.5 mm, α=52, f_s=0.15

7.4.1. Effect of TPAD length (h)

In TPAD-1, TPAD-2 and TP, D-3, all the parameters are constant except for TPAD height (h). The damage and von-mises stress contour at the onset of crack initiation for TPAD-1,2 and 3 are shown in Figure 7.12, Figure 7.13, Figure 7.14, Figure 7.15, Figure 7.16 and Figure 7.17 respectively. The followings are concluded:

- If h < H (Figure 7.18(a)) ⟶ Damage concentration happens in top section of TPAD which is desirable.
- If h > H (Figure 7.18(a)) ⟶ Damage concentration happens in middle to bottom section of TPAD which is not advantageous, since crack initiates earlier in TPAD plate which significantly reduces the ductility and the amount of energy dissipation of TPAD as shown in Figure 7.19 and Figure 7.20.
- According to Figure 7.19 and Figure 7.20, if the height of TPAD-X plate is h_x and the height of TPAD-Y plate is h_y and $h_y < h_x < H$ then crack initiation happens earlier in TPAD-Y, thus TPAD-X is more ductile compare to TPAD-

Y. Moreover, TPAD-Y yield stress, initial stiffness, and post-yield stiffness is higher than TPAD-X.

- Height of the TPAD has significant effect on TPAD plate behavior and based on the parametric study, TPAD height is recommended to be: $H - t < h < H$.

The height of TPAD plate (h) is less than H in this study for all 11 TPAD plates except for TPAD-3.

7.4.2. Effect of TPAD plate thickness (β)

In TPAD-1, TTPAD-4, and TPAD-5, all the parameters are constant except for TPAD thickness (t). Thickness parameter (t) is measured based on β which is the ratio of TPAD thickness and top width ($\beta = t/w_1$). The damage and von-mises stress contour at the onset of crack initiation for TPAD-4 and 5 are shown in Figure 7.21, Figure 7.22, Figure 7.23, and Figure 7.24 respectively. The followings are concluded:

- According to Figure 7.25, and Figure 7.26, if the thickness of TPAD-X plate is t_x and the thickness of TPAD-Y plate is t_y, and $t_x < t_y$ ($\beta_1 < \beta_2$), then crack initiation happens earlier in TPAD-Y, thus TPAD-X is more ductile compare to TPAD-Y. Moreover, TPAD-Y yield stress, initial stiffness, and post-yield stiffness is higher than TPAD-X.

- Thickness of the TPAD has significant effect on TPAD behavior and based on the parametric study, beta is recommended to be: $\beta = 0.1$.

7.4.3. Effect of TPAD tongue plate length (k)

In TPAD-1, TPAD-6, and TPAD-7, all the parameters are constant except for TPAD rectangular tongue plate length (k). The damage and von Mises stress contour at the onset of crack initiation for TPAD-6 and 7 are shown in Figure 7.27, Figure 7.28, Figure 7.29, and Figure 7.30 respectively. The followings are concluded:

- According to Figure 7.31, and Figure 7.32, if the rectangular height of TPAD-X plate is k_x and the rectangular height of TPAD-Y plate is k_y, and $k_x < k_y$, then crack initiation happens a little earlier in TPAD-Y, thus TPAD-X is a little more ductile compare to TPAD-Y. However, TPAD-Y yield stress, initial stiffness, and post-yield stiffness are similar to TPAD-X.
- Rectangular height of the TPAD (k) has negligible effect on TPAD behavior, however, based on the parametric study, k is recommended to be: $k = 0.2h$.

7.4.4. Effect of friction coefficient (f_s)

In TPAD-1, and TPAD-8, all the parameters are constant except for friction coefficient between the TPAD and fuse holder (f_s). The damage and von-mises stress contour at the onset of crack initiation for TPAD-8 are shown in Figure 7.33, and Figure 7.34 respectively. The followings are concluded:

-
- According to Figure 7.35, and Figure 7.36, if the friction coefficient of TPAD-X plate is f_{s_x} and the friction coefficient of TPAD-Y plate is f_{s_y}, and

$f_{s_x} < f_{s_y}$, then crack initiation happens earlier in TPAD-Y, thus TPAD-X is a bit more ductile compare to TPAD-Y. However, TPAD-Y yield stress, initial stiffness, and post-yield stiffness are similar to TPAD-X.

- Friction coefficient between the TPAD and fuse holder (f_s) has negligible effect on TPAD behavior, however, based on the parametric study, (f_s) is recommended to be as low as possible.

7.4.5. Effect of TPAD slope ratio (α)

In TPAD-9, TTPAD-10, and TPAD-11, all the parameters are constant except for TPAD slope ratio (α). The damage and von-mises stress contour at the onset of crack initiation for TPAD-9,10 and 11 are shown in Figure 7.37, Figure 7.38, Figure 7.39, Figure 7.40, Figure 7.41, and Figure 7.42 respectively. The followings are concluded:

- According to Figure 7.43, and Figure 7.44, if the slope ratio of TPAD-X plate is α_x and the slope ratio of TPAD-Y plate is α_y and $\alpha_x < \alpha_y$ then crack initiation happens earlier in TPAD-Y, thus TPAD-X is more ductile compare to TPAD-Y However, TPAD-Y yield stress, initial stiffness, and post-yield stiffness are similar to TPAD-X.
- Slope ratio of the TPAD (α) has little effect on TPAD behavior and based on the parametric study, α is recommended to be: $45 < \alpha < 60$.

7.4.6 Guideline for making optimal TPAD device based on parametric study

Based on the parametric study results, the most important factors in designing the TPAD device are found to be the TPAD thickness (t) and slope ratio (α). First, w_1 should be derived based on the width of link beam in EBFs, and plate length h can be designed once TPAD slope ratio (α) is decided since TPAD plate length h is related TPAD slope ratio (α). w_1 should be smaller than the width of link beam in EBFs, while, k should be long enough so that at the maximum rotational angle of the link beam, TPAD wouldn't slide outside the fuse holder. It is recommended that TPAD has the following parameters:

1. $H - t < h < H$
2. $\beta = 0.1$
3. $k = 0.2h$
4. $45 < \alpha < 60.$

Table 7.1 TPAD parametric study

TPAD	α	h	β=t/w_1	k	f_s
1	52	6	0.1	0.25h	0.15
2	52	5.4	0.1	0.25h	0.15
3	52	6.9	0.1	0.25h	0.15
4	52	6	0.05	0.25h	0.15
5	52	6	0.15	0.25h	0.15
6	52	6	0.1	0.2h	0.15
7	52	6	0.1	0.3h	0.15
8	52	6	0.1	0.25h	0.25
9	52	4.4	0.1	0.25h	0.15
10	45	4.4	0.1	0.25h	0.15
11	60	4.4	0.1	0.25h	0.15

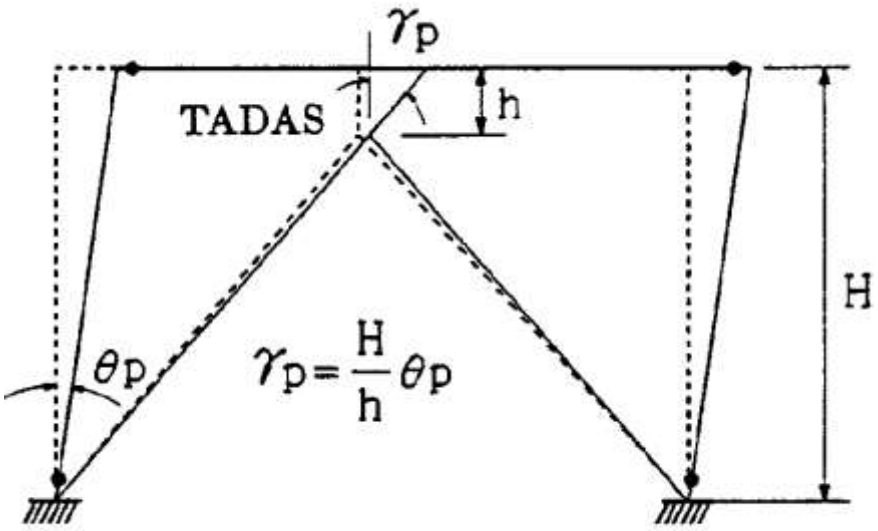

Figure 7.1 Schematic view of TADAS device in steel frame (Tsai, Chen [1])

Figure 7.2 TPAD plate schematic view

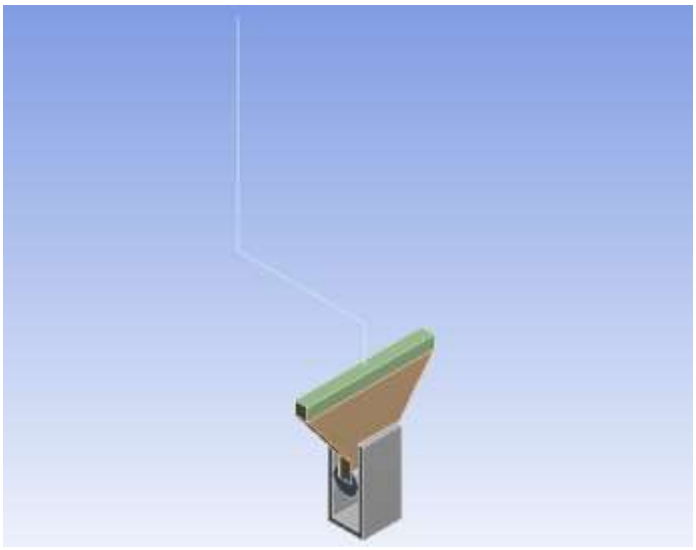

Figure 7.3 ANSYS model of replaceable hysteric damper

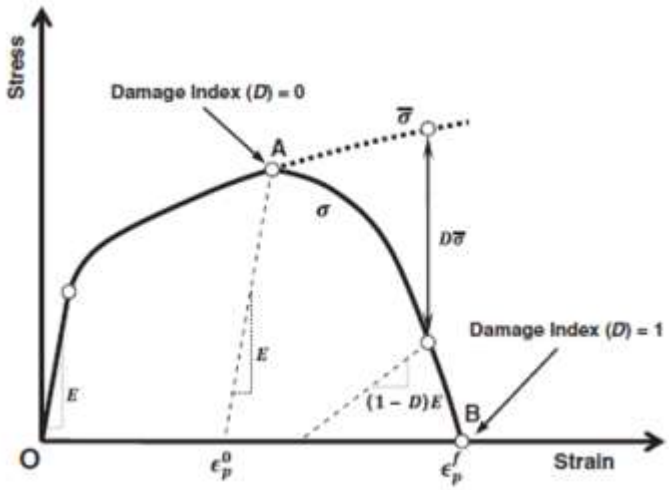

Figure 7.4 Stress-strain curve for damage initiation and evolution (Amiri, Aghakouchak [2])

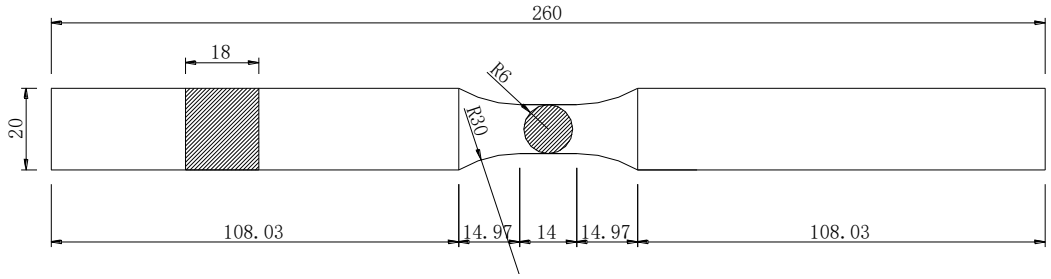

Figure 7.5 Schematic view of the experimental bar test

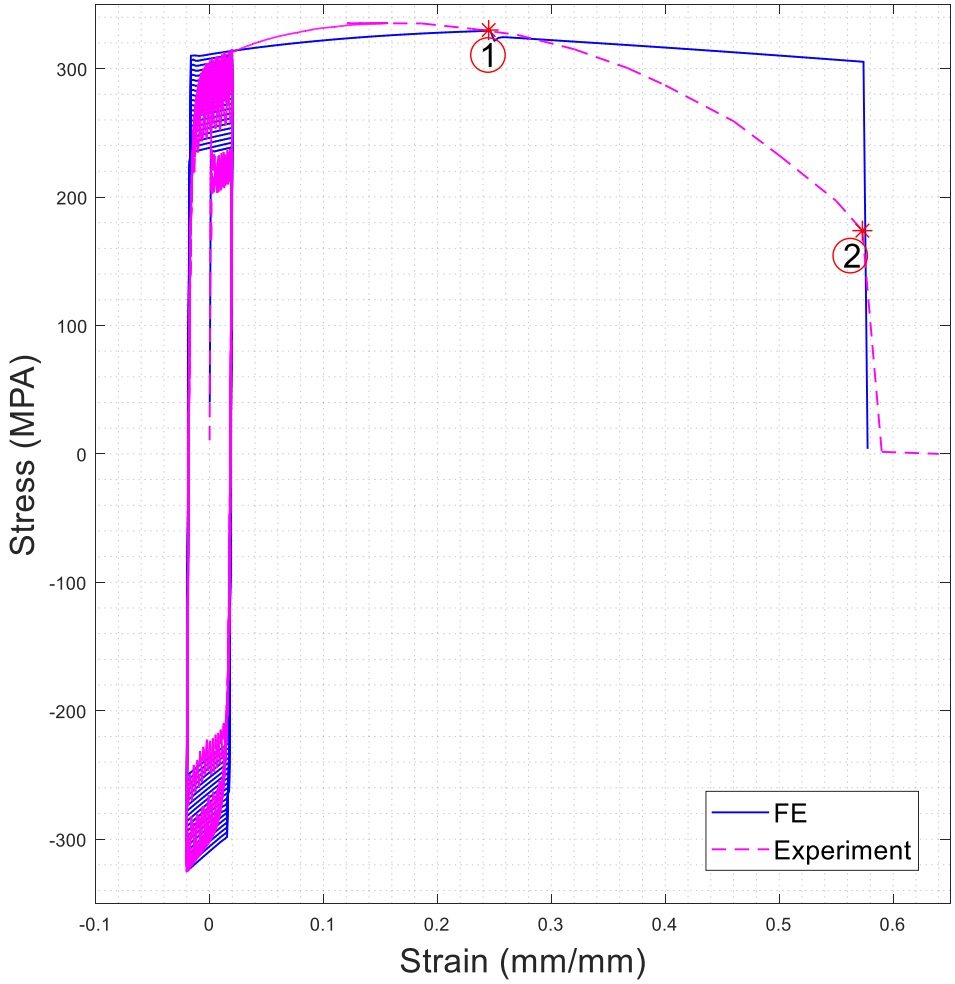

Figure 7.6 Calibration of the hysteresis curve

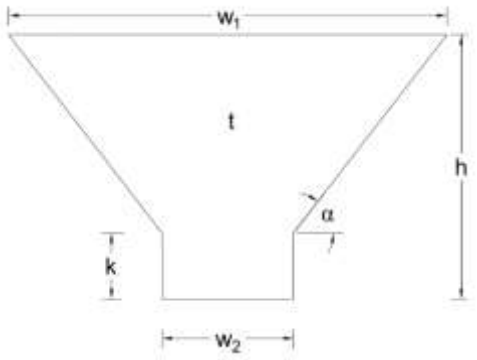

Figure 7.7 TPAD plate parameters

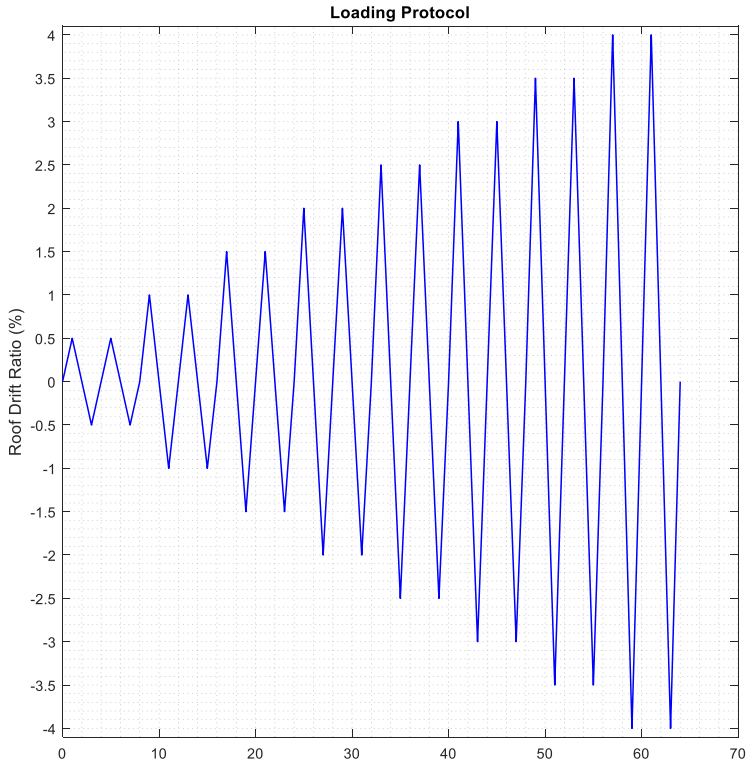

Figure 7.8 Loading protocol for parametric study of TPAD

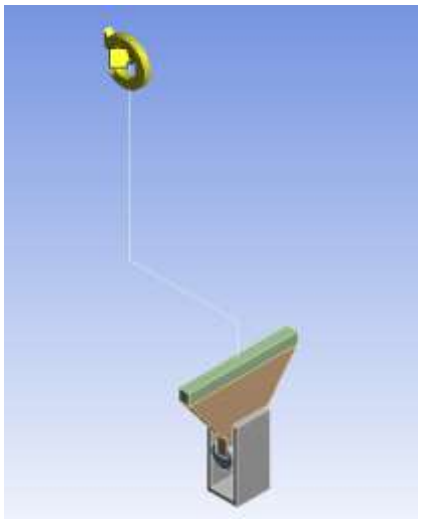

Figure 7.9 Pivot point location when rotational displacement in loading protocol is positive

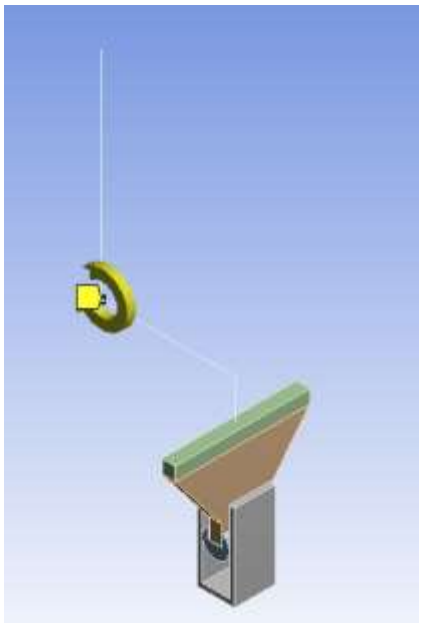

Figure 7.10 Pivot point location when rotational displacement in loading protocol is negative

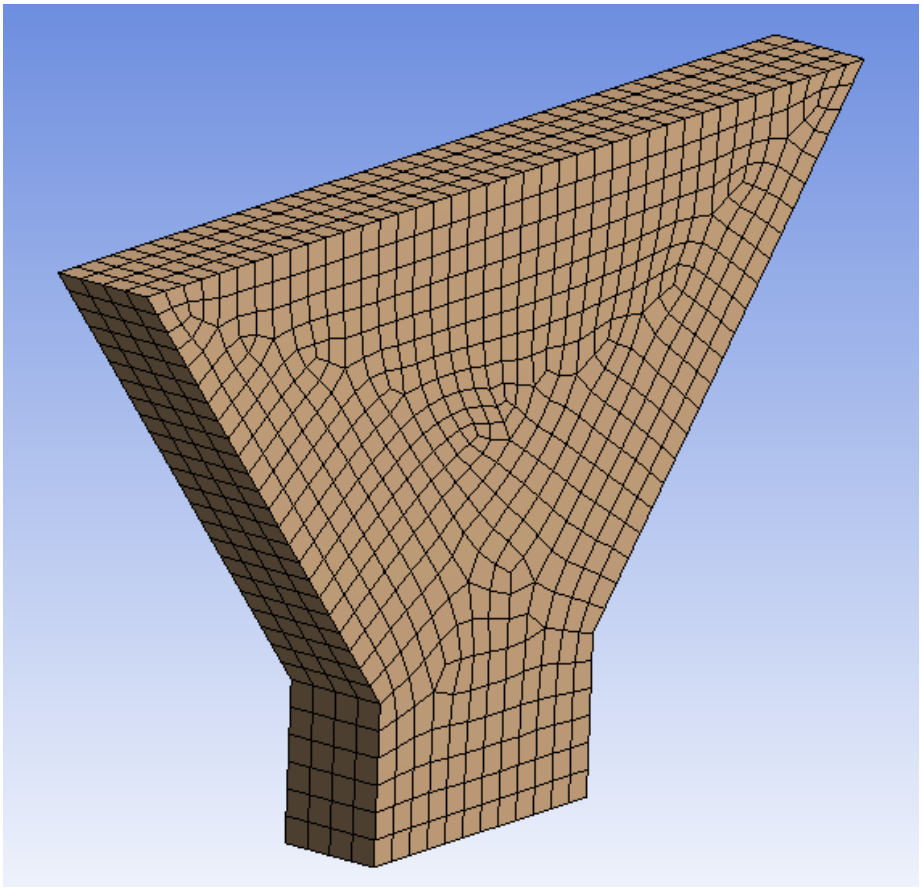

Figure 7.11 Meshed picture of TPAD plate

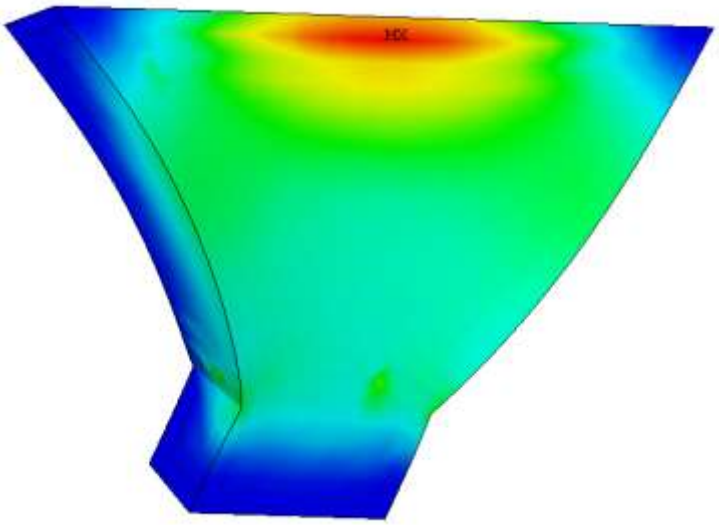

Figure 7.12 Damage counter for TPAD-1 at the onset of crack initiation

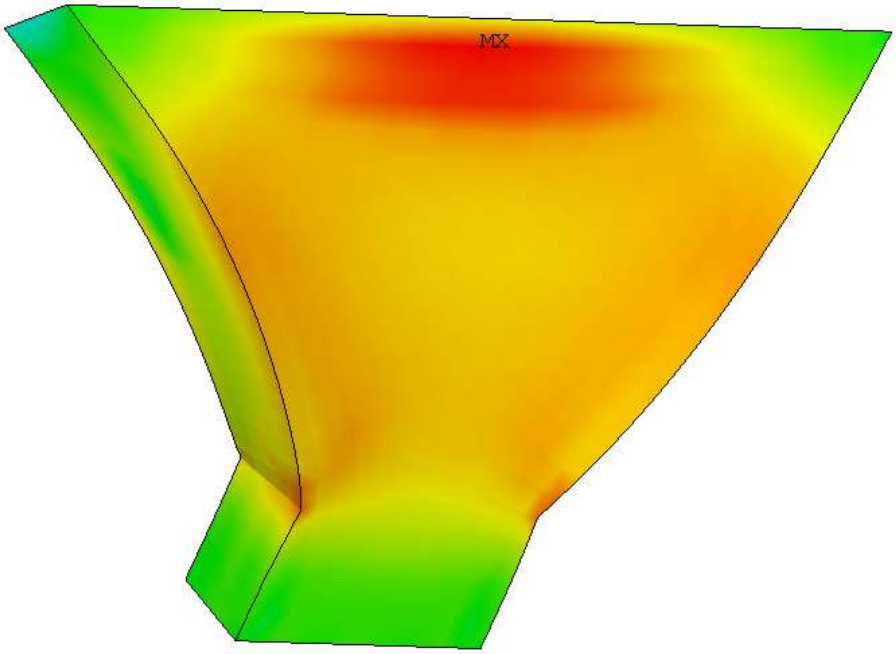

Figure 7.13 Von-mises stress counter for TPAD-1 at the onset of crack initiation

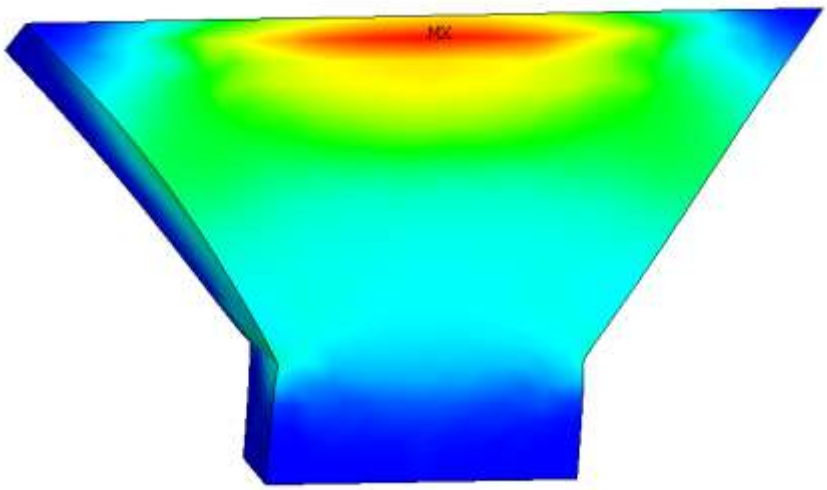

Figure 7.14 Damage counter for TPAD-2 at the onset of crack initiation

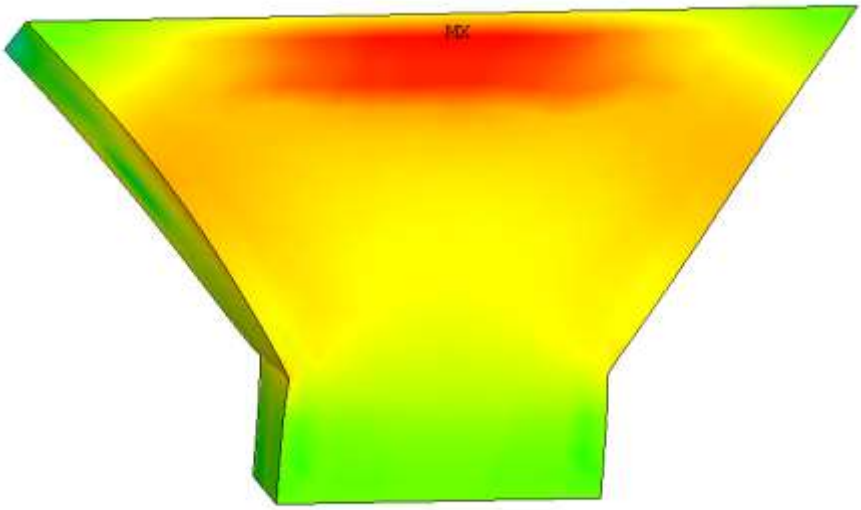

Figure 7.15 Von-mises stress counter for TPAD-2 at the onset of crack initiation

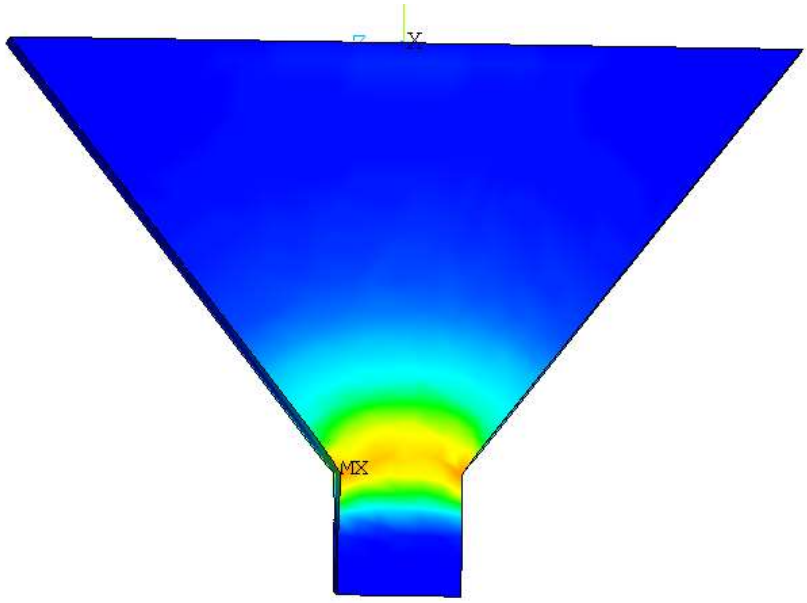

Figure 7.16 Damage counter for TPAD-3 at the onset of crack initiation

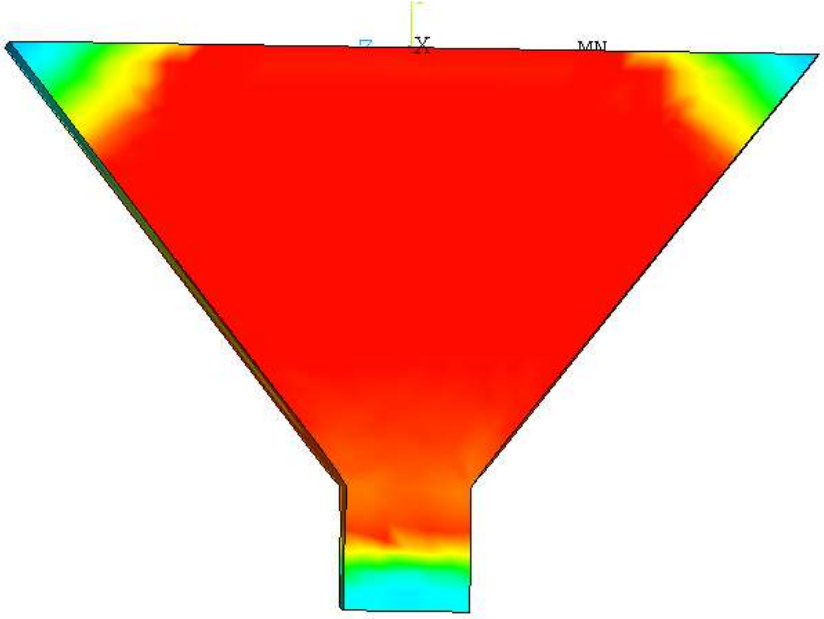

Figure 7.17 Von-mises stress counter for TPAD-3 at the onset of crack initiation

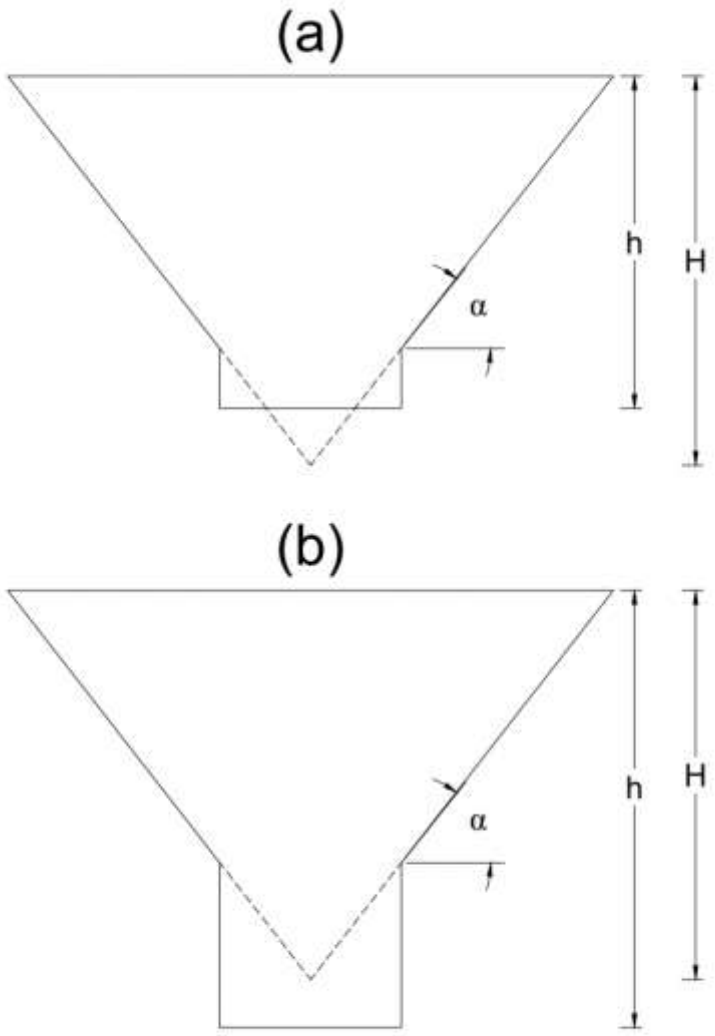

Figure 7.18 TPAD plate height parametric study: (a) $h<H$; (b) $h>H$

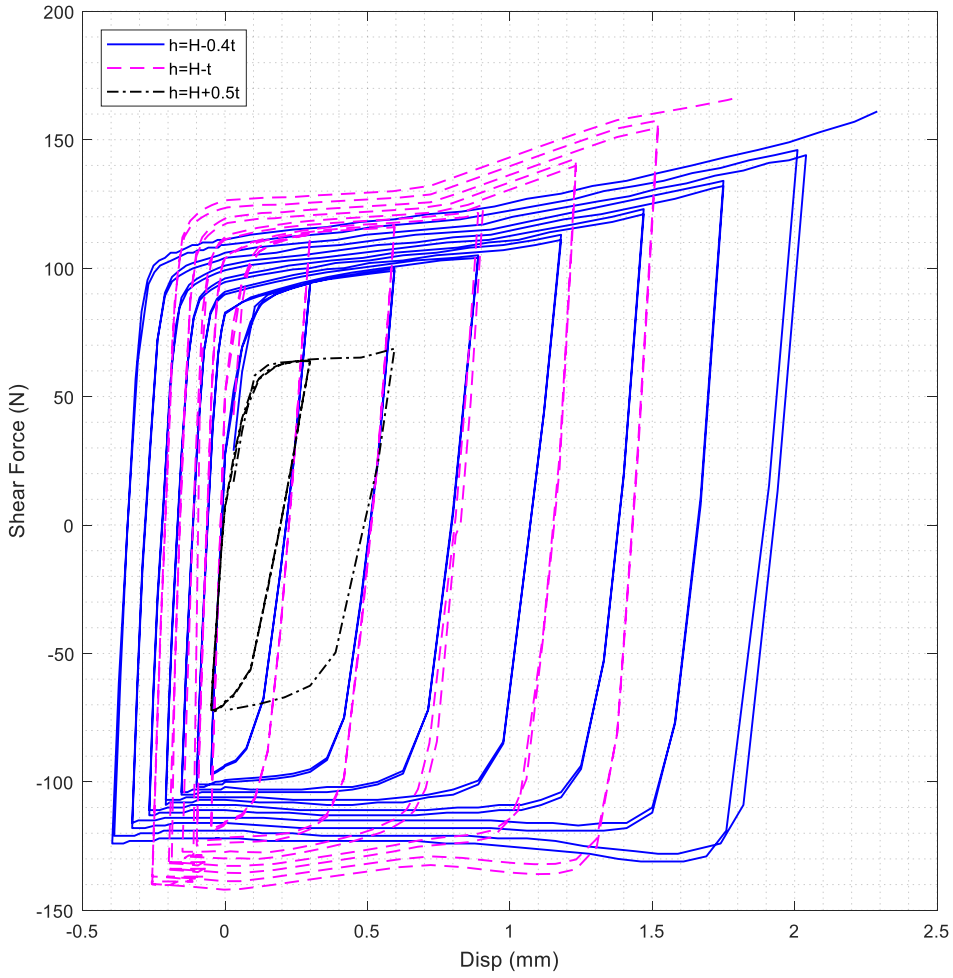

Figure 7.19 TPAD parametric study: height (h)

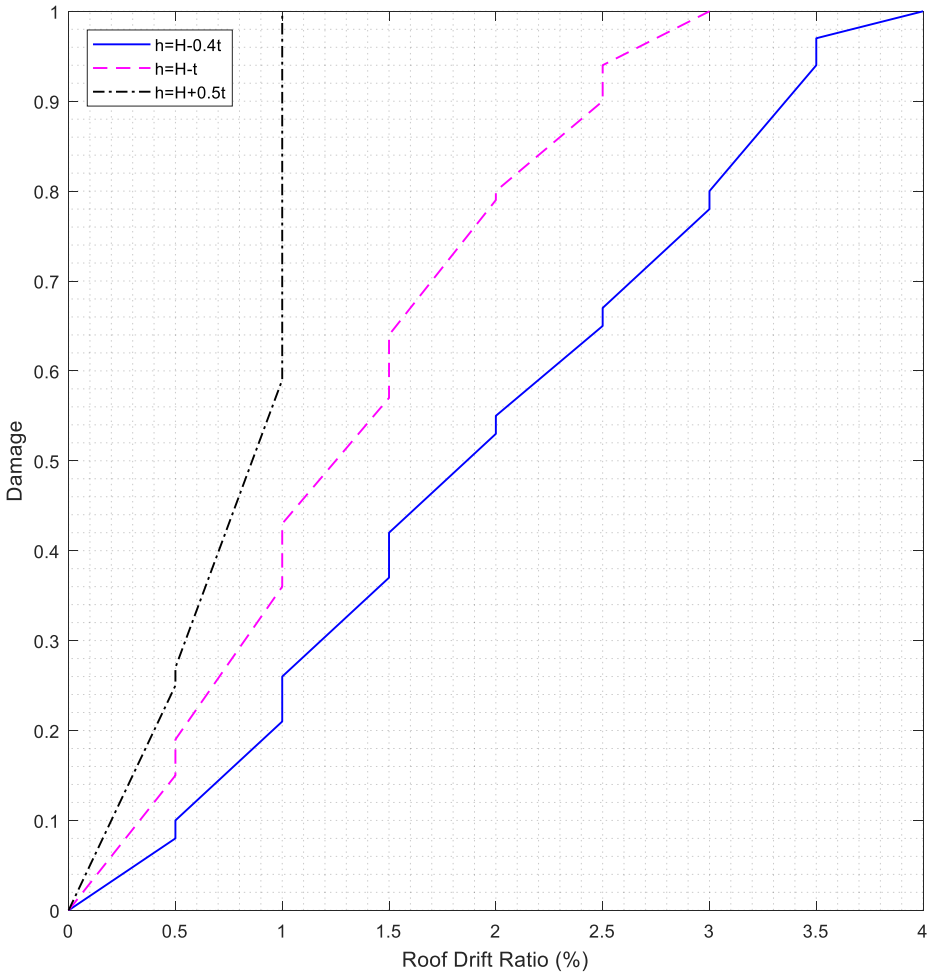

Figure 7.20 Effect of height (h) on ductility of TPAD

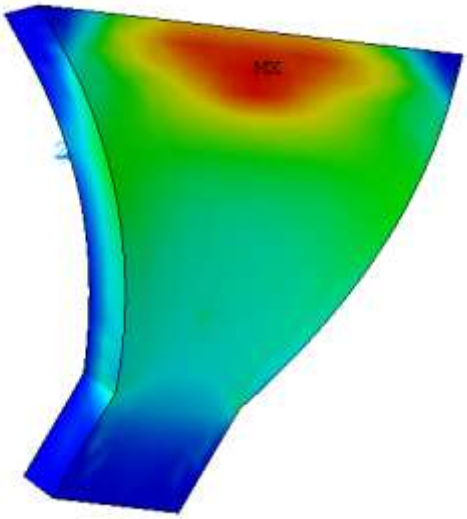

Figure 7.21 Damage counter for TPAD-4 at the onset of crack initiation

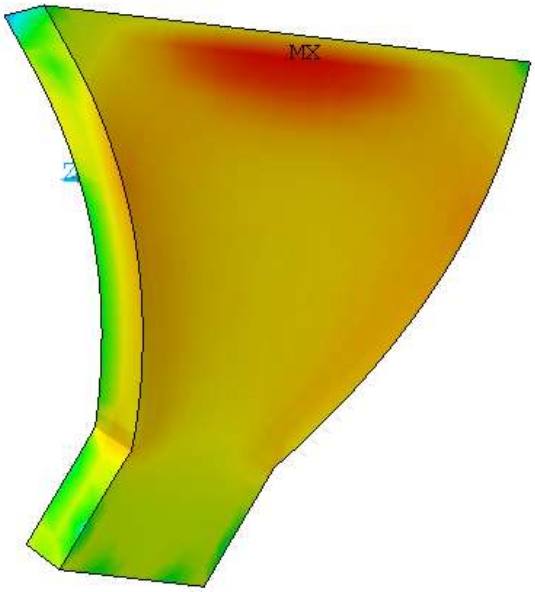

Figure 7.22 Von-mises stress counter for TPAD-4 at the onset of crack initiation

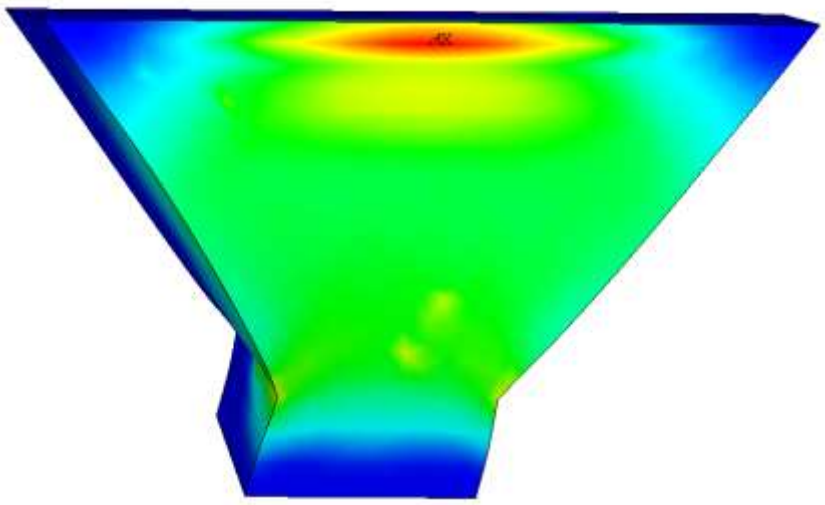

Figure 7.23 Damage counter for TPAD-5 at the onset of crack initiation

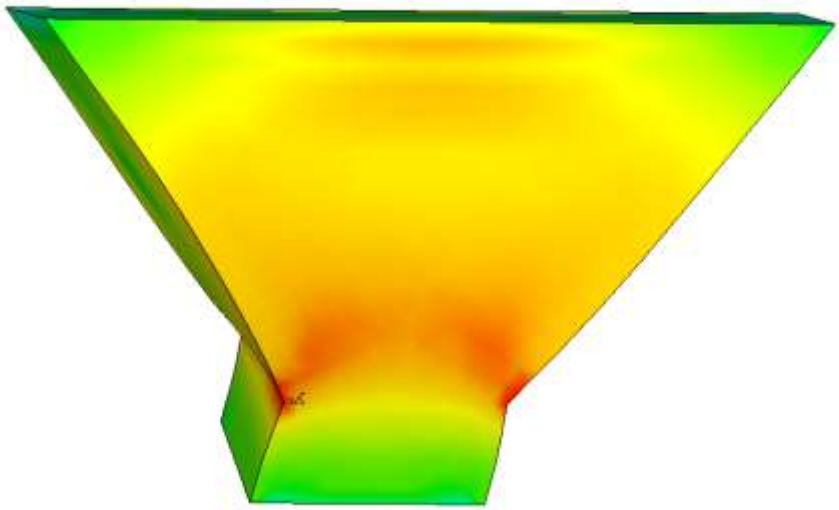

Figure 7.24 Von-mises stress counter for TPAD-5 at the onset of crack initiation

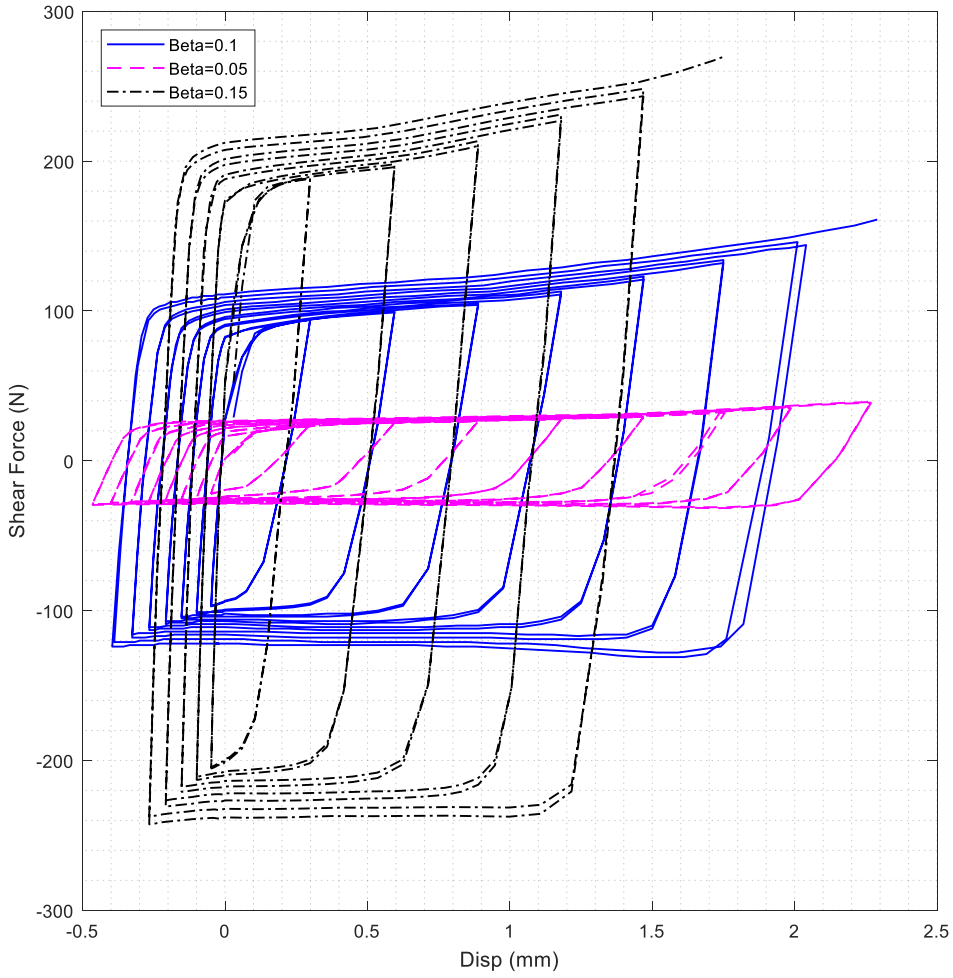

Figure 7.25 TPAD parametric study: beta (β)

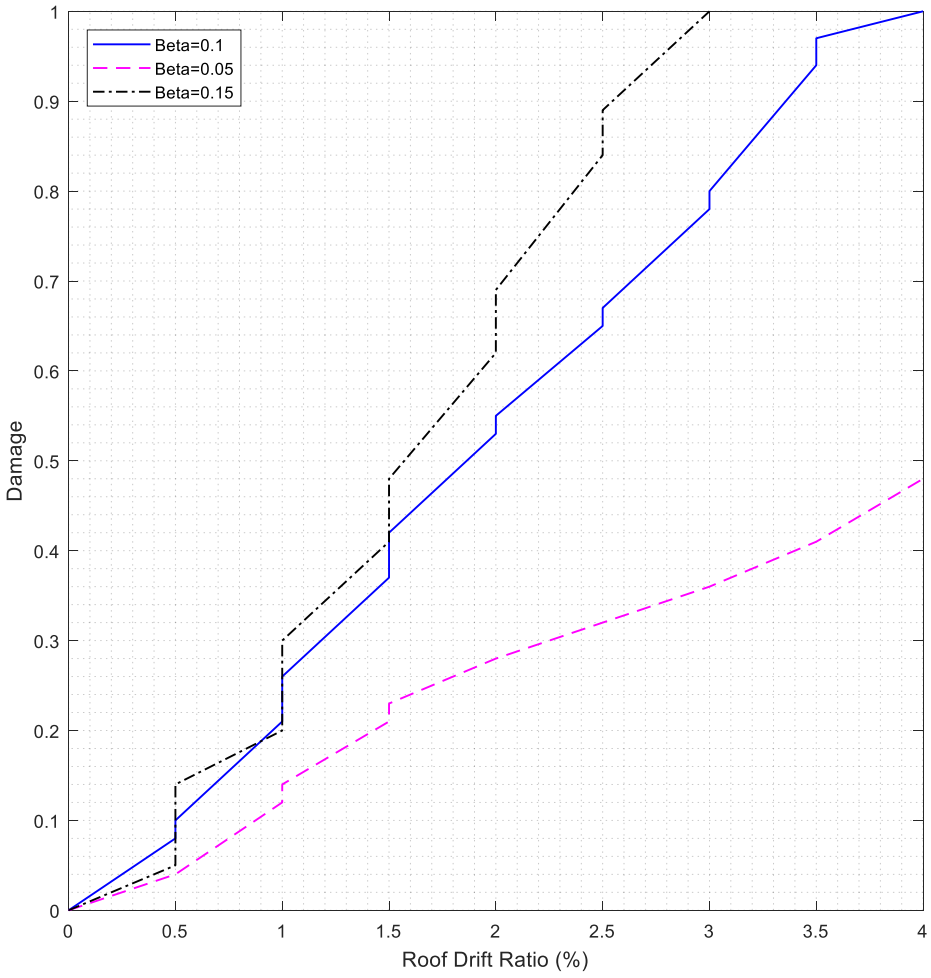

Figure 7.26 Effect of beta (β) on ductility of TPAD

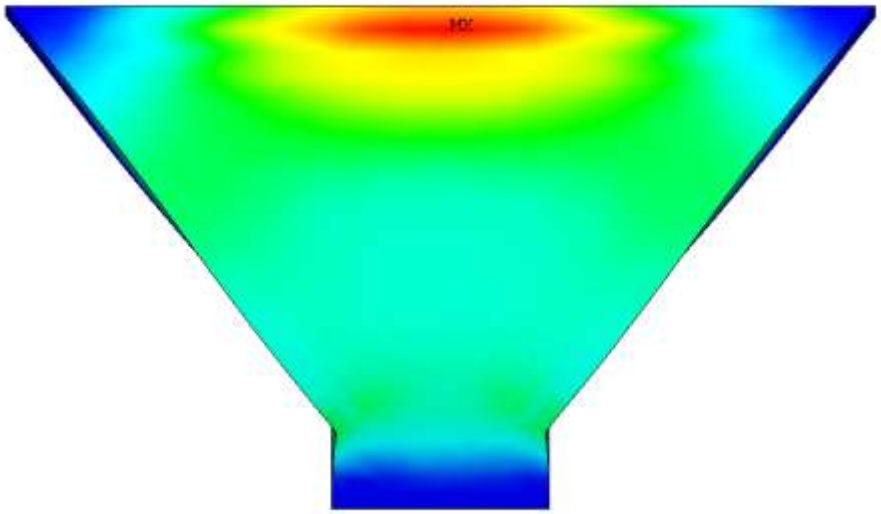

Figure 7.27 Damage counter for TPAD-6 at the onset of crack initiation

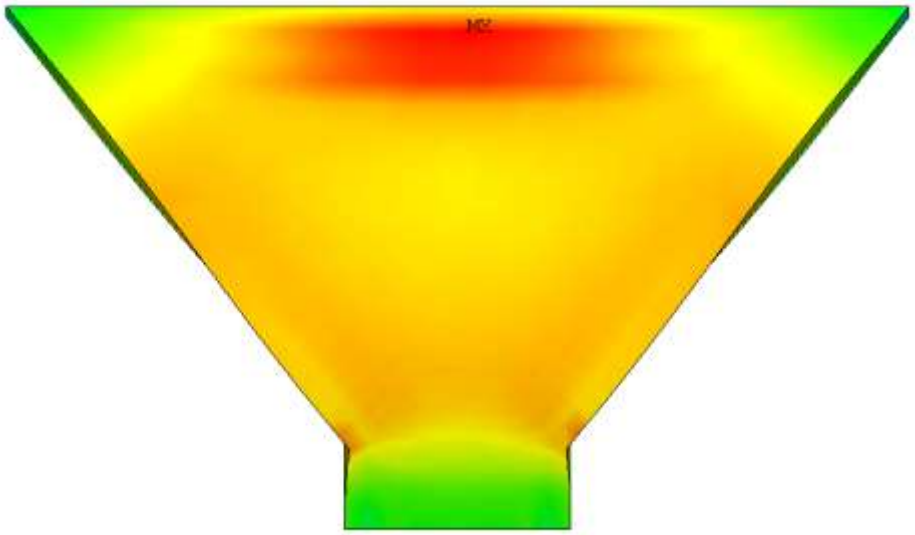

Figure 7.28 Von-mises stress counter for TPAD-6 at the onset of crack initiation

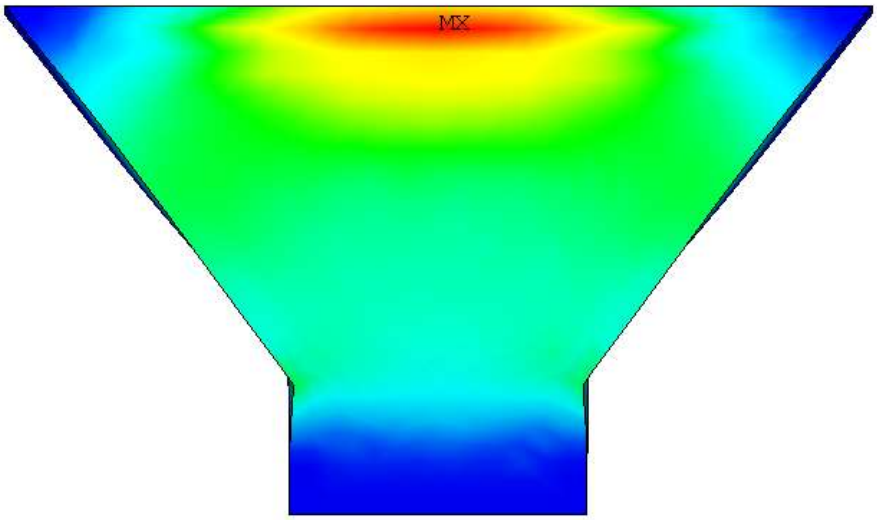

Figure 7.29 Damage counter for TPAD-7 at the onset of crack initiation

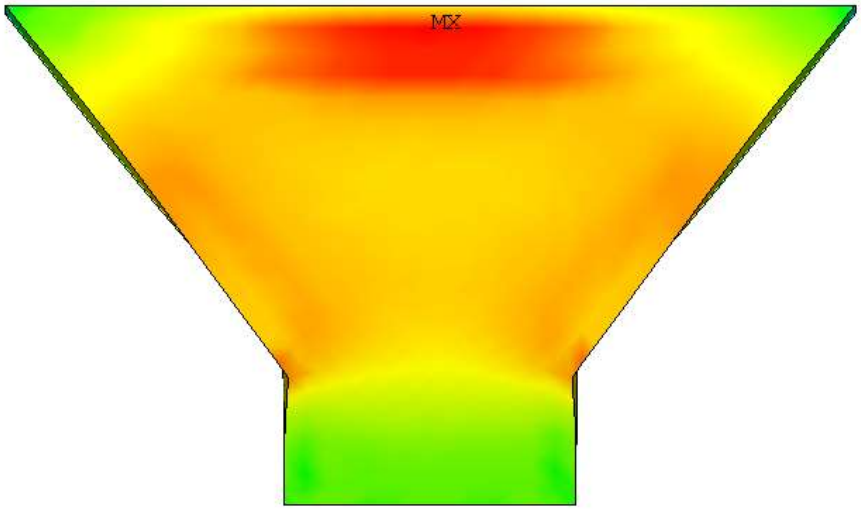

Figure 7.30 Von-mises stress counter for TPAD-7 at the onset of crack initiation

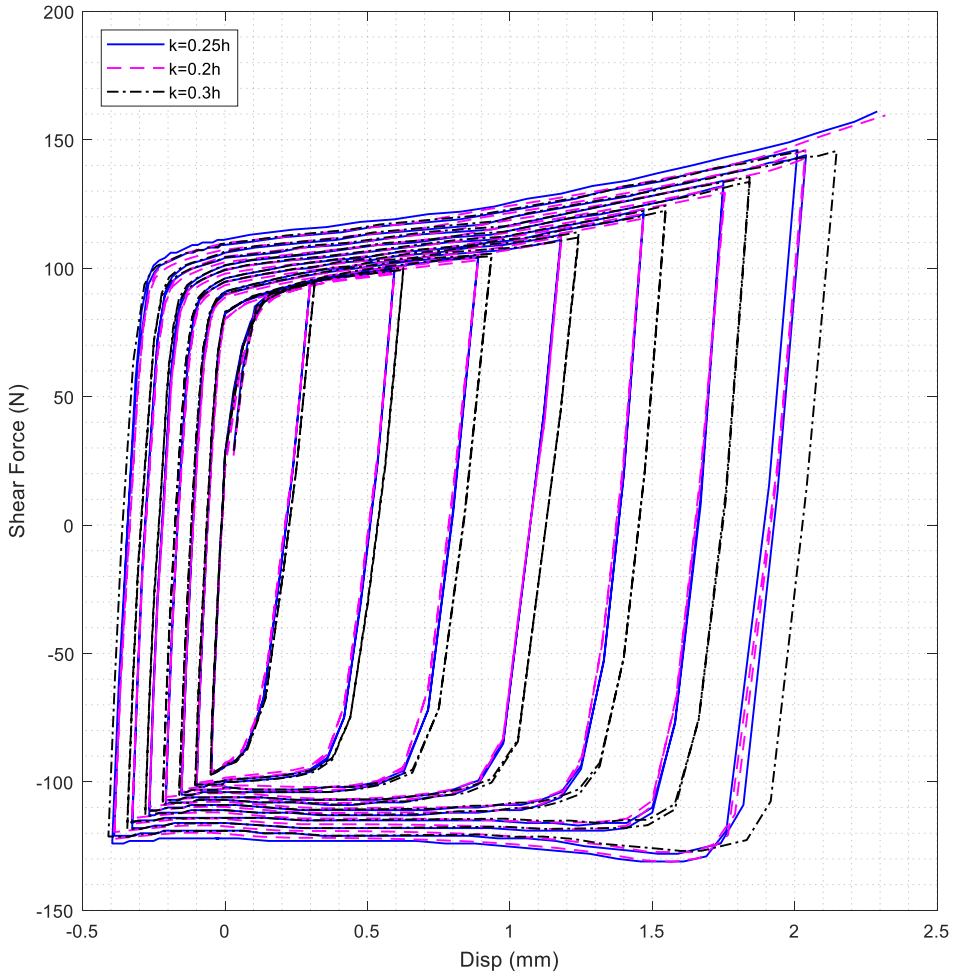

Figure 7.31 TPAD parametric study: rectangular height (k)

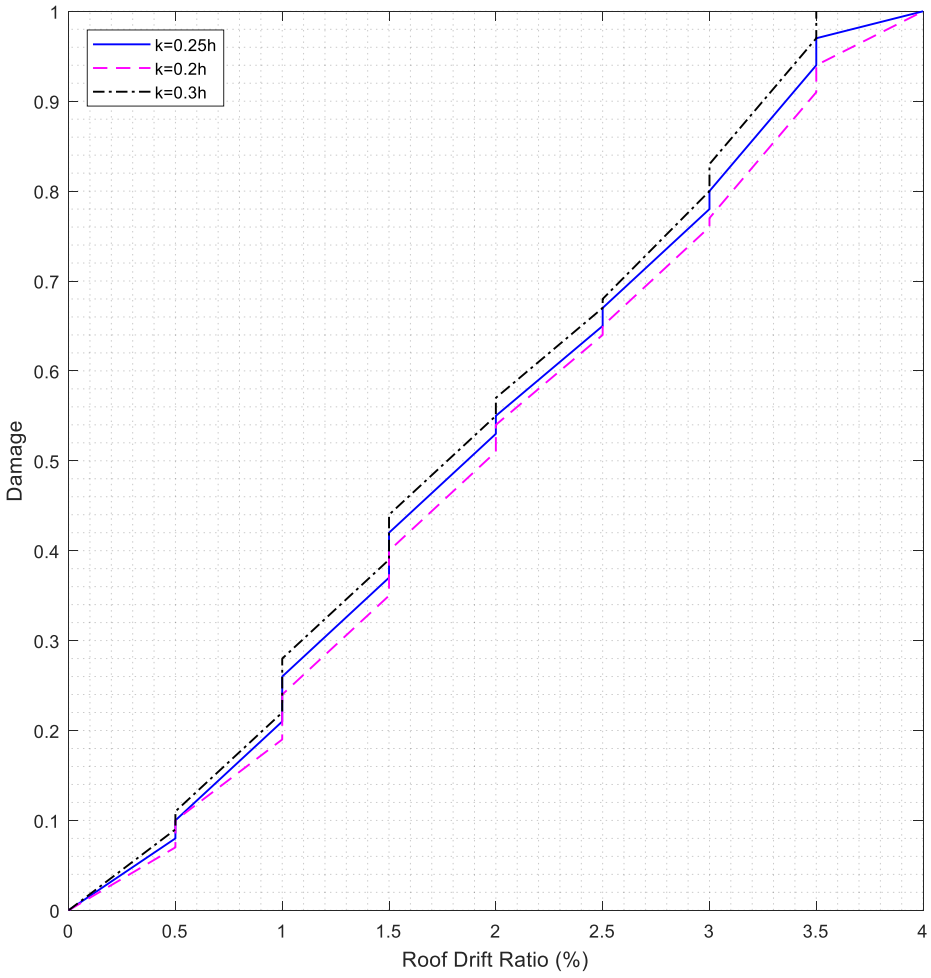

Figure 7.32 Effect of rectangular height (k) on ductility of TPAD

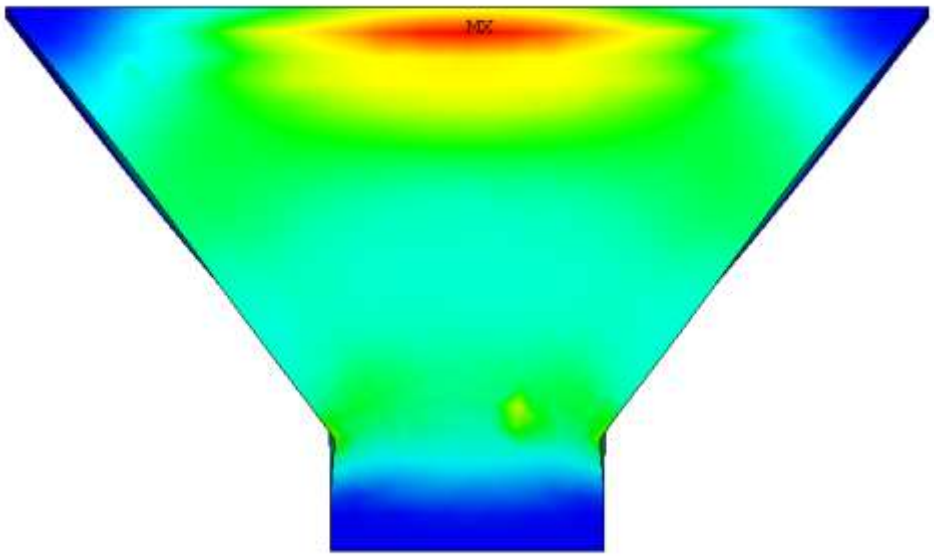

Figure 7.33 Damage counter for TPAD-8 at the onset of crack initiation

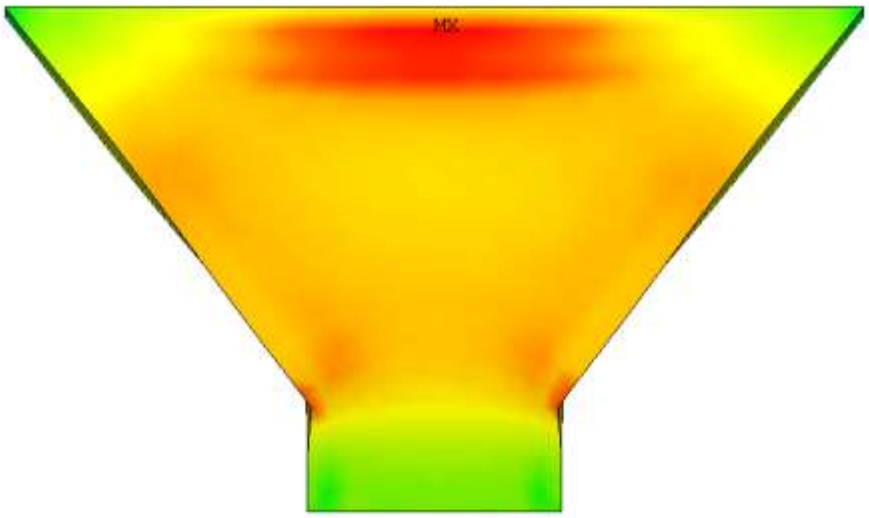

Figure 7.34 Von-mises stress counter for TPAD-8 at the onset of crack initiation

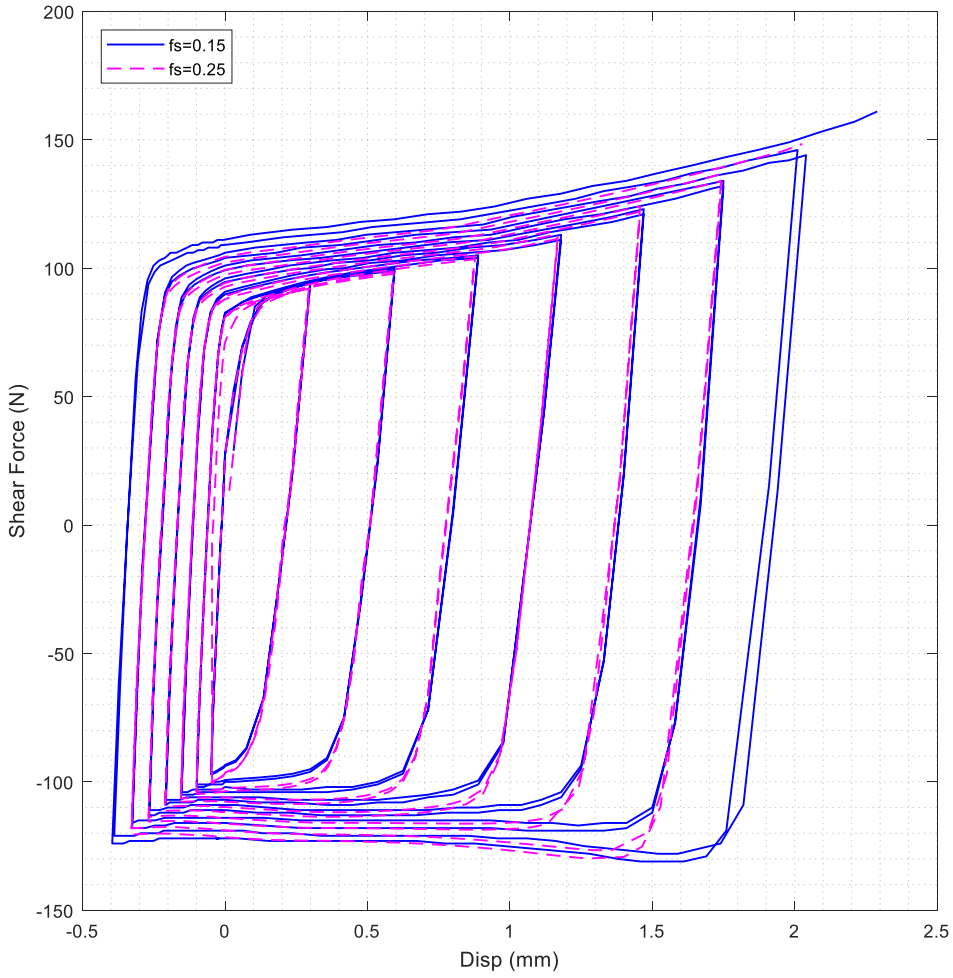

Figure 7.35 TPAD parametric study: friction coefficient (f_s)

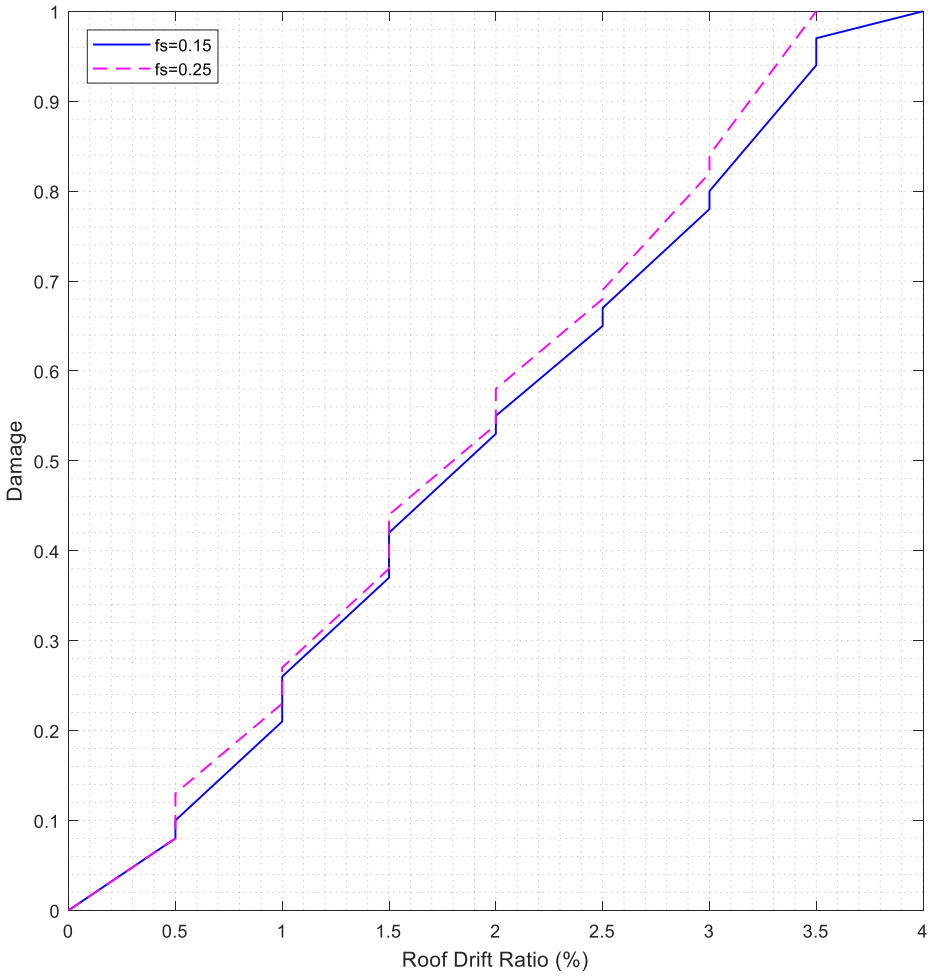

Figure 7.36 Effect of friction coefficient (f_s) on ductility of TPAD

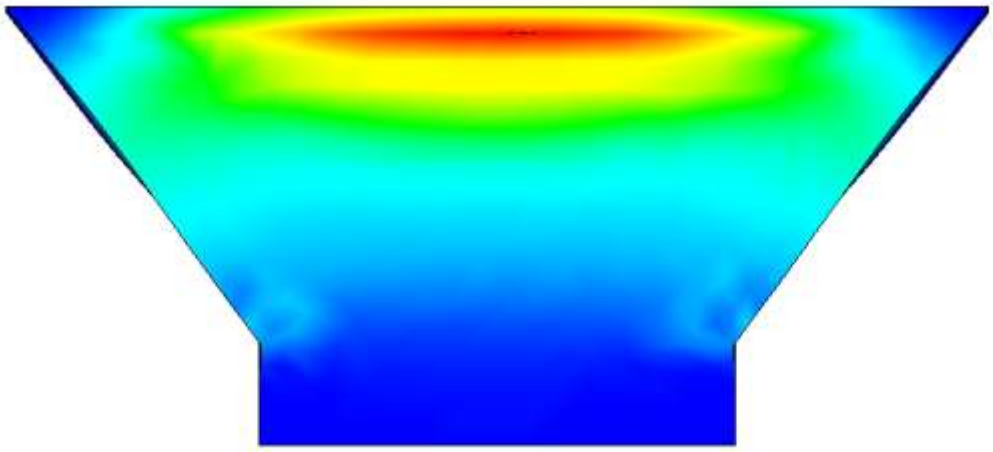

Figure 7.37 Damage counter for TPAD-9 at the onset of crack initiation

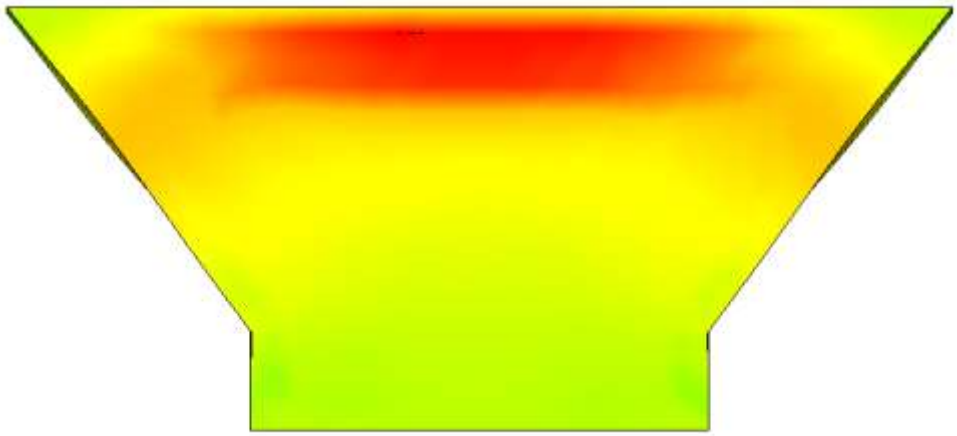

Figure 7.38 Von-mises stress counter for TPAD-9 at the onset of crack initiation

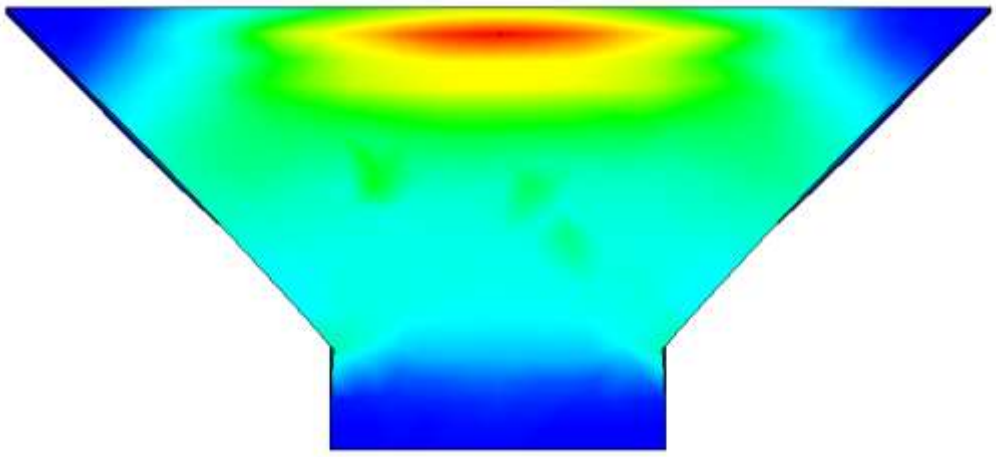

Figure 7.39 Damage counter for TPAD-10 at the onset of crack initiation

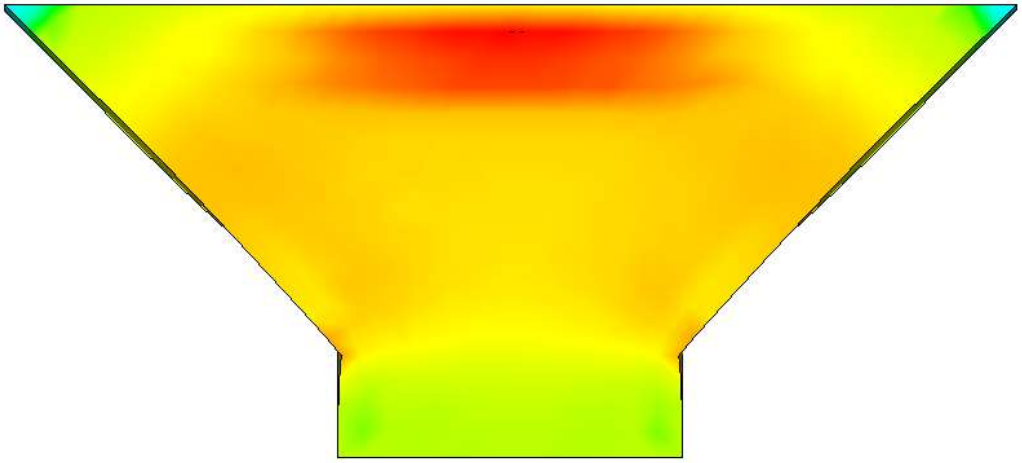

Figure 7.40 Von-mises stress counter for TPAD-10 at the onset of crack initiation

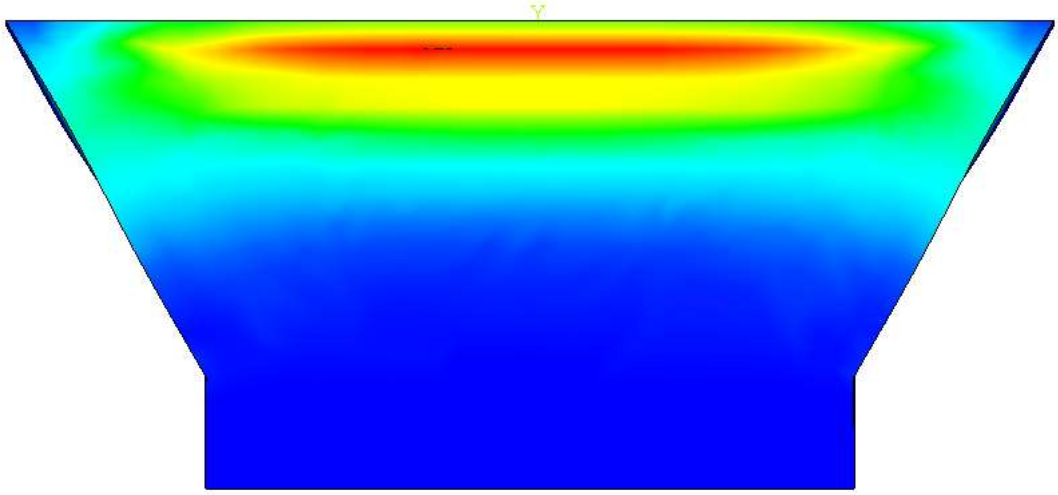

Figure 7.41 Damage counter for TPAD-11 at the onset of crack initiation

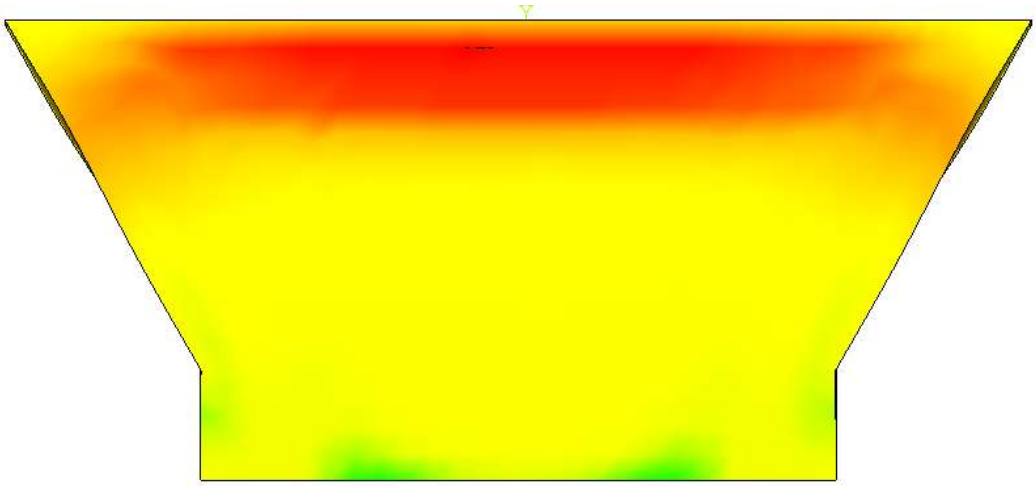

Figure 7.42 Von-mises stress counter for TPAD-11 at the onset of crack initiation

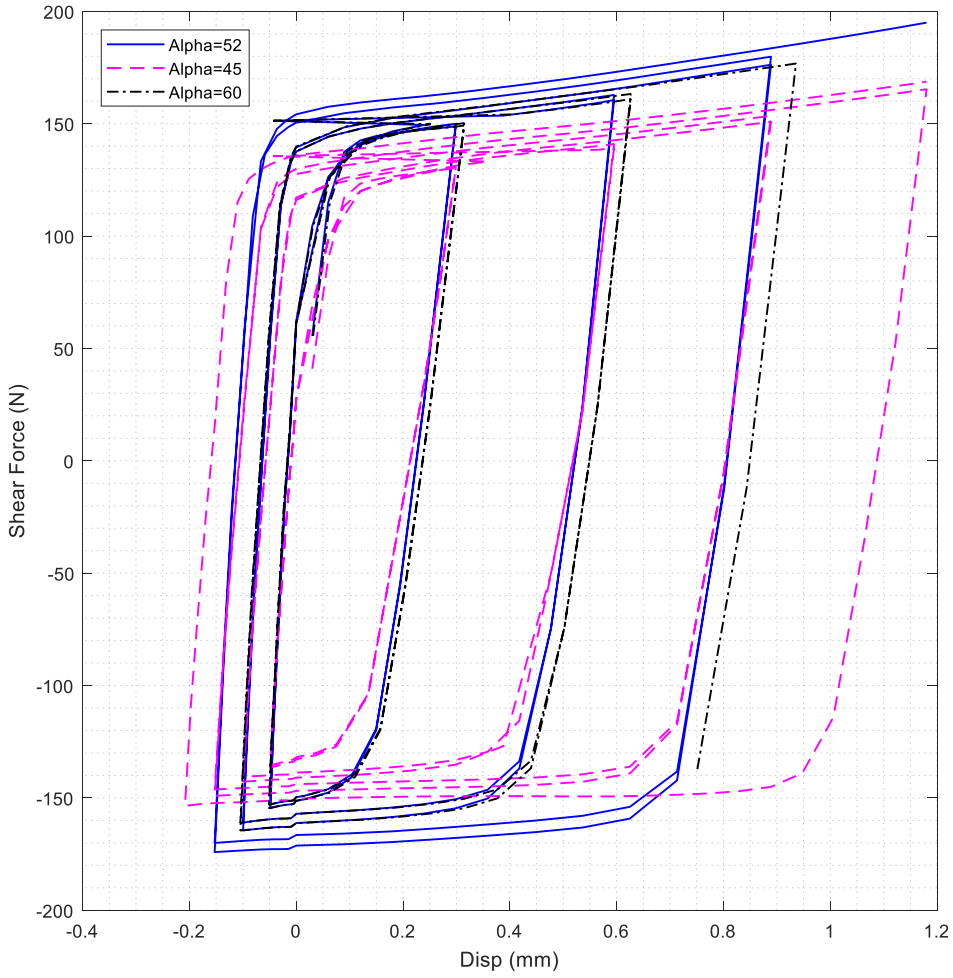

Figure 7.43 TPAD parametric study: alpha (α)

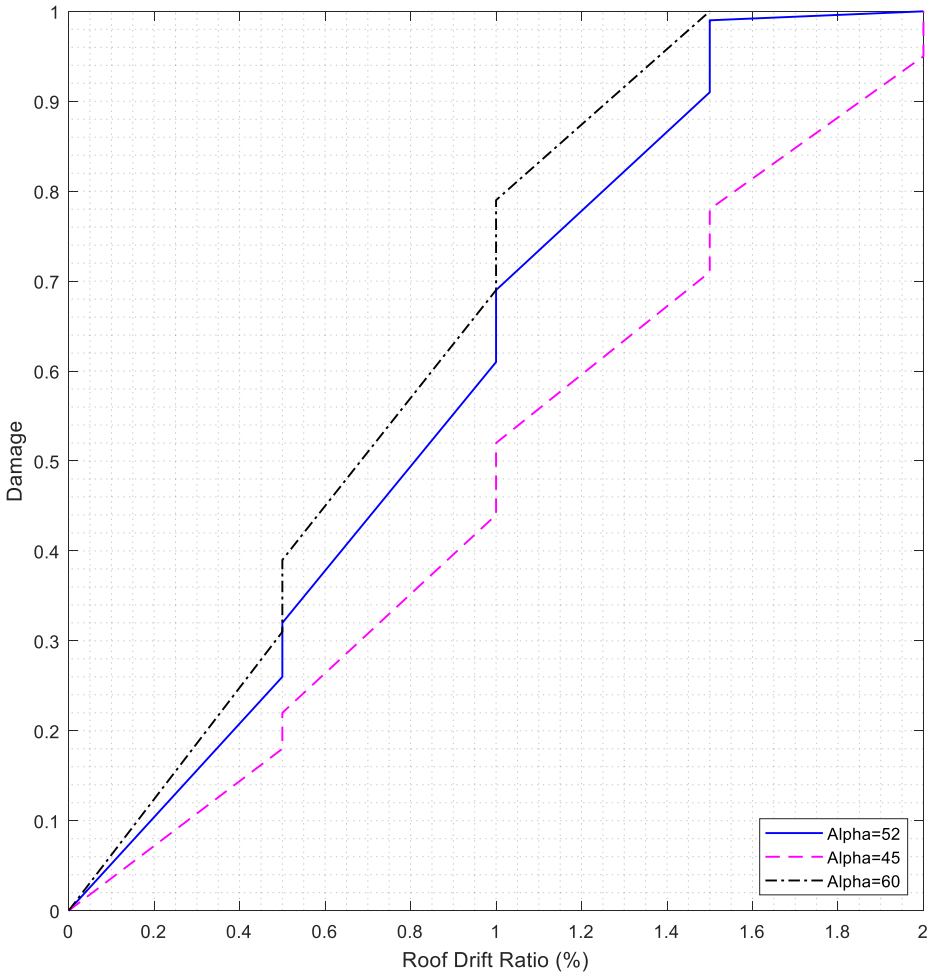

Figure 7.44 Effect of alpha (α) on ductility of TPAD

Chapter 8 Conclusions and Future Studies

8.1 Conclusions

In this study, three different configuration types of self-centering eccentrically braced frames (SCEBF) including SCEBF-K, SCEBF-D, and SCEBF-Y were proposed and then investigated through both analytical study and finite element simulation study. Experimental testing results of a full-scale one-story one-bay D-type SCEBF module frame specimen conducted by Tong, Zhang [50] was used to validate both the finite element simulation and analytical formulation.

It is found that after severe cyclic loading the SCEBF module frames with replaceable hysteric dampers exhibits almost identical stiffness, strength, re-centering ability, and energy dissipation capacity to that of the initial SCEBF structure. The behavior of different SCEBF systems are investigated through nonlinear static and nonlinear time history analysis. First, the behavior of SCEBFs with horizontal rocking link beam (SCEBF-K and SCEBF-D type) were investigated and compared with the conventional EBFs. Then the performance of SCEBFs with vertical rocking link beam (SCEBF-Y type) was studied and compared with the conventional EBFs. A summary of the research findings are listed as follows:

- In the SCEBF structures with horizontal rocking links (K-type and D-type), RHD devices are attached between the rocking link beam and neighboring

columns or beam joints to act as replaceable fuse devices, that would keep other members damage free, while post-tensioning cables are providing the primary re-centering force. Therefore, in the SCEBF structures, all primary structural members including rocking links are intended to remain undamaged and functional after design basis earthquakes with negligibly small residual drift. As the simulation results suggest, not only SCEBF can be designed to possess the strength and stiffness comparable to conventional EBF, but also it has the capability of re-centering itself after the design basis earthquake and potential for increased ductility and resilience. The parametric study shows that key structural parameters such as the equivalent yield strength, the post-gap opening stiffness of SCEBFs with horizontal rocking links (K-type and D-type) can be adjusted by selecting different post-tensioning cable length and initial stress levels. In the parametric study, based on nonlinear numerical analysis results, Case-A design which its PT cables have the lowest initial stress and length among all three cases, is preferred for both the K-type and D-type SCEBF structures since this case needs less pre-stressing cables and lower initial post-tensioning stress while residual drift is comparable (slightly lower) to the other two cases in this study.

- In the SCEBF-Y structures, RHD devices act as replaceable hysteric fuse devices which keep primary structural members elastic (except for column bases which develop plastic hinges at large roof drift ratio), while the re-centering capability is achieved by post-tensioning (PT) strands. It is worth

noting that recent full-scale experiments on RHD devices have shown that RHD devices can be quickly removed and replaced [50]. In the SCEBF-Y system, residual inter-story drift is negligibly small, and all primary structural members such as rocking links are intended to stay damage free and remain functional after design basis earthquake in active seismic regions.

- Prototype design and nonlinear finite element analysis results reveal that the SCEBF-Y system can be designed to have the strength and stiffness values comparable to conventional EBF systems. It is found that the flexural stiffness of the bracing assembly K_r controls the initial stiffness of the SCEBF-Y module structure. Since K_r depends on the brace section size, the braces in the SCEBF-Y structures should be designed as a beam-column member subjected to both axial force and bending moments transferred from the rocking links. Meanwhile, PT cable properties along with rocking link length are key design parameters controlling the post-gap opening stiffness of the SCEBF-Y structures. The parametric study demonstrates that by selecting different PT cable initial stress level and cable length, important structural properties of the SCEBF-Y structure such as the post-gap opening stiffness and equivalent "yield" strength can be tuned to desirable values. Based on the parametric study results, Case-A which its PT cables have the lowest initial stress and length among all three cases appears to be a very appealing design configuration since not only this case requires lower initial post-tensioning stress but also in this case PT cables length are within the story height. While this work is focused on

demonstrating the feasibility of the SCEBF-Y system in low-rise to mid-rise buildings, a one-story SCEBF-Y module frame can be prefabricated in a steel shop and installed to building frames on site; therefore, it can also be used for either high-rise buildings or retrofitting existing structures.

- A new metallic hysteric damper called TPAD was developed to be utilized in the proposed SCEBF structures. TPAD is a trapezoidal plate connected to a round bar, and its design is inspired by the design of TADAS devices [1]. It is optimized based on fracture investigation [2] through parametric studies. In parametric studies, cyclic loading has been applied to TPADs with different properties to investigate the overall behavior of TPADs. It is found that TPAD's height (h), slope ratio (α) and thickness (t) significantly affect the ductility of TPAD, while friction coefficient (f_s) and height of rectangular part of TPAD (k) has minor effects on the ductility of TPAD. Moreover, TPAD's height (h) and thickness (t) also have significant effects on its initial stiffness, post-yield stiffness and maximu, stress.

8.2 Future Studies

1. As mentioned in Chapters 4 and 5, for SCEBF K-type and D-type with the current design, the gap-opening expansion phenomenon still exists, and the relative displacement between columns is not zero. Special detailing (e.g., those proposed by Garlock, Sause [49] and Garlock and Li [26]) needs to be applied to keep the SCEBFs free of the floor slab restraints and to prevent

large axial force due to the restraint of the gap opening. The restraint of gap-opening expansion due to column is considered in this study; however, the restraint caused by floor slab is not considered in this study by assuming special detailing would be adopted for the current design. However, it is worth further study to develop refined practical detailing so that the restraints caused by both floor slabs and columns can be alleviated in future study of SCEBFs.

2. In this study, the overall performance of the proposed SCEBFs (K, D, and Y-type) are studied up to the DBE earthquake. Thus, future research is suggested to investigate the ultimate behavior of SCEBFs through maximum considered earthquake (MCE).
3. Experimental test of full-scale TPADs with different configurations is advisable for a thorough study of its performance. Moreover, a thorough TPAD FE simulation with full-scale dimensions along with further parametric studies are recommended.

Appendix

```
*deck,usermat     USERDISTRIB  parallel                    gal
     subroutine usermat(
    &               matId, elemId,kDomIntPt, kLayer, kSectPt,
    &               ldstep,isubst,keycut,
    &               nDirect,nShear,ncomp,nStatev,nProp,
    &               Time,dTime,Temp,dTemp,
    &               stress,ustatev,dsdePl,sedEl,sedPl,epseq,
    &               Strain,dStrain, epsPl, prop, coords,
    &               var0, defGrad_t, defGrad,
    &               tsstif, epsZZ,
    &               var1, var2, var3, var4, var5,
    &               var6, var7, var8)

cc**********************************************************************
******

#include "impcom.inc"
c
     INTEGER
```

```
     &                matId, elemId,
     &                kDomIntPt, kLayer, kSectPt,
     &                ldstep,isubst,keycut,
     &                nDirect,nShear,ncomp,nStatev,nProp
      DOUBLE PRECISION
     &                Time,   dTime,   Temp,   dTemp,
     &                sedEl,  sedPl,   epseq,  epsZZ
      DOUBLE PRECISION
     &                stress  (ncomp  ), ustatev (nStatev),
     &                dsdePl  (ncomp,ncomp),
     &                Strain  (ncomp  ), dStrain (ncomp  ),
     &                epsPl   (ncomp  ), prop    (nProp  ),
     &                coords  (3),
     &                defGrad (3,3),     defGrad_t(3,3),
     &                tsstif  (2)


      DOUBLE PRECISION var0, var1, var2, var3, var4, var5,
     &                var6, var7, var8


c****************** User defined part
**************************************
c           write(*,*) "UPF successful"
```

```
c --- parameters
c
      INTEGER         mcomp
      DOUBLE PRECISION SMALL,
     &                TWOTHIRD, sqTiny
      PARAMETER       (SMALL      = 1.d-08,
     &                sqTiny     = 1.d-20,
     &                TWOTHIRD   = 2.0d0/3.0d0,
     &                mcomp      = 6
     &                )
c
      EXTERNAL        vzero, vmove, get_ElmData
      DOUBLE PRECISION sigElp(mcomp), dsdeEl(mcomp,mcomp), G(mcomp),
     &                sigDev(mcomp), JM    (mcomp,mcomp), dfds(mcomp),
     &                sigi  (mcomp), strainEl(mcomp)

c     DATA G/1.0D0,1.0D0,1.0D0,0.0D0,0.0D0,0.0D0/
c
      INTEGER         i, j
      DOUBLE PRECISION pEl,   qEl,     pleq_t,  sigy_t , sigy,
     &                dpleq, pleq,
     &                young, posn,    sigy0,   dsigdep,
```

```
     &               elast1,elast2,
     &               fratio,  con1,    con2, dperr(3)
      DOUBLE PRECISION Et,Gs,d,landa,young0,dsigdep0
      DOUBLE PRECISION s1,s2,s3,s4,s5,s6,svon,d0,dsdeEl0(ncomp,ncomp)
      DOUBLE PRECISION Triax,Triax0,Pleqt,VGI,VGIC,VGIC0,Triaxav,alfa
      DOUBLE PRECISION dmg_key,VGIf,SEDf,sedPl0,dlast,
     &               Fract_index,ALPHA(ncomp),Pleqti,Pleqt2
     &      ,Stressi(ncomp),epsPli(ncomp),beta,Gs0,davg,sylast,hkey,pq
     &      ,pkin,piso,hard_key,HkeyC
     &      ,stiffness_key,yield_key
C     DOUBLE PRECISION EBULK,EFFG,EFFLAM,EFFHRD
c**********************************************************************
*****


c *** get props
      young0    = prop(1)
      posn      = prop(2)
      sigy0     = prop(3)
      Et        = prop(4)
      VGIC0     = prop(5)
      alfa      = prop(6)
      dmg_key   = prop(7)
```

```
c      IF (dmg_key.EQ.0.0) THEN
       VGIf   = prop(8)
c      ELSE
c       SEDf   = prop(8)
c      END IF
       beta   = prop(9)
       hkey   = prop(10)
       pq   = prop(11)
       pkin   = prop(12)
       piso   = prop(13)
       Hard_key   = prop(14)
       HkeyC   = prop(15)
       stiffness_key   = prop(16)
       yield_key   = prop(17)


c *** recall state variables
      pleq_t   = ustatev(1)
      pleq     = pleq_t
      Do i=1,ncomp
       epsPl(i)=ustatev(i+1)
       ALPHA(i)=ustatev(i+11)
```

```
      End Do
c      sigy=ustatev(8)
c      sigy=ustatev(8)
      d0=ustatev(9)
      d=d0
c      call vmove(ustatev(2), epsPl(1), ncomp)

      young=(1.0-d)**stiffness_key*young0
      Gs0     = young0 / (2.0*(1.0+posn))
      Gs      = young / (2.0*(1.0+posn))
      landa=young/((1.0-2.0*posn)*(1.0+posn))
C      ELAM=posn*landa
      elast1=posn*landa
      elast2=Gs

c *** define tsstif(1) since it is used for calculation of hourglass stiffness
      tsstif(1) = elast2
      dsigdep0  = young0*Et/(young0-Et)

      dsdeEl (1,1) =landa*(1.0 - posn)
      dsdeEl (2,2) =landa*(1.0 - posn)
      dsdeEl (3,3) =landa*(1.0 - posn)
```

```
      dsdeEl (4,4) = Gs
      dsdeEl (5,5) = Gs
      dsdeEl (6,6) = Gs
      dsdeEl (1,2) = posn * landa
      dsdeEl (1,3) = posn * landa
      dsdeEl (2,1) = posn * landa
      dsdeEl (3,1) = posn * landa
      dsdeEl (3,2) = posn * landa
      dsdeEl (2,3) = posn * landa

c      call vzero(sigi(1),ncomp)
      call get_ElmData ('ISIG', elemId,kDomIntPt, ncomp, sigi)
c
      do i=1,ncomp
        strainEl(i) = Strain(i) + dStrain(i) - epsPl(i)
      end do
c      call vzero(sigElp, 6)
      do i=1,ncomp
        sigElp(i) = sigi(i)
        do j=1,ncomp
c           dsdePl(j,i) = dsdeEl(j,i)
          dsdeEl0(i,j)=dsdeEl(i,j)
```

```
        sigElp(i) = sigElp(i)+dsdeEl(j,i)*strainEl(j)
      end do
    end do

    pEl = -(sigElp(1) + sigElp(2) + sigElp(3))/3.0

    IF (pEl.GT.0.0) Then
      dsigdep  = dsigdep0
      HKEY=HkeyC
    ELSE
      dsigdep  = (1-d)*dsigdep0
    END IF

    sigDev(1) = sigElp(1) + pEl
    sigDev(2) = sigElp(2) + pEl
    sigDev(3) = sigElp(3) + pEl
    sigDev(4) = sigElp(4)
    sigDev(5) = sigElp(5)
    sigDev(6) = sigElp(6)

c     qEl =
c    &  (sigDev(1)-ALPHA(1)) * (sigDev(1)-ALPHA(1))+
```

```
c     &  (sigDev(2)-ALPHA(2))*(sigDev(2)-ALPHA(2))+
c     &  (sigDev(3)-ALPHA(3))*(sigDev(3)-ALPHA(3))+
c     &  2.0*((sigDev(4)-ALPHA(4))*(sigDev(4)-ALPHA(4))+
c     &       (sigDev(5)-ALPHA(5))*(sigDev(5)-ALPHA(5))+
c     &       (sigDev(6)-ALPHA(6))*(sigDev(6)-ALPHA(6)))
c      qEl = sqrt((3.0/2.0) * qEl)

       qEl=(sigElp(1)-ALPHA(1)-sigElp(2)+ALPHA(2))**2
      &      +(sigElp(2)-ALPHA(2)-sigElp(3)+ALPHA(3))**2
      &      +(sigElp(3)-ALPHA(3)-sigElp(1)+ALPHA(1))**2
         DO i=NDIRECT+1,ncomp
          qEl=qEl+6.0*(sigElp(i)-ALPHA(i))**2
         END DO
          qEl=SQRT(qEl/2.0)
c      davg=1-(1-d)**0.25
c      sylast=ustatev(19)
       IF (dmg_key.EQ.0.0) THEN
       sigy=hkey**piso*sigy0
      &     +(1.0-hkey**piso)*(sigy0+dsigdep0*pleq)
       ELSE IF (dmg_key.EQ.0.25) THEN
       sigy=sqrt(sqrt(1-d))*(hkey**piso*sigy0
      &     +(1.0-hkey**piso)*(sigy0+(1-d)*dsigdep0*pleq))
```

```
      ELSE IF (dmg_key.EQ.0.5) THEN
      sigy=(1-d)**yield_key*(hkey**piso*sigy0
     &     +(1.0-hkey**piso)*(sigy0+dsigdep*pleq))
      ELSE
      sigy=(hkey**piso*sigy0
     &     +(1.0-hkey**piso)*(sigy0+(1-d)*dsigdep0*pleq))
      END IF
c
      fratio = (qEl / sigy) - 1.0

      IF (sigy .LE. 0.0 .or. fratio .LE. -1.d-08) Then

       do i=1,ncomp
         stress(i) = sigElp(i)
       end do

       do i=1,ncomp
         do j=1,ncomp
           dsdePl(j,i) = dsdeEl(j,i)
         end do
       end do
      ELSE
```

```
c       sigy_t = sigy


        DO i=1, ncomp
         dfds(i) = (3.0/2.0) * (sigDev(i)-ALPHA(i))/qEl
        END DO


        dpleq    = (qEl - sigy)/(3.0*Gs+dsigdep)
        pleq     = pleq_t + dpleq
c       sigy     = (1-d)*(sigy0)


        DO i=1, ncomp
C         Stressi(i) = Stress(i)
         epsPli(i) = epsPl(i)
        END DO
C       DO i = 1 , ncomp
c         stress(i) =  sigElp(i) - (2.0/3.0) * (qEl-sigy) * dfds(i)
C         stress(i) =  sigElp(i) - (qEl-sigy) * (sigDev(i)-ALPHA(i))/qEl
C     &              +  ALPHA(i)
C       END DO


        DO i = 1 , nDirect
         epsPl(i) = epsPl(i) + dfds(i) * dpleq
```

```
IF (hard_key.EQ.0.0) THEN
  ALPHA(i)=ALPHA(i)+TWOTHIRD*dsigdep*dfds(i)*dpleq*hkey**pkin
ELSE IF (hard_key.LT.0.0) THEN
ALPHA(i)=ALPHA(i)+TWOTHIRD*(1-D)*dsigdep0*dfds(i)*dpleq*hkey**pkin
ELSE
  ALPHA(i)=ALPHA(i)+TWOTHIRD*dsigdep0*dfds(i)*dpleq*hkey**pkin
END IF
  STRESS(i)=ALPHA(i)+TWOTHIRD*dfds(i)*sigy-pEL
 END DO
 DO i = nDirect + 1 , ncomp
  epsPl(i) = epsPl(i) + 2.0 * dfds(i) * dpleq
IF (hard_key.EQ.0.0) THEN
  ALPHA(i)=ALPHA(i)+TWOTHIRD*dsigdep*dfds(i)*dpleq*hkey**pkin
ELSE IF (hard_key.LT.0.0) THEN
ALPHA(i)=ALPHA(i)+TWOTHIRD*(1-D)*dsigdep0*dfds(i)*dpleq*hkey**pkin
ELSE
  ALPHA(i)=ALPHA(i)+TWOTHIRD*dsigdep0*dfds(i)*dpleq*hkey**pkin
END IF
  STRESS(i)=ALPHA(i)+TWOTHIRD*dfds(i)*sigy
 END DO
 epseq  = pleq
```

```
C       sedPl = sedPl + 0.5 * (sigy_t+sigy)*dpleq
        DO I=1,NCOMP
C         sedPl=sedPl+(STRESS(i)+Stressi(i))*(epsPl(i)-epsPli(i))/2.0
          sedPl=sedPl+STRESS(i)*(epsPl(i)-epsPli(i))
        END DO

      s1=stress(1)
      s2=stress(2)
      s3=stress(3)
      s4=stress(4)
      s5=stress(5)
      s6=stress(6)

      svon=sqrt((s1-s2)**2+(s1-s3)**2+(s3-s2)**2+6*(s4**2+s5**2+s6**2)
     &    )/sqrt(2.0)
      PEL=-(s1+s2+s3)/3.0
      IF (svon.LT.1.d-5) THEN
        Triax = 0.0
      ELSE
        Triax=PEL/svon
      END IF
      Pleqt = ustatev(10)
```

```
      VGIC=ustatev(8)
      Fract_index=ustatev(11)
      VGI = Fract_index*VGIC
      IF (Triax.LE.0.0) THEN
        Pleqt = ustatev(10)+dpleq
        ustatev(10)= Pleqt
        VGIC=VGIC0*exp(-alfa*Pleqt)
        ustatev(8)=VGIC
      END IF
      IF (Triax.GT.0.0 .AND. Triax.LT.10.0) THEN
C       Triaxav=(Triax0+Triax)/2.0
        Triaxav=Triax
        VGI = VGI-dpleq*exp(ABS(1.5*Triaxav))
      ELSE IF (Triax.LE.0.0 .AND. Triax.GT.-10.0) THEN
C       Triaxav=(Triax0+Triax)/2.0
        Triaxav=Triax
        VGI = VGI+dpleq*exp(ABS(1.5*Triaxav))
      ELSE
C       VGI = ustatev(11)*VGIC
      END IF
      Triaxav=ustatev(21)
      IF (VGI.LT.0.0) THEN
```

```
      VGI = 0.0
     END IF
     Fract_index=VGI/VGIC
c    davg=d
     IF (Fract_index.GE.1.0 .AND. Triax.LE.0.0) THEN
       IF (d.GE.0.99) THEN
       ELSE IF (VGI.GE.VGIf) THEN
        d=0.99
C        ELSE IF (dmg_key.EQ.0.0) THEN
C         d = (Pleqt/Pleqf)**BETA
       ELSE
       IF (ustatev(11).GE.1.0) THEN
        Pleqt2 = ustatev(20)+dpleq
       ELSE
        Pleqt2 = ustatev(20)+dpleq*(Fract_index-1.0)/
     &                        (Fract_index-ustatev(11))
       END IF
       ustatev(20)= Pleqt2
c       IF (ustatev(18).EQ.0.0) THEN
c        ustatev(18)=((1.0-ustatev(11))*Pleqt2+(Fract_index-1.0)*
c    &          (Pleqt2-dpleq))/(Fract_index-ustatev(11))
c        END IF
```

```
c       IF (ustatev(19).EQ.0.0) THEN
c        ustatev(19)=((1.0-ustatev(11))*VGI+(Fract_index-1.0)*
c     &           (VGI-dpleq*exp(ABS(1.5*Triaxav))))
c     &           /(Fract_index-ustatev(11))
c        END IF
c       Pleqti=ustatev(18)
C        d = (Pleqt/Pleqf)**BETA
        d = 1.0-exp(-beta*(Pleqt2)**(1.0-pq))
c        d = 1.0-exp(-beta*(Pleqt2 -ustatev(18))**(1.0-pq)
c     &              *(VGI-ustatev(19))**pq)
       END IF
      do i=1,ncomp
       strainEl(i) = Strain(i) + dStrain(i) - epsPl(i)
      end do
      do i=1,ncomp
       stress(i) = sigi(i)
       do j=1,ncomp
C          dsdePl(i,j) = (1.0-d)*dsdeEl(i,j)/(1.0-d0)
C        if (dstrain(j).ne.0.0) then
C          dsdePl(i,j)=(dsdePl(i,j)*strainEl(j)-dsdeEl(i,j)*strain(j))
C     &              /dstrain(j)
C        end if
```

```
          dsdeEl(i,j)=(1.0-d)**stiffness_key*dsdeEl(i,j)/
     &                (1.0-d0)**stiffness_key
          stress(i) = stress(i)+dsdeEl(i,j)*strainEl(j)
        end do
       end do
c      s1=stress(1)
c      s2=stress(2)
c      s3=stress(3)
c      s4=stress(4)
c      s5=stress(5)
c      s6=stress(6)

c      sylast=sqrt((s1-s2)**2+(s1-s3)**2+(s3-s2)**2+6*(s4**2+s5**2+s6**2)
c     &    )/sqrt(2.0)
c       ustatev(19)=sylast
c       davg=(d+d0)/2.0
c      ELSE
       END IF
       ustatev(11)=Fract_index
       sigy=sigy+((dsigdep+(1.0-d)*dsigdep/(1.0-d0))/2.0)*dpleq

       IF (qEl.LT.1.d-20) THEN
```

```
        con1 = 0.0
      ELSE
        con1 = (3.0*Gs/(3.0*Gs+dsigdep))*(qEl - sigy)/ qEl
      END IF
      con2 = TWOTHIRD*(3.0*Gs/(3.0*Gs+dsigdep) - con1)
C       DO i=1,ncomp
C         DO j=1,ncomp
C           JM(j,i) = 0.0
C         END DO
C       END DO
      DO i=1,nDirect
        JM(i,i) = 2.0/3.0
      END DO
      DO i=nDirect + 1,ncomp
        JM(i,i) = 1.0/2.0
      END DO
      JM(1,2) = -1.0/3.0
      JM(2,1) = JM(1,2)
      JM(1,3) = JM(1,2)
      JM(3,1) = JM(1,2)
      JM(2,3) = JM(1,2)
      JM(3,2) = JM(1,2)
```

```
      Gs=((1.0-d)**stiffness_key*Gs/(1.0-d0)**stiffness_key+Gs)/2.0
      DO i=1,ncomp
       DO j=1,ncomp
c          dsdeEl(i,j)=(dsdeEl0(i,j)+dsdeEl(i,j))/2.0
          dsdePl(i,j) =    dsdeEl(i,j) - 2.0*Gs
     &          * (  con2 * dfds(i) * dfds(j) + con1 * JM(i,j) )
       END DO
      END DO
      do i=1,ncomp
       do j=1,ncomp
         dsdePl(j,i) = dsdeEl(j,i)
       end do
      end do

C       for BISO
C       EFFG=Gs*sigy/qEL
C       EFFG=Gs*(sigy+dsigdep*dpleq)/qEL
C       EBULK=young/(3.0*(1.0-2.0*posn))
C       EFFLAM=(3.0*EBULK-2.0*EFFG)/3.0
C       EFFHRD=3.0*Gs*dsigdep/(3.0*Gs+dsigdep)-3.0*EFFG
C       DO i=1, NDIRECT
C        DO j=1, NDIRECT
```

```
C           dsdePl(j, i)=EFFLAM
C         END DO
C         dsdePl(i, i)=2.0*EFFG+EFFLAM
C       END DO
C       DO i=NDIRECT+1, ncomp
C         dsdePl(i, i)=EFFG
C       END DO
C       DO i=1, ncomp
C         DO j=1, ncomp
C           dsdePl(j,i)=dsdePl(j,i)+
C     &                 EFFHRD*TWOTHIRD*dfds(j)*TWOTHIRD*dfds(i)
C         END DO
C       END DO

c     END IF

      ustatev(1) = pleq
      do i=1,ncomp
        ustatev(i+1) = epsPl(i)
        ustatev(i+11) = ALPHA(i)
      end do
c
```

```
      END IF


      sedEl = 0.0
      DO i = 1 , ncomp
        sedEl = sedEl + 0.5*stress(i)*(Strain(i)+dStrain(i)-epsPl(i))
      END DO
c     ustatev(8) = sigy
      ustatev(9) = d
c
      return
      end
```

References

[1] Tsai K-C, Chen H-W, Hong C-P, Su Y-F. Design of steel triangular plate energy absorbers for seismic-resistant construction. Earthquake spectra. 1993;9:505-28.
[2] Amiri H, Aghakouchak A, Shahbeyk S, Engelhardt M. Finite element simulation of ultra low cycle fatigue cracking in steel structures. Journal of Constructional Steel Research. 2013;89:175-84.
[3] Roeder CW, Popov EP. Eccentrically Braced Steel Frames for Earthquakes. ASCE Journal of the Structures Division. 1978;104.
[4] Hjelmstad KD, Popov EP. Characteristics of Eccentrically Braced Frames. Journal of Structural Engineering. 1984;110:340-53.
[5] Kasai K, Popov EP. General behavior of WF steel shear link beams. J Struct Eng. 1986;112:362.
[6] Ricles JM, Popov EP. Dynamic analysis of seismically resistant eccentrically braced frames: University of California, Earthquake Engineering Research Center, Berkeley, California.; 1987.
[7] Engelhardt MD, Popov EP. On design of eccentrically braced frames. Earthquake Spectra. 1989;5:495.
[8] Garlock M, Li J, Blaisdell M. Floor diaphragm interaction with self-centering steel moment frames. Proc, 8th US National Conf on Earthquake Engineering (NCEE)2006.
[9] Zhou X. Experimental Study on Seismic Behavior of Self-centering Eccentrically Braced Steel Frame. Master Thesis, Department of Structural Engineering, Tongji University, Shanghai, China. . 2017.
[10] Kanvinde A, Deierlein G. Cyclic void growth model to assess ductile fracture initiation in structural steels due to ultra low cycle fatigue. Journal of engineering mechanics. 2007;133:701-12.
[11] Engelhardt MD, Popov EP. Earthquake Spectra. 1989;5:495.
[12] Libby JR. Eccentrically Braced Frames Construction—A Case History. AISC Engineering Journal. 1981;18:149.
[13] Popov EP, Manheim DN. Eccentric Bracing of Steel Frames in Seismic Design. Transactions. 1981;K.
[14] Popov EP, Engelhardt MD. Seismic eccentrically braced frames. Journal of Constructional Steel Research. 1988;10:321-54.
[15] Paul WR, Chia-Ming U. Testing Protocol for Short Links in Eccentrically Braced Frames. Journal of Structural Engineering. 2006;132:1183-91.
[16] Dusicka P, Itani AM, Buckle IG. Finite element investigation of steel built-up shear links subjected to inelastic deformations. Earthquake Engineering and Engineering Vibration. 2004;3:195-203.

[17] Zahrai SM, Bruneau M. Cyclic Testing of Ductile End Diaphragms for Slab-on-Girder Steel Bridges. Journal of Structural Engineering. 1999;125:987-96.
[18] Berman JW, Bruneau M. Tubular Links for Eccentrically Braced Frames. I: Finite Element Parametric Study. Journal of Structural Engineering. 2008;134:692-701.
[19] Berman JW, Bruneau M. Experimental and analytical investigation of tubular links for eccentrically braced frames. Eng Struct. 2007;29:1929.
[20] Okazaki T, Engelhardt MD. Cyclic loading behavior of EBF links constructed of ASTM A992 steel. J Constr Steel Res. 2007;63:751.
[21] Mansour N, Christopoulos C, Tremblay R. Experimental Validation of Replaceable Shear Links for Eccentrically Braced Steel Frames. Journal of Structural Engineering. 2011;137:1141-52.
[22] Nabil M, Constantin C, Robert T. Experimental Validation of Replaceable Shear Links for Eccentrically Braced Steel Frames. Journal of Structural Engineering. 2011;137:1141-52.
[23] Ghobarah A, Ramadan T. Bolted link-column joints in eccentrically braced frames. Eng Struct. 1994;16:33.
[24] Ricles J, Sause R, Peng SW, Lu LW. Experimental evaluation of earthquake resistant posttensioned steel connections. J Struct Eng. 2002;128:850.
[25] Rojas P, Ricles J, Sause R. Seismic performance of posttensioned steel moment resisting frames with friction devices. J Struct Eng. 2005;131:1.
[26] Garlock M, Li J. Steel self-centering moment frames with collector beam floor diaphragms. J Constr Steel Res. 2008;64:526.
[27] Garlock ME, Li J. Steel self-centering moment frames with collector beam floor diaphragms. Journal of Constructional Steel Research. 2008;64:526-38.
[28] Cheng C, Hsu C, Lin K. Seismic behavior of self-centering designed eccentrically braced frames. The 15th World Conference on Earthquake Engineering2012.
[29] Xu X, Zhang Y, Luo Y. Self-centering eccentrically braced frames using shape memory alloy bolts and post-tensioned tendons. Journal of Constructional Steel Research. 2016a;125:190-204.
[30] Xu X, Zhang Y, Luo Y. Self-centering modularized link beams with post-tensioned shape memory alloy rods. Engineering Structures. 2016b;112:47-59.
[31] Priestley MJN. Overview of PRESSS research program. PCI journal. 1991;36:50-7.
[32] El-Sheikh MT, Sause R, Pessiki S, Lu L-W. Seismic behavior and design of unbonded post-tensioned precast concrete frames. PCI journal. 1999;44:54-71.
[33] Kurama Y, Sause R, Pessiki S, Lu L-W. Lateral load behavior and seismic design of unbonded post-tensioned precast concrete walls. ACI Structural Journal. 1999;96:622-32.
[34] Garlock MEM. Design, analysis, and experimental behavior of seismic resistant post-tensioned steel moment resisting frames 2002.

[35] Ricles JM, Sause R, Garlock M, Zhao C. Post-tensioned seismic resistant connections for steel frames. J Struct Eng. 2001;127:113.
[36] Christopoulos C, Filiatrault A, Folz B. Seismic response of self-centring hysteretic SDOF systems. Earthquake engineering & structural dynamics. 2002a;31:1131-50.
[37] Christopoulos C, Filiatrault A, Uang CM, Folz B. Posttensioned energy dissipating connections for moment-resisting steel frames. J Struct Eng. 2002b;128:1111.
[38] Garlock MM, Ricles JM, Sause R. Experimental studies on full-scale post-tensioned steel connections. J Struct Eng. 2005;131:438.
[39] Tsai KC, Chou CC, Lin CL, Chen PC, Jhang SJ. Seismic self-centering steel beam-to-column moment connections using bolted friction devices. Earthquake Engineering & Structural Dynamics. 2008;37:627-45.
[40] Wolski M, Ricles JM, Sause R. Experimental study of a self-centering beam–column connection with bottom flange friction device. Journal of Structural Engineering. 2009;135:479-88.
[41] Lin Y-C, Sause R, Ricles JM. Seismic performance of steel self-centering, moment-resisting frame: hybrid simulations under design basis earthquake. Journal of Structural Engineering. 2013;139:1823-32.
[42] Lin Y-C, Sause R, Ricles J. Seismic Performance of a Large-Scale Steel Self-Centering Moment-Resisting Frame: MCE Hybrid Simulations and Quasi-Static Pushover Tests. Journal of Structural Engineering. 2013;139:1227-36.
[43] Roke DA. Damage-free seismic-resistant self-centering concentrically-braced frames: Lehigh University; 2010.
[44] Qiu C-X, Zhu S. High-mode effects on seismic performance of multi-story self-centering braced steel frames. Journal of Constructional Steel Research. 2016;119:133-43.
[45] Qiu C-X, Zhu S. Performance-based seismic design of self-centering steel frames with SMA-based braces. Engineering Structures. 2017;130:67-82.
[46] Qiu C, Zhu S. Shake table test and numerical study of self-centering steel frame with SMA braces. Earthquake Engineering & Structural Dynamics. 2017;46:117-37.
[47] Ghobarah A, Elfath HA. Rehabilitation of a reinforced concrete frame using eccentric steel bracing. Engineering structures. 2001;23:745-55.
[48] Massah SR, Dorvar H. Design and analysis of eccentrically braced steel frames with vertical links using shape memory alloys. Smart Materials and Structures. 2014;23:115015.
[49] Garlock MM, Sause R, Ricles JM. Behavior and design of post-tensioned steel frame systems. J Struct Eng. 2007;133:389.
[50] Tong L-W, Zhang Y, Zhou X, Keivan A, Li R. Experimental and Analytical Investigation of D-type Self-centering Steel Eccentrically Braced Frames with Replaceable Hysteretic. ASCE J Structural Engrg, in press. 2018.

[51] Hu X, Zhang Y, Moghaddasi B. NS. Seismic Performance of Reinforced Concrete Frames Retrofitted with Self-Centering Hybrid Wall. Advances in Structural Engineering. 2012;15:2131-43.
[52] Seo CY, Sause R. Ductility demands on self-centering systems under earthquake loading. ACI Struct J. 2005;102:275.
[53] Sause R, M Ricles J, Roke D, B Chancellor N, P Gonner N. Seismic Performance of a Self-Centering Rocking Concentrically-Braced Frame2010.
[54] Alehashem SMS, Keyhani A, Pourmohammad H. Behavior and performance of structures equipped with ADAS & TADAS dampers (a comparison with conventional structures). The 14th World Conference on Earthquake Engineering2008.
[55] Xia C, Hanson RD. Influence of ADAS element parameters on building seismic response. Journal of Structural Engineering. 1992;118:1903-18.
[56] Su Y, Hanson R. Comparison of effective supplemental damping equivalent viscous and hysteretic. Proceedings of the the 4th US National Conference on Earthquake Engineering1990.
[57] WHITTAKER A. EARTHQUAKE SIMULAT0R TESTING 0F STEEL PLATE ADDED DAMPING. EARTHQUAKE ENGINEERING. 1989.
[58] Bergman DM, Goel SC. Evaluation of cyclic testing of steel-plate devices for added damping and stiffness: Department of Civil Engineering, University of Michigan; 1987.
[59] Xu X, Zhang Y, Luo Y. Self-centering links using post-tensioned composite tendons. Advances in Structural Engineering. 2018;21:1302-12.
[60] Okazaki T, Arce G, Ryu H-C, Engelhardt MD. Experimental Study of Local Buckling, Overstrength, and Fracture of Links in Eccentrically Braced Frames. Journal of Structural Engineering. 2005;131:1526-35.
[61] Okazaki T, Engelhardt MD, Nakashima M, Suita K. Experimental Performance of Link-to-Column Connections in Eccentrically Braced Frames. ASCE Journal of Structural Engineering. 2006;132:1201-11.
[62] Speicher MS, Harris III JL. Collapse Prevention seismic performance assessment of new eccentrically braced frames using ASCE 41. Engineering Structures. 2016;117:344-57.
[63] Richards P, Uang CM. Testing protocol for short links in eccentrically braced frames. J Struct Eng. 2006;132:1183.
[64] Paul WR. Estimating the Stiffness of Eccentrically Braced Frames. Practice Periodical on Structural Design and Construction. 2010;15:91-5.
[65] CSI. SAP2000: Integrated finite element analysis and design of structures. Version 18.0, Computers and Structures Inc., Berkeley, California, USA. 2016.
[66] Okazaki T, Engelhardt MD, Nakashima M, Suita K. Experimental performance of link-to-column connections in eccentrically braced frames. J Struct Eng. 2006;132:1201.
[67] FEMA P. Commentary for the seismic rehabilitation of buildings. FEMA-356, Federal Emergency Management Agency, Washington, DC. 2000.

[68] Freddi F, Dimopoulos CA, Karavasilis TL. Rocking damage-free steel column base with friction devices: design procedure and numerical evaluation. Earthquake Engineering & Structural Dynamics. 2017;46:2281-300.
[69] Somerville PG, Smith NF, Graves RW, Abrahamson NA. Modification of empirical strong ground motion attenuation relations to include the amplitude and duration effects of rupture directivity. Seismological Research Letters. 1997;68:199-222.
[70] Moghaddasi NS, Zhang Y. Seismic analysis of diagrid structural frames with shear-link fuse devices. Earthquake Engineering and Engineering Vibration. 2013;12:463-72.
[71] Liu J, Bai Y, Xu C. Evaluation of ductile fracture models in finite element simulation of metal cutting processes. Journal of Manufacturing Science and Engineering. 2014;136:011010.